7-16-2009

EPR, ENDOR and DFT Studies on X-Irradiated Single Crystals of L-Lysine Monohydrochloride Monohydrate and L-Arginine Monohydrocloride Monohydrate

Yiying Zhou

EPR, ENDOR AND DFT STUDIES ON X-IRRADIATED SINGLE CRYSTALS OF L-LYSINE MONOHYDROCHLORIDE MONOHYDRATE AND L-ARGININE MONOHYDROCLORIDE MONOHYDRATE

by

YIYING ZHOU

Under the Direction of William H. Nelson

ABSTRACT

When proteins and DNA interact, arginine and lysine are the two amino acids most often in close contact with the DNA. In order to understand the radiation damage to DNA in vivo, which is always associated with protein, it is important to learn the radiation chemistry of arginine and lysine independently, and when complexed to DNA. This work studied X-irradiated single crystals of L-lysine monohydrochloride dihydrate (L-lysine·HCl·2H_2O) and L-arginine monohydrochloride monohydrate (L-arginine·HCl·H_2O) with EPR, ENDOR, EIE techniques and DFT calculations. In both crystal types irradiated at 66K, the carboxyl anion radical and the decarboxylation radical were detected. DFT calculations supported these assignments. Specifically, the calculations performed on the cluster models for the carboxyl anion radicals reproduced the proton transfers to the carboxyl group from the neighboring molecules through the hydrogen bonds. Moreover, computations supported the identification of one radical type as the guanidyl radical anion with an electron trapped by the guanidyl group. In addition, the radical formed by dehydrogenation of C5 was identified in the L-arginine·HCl·H_2O crystals

irradiated at 66K.

For both crystal types, the deamination radicals and the dehydrogenation radicals were identified following irradiation at 298K. Different conformations of main-chain deamination radicals were detected at 66K and at 298K. In L-lysine·HCl·$2H_2O$, these conformations are the result of the different rotation angles of the side chain. In L-arginine·HCl·H_2O, one conformation at 66K has no O-H dipolar protons while the others have two O-H dipolar protons. In L-lysine·HCl·$2H_2O$, two radicals with very similar sets of hyperfine couplings were identified as the result of dehydrogenation from C3 and C5. Two other radicals in low concentration detected only at 66K, were tentatively assigned as the radical dehydrogenated from C3 and the side-chain deamination radical. In L-argnine·HCl·H_2O, the radicals from dehydrogenation at C5 and C2 also were identified. DFT calculations supported these assignments and reproduced conformations of these radicals.

Finally, based on the radicals detected in the crystal irradated at 66K and at 298K, the annealing experiments from the irradiation at 66K, and the previous studies on the irradiated amino acids, the mechanisms of the irradiation damage on lysinie and arginine were proposed.

INDEX WORDS: EPR, ENDOR, EIE, L-lysine monohydrochloride dihydrate, L-arginine monohydrochloride monohydrate, Single crystal, Irradiation, Gaussian, DFT

EPR, ENDOR AND DFT STUDIES ON X-IRRADIATED SINGLE CRYSTALS OF L-LYSINE MONOHYDROCHLORIDE MONOHYDRATE AND L-ARGININE MONOHYDROCLORIDE MONOHYDRATE

by

YIYING ZHOU

A Dissertation Submitted in Partial Fulfillment of the Requirements for the Degree of

Doctor of Philosophy

in the College of Arts and Sciences

Georgia State University

2009

EPR, ENDOR AND DFT STUDIES ON X-IRRADIATED SINGLE CRYSTALS OF L-LYSINE MONOHYDROCHLORIDE MONOHYDRATE AND L-ARGININE MONOHYDROCLORIDE MONOHYDRATE

by

YIYING ZHOU

Committee Chair: Dr. William H. Nelson

Committee: Dr. Stuart A. Allison
Dr. Douglas Gies
Dr. Gary Hastings
Dr. Vadym Apalkov

Electronic Version Approved:

Office of Graduate Studies
College of Arts and Sciences
Georgia State University
August 2009

To my parents, Shujuan Dai and Lingyun Zhou

ACKNOWLEDGEMENTS

I would like to express my deepest gratitude to my supervisor, Dr. William H. Nelson, for his constant encouragement, useful suggestions, great patience and kindness. Without his invaluable guidance and continuous support I could not have worked out this thesis. My great gratitude also goes to my dissertation committee, Dr. Stuart A. Allison, Dr. Douglas Gies, Dr. Gary Hastings, Dr. Vadym Apalkov, Dr. Mark Stockman, Dr. A. G. Unil Perera, and Dr. Thomas L. Netzel for their valuable help, discussions, and suggestions for this research work.

I would also like to thank Dr. Tomek Wasowicz, Dr. Sibel Tokdemir and Dr. Nayana Jayatilaka for their kind help and friendship.

Finally, I am always indebted to my beloved family for their endless love and support. I dedicate my dissertation to my parents, my elder brother and my husband.

TABLE OF CONTENTS

LIST OF TABLES

LIST OF FIGURES

LIST OF ABBREVIATIONS

EPR	Electron Paramagnetic Resonance
ENDOR	Electron Nuclear DOuble Resonance spectroscopy
EIE	ENDOR-Induced EPR
DFT	Density Functional Theory
G03	Gaussian 03 program
Lys	Lysine
Arg	Arginine
DNA	Deoxyribonucleic Acid
NMR	Nuclear Magnetic Resonance

CHAPTER 1.

INTRODUCTION

Ionizing radiation effects on deoxyribonucleic acid (DNA) have been intensively studied for many years because the genetic information is encoded by DNA molecules. However, in order to understand the radiation chemistry of DNA in vivo, it is necessary to know how the cellular environments of DNA can modify the processes taking place in DNA itself. In the cell nucleus the DNA is tightly associated with special proteins (histones) and packaged into chromosomes.[1] The main objective of this work is to explore the effects of radiation on two of the most common amino acids in histones, lysine (Scheme 1a) and arginine (Scheme 1b). As will be reviewed briefly below, these two amino acids are most frequently in contact with DNA in chromosomes.

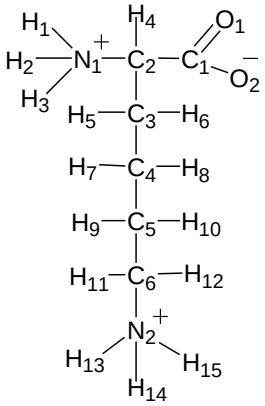

Scheme 1.1(a) *Lysine molecule in L-lys·HCl·2H₂O*

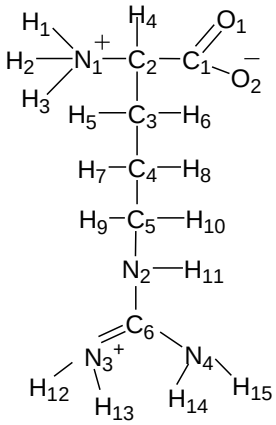

Scheme 1.1(b) *Arginine molecule in L-Arg·HCl·H₂O*

It is useful to review first some details about the organization of the chromosome in the cell nucleus. The chromosome is the largest and most visible physical structure involved in the transfer of genetic information.[1] The different levels of chromosome organization are shown in Fig. 1.1. Fundamentally, DNA molecules exist as long unbranched double helices consisting of two antiparallel polynucleotide chains. These two chains are held together by specific hydrogen bonds between four

organic bases: adenine (A) to thymine (T), via two bonds, and guanine (G) to cytosine (C), via three bonds[1]. The fundamental unit of a chromosome is the nucleosome, and its structure is shown in Fig. 1.2. In a nucleosome, the DNA double helix, consisting of approximately 146 base pairs, wraps 1⅔ superhelical turns around a histone octamer, consisting of 2 copies each of the core histones H2A, H2B, H3 an H4[2, 3] (see Fig. 1.2a). Also, linker histone H1 binds the core histones to the entry and exit sites of DNA[4, 5] (see Fig. 1.1), thus locking the DNA into a place allowing the formation of higher order structure[5]. The repeating nucleosomes with their intervening "linker" DNA resemble "beads on a string of DNA" under an electron microscope.[1, 6] A chain of nucleosomes can be folded into chromatin fiber with diameter of 30nm.[6] The chromatin fiber is arranged into loops along a central protein scaffold and then further compacted into metaphase chromosome. The chromosome packages the DNA into a smaller volume to fit within the cell, and to serve as a mechanism for controlling gene expression and DNA replication.

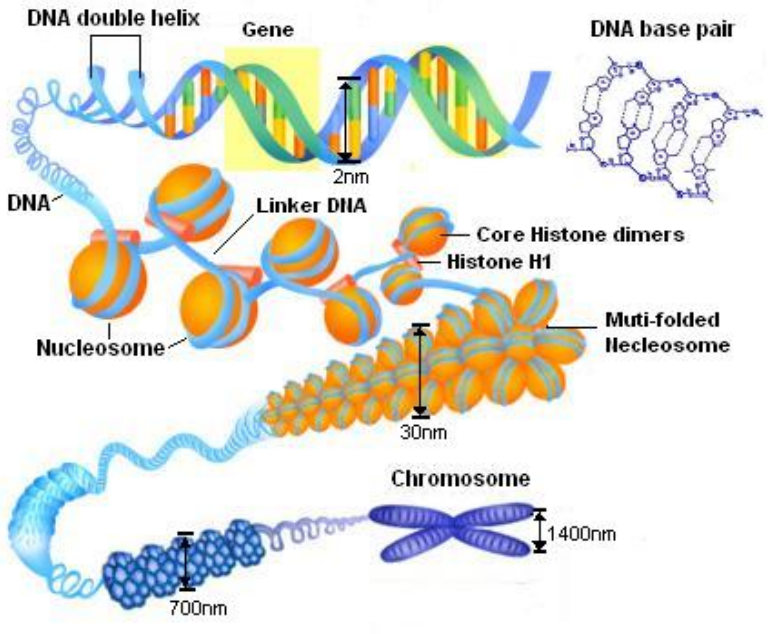

Fig. 1.1 *Structure of chromosome.*[7]

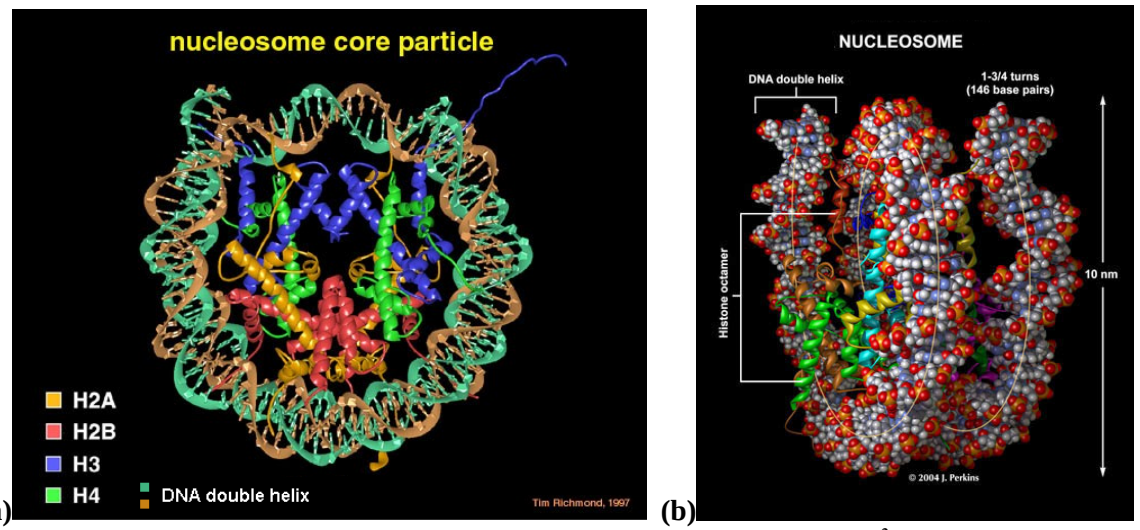

(a) **(b)**

Fig. 1.2 *Structure of nuleosome;* ***(a)*** *The view is down the DNA superhelix axis.*[2] ***(b)*** *The DNA superhelix is rotate 60° around the dyad axis compared to the view in (a).*[3, 8]

In the nucleosome, all the core histones are conserved in length and amino acid sequence, and they contain relatively large amounts of lysine and arginine (more than 20%): histones H2A and H2B contain more lysine, H3 and H4 contain more arginine. The linker histones (H1 or H5) are particularly rich in lysine and are slightly larger than the core histones. Both core histones and linker histones are highly basic, and this character facilitates histone-DNA interactions.[1] Each nucleosome contains more than 120 direct protein-DNA interactions and several hundred water mediated interactions.[3] The direct protein-DNA interactions, in terms of hydrogen bonds and van der Waals contacts, predominantly involve arginine and lysine residues.[3] In the hydrogen bonds between the amino acids and DNA bases, arginine and lysine strongly favor guanine but also very often interact with thymine and cytosine. In comparison to other amino acids, the long side chains of arginine and lysine allow them better access to the bases than for other amino acids. In addition, the main chain and side chain amino protons are important participants in hydrogen bonds with DNA bases or base pairs.[9] Several possible conformations of these hydrogen bonds are shown in Fig. 1.3(a-i). Specially, the main chain nitrogen of lysine is the acceptor in hydrogen bonds to the base pair G:C (see Fig. 1.3i). Due to the specificity of the hydrogen bonds between amino acids and DNA bases (or base pairs), a specific base sequence can be recognized by these DNA-binding amino acids. Hydrogen bonds between amino acids and the DNA backbone, and van der Waals contacts,

are important contributors to the stability of DNA-protein complexes. Arginine and lysine also make the largest number of these interactions in comparison to other amino acids.[9]

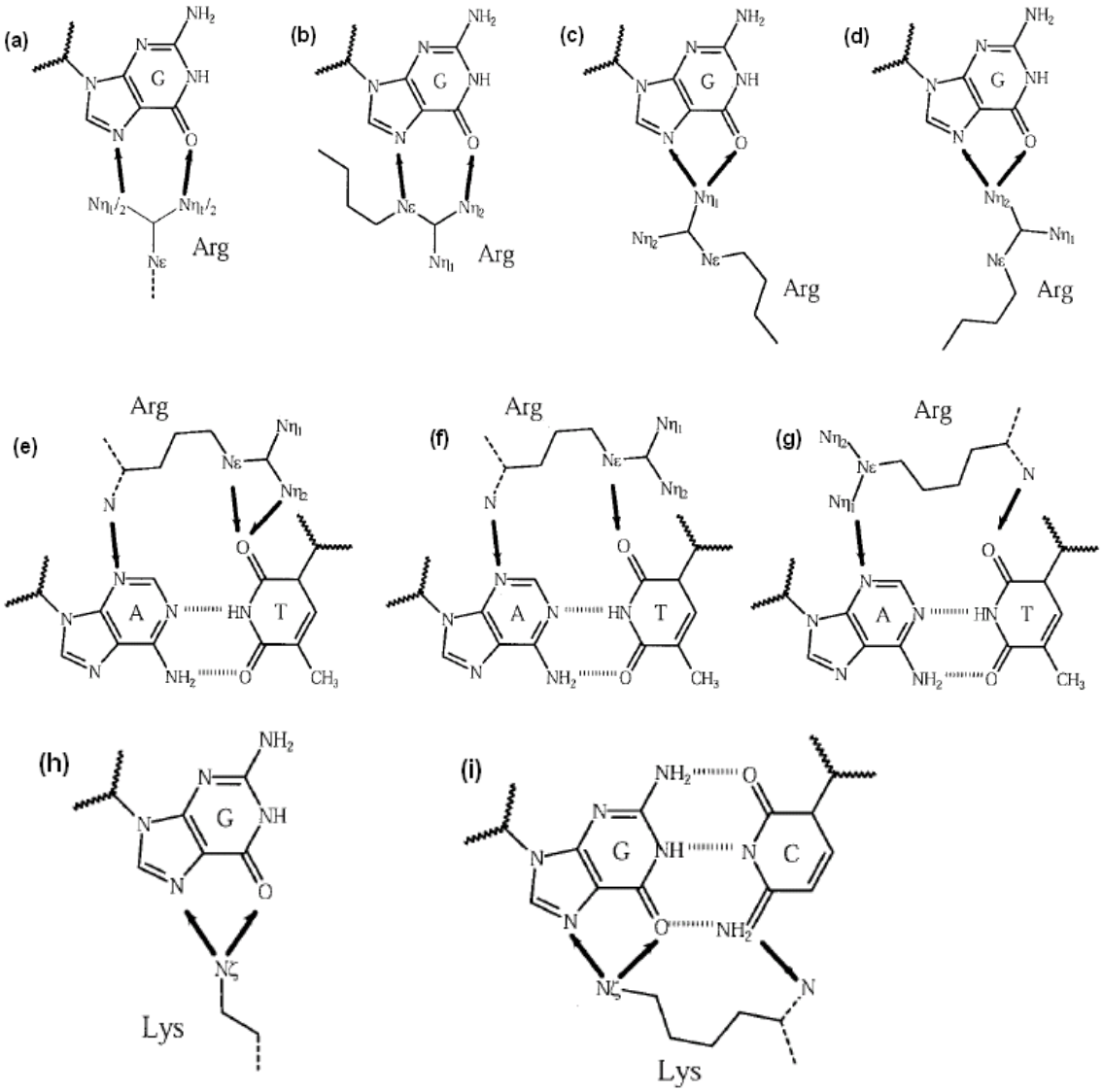

Fig. 1.3 *Schematic diagrams of hydrogen bonds between DNA base guanine and arginine* ***(a-d),*** *DNA base pair adenine: thymine and arginine* ***(e-g),*** *DNA base Guanine and lysine* ***(h),*** *and DNA base pair guanine: cytocine and lysine* ***(i)*** *in chromatin.*[9]

A variety of previous studies focused on the radiation effects of the DNA-histone complexes and isolated, purified DNA. One study of γ-irradiated DNH (deoxyribonucleohistone) in solution presented evidence that the DNA is protected by histone, i.e., DNA is much less degraded in DNH than in DNA only (Lloyd and Peacocke, 1965).[10] Another study focused on DNA strand breaks, and found evidence

that the number of single strand breaks is enhanced in uncomplexed DNA in comparison to DNA/histone complexes (Lückle-Huhle, Braun and Hagen, 1970).[11] In a later study of the irradiated DNA-histone complexes using EPR, Cullis et al.,[12] reported that electrons transfer from histone to DNA: specifically, they found a significant increase in the yield of DNA anions. The result was a significant increase in the yield of DNA anions (about two times) and detected no obvious increase of the DNA cations. This indicated that the DNA is more sensitive to the ionizing radiation in DNA/histone complexes. Faucitano and Buttafava, et al. (1987), reported similar results, that a significant fraction of electrons generated within the bulk of the histone octamers reaches sites with DNA.[13] Weiland and Hüttermann (2000) also found that the yield of DNA radicals in chromatin is about twice yield in DNA itself, and then proposed that damage, in the form of radicals, transfers from protein to DNA.[14] From annealing experiments, these authors also found that, once the radicals induced from the spin transfer stabilized (~77K), their subsequent reactions within histones and DNA took place independently. All these studies illustrate that histones have an important influence on the damaged nuclear DNA. Thus the histones affect the processes leading to radiation damage of DNA in vivo.

Because arginine and lysine are major constituents of histones, and also play important roles in histone-DNA interactions as described above, it is important to study the radiation-initiated chemical mechanisms for arginine and lysine independently and in association with DNA bases. This work is the first step and reports on the free radicals detected in X-irradiated single crystals of L-lysine monohydrochloride dihydrate (L-lys·HCl·2H_2O) and L-arginine hydrochloride monohydrate (L-arg·HCl·H_2O) with Electron Paramagnetic Resonance (EPR), Electron Nuclear DOuble Resonance (ENDOR) and ENDOR Induced EPR (EIE) techniques. These two lysine and arginine systems were chosen as the study models because they provide the basic NH_2 terminal tail (see scheme 1.1a and 1.1b), like those in histone-DNA interactions. The radiation-induced free radicals in lysine were studied previously by Fujimoto et al. in 1968 with EPR,[15] but no previous studies of irradiated arginine crystals have been reported. In this work, the free radicals in L-lys·HCl·2H_2O and L-arg·HCl·H_2O single crystals

X-irradiated at 66K and at 298K were detected with EPR, ENDOR and EIE techniques. With precisely measured coupling tensors from ENDOR, the free radicals were assigned and the configurations were analyzed. DFT (density functional theory) computations[16] supported the assignments of the radicals and provided additional insight into their structures. Reorientations of the radicals and the proton transfers were simulated by geometry optimization. Finally, mechanisms in which the free radicals formed in L-lysine·HCl·$2H_2O$ and L-arginine·HCl·H_2O single crystals were proposed and their possible effects to the chromatin and DNA are discussed (see Chapter 9).

References

1. A. Wolffe, *Chromatin structure and function*. Academic Press Inc., San Diego, CA, (1992).

2. K. Luger, A. W. Mader, R. K. Richmond, et al., Crystal structure of the nucleosome core particle at 2.8Å resolution. *Nature.* **389,** 251-260 (1997).

3. C. A. Davey, D. F. Sargent, K. Luger, et al., Solvent mediated interactions in the structure of the nucleosome core particle at 1.9 Å resolution. *Journal of Molecular Biology* **319,** 1097-1113 (2002).

4. Y.-B. Zhou, S. E. Gerchman, V. Ramakrishnan, et al., Position and orientation of the globular domain of linker histone h5 on the nucleosome. *Nature.* **395,** 402-405 (1998).

5. D. H. Farkas, *DNA simplified: The hitchhiker's guide to DNA*. AACC Press, Washington, D.C., (1996).

6. G. Felsenfeld and M. Groudine, Controlling the double helix. *Nature* **421 (6921),** 448-453 (2003).

7. http://activity.ntsec.gov.tw/lifeworld/english/content/gene_cc5.html

8. http://bio.research.ucsc.edu/people/boeger/ResearchInterests.htm

9. N. M. Luscombe, R. A. Laskowski and J. M. Thornton, Amino acid-base interactions: A three-dimensional analysis of protein-DNA interactions at an atomic level. *Nucl. Acids Res.* **29,** 2860-2874 (2001).

10. P. H. Lloyd and A. R. Peacocke, The action of γ -rays on deoxyribonucleohistone in solution. *Proceedings of the Royal Society of London. B* **164,** 40-62 (1966).

11. Lückle-Huhle, A. Braun and U. Z. Hagen, Oxygen effect in gamma-irradiated DNA. *Z. Natur. B* **25,** 1264-1266 (1970).

12. P. M. Cullis, G. D. D. Jones, M. C. R. Symons, et al., Electron transfer from protein to DNA in irradiated chromatin. *Nature* **330,** 773-774 (1987).

13. A. Faucitano, A. Buttafava, F. Martinotti, et al., EPR study of the direct radiolysis of DNA, DNA-histones and DNA-intercalators complexes. *Radiation physics and chemistry* **40,** 357-364 (1992).

14. B. Weiland and J. Hüttermann, Spin transfer from protein to DNA in X-irradiated 'dry' and hydrated chromatin: An electron spin resonance investigation of spectral components between 77k and room temperature. *International journal of radiation biology* **76,** 1075-1084 (2000).

15. M. Fujimoto, W. A. Seddon and D. R. Smith, Electron spin resonance studies of free radicals in γ-irradiated amino acid crystals: A-amino isobutyric acid and l-lysine·hcl·$2H_2O$. *J. Chem. Phys.* **48,** 3345-3350 (1968).

16. R. G. Parr and W. Yang, *Density-functional theory of atoms and molecules*. Oxford University Press, New York, (1989).

CHAPTER 2.

IONIZING RADIATION EFFECTS

2.1 Introduction

By definition, ionizing radiation has sufficient energy to ionize atoms and molecules by removing an electron. Most atoms and molecules have ionization potentials in the range of 5-15eV. Typical types of ionizing radiation are X- and γ-rays, α- and β- particles, and short wavelength UV (~200nm) light. These are distinct from low energy radiations (non-ionizing) such as radiowaves, microwaves, infrared, visible light, etc. Ionized molecules are very reactive and have short lifetimes. As such, they can initiate a large number of processes in a system, and lead to many products (ions, excited molecules, and free radicals, etc.). These produce reactions in a cell that may yield a macroscopic result such as cell death, cancer or genetic change. In the following sections, the basic effects of ionization radiation at the molecule level will be summarized.[1]

2.2 Radiation Effects on Molecules

For a molecule, the initial products of radiation are radical ions and excited molecules: [1,2]

$M + h\nu \rightarrow {}^{\bullet}M^{+} + {}^{\bullet}e^{-}$ (ionization; oxidation) (1)

$M + h\nu \rightarrow M^{*}$ (excitation) (2)

The symbols "*" and "•" represent the excitation and unpaired electron; superscripts "+" and "-" represent the net charge of the molecule.

In the most basic process of ionization, an electron is expelled from a molecule with the result being a cation radical (the oxidized product) as shown in (1). The cation radical is marginally stable and usually forms a neutral molecule by releasing a proton: [2]

${}^{\bullet}M^{+} \rightarrow {}^{\bullet}(M-H) + H^{+}.$ (deprotonation) (3)

With sufficient kinetic energy, the expelled electron may cause several additional ionizations and excitation; finally, it may may attach to another atom or molecule at some distance from the site of the initial ionization:[I] [2]

$$M + {}^{\bullet}e^{-} \rightarrow {}^{\bullet}M^{-}. \quad \text{(reduction)} \qquad (4)$$

The anion radical tends to form a neutral radical by adding a proton: [2]

$${}^{\bullet}M^{-} + H^{+} \rightarrow {}^{\bullet}(M+H). \quad \text{(protonation)} \qquad (5)$$

(In the solid state, the electron also may be not associated with any atom or molecule and can be trapped in the "lattice".[3])

The excited molecule is also very unstable and loses its extra energy rapidly by a variety of pathways. As shown in (6), it may decay back to the original state by emitting light or by converting the extra energy into various forms of internal energy. Alternatively, as shown in (7), bond cleavage may result in the formation of free radicals as secondary products.[2]

$$M^{*} \rightarrow M + h\nu \qquad (6)$$

$$M^{*} \rightarrow {}^{\bullet}(M\text{-}H) + {}^{\bullet}H \qquad (7)$$

From pathway (7), the released hydrogen atom also can attach to a molecule and form an other radical (8), and it can abstract a hydrogen atom from another molecule to form a hydrogen molecule and a free radical (9).[2] (Thus hydrogen atoms may lead to both hydrogen gain and hydrogen loss products.)

$$M + {}^{\bullet}H \rightarrow {}^{\bullet}(M+H) \qquad (8)$$

$$M + {}^{\bullet}H \rightarrow {}^{\bullet}(M\text{-}H) + H_2 \qquad (9)$$

Thus, radiation-induced free radicals may be positively charged cations, negatively charged anions, radicals neutralized by proton transfer (loss or gain), and/or radicals from hydrogen loss or gain. Subsequent reactions of these radicals are affected by temperature, and the type and concentration of surrounding molecules. Since most of these products are paramagnetic radicals, which contain unpaired electrons, Electron Paramagnetic Resonance (EPR) and Electron Nuclear DOuble Resonance (ENDOR) is

[I] The expelled electron also may recombination: "destroy" a cation by "healing" it.

a natural method to identify them. Because the lifetimes of many products are very short (milliseconds or shorter), study of these radiation products can be difficult. However, by using low temperatures, the lifetime of the unstable intermediates can be increased, and the reactions can be effectively slowed or even stopped. This procedure makes it possible to study the initial and secondary products.[1]

2.3 Radiation Effects on Amino Acids

Amino acids are the elementary units of proteins; thus studying the radiation mechanisms of the amino acids is fundamental to understand the radiation effects on the proteins and also on the protein-DNA complexes in chromatin. The radiation chemistry of amino acids has been intensively studied since the late 1950s. The most complete structural information on radicals was obtained by using single crystals, and EPR was the most common analytical technique. Advanced ENDOR techniques that provide significantly enhanced resolution in comparison to EPR spectra, permit the collection of more complete information on structures and reactions of the various amino acid free radicals. Also, recent advances in quantum chemistry calculations allow more accurate prediction of the structures, reactions and hyperfine coupling tensors of the free radicals. These more advanced techniques provide important updating and corrections to the free radical assignments from earlier experimental analysis.[4]

From previous studies, it can be seen that the different side chains in amino acids modify the radical formation process but that the irradiated amino acids have steps in their reaction routes common for all.[4] In this section, the similarities of these reaction routes are summarized and the general reaction scheme is indicated as shown in Fig. 2.1. (In solution and the solid state, the amino acids are zwitterions as indicated in the figure; also, "R" in the figure stands for the side chain of the amino acids.)

In the oxidation pathway, the primary product should be a cation with an electron removed and thereby leaving a hole in the molecule. The cation can have the depronated form (at amino group), as was identified in irradiated L-alanine (at ~80K)[5] and α-glycine (at 4.2K)[6]. The decay of the (deprotonated) cation radical can take several different pathways. One is by forming stable radicals from

dehydrogenation at the side chain or at C_α. An alternative pathway is by decarboxylation, into an unstable radical, followed by intermolecular hydrogen transfer into the stable radical. The decarboxylation radical is a common intermediate product of oxidation, and has been observed in many cases such as irradiated α-glycine (at 77K),[7, 8] L-*O*-Serine phosphate (at 77K),[9] and L-histidine (at 4.2K)[10] etc. The radical from deprotonation (or dehydrogenation) at the side chain, or at C_α, can also be formed from the reduction pathway as described in the following.

In the reduction pathway, the primary product is the carboxyl radical anion with an electron localized on the carboxyl group. Usually protonation takes place, neutralizing the surplus negative charge, by proton transfer through the (intermolecular) hydrogen bond bridges. The carboxyl radical anion and its protonated form are very commonly observed in amino acids irradiated at low temperature (<~120K). The hyperfine coupling constants of the carboxyl protons in the carboxyl radical anions formed in different irradiated amino acids are listed in Chapter 5, Table 5.5. If the temperature is increased gradually (>~120K), it is typical that a new radical forms from the anion radical by deamination. The deamination radical is a commonly observed stable radical in irradiated amino acids. The radical from dehydrogenation at the side chain or at C_α can be formed when the deamination radical abstracts a hydrogen atom from a neighboring molecule. This pathway was identified in irradiated α-glycine.[11]

In this work, the protonated form of carboxyl anion radicals and the decarboxylation radicals were observed in irradiated single crystals of L-lysine monohydrochloride dihydrate (L-lys·HCl·$2H_2O$) and L-arginine monohydrochloride monohydrate (L-arg·HCl·H_2O) at 66K. The deamination radical and the radical from dehydrogenation at the side chain were observed in both crystal systems following irradiation at room temperature. In L-arg·HCl·H_2O, another primary reduction product, with an electron trapped in the side chain guanidyl group, was identified following irradiation at 66K; also the radical from dehydrogenation at C_α was identified for irradiation at 298K. On the basis of the products yielded in these two crystal systems irradiated at 66K and at 298K, the mechanisms with which the radicals formed are tentatively proposed in Chapter 9.

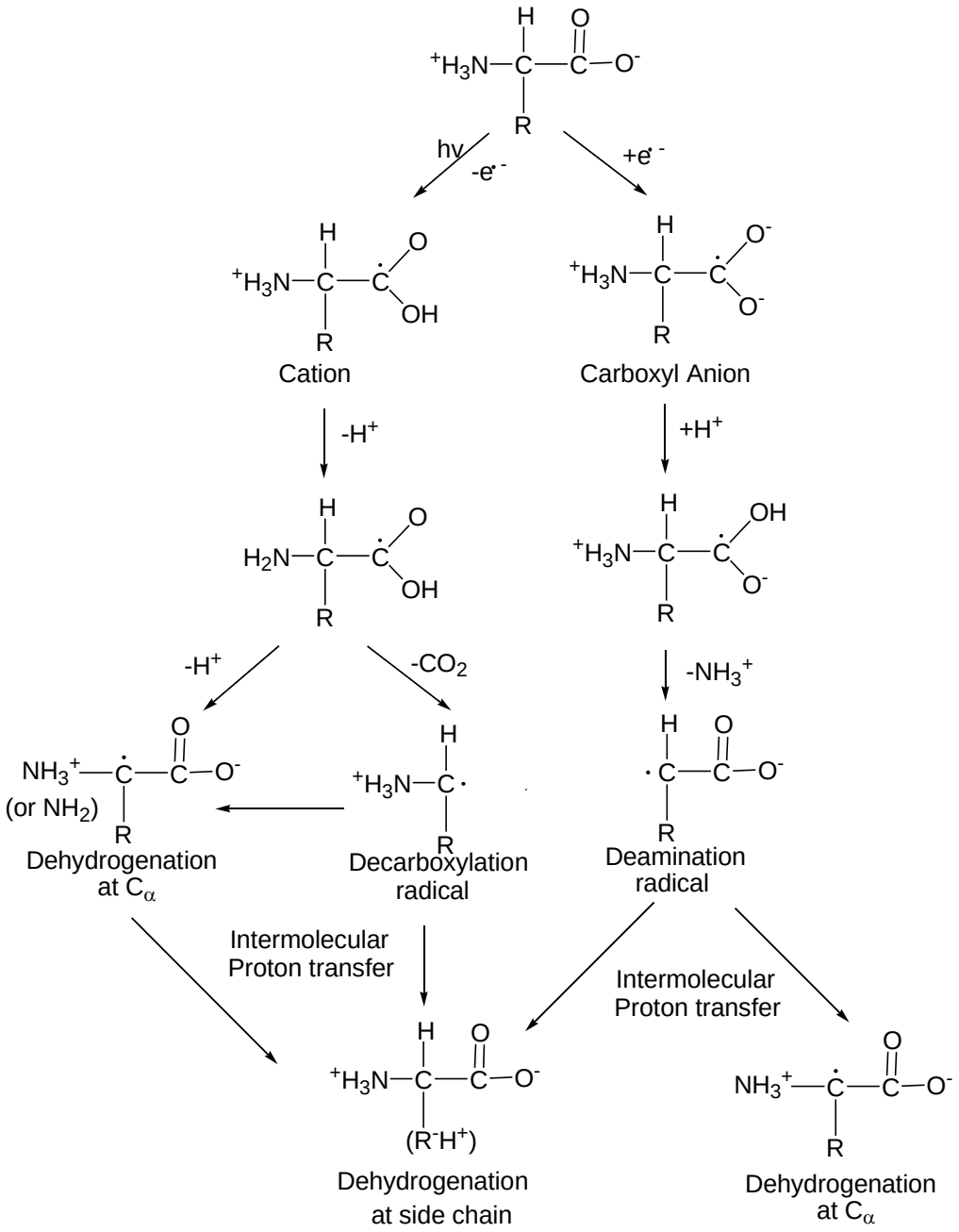

Fig. 2.1 *Typical reactions that take place in irradiated amino acid molecules.*

References

1. T. Henriksen and H. D. Maillie, *Radiation and health*. Taylor and Francis, New York, NY, (2003).

2. J. Hüttermann, W. Kohnlein, R. Teoule and A. J. Bertinchamps, *Effects of ionizing radiation on DNA*. Springer-Verlag, New York, NY, (1978).

3. H. C. Box, *Radiation effects-ESR and ENDOR analysis*. Academic Press, INC., New York, NY, (1977).

4. E. Sagstuen, A. Sanderud and E. O. Hole, The solid-state radiation chemistry of simple amino acids, revisited. *Radiation Research* **162,** 112-119 (2004).

5. E. A. Friday and I. Miyagawa, Search for a trapped hole in an irradiated crystal of L-alanine by the ESR technique. *J. Chem. Phys.* **55,** 3589-3594 (1971).

6. K. Nunome, H. Muto, K. Toriyama and M. Iwasaki, ESR study of oxidation product in irradiated α-amino acids: Nitrogen centered π radical in α-glycine. *J. Chem. Phys.* **65,** 3805-3807 (1976).

7. J. Sinclair, ESR study of irradiated glycine at low temperatures. *J. Chem. Phys.* **55,** 245-251 (1971).

8. C. Iacona, J. P. Michaut and J. Roncin, Structure of the $HNCH_2CO_2^-$] radical trapped in α-glycine single crystals. *J. Chem. Phys.* **67,** 5658-5660 (1977).

9. K. T. Øhman, A. Sanderud, E. O. Hole and E. Sagstuen, Single crystals of l-*o*-serine phosphate X-irradiated at low temperatures: EPR, ENDOR, EIE, and DFT studies. *J. Phys. Chem. A* **110,** 9585-9596 (2006).

10. F. Q.-H. Ngo, E. E. Budzinski and H. C. Box, Free radical formation in X-irradiated histidine HCl. *J. Chem. Phys.* **60,** 3373-3377 (1974).

11. A. Sanderud and E. Sagstuen, EPR and ENDOR studies of single crystals of α-glycine X-ray irradiated at 295 k. *J. Phys. Chem. B* **102,** 9353-9361 (1998).

CHAPTER 3.

INTRODUCTION TO EPR AND ENDOR SPECTROSCOPY

3.1 Introduction [1, 2]

This work uses EPR (Electron Paramagnetic Resonance) and ENDOR (Electron-Nuclear DOuble Resonance) techniques to study the free radicals in the single crystals induced by X-ray irradiation. Because of its specificity for paramagnetic species, EPR is powerful for detecting and identifying free radicals, transition ions, etc.. ENDOR, with its higher resolution, makes it possible to measure the magnetic parameters of the free radicals very precisely, and to detect even the small interactions that cannot be measured by EPR. From the magnetic parameters obtained from EPR and ENDOR, it is possible to identify the free radicals, to deduce their structure, to characterize their orientation and surroundings, and to measure their concentration. Understanding of EPR and ENDOR spectra requires an analysis the energy levels of the system and of the influence of the surroundings on these levels. This chapter describes the principles of EPR and ENDOR in a spin system of S= ½ and I =½ with quantum mechanics and describes the characteristics of the magnetic parameters.

3.2 Thermal Equilibrium, Spin Relaxation and Saturation [1-4]

Spin relaxation and saturation in a system interacting with a radiation field plays a crucial role in detection of magnetic resonance absorption. Consider a macroscopic sample containing a total of N non-interacting electron spins. In the absence of an external magnetic field, their magnetic moments will be randomly oriented and no net magnetization would be detected. Application of a static magnetic field (B_z) induces splitting of the energy states (Zeeman levels) and the spins will be oriented parallel or antiparallel to B_z as illustrated in Fig. 3.1.

At thermal equilibrium there is a slight excess of spins in the lower state, which gives rise to a small temperature-dependent paramagnetism, and the ratio of the populations in the two states follows Boltzmann's distribution law

$$\frac{N^0{}_\alpha}{N^0{}_\beta} = e^{-\Delta E/KT} = e^{-g\beta B/KT}, \qquad (1)$$

where $N^0{}_\alpha$ and $N^0{}_\beta$ are the spin populations in the upper and lower states at thermal equilibrium.

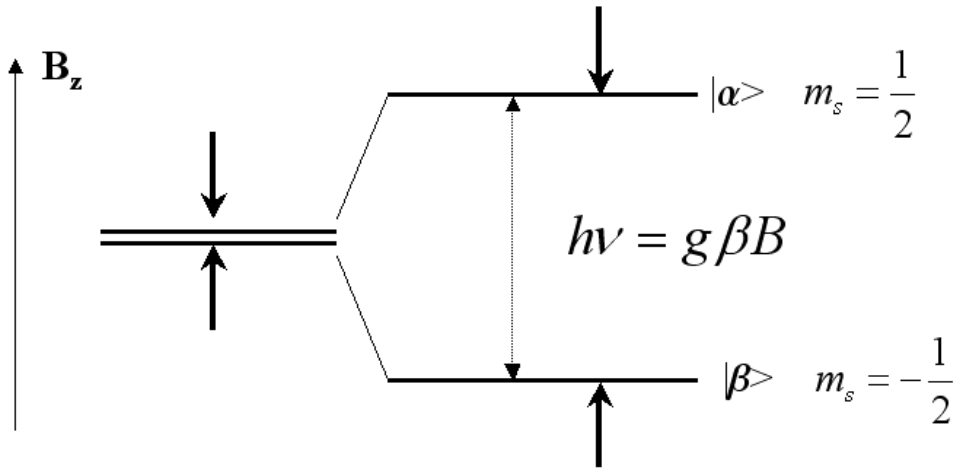

Fig. 3.1 *Electron spin levels in a magnetic field B_z.*

Defining the spin difference at thermal equilibrium as n^0, then

$$\begin{aligned} n^0 &= N^0{}_\beta - N^0{}_\alpha \\ N &= N^0{}_\alpha + N^0{}_\beta \end{aligned} \qquad (2)$$

and,

$$\frac{n^0}{N} = \frac{N^0{}_\beta - N^0{}_\alpha}{N^0{}_\alpha + N^0{}_\beta} = \frac{1 - e^{-g\beta B/KT}}{1 + e^{-g\beta B/KT}} \qquad (3)$$

For a K-band spectrometer (23GHz), the ratio (3) is ~0.0018 at 298K and ~0.0084 at 66K (~5 times larger than the ratio at 298K).

When a microwave electromagnetic field is applied to the spin system, three processes can occur: absorption, stimulated emission and spontaneous emission. However, the relative importance of

spontaneous emission depends strongly on the frequency, and in microwave region, it is completely negligible and can be disregarded in magnetic resonance.[4] Thus, the main processes are only absorption and stimulated emission. From time-dependent perturbation theory, the perturbation V(t) induces the probabilities of absorption ($P_{\uparrow}$ upward transitions) and emission ($P_{\downarrow}$ downward transitions) that are equal. Then the rate of change of spin population in the lower state is given by

$$\frac{dN_\beta}{dt} = N_\alpha P_\downarrow - N_\beta P_\uparrow = P(N_\alpha - N_\beta) \qquad (4)$$

where we denote N_α and N_β as the spin population at upper and lower level at any time and set $P \equiv P_\uparrow = P_\downarrow$. If we introduce the population difference at any time $n \equiv n_\beta - n_\alpha$, and the total spin $N = N_\alpha + N_\beta\,(= N^0{}_\alpha + N^0{}_\beta$ ect), we have

$$\begin{aligned} N_\alpha &= \frac{1}{2}(N - n) \\ N_\beta &= \frac{1}{2}(N + n) \end{aligned} \qquad (5)$$

Substituting the above into equation in (4),

$$\frac{d\frac{1}{2}(N+n)}{dt} = \frac{1}{2}\frac{dn}{dt} = -nP \qquad (6)$$

then

$$\frac{dn}{dt} = -2nP \qquad (7)$$

The solution of equation (7) is

$$n = n(0)e^{-2Pt} \qquad (8)$$

where $n(0)$ is the population difference at time $t = 0$. This solution indicates that although there is an initial difference $n(0)$, application of the resonant field results in the exponential decay of the population difference, and will eventually equalize the populations of the two levels.

The net rate of energy absorption of the spin system from the radiation field is given by

$$\frac{dE}{dt} = N_\beta P_\uparrow (E_\alpha - E_\beta) - N_\alpha P_\downarrow (E_\alpha - E_\beta) = Pn\triangle E \qquad (9)$$

The above equation indicated that the net absorption of energy from the radiation field requires a population difference between the spin states ($n \neq 0$). Therefore, when the spin populations are equal there will be no net absorption from the radiation field to the spin system, and no EPR signal could be detected. This condition is called complete *saturation*.

However, there are nonradiative interactions between the real spin system and the "lattice" or surroundings, which lead to *spin-lattice relaxation*. This process maintains a thermal equilibrium population difference between the two spin states (${N_\alpha}^0 < {N_\beta}^0$) by spin transitions up and down with different probabilities, which are denoted as $W_\uparrow$ and $W_\downarrow$ and $W_\uparrow \neq W_\downarrow$.

Thus the rate of change of N_β is given by

$$\frac{dN_\beta}{dt} = N_\alpha W_\downarrow - N_\beta W_\uparrow \qquad (10)$$

Substituting equation (5) in above equation,

$$\frac{dn}{dt} = -n(W_\downarrow + W_\uparrow) + N(W_\downarrow - W_\uparrow)$$

$$= -\left[n - \frac{N(W_\downarrow - W_\uparrow)}{W_\downarrow + W_\uparrow} \right](W_\downarrow + W_\uparrow) \qquad (11)$$

At thermal equilibrium, $\frac{dn}{dt} = 0$, so that

$$n = n^0 = \frac{N(W_\downarrow - W_\uparrow)}{W_\downarrow + W_\uparrow},$$

Thus we obtain

$$\frac{dn}{dt} = -\left[n - n^0 \right](W_\downarrow + W_\uparrow) \qquad (12)$$

and its solution is given by

$$(n - n^0)_t = (n - n^0)_0 \, \mathrm{e}^{-(W_\downarrow + W_\uparrow)t} \qquad (13)$$

This solution indicates that the population difference n would approach its thermal equilibrium value n_0 with a relaxation time, $T_1 = \frac{1}{(W_\downarrow + W_\uparrow)}$. Thus T_1 is called the *spin-lattice relaxation time*. That is, there is a competition between the radiation and the spin-lattice relaxation in magnetic resonance, while the former tends to equalize the populations of the spin levels, the latter tends to maintain the thermal equilibrium population difference.

Now combining equations (7) and (12), a more complete description of the spin system can be obtained,

$$\frac{dn}{dt} = -2nP - (\frac{n - n^0}{T_1}) . \qquad (14)$$

Consider the thermal equilibrium condition, $\frac{dn}{dt} = 0$, we have

$$n = \frac{n^0}{1 + 2PT_1} . \qquad (15)$$

With the above formula, the rate of energy absorption given in equation (9) can be more completely expressed as

$$\frac{dE}{dt} = nP\triangle E = n^0 \triangle E \frac{P}{1 + 2PT_1} . \qquad (16)$$

In equation (16), P is directly proportional to the square of the microwave field.[3] Thus for application of a low power field, for which $2PT_1 \ll 1$, can avoid the saturation easily. As the microwave power is increased and approaches $2PT_1 \gg 1$, the spin populations of the two spin levels approach equality and the EPR signal intensity decreases. This process is known as “power saturation”.

The above discussion considered the two spin levels interacting with a microwave electromagnetic field for EPR and introduced only the electron spin-lattice relaxation time T_1. As shown in Fig. 3.2 for the simplest ENDOR system with **S** = **I** = ½, there are at least three relaxation times[5,6] that maintain the spin populations of these levels: T_1, as mentioned above, related to the EPR transitions, $\Delta m_S = \pm 1, \Delta m_I = 0$;

nuclear spin-lattice relaxation time T_{1n}, associated with the ENDOR transitions, $\Delta m_S = 0, \Delta m_I = \pm 1$; and the "cross-relaxation" time T_x, associated with mutual "spin flips" transitions, $\Delta(m_S + m_I) = 0$, or T_{xx} with transitions $\Delta(m_S + m_I) = \pm 2$. It can be seen that for the $m_I = \frac{1}{2}$ EPR transition, there are two additional relaxation pathways, $T_{1n} + T_x$ and $T_{1n} + T_1 + T_{1n}$ that parallel the T_1 pathway.

Usually, $T_1 < T_x \ll T_{1n}$ [7], so only the T_1 relaxation path is effective for $m_I = \frac{1}{2}$ EPR transition. The pathway via T_x usually is effective, since T_{1n} in series with it is much longer. Now increase the microwave power to saturate the $m_I = \frac{1}{2}$ EPR transition. Then the application rf field of $h\upsilon_n^+$ will make $T_{1n} \to 0$, so that the relaxation path $(T_{1n} + T_x) \to T_x$, and this leads to the equivalent relaxation time for the system, $T_{eq} = \frac{T_x T_1}{T_x + T_1}$. T_1 in equation (16) now being T_{eq} in ENDOR system will then be decreased. Thus from equation (16), the rate of absorption energy $\frac{dE}{dt}$ can be enhanced, and an ENDOR signal is produced. For the two extreme cases, $T_x \gg T_1$ and $T_x \ll T_1$, $T_{eq} \to T_1$ and $T_{eq} \to T_x$, respectively. If $T_x \ll T_1$ and $T_{eq} \to T_x$, then $\frac{dE}{dt}$ is still increased and an ENDOR signal is produced. However, if $T_x \gg T_1$ and $T_{eq} \to T_1$, there is still only relaxation path T_1, which still makes $2PT_1 \gg 1$ (power saturation), thus no ENDOR could be detected. Similarly, the rf at $h\upsilon_n^-$ makes $T_{1n} \to 0$, then $(T_{xx} + T_{1n}) \to T_{xx}$ and $T_{eq} = \frac{T_{xx} T_1}{T_{xx} + T_1}$, so that an ENDOR signal can be produced due to the decrease of T_{eq} and the increase of $\frac{dE}{dt}$ from equation (16). If the $m_I = -\frac{1}{2}$ EPR transition is saturated, then the application of $h\upsilon_n^+$ and $h\upsilon_n^-$ leads to the corresponding ENDOR lines, which are governed by the same relaxation processes as shown in Fig. 3.2(b).

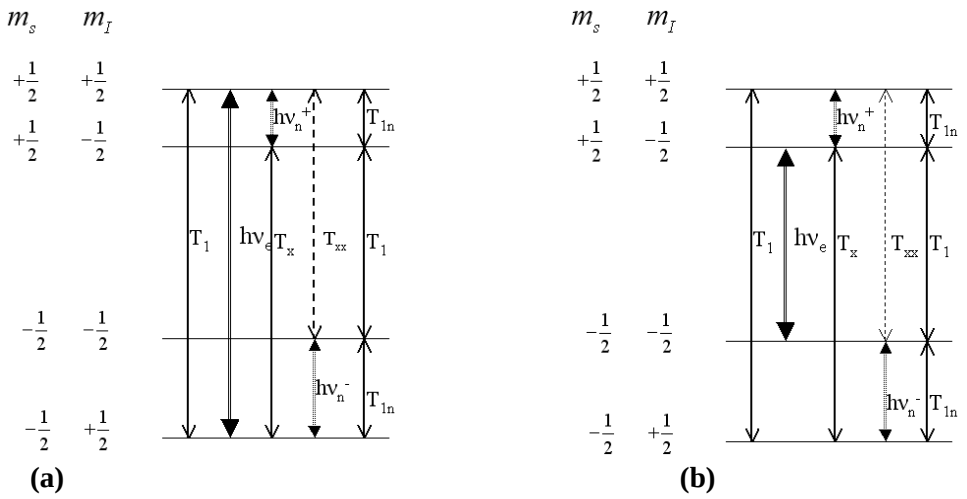

Fig. 3.2 *Steady state ENDOR system with* ***S*** *=* ***I*** *= ½ where the relaxation times* T_1 *and* T_x *(or* T_{xx}*) govern the ENDOR transitions.* ***(a)*** $m_I = \frac{1}{2}$ *EPR transition is saturated and ENDOR signals can be observed from* $h\upsilon_n^+$ *and* $h\upsilon_n^-$*, respectively.* ***(b)*** $m_I = -\frac{1}{2}$ *EPR transition is saturated and ENDOR signals can be observed from* $h\upsilon_n^+$ *and* $h\upsilon_n^-$*, respectively.*

In some sense, the spin transition rate W can be analogous to the current i (electron transfer rate). From above description, $W \propto \frac{1}{T}$, where T is the relaxation time; from Ohm's Law, $i \propto \frac{1}{R}$, where R is the resistance. Thus R can be analogous to relaxation time T, and the relaxation path in the ENDOR system shown in Fig. 3.2a can be analogous to the circuit as shown in Fig. 3.3, where $R_x \sim R_1$ and K_{1n} is a switch. In the $m_I = \frac{1}{2}$ EPR transition, T_{1n} is too large and makes the relaxation path $T_{1n} + T_x$ ineffective. This case corresponds to switch off K_{1n} ($\approx R_{1n} \to \infty$) in the circuit, so that no current can flow through the branch $K_{1n\,off} + R_x$, and only the branch with R_1 takes the current, and $R_{eq} = R_1$. Switch on K_{1n} ($\approx R_{1n} \to 0$), and R_1 and R_x become in parallel, and $R_{eq} = \frac{R_x R_1}{R_x + R_1}$, which are smaller than $R_{eq} = R_1$. This is similar to $T_{1n} \to 0$ and $T_{eq} = \frac{T_x T_1}{T_x + T_1}$ from application of $h\upsilon_n^+$, which will decrease T_{eq} and enhance

$\frac{dE}{dt}$. In the case of the $m_I = -\frac{1}{2}$ EPR transition and the application of $h\upsilon_n^+$ and $h\upsilon_n^-$, a similar circuit can also be built as an analogue of the relaxation paths in the ENDOR system and to simulate the change of T_{eq}.

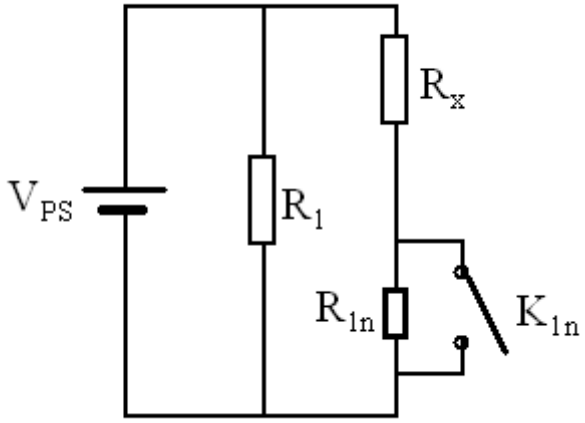

Fig. 3.3 *The circuit analogous to the relaxation path in the ENDOR system shown in Fig. 3.2a. V_{ps} stands for the voltage of the power supply. R_1, Rx and R_{1n} are three resistors, and K_{1n} is a switch.*

3.3 The Spin Hamiltonian [1, 7, 8]

The spin Hamiltonian is a useful mathematical tool in fundamental theory of EPR. It was introduced by Abragam and Pryce[7] in 1951, and is derived from the overall Hamiltonian. Consider a free atom, for which the complete Hamiltonian is the sum of at least eight components, i.e.,

$$H = \sum_{i=1}^{8} H_i \,, \qquad (17)$$

where H_1 is the most dominant term and combines the kinetic energy of the electrons with their coulomb interactions:

$$H_1 = \sum (\frac{\mathbf{p}^2}{2m_0} - \frac{Ze^2}{r_i}) + \sum_{i<K} \frac{e^2}{r_{ik}} \qquad (18)$$

But H_1 is spin-independent and plays no part in the spin Hamiltonian.

H_2 is that part of the potential energy arising from the electrostatic field of the neighboring atoms. It always termed the crystal field and thus plays a large part in the study of single crystals, particularly the transition metal group crystals.

H_3 is the orbit-spin coupling term, i.e., the interaction between orbital angular momentum **L** and electron spin **S**, and can be represented by $\lambda \mathbf{L} \cdot \mathbf{S}$, where λ is a parameter that may be + or -.

H_4, the Zeeman term, is mainly responsible for the paramagnetism and can be expressed as

$$H_4 = \beta \mathbf{B} \cdot (\mathbf{L} + \overleftrightarrow{\mathbf{g}} \cdot \mathbf{S}) \qquad (19)$$

where β is the Bohr magneton, the fundamental unit of electronic magnetic moment and $\mathbf{B}$ is the effective magnetic field. For a free radical, the expectation value of the orbital angular momentum **L** is zero, and the spin-orbit coupling is absent, therefore

$$H_4 = \beta \mathbf{B} \cdot \overleftrightarrow{\mathbf{g}} \cdot \mathbf{S} \qquad (20)$$

For most organic radicals, $\overleftrightarrow{\mathbf{g}} \approx g_e$ (2.00232). In later sections, $\overleftrightarrow{\mathbf{g}}$ will be replaced with g_e.

H_5 refers to the magnetic interactions between electrons. This term may be important only for some transition metal ion systems, and will not be discussed here.

H_6 describes the hyperfine interaction between the electron and nuclear spins

$$H_6 = g g_n \beta \beta_n \left[\frac{\mathbf{S} \cdot \mathbf{I}}{r^3} - \frac{3(\mathbf{S} \cdot \mathbf{r})(\mathbf{I} \cdot \mathbf{r})}{r^5} - \frac{8\pi}{3} \mathbf{S} \cdot \mathbf{I} \delta(r) \right] \qquad (21)$$

where g and g_n are the electronic and nuclear g-values, β_n is the nuclear magnetic moment, and r is the electron-nuclear distance. H_4 and H_6 are the most important terms in the EPR study of free radicals with most quantitative interaction coming from H_6. H_6 also includes the electrostatic interaction of the electron with the electric quadrupole moment **Q** of the nucleus.

$$H_6' = \frac{e^2\mathbf{Q}}{2I(2I-1)}\left[\frac{I(I+1)}{r^3} - \frac{3(\mathbf{r}\cdot\mathbf{I})^2}{r^5}\right] \qquad (22)$$

This interaction is generally very small (see Table 3.1) and is omitted in the discussion here. Equation (21) which will be considered in more detail in a later section can be written as

$$H_6 = \mathbf{S}\cdot\overleftrightarrow{\mathbf{A}}\cdot\mathbf{I} \qquad (23)$$

where $\overleftrightarrow{\mathbf{A}}$ is hyperfine coupling tensor.

H_7 is the nuclear Zeeman term,

$$H_7 = \sum g_n\beta_n\mathbf{B}\cdot\mathbf{I} \qquad (24)$$

It is small (see Table 3.1), but is extremely important in ENDOR spectroscopy and should also be considered in EPR studies of free radicals.

H_8 is mainly from the diamagnetic interaction,

$$H_8 = \frac{e^2}{8m_0c^2}\sum_i(\mathbf{H}\times\mathbf{r}_i)^2 \qquad (25)$$

This term deals only with the causes of diamagnetism, and thus it is not involved in the spin Hamiltonian.

The energy magnitude orders of the above Hamiltonian components are listed in Table 3.1.

From the above description, the total spin Hamiltonian should be

$$H_s = H_2 + H_3 + H_4 + H_6 + H_7 \qquad (26)$$

H_4, H_6 and H_7 are most fundamental components for normal EPR measurements, therefore, the spin Hamiltonian of interest is

$$H_s = H_4 + H_6 + H_7 = \beta\mathbf{B}\cdot\overleftrightarrow{\mathbf{g}}\cdot\mathbf{S} + \mathbf{S}\cdot\overleftrightarrow{\mathbf{A}}\cdot\mathbf{I} - g_n\beta_n\mathbf{B}\cdot\mathbf{I}\ . \qquad (27)$$

Table 3.1 *Orders of magnitude of energy for Hamiltonian components for a free atom.*

Hamiltonian Components	Orders of energy magnitude (eV)
H_1	10
H_2	1
H_3	10^{-2}
H_4	10^{-4}
H_5	10^{-4}
H_6	10^{-6}
H_6'	10^{-8}
H_7	10^{-7}
H_8	10^{-8}

3.4 Perturbation Theory on Spin Hamiltonian [1-4]

For most spin systems, the exact solutions of energies cannot be obtained. In the spin Hamiltonian discussed in the previous section, the term $g_e\beta_e \vec{B}\cdot\vec{S}$ is much larger than the other terms $\vec{S}\cdot\overleftrightarrow{A}\cdot\vec{I}$ and $g_n\beta_n \vec{B}\cdot\vec{I}$. Therefore, the spin Hamiltonian may be separated into two parts: $H_s^{(0)} = g_e\beta_e \vec{B}\cdot\vec{S}$ and $H_s' = (\vec{S}\cdot\overleftrightarrow{A} - g_n\beta_n \vec{B})\cdot\vec{I}$; then

$$H_s = H_s^{(0)} + H_s' = g_e\beta_e \vec{B}\cdot\vec{S} + (\vec{S}\cdot\overleftrightarrow{A} - g_n\beta_n \vec{B})\cdot\vec{I} \qquad (29)$$

where H_s' is small enough to be a genuine perturbation.

From perturbation theory, the general expression for the modified energies E_n and the wave functions Ψ_n are given by

$$E_i = \varepsilon_i^{(0)} + \langle i|H_s'|i\rangle + \sum_{j\neq i} \frac{\langle i|H_s'|j\rangle\langle j|H_s'|i\rangle}{\varepsilon_i - \varepsilon_j} + \ldots \qquad (30)$$

$$\Psi_i = \phi_n^{(0)} + \sum_{j\neq i} \frac{\langle i|H_s'|j\rangle}{\varepsilon_i - \varepsilon_j}\phi_j + \ldots \qquad (31)$$

where $\varepsilon_i^{(0)}$ is the zero-order energy and $\phi_n^{(0)}$ is the corresponding eigenfunction. The next two terms in (30) are the first-order and the second-order corrections to the energy. The sums above are over all the states.

Zero-Order Energies

For a system with electron spin $S=\frac{1}{2}$, there are two allowed states corresponding to $M_s=\pm\frac{1}{2}$. If the magnetic field is along direction **z**, then

$$H_s^{(0)}=g_n\beta_n BS_z \qquad (32)$$

Thus the zero-order energies for the two electron spin states $\left|\frac{1}{2}\right\rangle$ and $\left|-\frac{1}{2}\right\rangle$ are

$$\begin{aligned}\varepsilon_1^{(0)}&=g_n\beta_n B\left\langle\frac{1}{2}\middle|S_z\middle|\frac{1}{2}\right\rangle=\frac{1}{2}g_n\beta_n B\\ \varepsilon_2^{(0)}&=g_n\beta_n B\left\langle-\frac{1}{2}\middle|S_z\middle|-\frac{1}{2}\right\rangle=-\frac{1}{2}g_n\beta_n B\end{aligned} \qquad (33)$$

First-Order Energies

Now consider a system with electron spin $S=\frac{1}{2}$ and proton spin $I=\frac{1}{2}$. If the magnetic field is still along direction **z**, and parallel with a unit vector $\hat{l}$, i.e., $\hat{l}=\frac{\vec{B}}{\left|\vec{B}\right|}=l_x\hat{i}+l_y\hat{j}+l_z\hat{k}$ and $\vec{B}=\left|\vec{B}\right|\hat{l}=B\hat{l}$, then

$\vec{S}=\vec{S}_x+\vec{S}_y+S_z\hat{l}\rightarrow S_z\hat{l}$ for first-order approximation. The spin Hamiltonian becomes

$$\begin{aligned}H_s&=g_e\beta_e B\hat{l}\cdot\vec{S}+(\vec{S}\cdot\overleftrightarrow{A}-g_n\beta_n B\hat{l})\cdot\vec{I}\\&=g_e\beta_e BS_z+(S_z\hat{l}\cdot\overleftrightarrow{A}-g_n\beta_n B\hat{l})\cdot\vec{I}\\&=H_s^{(0)}+H_s^{(1)}\end{aligned} \qquad (34)$$

If the z-direction of the nuclear spin $\vec{Z}_n=(S_z\hat{l}\cdot\overleftrightarrow{A}-g_n\beta_n B\hat{l})$ and the unit vector $\hat{z}_n$ is along $\vec{Z}_n$, then $\vec{Z}_n=\left|\vec{Z}_n\right|\hat{z}_n$, and $\vec{Z}_n\cdot\vec{I}=\left|\vec{Z}_n\right|\hat{z}_n\cdot\vec{I}=\left|\vec{Z}_n\right|I_z$. Thus, $H_s=g_e\beta_e BS_z+\left|\vec{Z}_n\right|I_z$. From perturbation theory, the first-order hyperfine energy for this spin system is given by

$$E_{m_sm_I}=\left\langle m_sm_I\middle|H_s\middle|m_sm_I\right\rangle$$

$$
\begin{aligned}
&= g_e\beta_e Bm_s + \left\langle m_I \left| (m_s \hat{l}\cdot\overleftrightarrow{A} - g_n\beta_n B\hat{l})\cdot\vec{I} \right| m_I \right\rangle \\
&= g_e\beta_e Bms + \left\langle m_I \left| \vec{Z}_n \right| I_z \left| m_I \right\rangle \right. \\
&= g_e\beta_e Bms + \left| m_s \hat{l}\cdot\overleftrightarrow{A} - g_n\beta_n B\hat{l} \right| m_I \\
&= g_e\beta_e Bms + m_s m_I \sqrt{\hat{l}\cdot\overleftrightarrow{A}\cdot\overleftrightarrow{A}\cdot\hat{l} - \frac{2}{m_s} g_n\beta_n B\hat{l}\cdot\overleftrightarrow{A}\cdot\hat{l} + (\frac{g_n\beta_n B}{m_s})^2}
\end{aligned}
\tag{35}
$$

For the four spin states $\left|\frac{1}{2},\frac{1}{2}\right\rangle, \left|\frac{1}{2},-\frac{1}{2}\right\rangle, \left|-\frac{1}{2},\frac{1}{2}\right\rangle$ and $\left|-\frac{1}{2},-\frac{1}{2}\right\rangle$, the energies are

$$
\begin{aligned}
E_{\frac{1}{2},\frac{1}{2}} &= \frac{1}{2} g_e\beta_e B + \frac{1}{4}\sqrt{\hat{l}\cdot\overleftrightarrow{A}\cdot\overleftrightarrow{A}\cdot\hat{l} - 4g_n\beta_n B\hat{l}\cdot\overleftrightarrow{A}\cdot\hat{l} + 4(g_n\beta_n B)^2} \\
E_{\frac{1}{2},-\frac{1}{2}} &= \frac{1}{2} g_e\beta_e B - \frac{1}{4}\sqrt{\hat{l}\cdot\overleftrightarrow{A}\cdot\overleftrightarrow{A}\cdot\hat{l} - 4g_n\beta_n B\hat{l}\cdot\overleftrightarrow{A}\cdot\hat{l} + 4(g_n\beta_n B)^2} \\
E_{-\frac{1}{2},\frac{1}{2}} &= -\frac{1}{2} g_e\beta_e B - \frac{1}{4}\sqrt{\hat{l}\cdot\overleftrightarrow{A}\cdot\overleftrightarrow{A}\cdot\hat{l} + 4g_n\beta_n B\hat{l}\cdot\overleftrightarrow{A}\cdot\hat{l} + 4(g_n\beta_n B)^2} \\
E_{-\frac{1}{2},-\frac{1}{2}} &= -\frac{1}{2} g_e\beta_e B + \frac{1}{4}\sqrt{\hat{l}\cdot\overleftrightarrow{A}\cdot\overleftrightarrow{A}\cdot\hat{l} + 4g_n\beta_n B\hat{l}\cdot\overleftrightarrow{A}\cdot\hat{l} + 4(g_n\beta_n B)^2}
\end{aligned}
\tag{36}
$$

First-order EPR

In standard EPR transitions, only the electron spin changes while the nuclear spin remains unchanged ($\Delta m_s = \pm 1$ and $\Delta m_I = 0$). Thus for the spin system we considered ($S = I = \frac{1}{2}$), the two allowed transitions are $\left|\frac{1}{2},\frac{1}{2}\right\rangle \leftrightarrow \left|-\frac{1}{2},\frac{1}{2}\right\rangle$ and $\left|\frac{1}{2},-\frac{1}{2}\right\rangle \leftrightarrow \left|-\frac{1}{2},-\frac{1}{2}\right\rangle$. Using formula (36), the energies for these transitions are

$$
\begin{aligned}
\Delta E_{m_I=\frac{1}{2}} &= E_{\frac{1}{2},\frac{1}{2}} - E_{-\frac{1}{2},\frac{1}{2}} = g_e\beta_e B + \frac{1}{4}(\sqrt{D^-} + \sqrt{D^+}) \\
\Delta E_{m_I=-\frac{1}{2}} &= E_{\frac{1}{2},-\frac{1}{2}} - E_{-\frac{1}{2},-\frac{1}{2}} = g_e\beta_e B - \frac{1}{4}(\sqrt{D^-} + \sqrt{D^+})
\end{aligned}
\tag{37}
$$

where $D^{\pm} = \hat{l}\cdot\overleftrightarrow{A}\cdot\overleftrightarrow{A}\cdot\hat{l} \pm 4g_n\beta_n B\hat{l}\cdot\overleftrightarrow{A}\cdot\hat{l} + 4(g_n\beta_n B)^2$.

Since the hyperfine interaction is isotropic, a coupling constant "a" can replace the tensor $\overleftrightarrow{A}$. ("a" has the dimensions of energy.) The two terms under the square roots of formula (36), can be written as $(\hat{l}\cdot\overleftrightarrow{A}\cdot\overleftrightarrow{A}\cdot\hat{l}\mp 4g_n\beta_n B\,\hat{l}\cdot\overleftrightarrow{A}\cdot\hat{l}) \rightarrow a^2 \mp 4g_n\beta_n Ba$, then the transition energies become

$$\Delta E_{m_I=\frac{1}{2}} = g_e\beta_e B + \frac{1}{2}a\,,\ \Delta E_{m_I=-\frac{1}{2}} = g_e\beta_e B - \frac{1}{2}a\,. \qquad (38)$$

The resonance conditions $\Delta E_{m_I=\pm\frac{1}{2}} = h\nu = g_e\beta_e B \pm \frac{1}{2}a$ can be obtained under the condition: constant magnetic field and the frequency being swept or constant microwave frequency and the magnetic field being swept slowly. Typically, the EPR signal is observed under the second condition. Then with constant microwave frequency ν, the transitions to the first-order approximation will occur at two resonant fields: $B_1 = \frac{h\nu - 1/2\,a}{g_e\beta_e}$ and $B_2 = \frac{h\nu + 1/2\,a}{g_e\beta_e}$ with equal intensities. A typical first-derivative spectrum in an increasing magnetic field is depicted in Fig. 3.4a. The separation between the two resonant signals is $B_2 - B_1 = a/g_e\beta_e \equiv a_0$, where a_0 is hyperfine splitting constant in magnetic-field units.

Most free radicals contain several magnetic nuclei. The hyperfine interaction between the unpaired electron and the nuclei will lead to a multi-line spectrum. By analyzing the line pattern successfully, we can obtain information on how these nuclei couple to the unpaired electron. However, most samples contain more than one radical, and the patterns from each radical may overlap each other. That makes the spectrum complicated so that it is difficult to analyze the hyperfine interaction and identify the radicals. Therefore, the ENDOR technique is important to use because it increases the resolution by producing separated lines for each hyperfine coupling.

First-order ENDOR

ENDOR is a widely used multiple resonance technique to study the hyperfine structure of free radicals. In ENDOR experiments, one monitors the enhancement of an EPR transition while simultaneously exciting a nuclear spin transition. Spin relaxation processes in the system are critical for

the ENDOR response. The electron and nuclear spin relaxation need to be completely independent so that the saturation of the electron resonance does not alter the nuclear spin populations. An ENDOR spectrum is generally much better resolved than EPR. The main reason is that the ENDOR spectrum can produce a much narrower resonance peak than EPR. (The relaxation time in ENDOR is much longer than that in EPR; from $\Delta E \Delta t \geq \hbar$, the line width in ENDOR will be much narrower.) Also, the reason of the better resolution is that ENDOR only produces one line for each distinct group of nuclei with a particular hyperfine splitting constant. However, the EPR spectrum produces 2^n lines for n equivalent nuclei, and it will overlap badly for more sets of equivalent protons in the system.

First-order ENDOR transitions are governed by the selection rules $\Delta m_s = 0, \Delta m_I = \pm 1$. These describe the transitions are only between the nuclear Zeeman levels, i.e., NMR transitions. For the spin system $S = I = \frac{1}{2}$, there are two possible ENDOR transitions $\left|\frac{1}{2},\frac{1}{2}\right\rangle \leftrightarrow \left|\frac{1}{2},-\frac{1}{2}\right\rangle$ and $\left|-\frac{1}{2},\frac{1}{2}\right\rangle \leftrightarrow \left|-\frac{1}{2},-\frac{1}{2}\right\rangle$. In an ENDOR experiment, the radio frequency ν is scanned slowly with the magnetic field set to an EPR transition. Using formula (36), the two resonances are given by

$$\begin{aligned} h\nu_1 &= E_{\frac{1}{2},\frac{1}{2}} - E_{\frac{1}{2},-\frac{1}{2}} = \frac{1}{2}\sqrt{\hat{I}\cdot\overleftrightarrow{A}\cdot\overleftrightarrow{A}\cdot\hat{I} - 4g_n\beta_n B\,\hat{I}\cdot\overleftrightarrow{A}\cdot\hat{I} + 4(g_n\beta_n B)^2} \\ h\nu_2 &= E_{-\frac{1}{2},-\frac{1}{2}} - E_{-\frac{1}{2},\frac{1}{2}} = \frac{1}{2}\sqrt{\hat{I}\cdot\overleftrightarrow{A}\cdot\overleftrightarrow{A}\cdot\hat{I} + 4g_n\beta_n B\,\hat{I}\cdot\overleftrightarrow{A}\cdot\hat{I} + 4(g_n\beta_n B)^2} \end{aligned} \tag{39}$$

Using the free proton frequency (or Larmor frequency) $\nu_n \equiv \frac{g_n\beta_n B}{h}$, equation (39) becomes

$$\begin{aligned} h\nu_1 &= E_{\frac{1}{2},\frac{1}{2}} - E_{\frac{1}{2},-\frac{1}{2}} = \frac{1}{2}\sqrt{\hat{I}\cdot\overleftrightarrow{A}\cdot\overleftrightarrow{A}\cdot\hat{I} - 4h\nu_n\,\hat{I}\cdot\overleftrightarrow{A}\cdot\hat{I} + 4(h\nu_n)^2} \\ h\nu_2 &= E_{-\frac{1}{2},-\frac{1}{2}} - E_{-\frac{1}{2},\frac{1}{2}} = \frac{1}{2}\sqrt{\hat{I}\cdot\overleftrightarrow{A}\cdot\overleftrightarrow{A}\cdot\hat{I} + 4h\nu_n\,\hat{I}\cdot\overleftrightarrow{A}\cdot\hat{I} + 4(h\nu_n)^2} \end{aligned} \tag{40}$$

From equation (40), the square of the observed frequencies ν_1^2 and ν_2^2 are

$$\nu_1^2 = \hat{l}\cdot(\frac{1}{4}\overleftrightarrow{A_\nu}\cdot\overleftrightarrow{A_\nu} - \nu_n\overleftrightarrow{A_\nu})\cdot\hat{l} + \nu_n^2$$
$$\nu_2^2 = \hat{l}\cdot(\frac{1}{4}\overleftrightarrow{A_\nu}\cdot\overleftrightarrow{A_\nu} + \nu_n\overleftrightarrow{A_\nu})\cdot\hat{l} + \nu_n^2 \qquad (41)$$

Here $\overleftrightarrow{A_\nu} = \frac{\overleftrightarrow{A}}{h}$ is the hyperfine coupling tensor (in frequency units). By setting $a_\nu = \hat{l}\cdot\overleftrightarrow{A}\cdot\hat{l}$, and if only consider the isotropic effect, then $\hat{l}\cdot\overleftrightarrow{A}\cdot\overleftrightarrow{A}\cdot\hat{l} = a_\nu^2$ approximately, and equation (41) becomes $\nu_{1,2}^2 = \frac{1}{4}a_\nu^2 \mp \nu_n a_\nu + \nu_n^2$. Thus the first-order ENDOR frequencies are given by

$$\nu_{1,2} = \left|\nu_n \mp \frac{1}{2}a_\nu\right| \qquad (42)$$

It is common for proton ENDOR that $\nu_n > \frac{1}{2}a_\nu$. Therefore two ENDOR lines approximately are separated by a_ν and centered at ν_n (see Fig. 3.4b). For K-band ENDOR, ν_n is ~36.0MHz with the magnetic field is around 8500G.

Hyperfine coupling tensor

For free radicals trapped in a single crystal, the hyperfine interactions contain the isotropic and anisotropic (dipolar) components and can be described by the hyperfine coupling tensor $\overleftrightarrow{A}$, which is an important magnetic parameter for analyzing the free radical. $\overleftrightarrow{A}$ is generally represented as three principal values and three eigenvectors each associated with one principal value.

The ENDOR frequency in equation (41) for the case $m_s = \frac{1}{2}$ is given by $\nu_1^2 = \hat{l}\cdot(\frac{1}{4}\overleftrightarrow{A_\nu}\cdot\overleftrightarrow{A_\nu} - \nu_n\overleftrightarrow{A_\nu})\cdot\hat{l} + \nu_n^2$, then $\nu_1^2 - \nu_n^2 = \hat{l}\cdot(\frac{1}{4}\overleftrightarrow{A_\nu}\cdot\overleftrightarrow{A_\nu} - \nu_n\overleftrightarrow{A_\nu})\cdot\hat{l}$. Thus it is very convenient to use a real 3x3 symmetric tensor

$$\overleftrightarrow{T} = \frac{1}{4}\overleftrightarrow{A_\nu}\cdot\overleftrightarrow{A_\nu} - \nu_n\overleftrightarrow{A_\nu}. \qquad (43)$$

We have

$$\nu_1^2 - \nu_n^2 = \hat{l}\cdot\overleftrightarrow{T}\cdot\hat{l}. \qquad (44).$$

Since $\hat{l} = l_x \hat{i} + l_y \hat{j} + l_z \hat{k}$ is the unit vector along the direction of $\vec{B}$, then

$$\hat{l} \cdot (\overleftrightarrow{T}) \cdot \hat{l} = (l_x l_y l_z) \begin{pmatrix} T_{xx} & T_{xy} & T_{xz} \\ T_{yx} & T_{yy} & T_{yz} \\ T_{zx} & T_{zy} & T_{zz} \end{pmatrix} \begin{pmatrix} l_x \\ l_y \\ l_z \end{pmatrix} \qquad (45)$$

$$= l_x^2 T_{xx} + l_y^2 T_{yy} + l_z^2 T_{zz} + 2(l_x l_y T_{xy} + l_x l_z T_{xz} + l_y l_z T_{yz})$$

and the observed ENDOR frequency can be described by the elements of tensor $\overleftrightarrow{T}$, that is,

$$v_{obs}^2 - v_n^2 = l_x^2 T_{xx} + l_y^2 T_{yy} + l_z^2 T_{zz} + 2(l_x l_y T_{xy} + l_x l_z T_{xz} + l_y l_z T_{yz}) \qquad (46)$$

where $l_x^2 + l_y^2 + l_z^2 = 1$. If the magnetic field direction (l_x, l_y and l_z) is known, the components of tensor $\overleftrightarrow{T}$ can be obtained by six independent equations of (46). (Since the tensor is symmetric with T_{xy}=T_{yx} etc.) This can be done by a linear fitting analysis of the data from three independent rotations.[9] Tensor $\overleftrightarrow{T}$ relates hyperfine coupling tensor $\overleftrightarrow{A}$ with equation (43): for the eigenvalues, $\xi_T = \frac{1}{4}\xi_A^2 - v_n \xi_A$, where ξ_T and ξ_A are principal values of $\overleftrightarrow{T}$ and $\overleftrightarrow{A}$; their eigenvectors are the same.

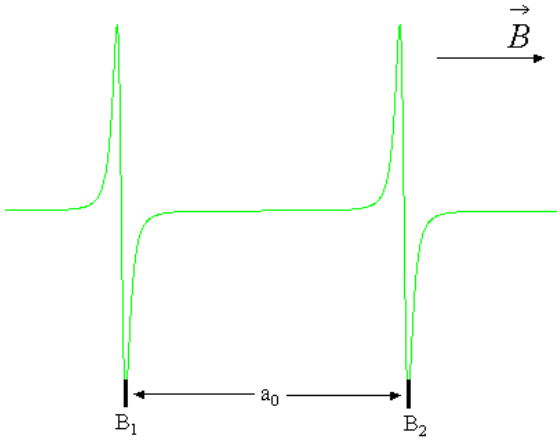

Fig. 3.4(a) *Sample of a first-derivative EPR spectrum with two magnetic resonant positions and hyperfine splitting constant a_0.*

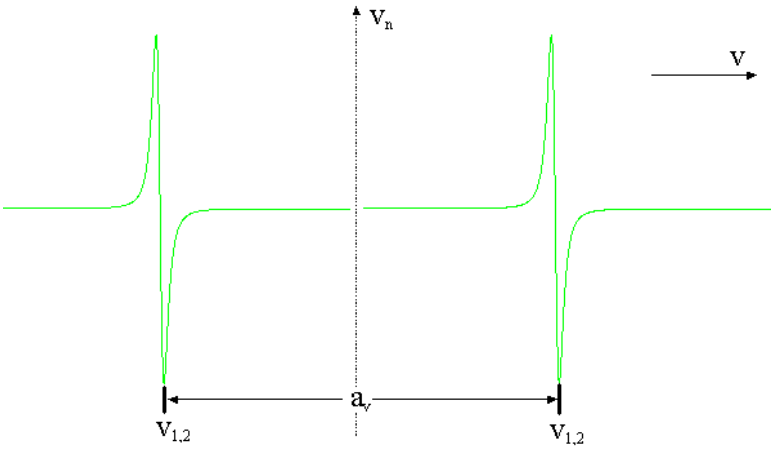

Fig. 3.4(b) *Sample of a first-derivative ENDOR spectrum with two observed frequencies and hyperfine splitting* a_ν.

The second-order hyperfine interaction

In the first-order approximation, we take $\vec{S}\cdot\vec{I} = S_x I_x + S_y I_y + S_z I_z \to S_z I_z$. The effects from $S_x I_x + S_y I_y$ will produce a second order correction for hyperfine interaction. For the system only containing isotropic hyperfine interaction a, i.e., $\overleftrightarrow{A} \to a$, the Hamiltonian in equation (29) can be written as

$$\begin{aligned} H_s &= g_e\beta_e BS_z + (aS_z - g_n\beta_n B)I_z + a(S_x I_x + S_y I_y) \\ &= H_s^{(0)} + H_s^{(1)} + H_s^{(2)} \end{aligned} \qquad (47)$$

To solve the second-order term, it is convenient to define two operators,

$$\begin{aligned} S^+ &\equiv S_x + iS_y \\ S^- &\equiv S_x - iS_y \end{aligned} \qquad (48)$$

S^+ and S^- are called the raising operator and the lowing operator: using S^+ on a spin state, m_s will increase by 1; while using S^- on it, m_s will decrease by 1. Thus for the system $S = \frac{1}{2}$ and $m_s = \pm\frac{1}{2}$, there are

$$
\begin{aligned}
&S^{+}\left|\frac{1}{2}\right\rangle = 0 \\
&S^{+}\left|-\frac{1}{2}\right\rangle = \left|\frac{1}{2}\right\rangle \Rightarrow \left\langle \frac{1}{2}\middle| S^{+} \middle| -\frac{1}{2}\right\rangle = 1 \\
&S^{-}\left|\frac{1}{2}\right\rangle = \left|-\frac{1}{2}\right\rangle \Rightarrow \left\langle -\frac{1}{2}\middle| S^{-} \middle| \frac{1}{2}\right\rangle = 1 \\
&S^{-}\left|-\frac{1}{2}\right\rangle = 0
\end{aligned}
\qquad (49)
$$

Similar the operators for the nuclear spins are

$$
\begin{aligned}
&I^{+} \equiv I_x + iI_y \\
&I^{-} \equiv I_x - iI_y
\end{aligned}
\qquad (50)
$$

and the operate on nuclear spin states in same way:

$$
I^{+}\left|\frac{1}{2}\right\rangle = 0; I^{+}\left|-\frac{1}{2}\right\rangle = \left|\frac{1}{2}\right\rangle; I^{-}\left|\frac{1}{2}\right\rangle = \left|-\frac{1}{2}\right\rangle; I^{-}\left|-\frac{1}{2}\right\rangle = 0 \qquad (51)
$$

From equations (48) and (50), it can be derived that

$$
H_s^{(2)} = a(S_x I_x + S_y I_y) = \frac{1}{2}a(S^{+}I^{-} + S^{-}I^{+}) \qquad (52)
$$

From (49) and (51), the operator $S^{+}I^{-}$ will shift the state $\left|-\frac{1}{2},\frac{1}{2}\right\rangle$ to $\left|\frac{1}{2},-\frac{1}{2}\right\rangle$, and gives zero for other states; while the operator $S^{-}I^{+}$ will shift $\left|\frac{1}{2},-\frac{1}{2}\right\rangle$ to $\left|-\frac{1}{2},\frac{1}{2}\right\rangle$, and annihilates other states. Thus the only non-zero terms of the two operators are $\left\langle -\frac{1}{2},\frac{1}{2}\middle| S^{-}I^{+} \middle| \frac{1}{2},-\frac{1}{2}\right\rangle = 1$ and $\left\langle \frac{1}{2},-\frac{1}{2}\middle| S^{+}I^{-} \middle| -\frac{1}{2},+\frac{1}{2}\right\rangle = 1$. Using the perturbation theory, the energies to the second-order are

$$
\begin{aligned}
E_1 &= \frac{1}{2}g_e\beta_e B - \frac{1}{2}g_n\beta_n B + \frac{1}{4}a \\
E_2 &= \frac{1}{2}g_e\beta_e B + \frac{1}{2}g_n\beta_n B - \frac{1}{4}a + \frac{a^2}{4(g_e\beta_e B + g_n\beta_n B)} \\
E_3 &= -\frac{1}{2}g_e\beta_e B - \frac{1}{2}g_n\beta_n B - \frac{1}{4}a - \frac{a^2}{4(g_e\beta_e B + g_n\beta_n B)} \\
E_4 &= -\frac{1}{2}g_e\beta_e B + \frac{1}{2}g_n\beta_n B + \frac{1}{4}a
\end{aligned}
\qquad (51)
$$

Their modified wave functions are:

$$\Psi_1 = \left|\frac{1}{2},\frac{1}{2}\right\rangle$$
$$\Psi_2 = \left|\frac{1}{2},-\frac{1}{2}\right\rangle + \frac{a}{2(g_e\beta_e B + g_n\beta_n B)}\left|-\frac{1}{2},\frac{1}{2}\right\rangle$$
$$\Psi_3 = \left|-\frac{1}{2},\frac{1}{2}\right\rangle - \frac{a}{2(g_e\beta_e B + g_n\beta_n B)}\left|\frac{1}{2},-\frac{1}{2}\right\rangle \qquad (52)$$
$$\Psi_4 = \left|-\frac{1}{2},-\frac{1}{2}\right\rangle$$

These demonstrate that in the second-order approximation, $\left|\frac{1}{2},\frac{1}{2}\right\rangle$ and $\left|-\frac{1}{2},-\frac{1}{2}\right\rangle$ are unaffected but $\left|-\frac{1}{2},\frac{1}{2}\right\rangle$ and $\left|\frac{1}{2},-\frac{1}{2}\right\rangle$ are mixed together. These modified spin states with their energies are shown in Fig. 3.5.

Forbidden transitions-The second-order EPR spectrum

Because of the second-order modifications, the allowed EPR transitions occur at slight different energies but the separation between them still gives the value of a. Their intensities are slightly reduced because small changes are in their wave functions.

To first-order, the transition $\left|\frac{1}{2},-\frac{1}{2}\right\rangle \leftrightarrow \left|-\frac{1}{2},\frac{1}{2}\right\rangle$ is strictly forbidden. Now it is weakly allowed if the oscillating magnetic field is polarized parallel to the static magnetic field. Using the wavefunctions in (52), and denoting λ as the mixing coefficient $\frac{a}{2(g_e\beta_e B + g_n\beta_n B)}$, then the perturbation $2g_e\beta_e B_z \boldsymbol{S}_z \cos\omega t$ has the element

$$\left\langle \Psi_2 \left| S_z \right| \Psi_3 \right\rangle = \left(\left\langle \frac{1}{2},-\frac{1}{2}\right| + \lambda\left\langle -\frac{1}{2},\frac{1}{2}\right|\right) S_z \left(\left|-\frac{1}{2},\frac{1}{2}\right\rangle - \lambda\left|\frac{1}{2},-\frac{1}{2}\right\rangle\right) = -\lambda \qquad (53)$$

Thus its corresponding transition probability is proportional to λ^2. Since λ is small, for high fields, λ^2 is negligible. At low field strength, however, the transition $\left|\left\langle \Psi_2 \left| S_z \right| \Psi_3 \right\rangle\right|^2$ should be detectable.[3] The forbidden transitions ($\Delta m_s = 1$, $\Delta m_I = 1$) are also shown in Fig. 3.5.

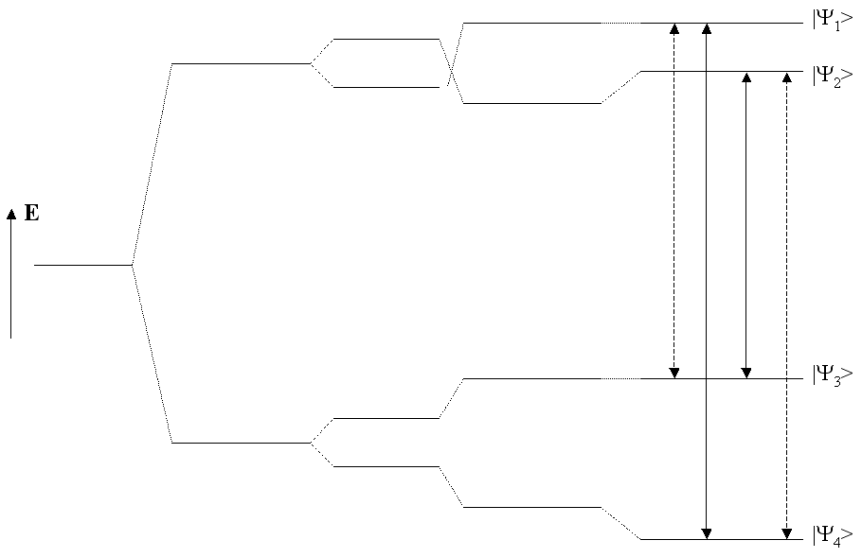

Fig. 3.5 *Spin energy levels of a spin system with* $S = I = \frac{1}{2}$*, the allowed EPR transitions (solid lines) and the forbidden transitions (dotted lines).*

3.5 Origin of The Hyperfine Coupling [1, 3, 8]

The hyperfine coupling to be considered is the magnetic dipolar interaction of the electron-spin magnetic dipole with that of the nuclei in the vicinity. The classical interaction energy between two magnetic dipoles is given by

$$E = \frac{\vec{\mu}_e \cdot \vec{\mu}_n}{r^3} - \frac{3(\vec{\mu}_e \cdot \vec{r})(\vec{\mu}_n \cdot \vec{r})}{r^5} \qquad (54)$$

where $\vec{\mu}_e$ is the electron magnetic moment, $\vec{\mu}_n$ is the nuclear magnetic moment and $\vec{r}$ is the vector between the two moments. The dipolar interaction Hamiltonian is given by the quantum mechanical version with $\vec{\mu}_e = -g_e \beta_e \vec{S}$ and $\vec{\mu}_n = g_n \beta_n \vec{I}$:

$$H_{dip} = -g_e \beta_e g_n \beta_n \{\frac{\vec{S} \cdot \vec{I}}{r^3} - \frac{3(\vec{S} \cdot \vec{r})(\vec{I} \cdot \vec{r})}{r^5}\} \ . \qquad (55)$$

Since the electron is not localized at one position in space, the expression (55) has to be averaged over the entire distribution function. Then the dipolar interaction Hamiltonian is

$$\left\langle H_{dip} \right\rangle = -g_e \beta_e g_n \beta_n \vec{S} \cdot \left\langle \frac{\overleftrightarrow{1} - 3\hat{r}\hat{r}}{r^3} \right\rangle \cdot \vec{I} \quad . \qquad (56)$$

Also, we noticed that in equation (56), $H_{dip} \to \infty$, when r =0. However, this is not a problem because most of the orbitals (p, d, f etc.) with none-zero orbital momentum approach zero exponentially as r →0. Only the s orbital has a non-zero probability density at the nucleus (r = 0), but the s orbital is spherically symmetric, and $\left\langle \frac{\overleftrightarrow{1} - 3\hat{r}\hat{r}}{r^3} \right\rangle$ = 0. That is, the dipolar coupling does not come from the s orbital. The asymmetric orbitals (p, d, f, etc.) with non-zero spatial integrals in (56) will contribute to the dipolar hyperfine coupling. By expanding the vectors in (56) with coordinates x, y, z, the terms of $g_e \beta_e g_n \beta_n \left\langle \frac{\overleftrightarrow{1} - 3\hat{r}\hat{r}}{r^3} \right\rangle$ become a symmetric and traceless tensor with the elements:

$$T_{ii} = -g_e \beta_e g_n \beta_n \left\langle \frac{r^2 - 3\hat{i}^2}{r^5} \right\rangle$$
$$T_{ij} = g_e \beta_e g_n \beta_n \left\langle \frac{3\hat{i}\hat{j}}{r^5} \right\rangle \qquad (57)$$

where $r = x\hat{i} + y\hat{j} + z\hat{k}$, and $rr = x^2 \hat{i}\hat{i}, xy\hat{i}\hat{j}$, etc.

There is also a hyperfine coupling from the quantum mechanical interaction of electrons and nuclei, and it is called contact interaction. It has the form (given by Fermi [10, 11])

$$H = \frac{8\pi}{3} g_e \beta_e g_N \beta_N \vec{S} \cdot \vec{I} \left| \Psi(0) \right|^2 \qquad (58)$$

where $\Psi(0)$ represents the electron wavefunction evaluated at the nucleus. Hence the contact interaction only occurs for the electron having non-zero probability density at the nucleus. Since the electron density

at nuclei is non-zero only for the s orbital, any isotropic couplings must come from the s-orbital. By virtue of the spherical symmetry of s orbital, the hyperfine interaction is of course isotropic, and it generally is called isotropic coupling.

Thus, the magnetic hyperfine interaction in general contains both isotropic and dipolar components. In the spin Hamiltonian (27), the hyperfine term is $H = \vec{S} \cdot \overleftrightarrow{A} \cdot \vec{I}$. The hyperfine coupling tensor can be given as $\overleftrightarrow{A} = a\,\overleftrightarrow{1} + \overleftrightarrow{T}$, where a is the isotropic coupling, $\overleftrightarrow{1}$ is the 3x3 unit matrix, and $\overleftrightarrow{T}$ is the traceless tensor from the dipolar interaction with the elements given in (57). Also, we define the scalar a as

$$a = \frac{1}{3} tr(\overleftrightarrow{A}) \qquad (59)$$

The type (α- or β-) of the hyperfine coupling can be identified from the anisotropy it exhibits as described in the next section.

Types of hyperfine couplings

In a free radical with a group of atoms (see Fig. 3.6, the "•" denotes the unpaired electron), the unpaired electron will interact with the nuclei in its surroundings. These interactions display different characteristics for different nuclei that depend upon the positions of the nuclei corresponding to the unpaired spin. Thus understanding these characteristics is important for identifying the radicals and exhibiting the geometry information of the radical from the data. Three types of hyperfine couplings are most common: 1) direct type coupling: the unpaired spin interacts with nucleus of the atom where it is mainly localized (X), 2) α-type coupling: the magnetic nucleus is one bond away from the unpaired spin (Y or H_α), 3) β-type coupling: the nucleus is two bonds away ((Z or H_β). For the nuclei farther away from the unpaired spin, the couplings are usually negligible since the dipolar coupling is proportional to r^{-3}.

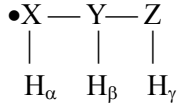

Fig. 3.6 *Unpaired electron with neighboring nuclei.*

The molecules in most biosystems contain ^{12}C, ^{16}O, ^{14}N, ^{1}H, and ^{2}H, and I = 0 for ^{12}C, ^{16}O and ^{2}H, thus the magnetically active nuclei are only ^{14}N (I = 1) and ^{1}H (I = 1/2). In this study, the unpaired spins of all the radicals are mainly located on ^{12}C, thus no direct coupling is observable. The α- and β- type couplings will be described as follows.

α-type couplings

The α-type hyperfine coupling always exhibits a large anisotropy with three distinct eigenvalues. For a commonly observed Ċ-H coupling, their magnitudes are approximately 3a, 2a and a. In this study, a is ~30MHz. The isotropic component (with magnitude of ~2a) is negative because of *spin polarization*.[1] As shown in Fig. 3.7a and 3.7b, there are two possibilities for assigning the spins in the C-H σ bond. (Here it is assumed that the $2p_z$ orbital of the carbon atom is perpendicular to the C-H bond; the $2p_x$, $2p_y$ and 2s orbitals of the carbon atom form sp^2 hybrids. The hydrogen atom bonds to one of these three coplanar hybrids.) If there were no electron in the $2p_z$ orbital, these two electron configurations would be equally probable. However, if an electron is in the $2p_z$ orbital with spin ↑, according to the Hund's rules, the configuration in Fig. 3.7a with two parallel spins on carbon atom is more stable and hence more probable than the configuration in Fig. 3.7b with two antiparallel spins on carbon. That is, because of the positive spin density at the carbon nucleus, the net negative electron spin density is at the proton. Thus the proton couplings should be negative.

According to the McConnell relation [12], the isotropic value of α-coupling can be described as

$$a_{iso}(H_\alpha) = Q\rho_c \qquad (60)$$

where Q is a proportionality constant in magnetic-field units, and ρ_c is the unpaired spin density of the carbon atom. (Usually ρ_c, the unpaired spin of the $2p_z$ orbital of the carbon atom is significantly smaller than unity due to delocalization of the unpaired electron.) For the radicals formed in amino acids, the typical Q value is –73.4MHz.[13] From the Gordy-Bernhard relation[14, 15], the spin density on carbon can also be estimated from the most positive dipolar components $a_z(H_\alpha)$:

$$a_z(H_\alpha) = Q^z_{dip}\rho_c \qquad (61)$$

where the proportionality constant Q^z_{dip} = 38.7MHz. The isotropic value of an α-coupling is more sensitive to radical geometry than the dipolar coupling, and spin density calculated from the McConnell relation (60) will be affected accordingly. Thus the spin density in (61) is more reliable. Also, comparison of the spin densities from (60) and (61) is helpful as an indication of whether the α-proton is bending about the nodal plane of the p-orbital.[16-18]

In an α-coupling, if the radical center is planar, the eigenvector with the most positive dipolar value is along the ·X-H direction; that with the intermediate eigenvalue is along the spin orbital; and that with the most negative eigenvalue is perpendicular to the above two directions. (see Fig. 3.8) Thus the eigenvectors from an α-coupling are important for assigning the coupling to a particular proton.

β-type coupling

Because the dipole-dipole interaction is r^{-3} dependent and a β-proton is farther away from the radical center, the β-coupling always has much smaller anisotropy than α-coupling. Also, the β-proton is not limited to the nodal plane of the radical center, and spin polarization is not a involved in β-couplings. Thus the principal values of a β-coupling can be defined as positive. The anisotropic values show characteristics of axial symmetry with the ratio of *2b : -b : -b*. (The two small components are almost equal and both negative; the maximum component is about twice the absolute value of the smaller one.) For a typical Ċ-C-H coupling, b is ~7-9MHz, and for Ċ-O-H, b is a little larger (~13-22MHz, see Chapter 5). It is not difficult to distinguish β-couplings from α-couplings due to these characteristics. Also, the eigenvector with the maximum anisotropic value is along the direction of the β-proton to the radical center atom (see Fig. 3.9). This is always useful for β-coupling assignment. The Heller-McConnell expression[19] also gives the relation between the isotropic value of β-coupling, $a_{iso}\ (H_\beta)$ and the spin density on the radical center ρ:

$$a_{iso}\ (H_\beta) = (B_0 + B_1\cos^2\theta)\rho \qquad (62)$$

where θ is the dihedral angle between the p-orbital and C_b-H_b bond as shown in Fig. 3.9, and B_0 and B_1 are factors depending on the specific atoms and their structure of the radical. In this work, the B_0 is

usually taken as 0MHz for Ċ-C-H coupling or –4MHz for Ċ-O-H coupling, and B_1 is about 55-140MHz.[20-22]

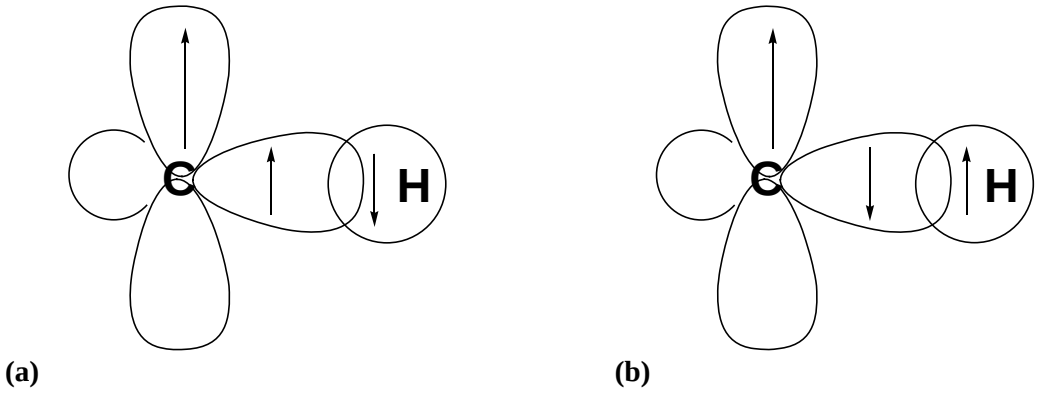

Fig. 3.7 *Possible spin configuration in a Ċ-H fragment.*

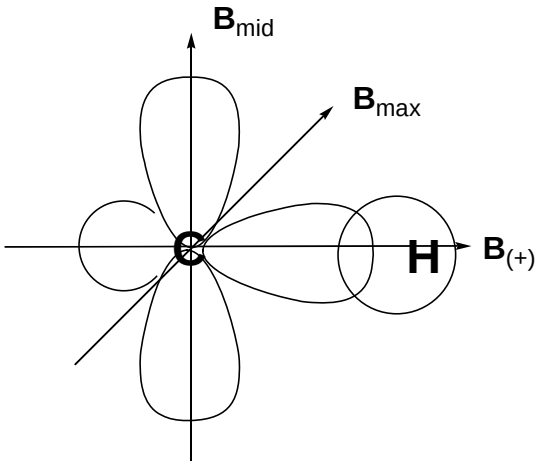

Fig. 3.8 *Dipolar vectors of an α-coupling accociated with the direction in a Ċ-H fragment.*

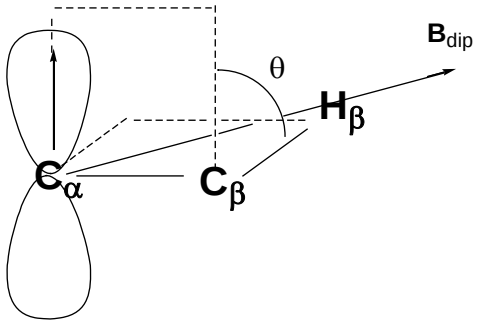

Fig. 3.9 *The dihedral angle θ for a β-proton and the dipolar vector of the β-coupling associated with the direction in a Ċ-C-H fragment.*

References:

1. J. A. Weil, J. R. Bolton and J. E. Wertz, *Electron Paramagnetic Resonance-Elementary Theory and Practicla Applications*. John Wiley & Sons, Inc., New York, NY, (1994).

2. L. Kevan and L. D. Kispert, *Electron Spin Double Resonance Spectroscopy*. John Wiley & Sons, Inc., New York, NY, (1976).

3. A. Carrington and A. D. McLachlan, *Introduction to Magnetic Resonance-with Applications to Chemistry and Chemical Physics*. Harper & Row, Publishers, Incorporated, New York, NY, (1967).

4. N. M. Atherton, *Principles of Electron Spin Resonance*. Ellis Horwood Limited, Chichester, England, (1993).

5. M. J. Stephen and G. K. Fraenkel, Theory of saturation in electron spin resonance spectra. *J. Chem. Phys.* **32,** 1435-1444 (1960).

6. M. J. Stephen, The calculation of saturation effects in magnetic resonance. *J. Chem. Phys.* **34,** 484-489 (1961).

7. A. Abragam and B. Bleaney, *EPR of Transition Ions, Chapter 4*. Oxford University Press, London, England, (1970).

8. H. M. Assenheim, *Introduction to Electron Spin Resonance*. Plenum Press, New York, NY, (1967).

9. W. H. Nelson, Estimation of Errors in Eigenvalues and Eigenvectors from Magnetic Resonance Results by Use of Linear Data - Fitting Techniques. *Journal of magnetic resonance* **38,** 71-78 (1980).

10. M. Fujimoto, W. A. Seddon and D. R. Smith, Electron Spin Resonance Studies of Free Radicals in γ-Irradiated Amino Acid Crystals: α-Amino Isobutyric Acid and L-Lysine·HCl·$2H_2O$. *J. Chem. Phys.* **48,** 3345-3350 (1968).

11. G. T. Rado, Simple derivation of the electron-nucleus contact superfine interaction. *America Journal of Physics* **30,** 716-718 (1962).

12. H. M. McConnell and D. B. Chesnut, Theory of isotropic hyperfine interactions in π-electron radicals. *J. Chem. Phys.* **28,** 107-117 (1958).

13. R. W. Fessenden and R. H. Schuler, Electron Spin Resonance Studies of Transient Alkyl Radicals. *J. Chem. Phys.* **39,** 2147-2195 (1963).

14. W. Gordy, *Theory and Application of Electron Spin Resonance*. John Wiley & Sons, Inc, New York, NY, (1980).

15. W. A. Bernhard, The use of alpha hyperfine coupling tensors as a measure of unpaired spin density and free radical geometry. *J. Chem. Phys.* **81,** 5928-5936 (1984).

16. A. J. Dobbs, B. C. Gilbert and R. O. C. Norman, Electron spin resonance studies. XXVII. The geometry of oxygen substituted alkyl radical. *Journal of the Chemical Society A* **1,** 124-135 (1971).

17. P. A. Erling and W. H. Nelson, Dependence of α-Proton Hyperfine Couplings on Free Radical Geometry. *The Journal of Physical Chemistry A* **108,** 7591-7595 (2004).

18. W. H. Nelson, ESR and ENDOR studies of radicals produced in hydroxyproline single crystals by X-irradiation at low temperatures. 2. *J. Phys. Chem.* **92,** 554-561 (1988).

19. C. Heller and H. M. McConnell, Radiation Damage in Organic Crystals. II. Electron Spin Resonance of $(CO_2H)CH_2CH(CO_2H)$ in β-Succinic Acid. *J. Chem. Phys.* **32,** 1535-1539 (1960).

20. A. Horsfield, J. R. Morton and D. H. Whiffen, The electron-spin resonance spectrum of ·(CH3)CH (CO2H) between 100 K and 200 K. *Mol. Phys.* **5,** 115-120 (1962).

21. A. Horsfield, J. R. Morton and D. H. Whiffen, The electron spin resonance spectrum of CH3CHCOOH at 77 K in L-α-alanine. *Mol. Phys.* **4,** 425-431 (1961).

22. J. R. Morton, Electron Spin Resonance Spectra of Oriented Radicals. *Chemical Reviews* **64,** 453-471 (1964).

CHAPTER 4.

EXPERIMENTAL METHODS

4.1 Introduction

The major experimental steps used in this work are preparation of appropriate samples (the single crystals), exposure of the samples to radiation, and analysis of the resulting molecular products. The irradiation of organic molecules in a single crystal creates free radicals that are paramagnetic and can be studied by EPR and ENDOR spectroscopies. EPR is a powerful tool to detect and (in favorable circumstances) to identify free radicals with high specificity. The field began with the observation of an EPR spectrum (Zavoisky, 1945)[1] and grew rapidly after the World War II because of the development of microwave techniques. ENDOR spectroscopy[2] was developed later and is becoming of increasing importance because it can increase the effective resolution of EPR spectra.

In the following sections, the typical procedures of crystal mounting and orientation, X-ray irradiation, temperature control, data collection and analysis, and theoretical computation with the Guassian 03 package will be described in some detail. The methods of the crystal growth specific to each molecule system will be discussed in the relevant chapters (Chapters 5 and 7).

4.2 Mounting and Orienting The Crystals

To make full use of the EPR/ENDOR results, we need to establish an orthogonal reference coordinate system with a known relationship to the crystallographic axes by using the existing crystallographic information. The orthogonal reference axes generally include at least one of the crystallographic axes, and the other two axes are choosen according to the properties of the crystal, such as the growth habit.

In this work, the crystals were oriented by X-ray diffraction using a Buerger X-ray precession camera (Charles Supper Co.). The crystal was attached to a copper post, mounted on a standard two-circle

goniometer, using DUCO cement thinned with amyl acetate and the goniometer was placed onto the precession camera. In the precession method, the camera and the crystal rotate around an axis (the "dial" axis) normal to the X-ray beam. The diffraction pattern taken by the precession camera provides an accurate indication of the alignment between the X-ray beam and direct-lattice vectors in the crystal system. To establish the actual orientation, the crystal orientation is adjusted so that the rotation about the dial axis can bring two direct lattice vectors into alignment with the X-ray beam. When this is done, the dial axis is accurately parallel to a reciprocal lattice vector, and the angular positions of the two direct lattice vectors for rotations about the dial are also accurately known.

After establishing the orientation, the crystal will be transferred to a second copper post designed to fit the experimental cavity without loss of orientation with a device designed for the this purpose (Charles Supper Co.). For the final mounting of the crystal, a silver-bearing epoxy (Tra-Con 2902) was used since it does not produce an EPR signal after the irradiation. In addition, the silver improves the heat conductivity between the sample and mounting post. With this procedure, the rotation axis of the crystal for the experiments is the same as the dial axis established from the crystal orientation.

4.3 Temperature Control

Temperature control of the sample during irradiation and data collection is accomplished by attaching the copper mounting post to an Air Products Heli-Tran cold-finger style refrigerator. Temperature monitoring is done by using a temperature controller (Lakeshore model 330) with the sensor mounted at the joint between the sample post and the cold finger of the refrigerator. By pumping the liquid nitrogen, a stable reading at 66K can be obtained generally.

4.4 X-ray Irradiation

The crystals were irradiated with X-rays from a rhodium (Philips PW 2182/00) target tube connected to a constant potential generator (Phillips) and filtered by a 0.05mm Al films. To achieve the desired

radical concentration, the crystals were irradiated for three to four hours with the X-ray tube operated at typical voltage and current settings of 65kV/45mA. Under these conditions, the crystals received a total dose of ~100kGy (1Gy ≡ 1J/kg). (Considering a typical crystal mass of 10 – 20 mg, an energy amount of approximately 1-2 Joules were absorbed.) After irradiation, the sample was lowered into the cavity for data collection. The vacuum shroud for the refrigeration system has a telescoping design that permits the sample to be irradiated through an aluminum window and to move out and in the cavity without changing the temperature of the sample.

4.5 Spectrometer

The EPR, ENDOR, and EIE measurements were done using a homemade K-band spectrometer with microwave frequency of ~24 GHz as indicated by the block diagram shown in Figure 4.1. The microwave circuitry is that of a typical reflection bridge design employing a reference arm with a waveguide-based path length equalizer.[3] The microwave energy is provided by a klystron (OKI 24V10) with about 140 mW microwave power continuously measured with a sensor connected to the main arm through a 10dB coupler. An automatic frequency control (AFC) system stabilizes the microwave frequency by locking the klystron frequency to the sample cavity's resonant frequency. The actual frequency is measured by a Hewlett-Packard 5351A counter. The microwave cavity is cylindrical and resonates in the TE_{011} mode.[4] The cylindrical symmetry of this mode provides a microwave magnetic field pattern ideal for studies in which the sample is rotated. The microwave signal containing the absorption information was demodulated by a single-ended diode detector. The level of microwave power can be adjusted with an attenuator over the range of 0 – 60 dB.

The EPR cavity also contains a "standard" sample of MgO doped with (0.02 atom %) Cr^{+3} ions. The Cr:MgO sample provides a g-value standard and an intensity standard. From the procedures for calibrating the Cr:MgO sample as an intensity standard, it was found that the minimum number of spins in the cavity detectable by EPR is of the order 10^{14}. The typical crystals used in these experiments with

average masses of 10-20 mg contained approximately 10^{20} molecules. Therefore, with this spectrometer, it is possible to detect radical concentrations in the order of one part per million (1 ppm).

The magnetic field was produced by a water-cooled 9.5 inch Magnion (or Harrey-Wells) electromagnet with a 5 kW power supply (HS-1050 B) and was controlled by a Hall-effect field controller (Bruker BH-15). For some experiments, the magnetic field at the sample was measured by a NMR (Nuclear Magnetic Resonance) probe (Bruker ER/035m) placed in front of the microwave cavity.

The EPR spectra were taken by sweeping the magnetic field through a range of ~200 Gauss. The field was double modulated by 50 kHz and 33 Hz signals applied through two small coils connected in series and located on either side of the cavity within the vacuum shroud. Phase sensitive detection was accomplished by lock-in amplifiers at 50 kHz (Stanford model SR810 DSP), and at 33 Hz (EG&G model 5209). The procedure leads to EPR patterns in the second derivative representation of the absorption.

In the ENDOR experiment, the radio frequency was produced by a frequency generator (Wavetek model 3001) with the frequency set by computer and amplified by a power amplifier (ENI model 3200L). The radio frequency was introduced into the cavity with a two-turn coil in a parallel-wire arrangement along the axis of the cavity. The frequency was modulated at 25 kHz and detected by a lock-in amplifier (Stanford model SR810 DSP). With the single modulation, the first derivative ENDOR signal is observed.

ENDOR Induced EPR) experiments, the magnetic field was swept after setting the ENDOR frequency to the peak of the first derivative ENDOR line. Since the ENDOR frequency varies with the field value in proportion to the nuclear g-value, this frequency was adjusted as the field was being swept according to the specific relation between field and frequency:

$$v = v_0 + (g_n \beta_n / h)(H_0 - H)$$

where v_0 is the ENDOR frequency at initial field H_0. The EIE spectrum will show the magnetic profile of the ENDOR response, if the ENDOR line is well resolved. It is important to note that resulting pattern comes from only the radical producing the chosen ENDOR line.

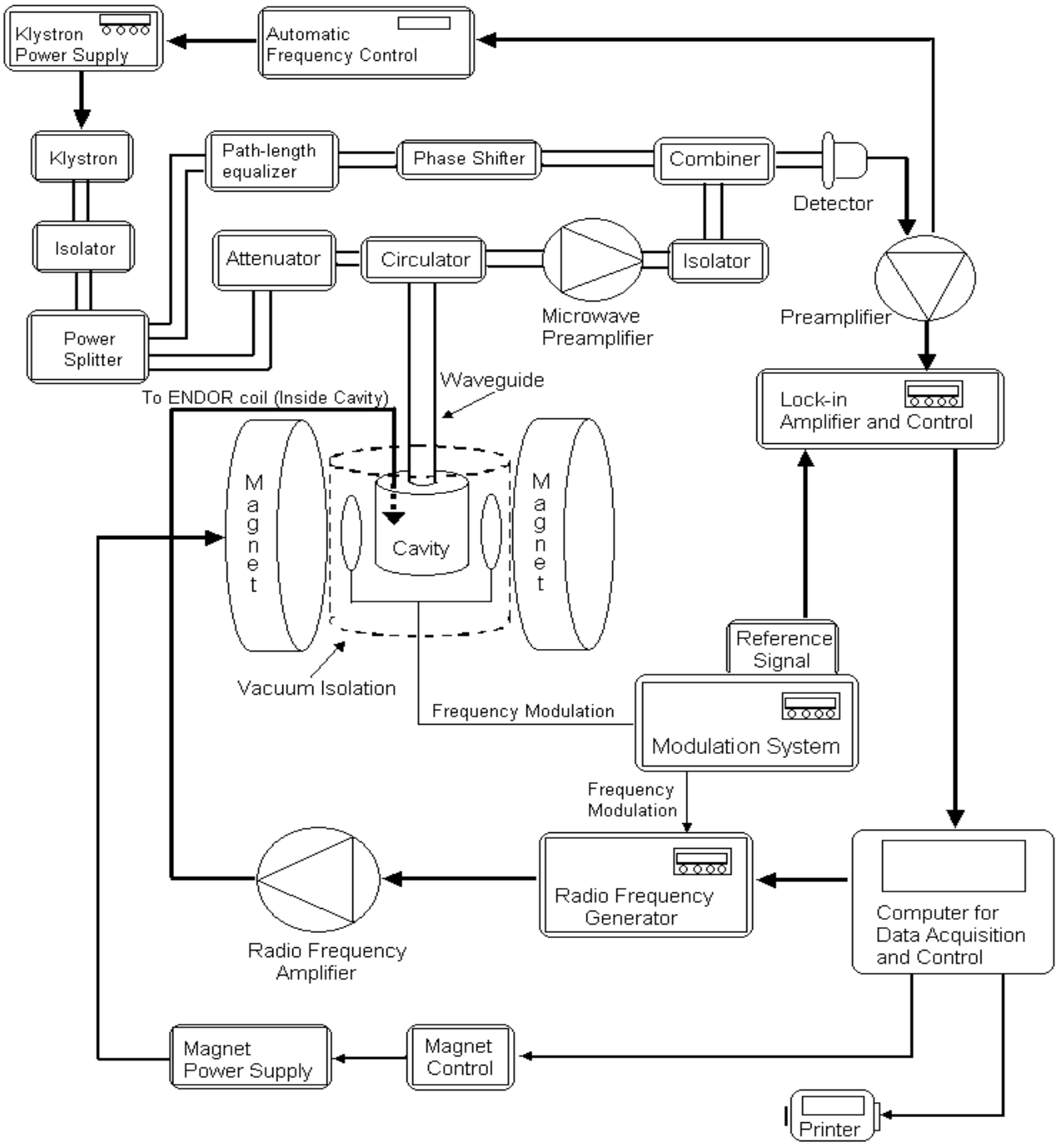

Fig. 4.1 *Block diagram of the EPR and ENDOR spectrometer.*

4.6 Data Collection and Analysis

EPR spectra were generally recorded with the crystal rotation around an oriented axis at 10° intervals over a 180° range. The estimated relative error for setting these angular positions is < 0.5°; while the absolute error for orientation is affected by the total errors accumulated in the step of transferring the X-ray-based oriented crystal to the mounting post fit for the cavity of the spectrometer. On the other hand, the data properties will reflect the crystallographic symmetry and permit the identification of systematic errors, which can be corrected during data analysis. The magnetic field was swept typically over a range of 200 G in 0.1 G increments using a computer-based control system. At each field position, the recorded spectrum is the accumulation of 30 measurements with ~2ms required for each. The typical sweep rate is 1/6 G/s—or 10 G/min. The time constant of the 33 Hz lock-in is set at 100ms and the 50 kHz lock-in is always set at the minimum time constant of 1ms.

ENDOR spectra were recorded with the crystals rotated in 5° increments. In order to provide the most complete possible picture of the individual hyperfine interactions, ENDOR spectra were always taken at more than one EPR peak. Typically, the ENDOR frequency was swept over a range of 30 MHz in 0.005 MHz increments. Each point in the recorded spectrum was the accumulation of 25 measurements with ~2 ms / sample. The typical ENDOR sweep rate was 6 MHz/min, and the lock-in time constant was set at 1sec. At the magnetic field value for K-band EPR, the free proton frequency is about 36 MHz.

Typically EIE spectra were taken at crystallographic axes in order to avoid the complications of magnetic site splitting. The EIE spectrum was collected at each ENDOR peak for comparison to the others. Basis on these comparisons, the ENDOR lines were grouped and associated with individual radicals.

The primary data used for analyzing the results were provided by the ENDOR spectra. Firstly, since the ENDOR lines were recorded as the first derivative of the actual lineshape, the midpoint frequencies of the lines were marked at the corresponding angular position on a sheet of graph paper overlaid onto the recorded spectrum. After collecting ENDOR spectra for one whole rotation plane, the frequencies thought

to belong to the same coupling were connected by hand-drawn curves. By comparing the frequencies of the ENDOR lines taken at same crystallographic axes from different rotation planes, the angular curves from same coupling can be estimated. By doing these, the frequencies of each coupling from at least three rotation planes can be read from the graph paper. The magnetic parameters (the proton hyperfine coupling tensors) are obtained and refined with the software program "magres82" developed in this lab for analyzing these recorded data[5]. The refine function is based on the spin Hamiltonian including the nuclear Zeeman term as described in Chapter 3 (see equation 30). The statistical analysis provides estimated uncertainties in addition to the coupling parameters.

Once a hyperfine coupling tensor is obtained, it is possible to ascribe the coupling to an α- or β- type from the characteristics of its eigenvalues (see Chapter 3). This is quite useful information for identifying the radical. Also, it is typically useful to compare directions of the eigenvectors to the corresponding directions in the undamaged molecule. Using the crystallographic coordinates, the specific directions in the undamaged molecule can be calculated in an Excel file. In addition, from the relationship between the isotropic value and the dihedral angle of the corresponding proton in the radical, the configuration of the radical can be estimated. However, for radicals that undergo large reorientations, the above analysis becomes uncertain. Useful information for the radical assignment and the extent of geometry reorientation can be provided by the theoretical modeling computations.

4.7 EPR Spectrum Simulations

The EPR patterns of the radicals can be simulated using measured proton coupling tensors with the SIMULATION program to compare with the experimental pattern for testing the radical assignments (i.e., "tensor simulation"). For the radicals with nitrogen couplings, or those having proton couplings undetected in ENDOR experiments, the WINSIM program was used to simulate the EPR pattern.[6, 7] WINSIM can optimize coupling parameters and refine the nitrogen couplings, and "missing" proton couplings estimated from the EPR pattern, the measured proton couplings, the g-shift, and the linewidth

to get the best match of the simulation to experiment (the minimum rms error). For an EPR from multiple radicals, the optimization process also refines the relative concentrations of each radical. Details of EPR simulation will be discussed in later chapters (see Chapter 5-8).

4.8 Theoretical Modeling Computations

To help with identifying the free radicals and reproducing the possible structure of the radical, density functional theory (DFT) computations[8] were performed using the Gaussian 03 program (G03)[9]. Theoretical work concerning the molecular structures of free radicals has become increasingly popular, largely due to the considerable success of density functional theory (DFT) methods in predicting hyperfine coupling constants to a very good degree of accuracy.

In this work, all the initial atomic coordinates of the radicals were from the corresponding crystallographic studies. These initial radical geometries were optimized in Density Functional Theory (DFT) framework by using Becke's three parameter hybrid functional B3LYP[10] in conjugation with Pople and coworker's 6-31G(d,p) basis set. In the geometry optimization, the structure of a radical in its minimum energy configuration can be found from the G03 program. The single point calculations for hyperfine coupling constants of the radicals were performed using a higher basis set 6-311G(2d,f). The keyword "NOSYMM" was used for both the optimization and the single point calculation to keep the Cartesian coordinates of the radical model from rotating or shifting with respect to the reference frame.[11] In this way, the calculated tensor directions were generated with respect to the crystal reference frame and allowed for a direct comparison with the experiment. This procedure follows from our aim to establish as good as possible agreement between the experimental and calculated hyperfine coupling tensor principal axes. Different theoretical models were constructed for studying the corresponding radicals as described below (Chapter 5-8). Two strategies were used for the comparisons of the calculated and the experimental hyperfine coupling tensors: 1) the differences between the coupling values are < 15MHz; 2) the angular differences between the eigenvectors* are < 25°.[12] Only if all the calculated tensors satisfy the two

strategies, the experimental tensors are regarded as being reproduced and the calculated model is acceptable. Sometimes the atomic coordinates in the optimized model need to be changed manually to mimic the reorientation of the radical and to reproduce the experimental tensors.

References

1. E. Zavoiskii, Spin-magnetic resonance in paramagnetic substances. *Journal of Physics (Moscow)* **9,** 245 (1945).

2. G. Feher, Observation of nuclear magnetic resonances via the electron spin resonance line. *Phys. Rev.* **103,** 834-835 (1956).

3. J. C. M. Henning, Homodyne balanced mixer electron spin resonance spectrometer. *Rev. Sci. Instrum.* **32,** 35-40 (1960).

4. A. B. Bronwell and R. E. Beam, *Theory and aplication of microwaves*. McGraw-Hill Book Company Inc., New York, (1974).

5. W. H. Nelson, Estimation of errors in eigenvalues and eigenvectors from magnetic resonance results by use of linear data - fitting techniques. *J. Magn. Reson.* **38,** 71-78 (1980).

6. D. R. Duling, A. G. Motten and R. P. Mason, Generation and evaluation of isotropic ESR spectrum simulations. *J. Magn. Reson.* **77,** 504-511 (1988).

7. D. R. Duling, Simulation of multiple isotropic spin-trap EPR spectra. *J. Magn. Reson. B* **104,** 105-110 (1994).

8. R. G. Parr and W. Yang, *Density-functional theory of atoms and molecules*. Oxford University Press, New York, (1989).

9. M. J. Frisch, G. W. Trucks, H. B. Schlegel, G. E. Scuseria, M. A. Robb, J. R. Cheeseman, J. A. Montgomery, T. V. Jr., K. N. Kudin, J. C. Burant, J. M. Millam, S. S. Iyengar, J. Tomasi, V. Barone, B. Mennucci, M. Cossi, G. Scalmani, N. Rega, G. A. Petersson, H. Nakatsuji, M. Hada, M. Ehara, K. Toyota, R. Fukuda, J. Hasegawa, M. Ishida, T. Nakajima, Y. Honda, O. Kitao, H. Nakai, M. Klene, X. Li, J. E. Knox, H. P. Hratchian, J. B. Cross, C. Adamo, J. Jaramillo, R. Gomperts, R. E. Stratmann, O. Yazyev, A. J. Austin, R. Cammi, C. Pomelli, J. W. Ochterski, P. Y. Ayala, K. Morokuma, G. A. Voth, P. Salvador, J. J. Dannenberg, V. G. Zakrzewski, S. Dapprich, A. D. Daniels, M. C. Strain, O. Farkas, D. K. Malick, A. D. Rabuck, K. Raghavachari, J. B. Foresman, J. V. Ortiz, Q. Cui, A. G. Baboul, S. Clifford, J. Cioslowski, B. B. Stefanov, G. Liu, A. Liashenko, P. Piskorz, I. Komaromi, R. L. Martin, D. J. Fox, T. Keith, M. A. Al-Laham, C. Y. Peng, A. Nanayakkara, M. Challacombe, P. M. W. Gill, B. Johnson, W. Chen, M. W. Wong, C. Gonzalez and J. A. Pople, **Gaussian 03,**(Gaussian Inc., Wallingford CT, 2004)

10. A. D. Becke, Density-functional thermochemistry. IV. A new dynamical correlation functional and implications for exact-exchange mixing. *J. Chem. Phys.* **104,** 1040-1046 (1996).

11. G. C. A. M. Vanhaelewyn, B. Jansen, E. Pauwels, E. Sagstuen, M. Waroquier and F. J. Callens, Experimental and theoretical electron magnetic resonance study on radiation-induced radicals in α-l-sorbose single crystals. *J. Phys. Chem. A* **108,** 3308-3314 (2004).

12. E. Pauwels, V. Van Speybroeck and M. Waroquier, Evaluation of different model space approaches based on DFT to examine the EPR parameters of a radiation-induced radical in solid-state α-glycine. *J. Phys. Chem. A* **108,** 11321-11332 (2004).

CHAPTER 5.

L-LYSINE · HCl · $2H_2O$ SINGLE CRYSTALS IRRADIATED AT 66K

Abstract

EPR (Electron Paramagnetic Resonance), ENDOR (Electron-Nuclear DOuble Resonance) and EIE (ENDOR-Induced EPR) results indicated at least three radicals produced in L-lysine·HCl·$2H_2O$ crystals irradiated at 66K. Radical R1 dominated the EPR spectra and was identified as the carboxyl anion, ($H_2OO\dot{C}$) CH $(NH_3)^+$ $(CH_2)_4$ $(NH_3)^+$. DFT (Density-Functional Theory) calculations supported the assignment and indicated that the carboxyl group transformed to a pyramidal configuration from a pure planarity following the electron trapped. The two small couplings detected in R1 were ascribed to the neighboring protons transferred to the carboxyl group through the intermolecular hydrogen bonds. Radical R2 was identified as the product of decarboxylation, $\dot{C}H$ $(NH_3)^+(CH_2)_4$ $(NH_3)^+$. Although the α-coupling tensor of R2 cannot be obtained from experiment, the assignment was confirmed with WINSIM simulations and DFT calculations. Radical R3 indicated several β-couplings in only the <bc> plane and thus were impossible to be assigned. Finally, the transferred protons in the carboxyl anion radical were discussed and the importance of the decarboxylation radical was estimated.

5.1 Introduction

As early as in 1968, Fujimoto and his colleagues had studied the free radicals in γ-irradiated L-lysine·HCl·$2H_2O$ (see scheme 5.1) single crystal [1]. With EPR spectra, they identified the carboxyl radical anion (primary radical, see scheme 5.1) and tentatively assigned the radical centered at the main chain nitrogen (see scheme 5.3) for irradiation at 77K. In addition, with controlled annealing experiments, the carboxyl anion was identified as the precursor of the main chain deamination radical (the stable radical, see scheme 5.4). However, the studies on the radiation chemistry of lysine was limited in 1960-70's, and no detailed studies on the radiation behavior of lysine have been reported recently.

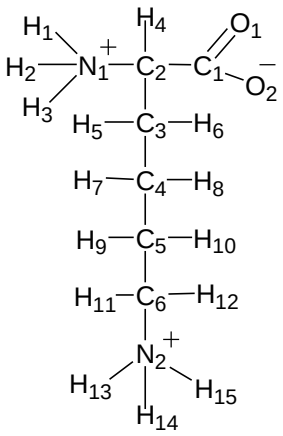

Scheme 5.1 *Lysine molecule in L-lys·HCl·2H₂O*

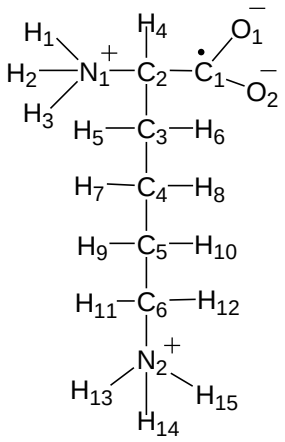

Scheme 5.2 *Carboxyl anion radical in L-lys·HCl·2H₂O*

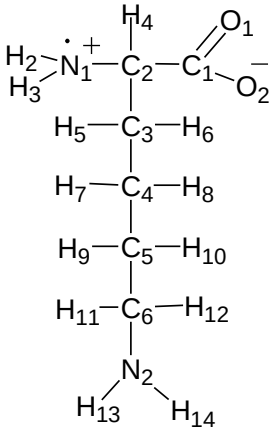

Scheme 5.3 *The radical detected in L-Lys·HCl·2H₂O*

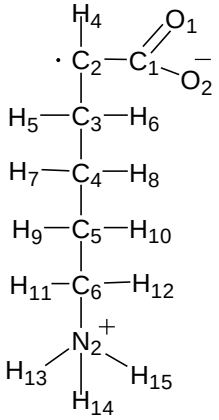

Scheme 5.4 *The deamination radical in L-Lys·HCl·2H₂O*

This work describes the free radicals in L-lysine·HCl·2H$_2$O X-irradiated at 66K that are detected with EPR, ENDOR and EIE techniques. With precise measured coupling tensors from ENDOR, the free radicals were assigned and the configurations of the radicals were analyzed. The DFT (density functional theory) [2] computations supported the assignments of the radicals. Reorientations of the radicals and the proton transfers were simulated by geometry optimizations. The radical tentatively assigned by Fujimoto et al. (shown in Scheme 5.3) was not detected in our experiment. The stable radicals formed at room temperature and their geometrical characteristics are alsp described in the following report.

5.2 Experimental

Single crystals of L-Lys·HCl·2H_2O (Sigma Chem. Co.) were grown from saturated aqueous solution by slow evaporation at room temperature. Neutron diffraction [3, 4] and X-ray diffraction [5] studies found that the crystal is monoclinic ($P2_1$) with two molecules per unit cell and with one molecule in the asymmetric unit. The crystals generally were pyramidal and elongated along <c*>; thus the crystallographic <a>, <b> and <c*> axes were chosen as the orthogonal reference system in this work.

In the crystal, the lysine molecule is a zwitterionic cation with an extra charge on the side chain amino group as shown in Scheme 5.1. All hydrogen atoms bonded to nitrogen or oxygen are involved in intermolecular hydrogen bonds. Two carboxyl oxygen atoms are hydrogen bonded to four hydrogen atoms in neighboring molecules and these four hydrogen atoms were denoted as H1'-H4' in the following text and as shown in Fig. 5.2. The N1'-H2'…O2 bond has the shortest H'…O distance (1.74Å) and the longest N-H bond length (1.059Å). (The prime denotes the atom is in a neighboring molecule.) No intramolecular hydrogen bonds were found in the crystal.

The crystals were oriented along <a*>, <b>, and <c*>, respectively by X-ray diffraction using a Buerger X-ray precession camera (Charles Supper Co.) and were transferred to a copper post for mounting on the refrigerator without loss of orientation. Temperature monitoring and control were done by using a temperature controller (Lakeshore model 330) with the sensor mounted at the joint between the sample post and the cold finger of the refrigerator. By pumping liquid nitrogen, a stable reading at 66K can be obtained. The crystals were irradiated to a dose of 100-200kGy at 66K with X-rays from a Rh-target tube operated at 65kV and filtered by a 0.05mm Al film. Subsequently, the crystals were lowered into the EPR chamber, and the K-band of EPR, ENDOR and EIE spectra were recorded at 66K. In each rotation plane, ENDOR spectra were recorded at 5° intervals.

The proton hyperfine coupling tensors were obtained and refined with the MAGRES program [6]. EIE patterns were simulated using actual coupling tensors with the SIMULATION program for comparison to the experimental spectra to test the radical assignments. For the radicals with nitrogen couplings, or those

having couplings undetected in ENDOR experiments, the WINSIM program [7, 8] was used to simulate the EIE.

To help with identifying the radicals, DFT calculations were performed using the Gaussian 03 program[9]. The coordinates for all the initial radical geometries were from the neutron diffraction studies.[3] In this work, two calculation models were constructed. In order to reproduce the proton transfer, the cluster model included neighboring molecules of hydrogen bonded to the radical. Considering the computation efficiency, some parts of the neighboring molecules were simulated by a methyl group. The second is the individual model and for it, the environmental effects were simulated by two approaches during geometry optimizations: one was to freeze some of the atom coordinates (generally those involved in the intermolecular hydrogen bonds) and the other was to use the PCM model (Polarizable Continuum Model) by adding the keyword of "scrf=PCM" [10-13]. In the PCM approach, the radical is embedded in a cavity surrounded by a continuum dielectric. In this study, the solvent for all PCM optimizations was water with dielectric constant of 78.39. For reproducing the magnetic parameters, some parts of the optimized radical needed to be rotated or bent manually. All of the radicals were optimized with the B3LYP functional[14] and the 6-31G (d, p) basis set. The magnetic parameters were calculated subsequently on the final radical structure with single point calculations using the 6-311G (2d, p) basis set. The "NOSYMM" keyword[15] was used for both the geometry optimization and the single point calculation, and the Cl^- atom was omitted from all calculation models. When comparing the coupling tensors from experiments and modeling calculations, we used two strategies[16]: 1) the differences between isotropic values are <15MHz; 2) the angular differences between eigenvectors[I] are $<25^0$. That is, only if all the tensors from one model satisfy the two strategies, is the model accepted as the one reproducing the reoriented structure of the radical.

[I] The eigenvectors are those associated with the maximum eigenvalue for β-couplings.

5.3 Results and Analysis

Fig. 5.1a shows the EPR spectrum from an L-lys·HCl·2H_2O crystal taken after irradiation at about 66K. At most orientations, a doublet dominated the center of EPR spectra with weak satellite lines on both sides. EIE patterns indicated the presence of at least three distinct radicals. The center doublet is due to radical R1, while R2 and R3 give some of the satellite lines in the EPR spectra. The EIE patterns of R1- R3 are shown in Fig. 5.1b – d, respectively.

As indicated in Fig. 5.1e, ENDOR lines were grouped for the three radicals based on EIE patterns. The very strong ENDOR peak located at 50.5MHz is coupling 1 of R1 that gives the ~9G-doublet in the EPR spectrum. In addition, there are at least seven small couplings associated with R1, but only four of these are shown in Fig. 5.1e, labeled as 4'- 7'. Couplings 1' - 3' have much smaller ENDOR frequencies at this orientation and are obscured by the free proton line. The couplings of R2 are denoted as A-E, but coupling D is not displayed in Fig. 5.1e because it also is obscured by the free proton line. Coupling E was only detected for rotation about <a*> and has anisotropy characteristics of an α coupling. The very weak peaks I- III located around 60 MHz were associated with R3. These lines could be detected only for rotation about <a*>, and have anisotropy characteristics of β couplings, but it was not possible to identify R3. In the following sections, the characteristics and assignments of radicals R1 and R2 will be discussed.

Radical R1: the carboxyl anion radical

Using ENDOR results, the hyperfine coupling tensors of lines 1, 1' - 3' were calculated and are listed in Table 5.1. ENDOR lines from the small couplings 4'-7' overlapped with the free proton line at most orientations and therefore their tensors could not be obtained. We ascribed coupling 1 to a β proton because of its characteristics of slight anisotropy and axial symmetry, and it is this coupling that yields the dominant doublet in EPR spectra at most orientations. Coupling 1' also is characteristic of a β–coupling with the maximum anisotropic value of about 14 MHz, which is typical of O-H or N-H β-couplings. As is analyzed in the following, couplings 1' and 2' are identified as two O-H β couplings, and coupling 3' is identified as a distant coupling.

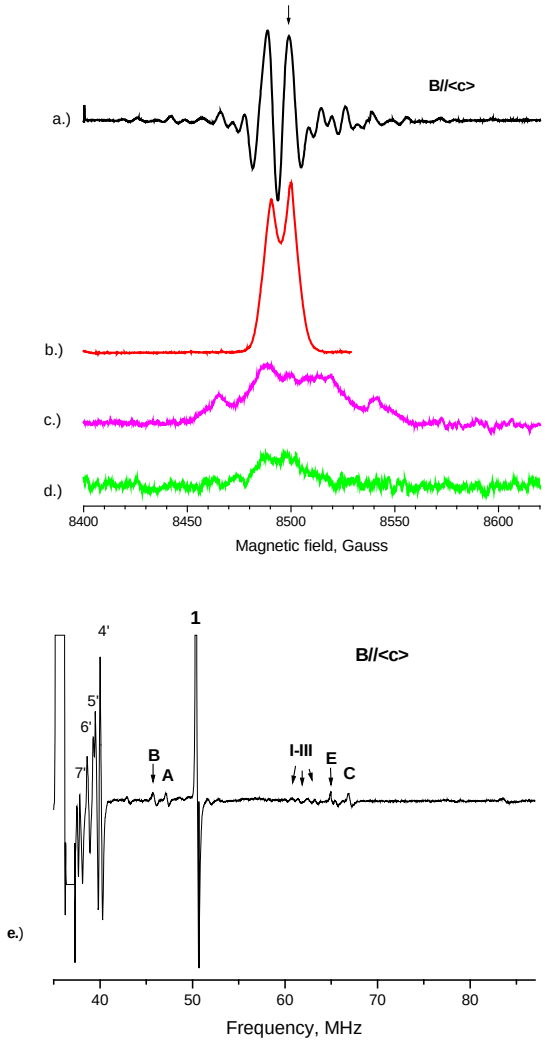

Fig. 5.1 (a) *Second-derivative EPR spectrum of L-Lys·HCl·2H_2O single crystals irradiated and measured at 66K with magnetic field along <c>;* ***(b-d)*** *EIE spectra for R1* ***(b)****, R2* ***(c)*** *and R3* ***(d)*** *under the same conditions and at same orientation as (a);* ***(e)*** *First-derivative ENDOR spectrum with the magnetic field locked to one peak of the central doublet in (a) and the ENDOR lines were grouped with EIE patterns shown in (b-d) as described in the text.*

From the above results, R1 shows features typical of carboxyl anions, which are common reduction products in amino acids irradiated at low temperatures[20]. Scheme 5.2 represents the chemical structure of the carboxyl anion radical from L-lys·HCl·2H_2O single crystal, which has the unpaired spin mainly located on C1. On this basis, coupling 1 was ascribed to H4, couplings 1' and 2' were ascribed to the two protons transferred from neighboring molecules to the carboxyl group through hydrogen bonds.

Previous studies of carboxyl anion radicals from irradiated amino acids, have shown that the coupling to H4 (coupling 1 in this case) can be expressed with the Heller-McConnell relation [18]

$$a_{C\text{-}H} = B_1 \rho \cos^2\theta_d, \qquad (1)$$

where $a_{C\text{-}H}$ is the isotropic value of the C- H β coupling, B_1 is a constant related to the geometry of the radical, ρ is spin density on carbon atom of radical center, and θ_d is the dihedral angle between directions of H4-C2 bond and the spin orbital. For the anions, the conventional value of B_1 ρ for C-H β proton is 77.3MHz[19]. In this case, the isotropic value of 25.9MHz for coupling 1, indicates a dihedral angle of 54.6°. From crystallographic data and the assumption that the spin orbital is normal to the carboxyl plane in the undamaged molecule, the dihedral angle of H4 was calculated to be 46.1°, which is ~8° different from the dihedral angle calculated above. Moreover, as is shown in Table 5.1, the maximum eigenvector[I] of coupling 1 is very close to the direction H1…C1 in the undamaged molecule.

For couplings 1' - 2', based on the results shown in Table 5.2, the directions of H1'…C1 and H2'…C1 in the crystal lattice are closest to the maximum eigenvectors[I] of couplings 1' and 2', respectively. Therefore, couplings 1' and 2' can be ascribed to H1' and H2', respectively. On the other hand, both isotropic values are small, and indicate that the transferred protons are close to the nodal plane of the anion radical. This can be analyzed with the relation[20]

$$a_{O\text{-}H} = -4\text{MHz} + B_1 \rho \cos^2\theta_d \qquad (2)$$

where $a_{O\text{-}H}$ is the isotropic value of the O- H β coupling and the other parameters are the same as described for formula (1). With the conventional value of B_1 ρ as 40.32MHz for an O- H β coupling of a carboxyl anion radical[20], the dihedral angle for coupling 1' is 63.4° and for coupling 2' it is very close to 90°. Taking the spin orbital of the anion radical as normal to the planar carboxyl group in the undamaged molecule, and comparing the dihedral angle (θ_d) of the four neighboring protons hydrogen bonded to the carboxyl group, as shown in Table 5.3, only H2' gives a large dihedral angle. All the other protons have much smaller dihedral angles as compared to the calculated ones with formula (2). From the above results, for coupling 1', the dihedral angle calculated with the formula (2) is quite different from the value

expected for proton H1' in the undamaged crystal. However, the reorientation of the radical anion, especially the pyramidalization of the carboxyl group after the electron captured, and the transfer of H1' to carboxyl group, will make H1' much closer to the nodal plane of the radical; i.e., the dihedral angle of H1' should be much larger than that expected in the undamaged crystal. This explanation was supported with DFT geometry optimization as indicated in the following. Similarly, from Table 5.2, H4'…C1 is closest to the eigenvector[I] of coupling 3'. Thus coupling 3' was ascribed to H4', the proton in the neighboring water molecule.

Table 5.1 *Hyperfine coupling tensors for radical R1 in L-lys·HCl·2H_2O single crystals irradiated at 66K.*[a,b,c]

				Eigenvectors[b]		
Tensor	Principal values[a,b]	Isotropic Values[a]	Anisotropic values[a]	<a>	<b>	<c*>
	37.34(2)		11.47	0.523(1)	-0.343(4)	0.780(2)
1	21.19(2)	25.87	-4.68	0.344(1)	0.922(1)	0.175(5)
	19.07(2)		-6.80	0.780(0)	-0.177(3)	-0.601(1)
	18.40(3)		14.27	0.974(0)	0.066(7)	0.215(5)
1'	-1.63(16)	4.13	-5.76	0.114(2)	0.681(24)	-0.724(23)
	-4.38(16)		-8.51	0.194(2)	-0.730(22)	-0.656(24)
	7.49(30)		11.75	0.111(5)	0.149(6)	0.983(1)
2'	-8.32(4)	-4.26	-4.06	0.075(6)	-0.987(1)	0.142(7)
	-11.95(4)		-7.69	0.991(1)	0.058(7)	-0.121(4)
	13.73(4)		12.05	0.008(3)	-0.866(25)	0.500(9)
3'	-1.87(8)	1.68	-3.55	0.351(1)	-0.466(5)	-0.812(12)
	-6.82(24)		-8.50	0.936(1)	0.182(8)	0.301(22)
Crystallographic direction			H4…C1	0.572	-0.164	0.804
~10.7° angular difference with eigenvector[c] of coupling 1						

[a]All these values are in units of MHz. [b]Numbers in parentheses are the estimated uncertainties in the last digit quoted as reported by the statistical analysis. [c]This eigenvector is the principal direction associated with the largest coupling component.

Table 5.2 *Comparison the eigenvectors[a] of couplings 1' - 3' of radical R1 in L-lys·HCl·2H$_2$O single crystals irradiated at 66K and the corresponding crystallographic directions.[b, c]*

	Eigenvectors[a]				Directions of Hx'….C1[b]			
Coupling	<a>	<b>	<c*>	Protons[b]	<a>	<b>	<c*>	Angle Diff (°)[c]
1'	0.974	0.066	0.215	H1'	-0.994	0.023	-0.105	8.4
				H2'	0.138	-0.023	-0.990	85.4
				H3'	0.972	-0.047	-0.229	26.6
				H4'	-0.311	0.898	-0.311	71.9
2'	0.111	0.149	0.983	H1'	-0.994	0.023	-0.105	77.9
				H2'	0.138	-0.023	-0.990	16.0
				H3'	0.972	-0.047	-0.229	82.9
				H4'	-0.311	0.898	-0.311	78.1
3'	0.008	-0.866	0.500	H1'	-0.994	0.023	-0.105	85.4
				H2'	0.138	-0.023	-0.990	61.7
				H3'	0.972	-0.047	-0.229	86.2
				H4'	-0.311	0.898	-0.311	20.7

[a]The eigenvectors are the principal directions associated with the largest coupling components. [b] Hx' are the neighboring protons hydrogen bonded to the carboxyl group of lysine molecule, H1'- H4', as denoted in Fig. 5.2 [c]"Angle Diff (°)" are the angular differences between the experimental eigenvectors and the crystallographic directions in units of degrees.

Table 5.3 *The dihedral angles (in degrees) between H1'-H4' (as denoted in Fig. 5.2) with the expected unpaired spin orbital of the carboxyl anion radical in L-lys·HCl·2H$_2$O single crystals.*

Protons	Dihedral angle(°)
H1'	22.8
H2'	71.2
H3'	30.7
H4'	48.8

DFT calculations on radical R1: In order to mimic the reorientation of the anion radical and identify which of the neighboring protons is transferred, the geometry optimization model should include the four neighboring protons H1'-H4', which are hydrogen bonded to the carboxyl group of lysine. We take the lysine molecule with one electron added as the central radical. The environment was simulated by one water molecule and the amino groups from three neighboring lysine molecules. The remainder of each neighboring molecule was simulated by a methyl group. As shown in Fig. 5.2a and 5.2c, H1' – H3' are amino protons in groups A-C, respectively. Groups A and B represent the side chain aminos of two neighboring molecules, while group C represents the main-chain amino of a third neighbor, along with

H4', the proton within water D. Considering the other hydrogen bonds and environmental effects on the anion model, some of the atoms were frozen during the geometry optimization. These atoms are marked "f" in Fig. 5.2b. The optimizations used the 6-31G(d, p) basis, and the resulting geometry (see Fig. 5.2b) shows that the anion reorients mainly at the carboxyl group. The bond lengths C1-O1 and C1-O2 increased by about 0.1Å. The deviation from planarity is such that the torsion angle O1-C2-O2-C1 is ~24°. Similarly, H1'… O1 and H2'…O2 are shortened by ~0.5Å and ~0.7Å, respectively, while there is almost no change for H3'…O2, and H4'…O1 increased by 0.9 Å. Upon formation of the anion, a single point calculation at 6-311G(2d,p) on the complete cluster showed that the spin density is mainly on atoms of the carboxyl group: ρ(C1) = 0.58, ρ(O1) = 0.21, and ρ(O2) = 0.08. In this calculation, the isotropic value of H4 coupling is only ~4MHz, which is much smaller than the experimental value of 25.9MHz. Also there is an ~23MHz isotropic coupling to N1, but this was not observed in the EPR and EIE patterns. Because the isotropic value is a function of geometry, the next step was to seek a more compatible structure by rotating the side chain of the radical from C2 about C1-C2 bond in steps of 10° with single point calculations on the clusters performed at each step. The relation between isotropic values (for H4 and N1) and rotation angle is shown in Fig. 5.3. The calculated value in best agreement with the experimental value of coupling 1 corresponds to a rotation angle between 30°-40°. The calculated results with the rotation angle of 30° are listed in Table 5.4. All the calculated tensors are satisfied with the two strategies when compared to the corresponding experimental ones. Thus the model (with the side chain rotated by ~30°) is the structure that best reproduces the experimental couplings of the carboxyl anion.

Proton transfer in radical R1: In radical R1 (the carboxyl anion radical), at least seven small couplings (1'-7') were detected and tensors from three of them (1'-3') were obtained. The maximum anisotropic value for 1' is a value typical of O-H coupling in the anion (see Table 5.5)[20-24], while the eigenvector[I] of 1' is ~parallel with direction C1…H1' in the undamaged crystal and in the optimized model. Thus we conclude that 1' is the result of the transferred proton H1'. The maximum anisotropic values for 2' and 3' appear a little smaller than the typical anisotropic value for O-H couplings as shown

in Table 5.5. However, the anion cluster optimization indicated that the H2'…O2 distance was shortened to 1.04 Å on anion formation, and was within the range of an O-H bond. Moreover, in the undamaged crystal, the distance H2'… O2 is the shortest (1.74 Å) of the four intermolecular hydrogen bonds to the carboxyl oxygen atoms, while the length of N'-H2' is longer than other N-H bonds in lysine. Thus H2' may transfer more easily to O2 after the electron is trapped by the carboxyl group. From the evidence above, and the result that the eigenvector[I] of 2' is ~parallel to the direction H2'…C1, we assigned H2' as the transferred proton giving coupling 2'.

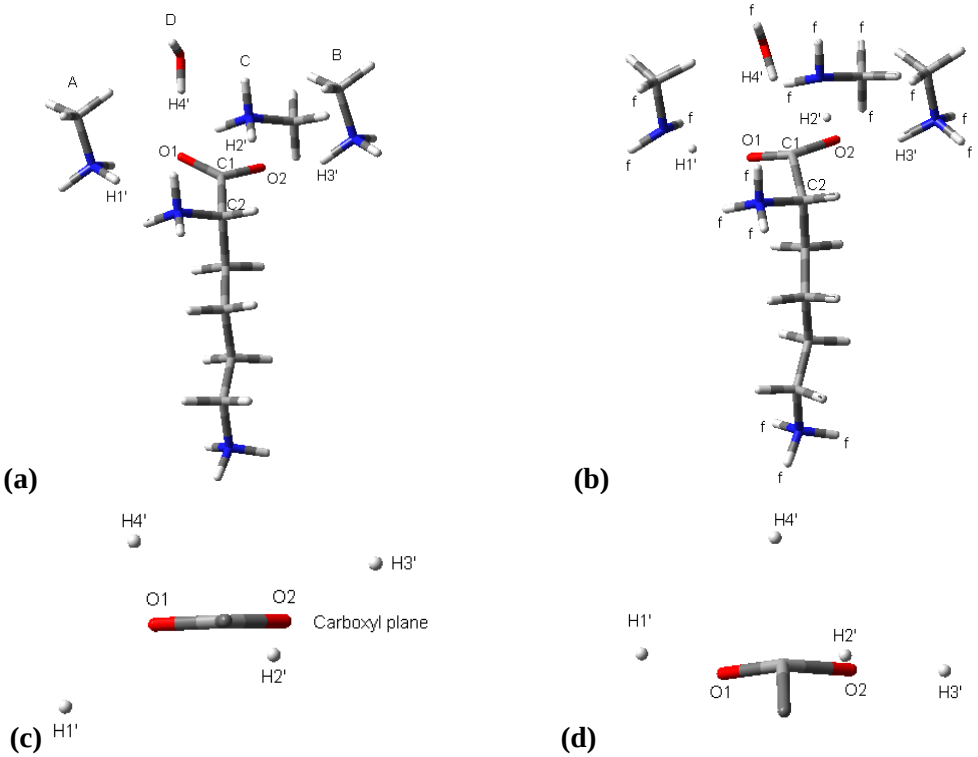

Fig. 5.2 *The DFT calculation model for the carboxyl anion of L-Lys·HCl·2H$_2$O single crystals irradiated at 66K.* ***(a)*** *The model before geometry optimization. H1'-H4' in neighboring groups A-D are protons hydrogen bonded to carboxyl group of the central radical.* ***(b)*** *The model after optimization. The "f"s denote the frozen atoms during optimization.* ***(c)-(d)*** *The detail structures of the carboxyl group and the neighboring protons H1'-H4' before* ***(c)*** *and after* ***(d)*** *the geometry optimization.*

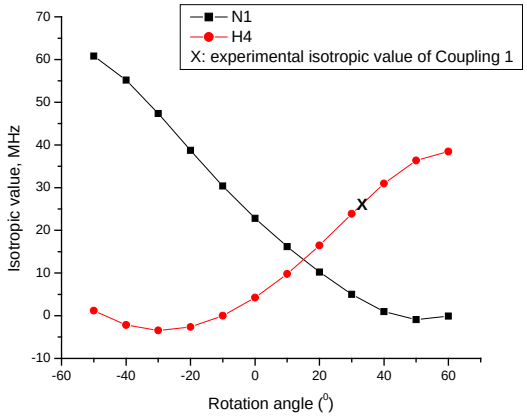

Fig. 5.3 *The relation between the isotropic values from H4 and N1 and the rotation angle (see Scheme 5.2 for the atom labeling).*

Table 5.4 *The DFT calculated hyperfine-coupling tensors from the cluster model of the carboxyl anion, and the angular differences between the calculated and experimental eigenvectors.*[a, b]

				Eigenvectors				
Proton	Principal Value[a]	Isotropic value[a]	Anisotropic value[a]	<a>	<b>	<c*>	:Coupling	Angle diff (°)[b]
	34.25		10.39	0.505	-0.021	0.863	: 1	19.2
H4	19.59	23.86	-4.27	-0.221	0.963	0.153		
	17.74		-6.12	0.834	0.268	-0.482		
	10.92		10.33	0.996	0.020	0.093	: 1'	8.6
H1'	-3.74	0.59	-4.33	-0.028	0.996	0.088		
	-5.41		-6.00	-0.091	-0.090	0.992		
	7.04		13.17	0.041	0.153	0.987	: 2'	4.0
H2'	-11.36	-6.13	-5.23	-0.702	0.707	-0.081		
	-14.07		-7.94	0.711	0.690	-0.136		
	15.59		20.98	-0.187	0.902	-0.389	: 3'	12.3
H4'	-15.19	-5.39	-9.80	0.344	0.431	0.834		
	-16.56		-11.17	0.920	0.022	-0.391		

[a] All these values are in units of MHz. [b] The "Angle diff (°)" is the angular difference between the calculated and the experimental eigenvectors associated with the maximum eigenvalues in units of degrees.

Table 5.5 *Couplings for O-H Proton of carboxyl anion radicals in single crystals; "bonded" stands for the proton bonded to the carboxyl oxygen before the irradiation damage; "transfer" stands for the proton transferred to the carboxyl oxygen after the anion radical formed.*

Crystals	Couplings	a_{iso} (MHz)	B_{max} (MHz)	B_{mid} (MHz)	B_{min} (MHz)	Reference
L-alanine	H' (transfer)	39.84	18.31	-6.86	-11.45	20
succinic acid	H (bonded)	-1.40	17.30	-7.62	-9.72	21
	H' (transfer)	2.38	17.50	-7.64	-9.86	
L-valine·HCl·H2O	H (bonded)	16.13	18.06	-8.34	-9.74	22
	H' (transfer)	36.57	20.89	-8.12	-12.74	
α-glycine	H' (transfer)	4.20	14.00	-4.76	-8.96	23
	H' (transfer)	-4.73	14.06	-5.40	-8.65	
α-amio isobutyric	H' (transfer)	8.20	16.24	-7.17	-9.04	23
acid	H' (transfer)	-2.69	13.19	-5.82	-7.39	
L-o-serine	H (bonded)	-5.59	15.84	-5.90	-9.94	24
phosphate (10K)	H' (transfer)	31.03	20.11	-8.72	-11.40	
L-o-serine	H (bonded)	8.88	18.48	-8.36	-10.13	24
phosphate (77K)	H' (transfer)	77.75	13.74	-4.75	-9.00	
L-lys·HCl·$2H_2O$	H' (transfer)	4.13	14.27	-5.76	-8.51	Chapter 5
	H' (transfer)	-4.26	11.75	-4.06	-7.69	
L-arg·HCl·H_2O	H' (transfer)	9.30	14.33	-6.27	-8.06	Chapter 7
Molecule A	H' (transfer)	1.69	15.21	-5.41	-9.80	
L-arg·HCl·H_2O	H' (transfer)	-4.53	14.94	-5.19	-9.75	Chapter 7
Molecule B	H' (transfer)	-7.27	16.43	-6.47	-9.96	

Radical R2: the decarboxylation radical

Table 5.6 lists the hyperfine coupling tensors from lines A-D (Fig. 5.1e with D obscured by the free proton signal). All four are β-couplings as indicated by the small anisotropy and approximate axial symmetry. The tensor of coupling E could not be calculated because its ENDOR lines were only detected for rotation about <a*>. However, coupling E exhibits very large anisotropy in this plane and thus was assigned as an α–coupling. WINSIM simulations of the EIE pattern associated with R2, such as that shown in Fig. 5.4, were used to identify any additional couplings that were not obtained from ENDOR experiments. The simulations indicated that only one coupling was missing from the ENDOR data and

that it is unlikely to be nitrogen coupling. The simulations also indicated that the missing coupling was approximately 31G at <b> and <c>, and approximately 34G at <a>. This evidence indicates that the coupling has very little anisotropic character. Thus it was assigned as a β-coupling, denoted as coupling F. Therefore, R2 has one α and five β couplings, for which there are two possible structures: 1) the product of decarboxylation radical (scheme 5.5) with spin mainly located on C2; 2) the product of dehydrogenation from C6 (scheme 5.5).

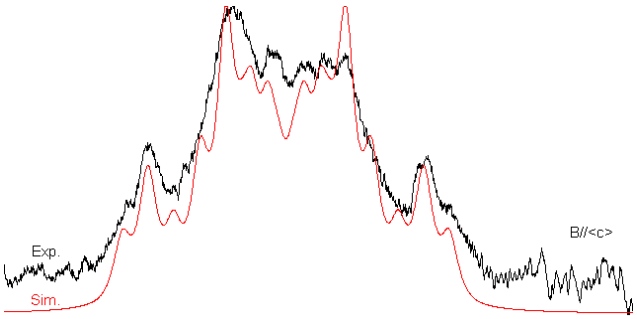

Fig. 5.4 *WINSIM simulation of the EIE pattern of radical R2 in L-Lys·HCl·2H$_2$O single crystals irradiated at 66K with magnetic field along <c> axis. "Sim."- the simulated spectrum; "Exp."- the experimental spectrum.*

Table 5.7 lists the related crystallographic directions of the two possibilities in comparison with the experimental eigenvectors[I] for couplings A-D. All of these eigenvectors[I] correspond well with the crystallographic directions associated with the decarboxylation radical. For the dehydrogenation radical, the eigenvectors[I] of couplings B-D are close to the directions of the three amino protons H15, H13 and H14 to C6, respectively, but the eigenvector[I] of coupling 2 is very different from all the crystallographic directions from β protons of C6. The large angular differences to crystallographic directions of H9…C6 and H10…C6 for coupling 2 are very unlikely from the reorientations after the radical formed. Thus the experimental evidence supports the assignment of R2 as the decarboxylation radical, the common oxidation product in amino acids irradiated at low temperature[17].

Table 5.6 *Hyperfine coupling tensors for radical R2 in L-lys·HCl·2H_2O single crystals irradiated at 66K.*[a, b, c]

Tensors	Principal values[a,b]	Isotropic Values[a]	Anisotropic values[a]	Eigenvectors[b] <a>	<b>	<c*>
	34.87(3)		10.65	0.924(0)	-0.039(4)	-0.381(3)
A	19.66(3)	24.22	-4.56	0.168(2)	0.935(4)	0.312(11)
	18.14(3)		-6.08	0.344(1)	-0.352(11)	0.871(4)
	34.06(2)		11.33	0.294(1)	-0.883(28)	-0.365(22)
B	17.32(5)	22.73	-5.41	0.599(1)	-0.127(16)	0.791(5)
	16.82(4)		-5.91	0.745(1)	0.452(19)	-0.491(30)
	75.80(2)		9.54	0.542(1)	0.808(7)	0.231(4)
C	62.01(2)	66.26	-4.25	0.426(1)	-0.501(3)	0.754(5)
	60.96(2)		-5.30	0.725(1)	-0.310(6)	-0.615(7)
	17.08(8)		9.91	0.308(8)	-0.884(30)	-0.351(19)
D	3.95(18)	7.17	-3.22	0.567(2)	-0.126(11)	0.814(4)
	0.47 (24)		-6.70	0.764(6)	0.450(19)	-0.463(30)
E[c]		74.30		along <b>		
(α-coupling)		65.10		along <c>		

[a.] All of the values are in units of MHz. [b] Numbers in parentheses are the estimated uncertainties in the respective values as reported by the statistical analysis. [c] α-Coupling E was only detected in <ac> plane.

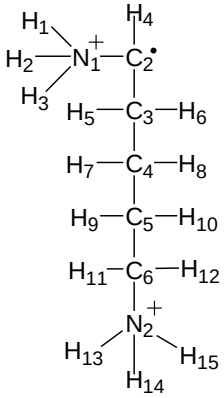

Scheme 5.5(a)*: Chemical structure of the decarboxylation radical*

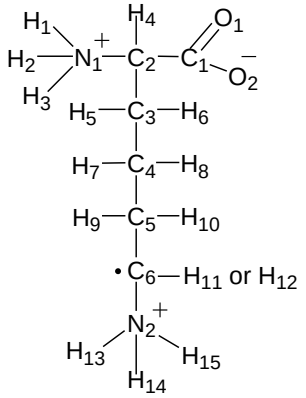

Scheme 5.5(b)*: Chemical structure of the dehydrogenation from C6*

Table 5.7 *Comparison the eigenvectors of couplings A-D of radical R2 and the crystallographic directions in undamaged L-lys·HCl·2H_2O single crystal.*[a, b, c]

	Eigenvector[a]				Direction of Hx….C2[b]			
Coupling	<a>	<b>	<c*>	β proton	<a>	<b>	<c*>	Angle Diff (°)
Decarboxylation radical								
A	0.924	-0.039	-0.381	H2	-0.909	0.189	0.372	8.5
B	0.294	-0.883	-0.365	H1	-0.419	0.819	0.393	8.2
C	0.542	0.808	0.231	H5	-0.567	-0.795	-0.216	1.7
D	0.308	-0.884	-0.351	H6	0.242	-0.911	-0.334	4.4
Dehydrogenation radical								
A	0.924	-0.039	-0.381	H9	-0.346	0.214	-0.914	88.8
				H10	0.429	0.106	-0.900	42.7
B	0.294	-0.883	-0.365	H15	-0.186	0.914	0.361	6.5
C	0.542	0.808	0.231	H13	-0.411	-0.818	-0.403	12.4
D	0.308	-0.884	-0.351	H14	0.342	-0.908	-0.242	6.8

[a] The eigenvectors are the principal directions associated with the largest coupling components. [b] The "Hx"s denote the corresponding β protons of the decarboxylation radical. [c]The "Hx"s denote the corresponding β protons of the radical of dehydrogenation from C6.

Other quantitative evidence supporting this assignment can be derived from the relation (1). For a neutral π radical, B_1 is approximately 125MHz for both CCH_β and CNH_β couplings[18]. It was not possible to obtain the α-coupling's tensor for R2 (coupling E), but the data for rotation about <a*> is consistent with a coupling from $\rho \approx 0.8$. With these values and the experimental isotropic couplings, the dihedral angle can be estimated as follows: for coupling A, $\theta_d \approx 60.5°$; for coupling B, $\theta_d \approx 61.5°$; for coupling C, $\theta_d \approx 35.5°$; for coupling D, $\theta_d \approx 74.5°$.

From crystallographic data, and assuming that the unpaired electron is in an orbital near the direction of the previous C1-C2 bond, the corresponding dihedral angles are: for C2…H1, $\theta_d = 49.2°$; for C2…H2, $\theta_d = 71.6°$; for C2…H3, $\theta_d = 13.7°$; for C2…H5, $\theta_d = 55.6°$; for C2…H6, $\theta_d = 66.3°$. These correspond well with estimates above from relation (1) for the associations indicated in Table 5.7. The table does not include the coupling from C2…H3. However, the dihedral angle estimated from the crystallographic data is ~14° and indicates a coupling near 90MHz (~33G). This is comparable to the missing coupling identified by the WINSIM simulations.

The above analysis indicates very little reorientation for the decarboxylation radical. This is typical of decarboxylation radicals in other irradiated amino acids[24]. In the crystal lattice, this radical evidently is stabilized by the intermolecular hydrogen bonds to the two amino groups bonded to C2 and C6 and these significantly reduce the possibilities for reorientation. The main reorientation should be from bending of the C2-H4 bond due to the sp^2 rehybridization following the C1-C2 bond breakage.

DFT calculation results on R2: The optimization model for the decarboxylation radical was obtained by removing the carboxyl group from a single molecule of lysine. Considering the environmental effects on the radical, during optimizations we tried two approaches to optimize the structure. One was to include the effects of intermolecular hydrogen bonds by freezing the hydrogen bond related atoms, i.e., the protons of both amino groups (main-chain and side-chain) in the decarboxylation radical model. The other was to include the crystal lattice effects by using the PCM method with keyword of "SCRF=PCM". Ban et al. used a similar model (Onsager Model) successfully to compute the expected principal values of alanine and glycine radicals[25, 26]. For the work described here, results from the PCM calculations, especially the eigenvectors, are in better agreement with experimental values. Because the experimental tensors for the α-coupling E and the large β-coupling F could not be obtained, it is not possible to compare them to the corresponding calculated values. However, the computed α-coupling for the <bc> plane was compared to the experimental data from that plane as shown in Fig. 5.5. For the comparison, the computed isotropic value was reduced by ~20MHz and the eigenvectors were slightly adjusted. Such a change is consistent with a structure with the bond of α-hydrogen bent. In this case, bending the bond by ~10° created a structure with the appropriate isotropic value as is shown by Fig. 5.6.[II] Also, for the missing coupling F, the WINSIM values are 31G (~90 MHz) at <b> and <c>, 34G (~100MHz) at <a>, which are comparable to the calculated value of ~106MHz for H3. Then the only

[II] The other option with the dihedral angle of ~-30° was rejected because the isotropic values and eigenvectors of other atoms are not in good agreement with experimental one based on the two strategies mention in the "Experiment" section.

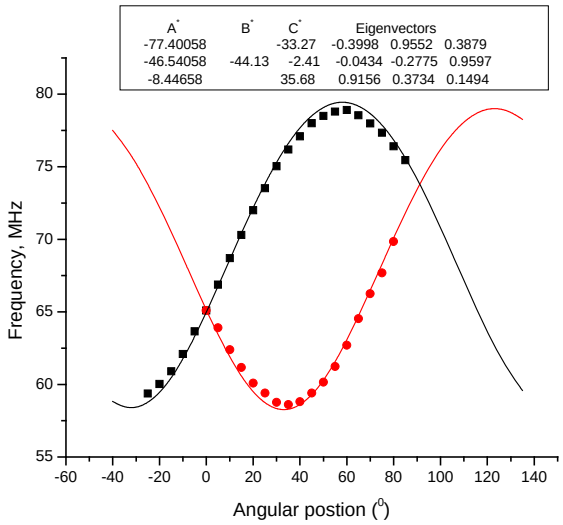

Fig. 5.5 *Experimental ENDOR data from coupling E of radical R2 vs. the angular dependence curves predicted by the computed tensor for rotation about <a*>. The square and solid dots are experimental ENDOR data. The two sites of the coupling are represented in red and black respectively. The solid lines are the curve using the parameters listed above the figure. The parameters listed were corrected from the DFT calculated tensor of H3 in the PCM optimized structure. A*, B*, C* are principal values, isotropic values and anisotropic values in MHz, respectively.*

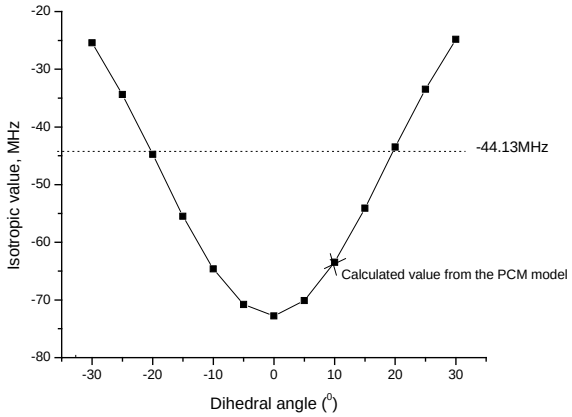

Fig. 5.6 *Isotropic values (in MHz) of α coupling E vs. the dihedral angle H4-C3-N1-C2. The dotted line indicates the value -44.13 MHz estimated from Fig. 5.5; the star in the curve corresponds to the calculated value from PCM optimization. This analysis indicates that ~10° is the approximate adjustment needed for the dihedral angle (from 10° to 20°).*

significant differences were those for the isotropic values of H5 and H6 vs. the experimental values for C and D. The calculated isotropic value of H5 was 51MHz less than that of coupling C, and the calculated isotropic value of H6 was 37MHz larger than that of coupling D. Because the isotropic value of a β

coupling is related to the dihedral angle θ_d, the complete side chain of the decarboxylation model was rotated about the C2-C3 axis by 25°. Finally, by rotating the amino group about the N1-C2 bond by ~9° on the adjusted structure, the calculated couplings of amino protons H2 and H1 are in best agreement with experimental couplings A and B, respectively. Calculated results following these modifications agree well with experimental parameters as are shown in Table 5.8: differences from isotropic values are < 6MHz and from eigenvectors[l] are <23.3°.

Table 5.8 *The DFT calculated hyperfine-coupling tensors on adjusted structure of decarboxylation radical and the angular difference between the calculated and experimental maximum dipolar vectors.*[a, b]

				Eigenvector				
Proton	Principal Value[a]	Isotropic value[a]	Anisotropic value[a]	<a>	<b>	<c*>	:Coupling	Angle diff(°)[b]
	32.21		12.08	-0.400	0.877	0.265	:B	8.4
H1	14.46	20.13	-5.67	0.063	-0.262	0.963		
	13.71		-6.42	0.914	0.402	0.050		
	33.26		11.53	0.953	-0.295	-0.071	:A	23.3
H2	16.32	21.73	-5.41	-0.149	-0.656	0.740		
	15.61		-6.12	0.265	0.694	0.669		
	114.45		8.65	0.650	-0.406	-0.643		
H3	102.77	105.80	-3.03	0.396	-0.541	0.742		
	100.18		-5.62	0.649	0.737	0.191		
	-80.89		-36.92	-0.409	0.880	0.241		
H4	-48.47	-43.97	-4.50	-0.294	-0.377	0.878		
	-2.55		41.42	0.864	0.289	0.413		
	71.74		10.77	0.489	0.801	0.346	:C	7.2
H5	55.74	60.97	-5.23	0.445	-0.570	0.691		
	55.43		-5.54	0.750	-0.184	-0.635		
	15.63		10.10	-0.311	0.946	0.097	:D	15.0
H6	1.08	5.53	-4.45	-0.153	-0.150	0.977		
	-0.12		-5.65	0.938	0.289	0.191		

[a]All the values are in units of MHz. [b] "Angle differ(°)" is the angular difference between the calculated and the experimental eigenvectors associated with the maximum eigenvalues.

Radical R3: the unknown radical

ENDOR lines I-III (see Fig. 5.1e) were assigned to R3 based on the EIE pattern as shown in Fig. 5.1d. These lines were detected only in <bc> plane and indicate the characteristics of β-couplings. Since no additional information could be obtained, it was not possible to identify R3. This radical is thought to be in minor concentration, because its ENDOR lines and EIE pattern are very weak.

5.4 Discussion

In this study, two main radicals in the L-lys·HCl·$2H_2O$ crystal irradiated at 66K were identified as the carboxyl anion and the decarboxylation radical. For the carboxyl anion, we identified two neighboring protons transferred to the carboxyl group following the electron trapping: H1'→O1 and H2'→O2. Such proton transfer is common for carboxyl radical anions[20-24]. Miyagawa et al.[27] proposed a proton-tunneling model to explain the proton addition to the alanine carboxyl anion as follows. Before irradiation, the energy surface for the proton in hydrogen bond of N-H…O (Fig. 5.7a) has the H in the deeper part of the potential well near the N, and quantum tunneling can take place only for excited vibrational states. After irradiation and formation of the carboxyl anion, additional negative charge is on the oxygen atom, which increases its proton affinity. As a result, the energy minimum on the side of O atom becomes deeper (Fig. 5.7b), and the proton can tunnel more easily through the energy barrier and bond to the O atom. Also, this tunneling model suggested that the tunneling rate (the proton transfer rate) is proportional to the hydrogen bond distance. That is, a shorter hydrogen bond may induce higher probability of the proton transfer. Iwasaki et al. also applied the tunneling model to describe formation of OH radicals and of carboxyl radical in irradiated carboxylic acid[28]. A similar mechanism can explain the proton transfers in the lysine carboxyl anion. For example, H2'…O2 is the shortest intermolecular hydrogen bond in the crystal, and thus H2' will have the highest tunneling rate or transfer rate to form the O2-H2' bond according to this model. In the two hydrogen bonds N2'-H1'…O1 and O_{w1}-H4'…O1, H1' bonds to a side chain amino group of a neighboring molecule while H4' bonds to the oxygen atom of water in the crystal. From our

model calculations, the energy for deprotonation of NH_4^+ is lower than that of H_2O by ~900kJ/mol[III]. Thus H1' can more easily tunnel from the neighboring NH_3^+ to form the O1-H1' bond than H4' from the water. The two proton transfers (to O1 and to O2) indicate that the proton affinity of the carboxyl group is sufficiently high to allow the second proton transfer.

As described before, the identification of the decarboxylation radical was confirmed by the DFT calculation and WINSIM simulation, even though two coupling tensors could not be obtained from the experiments. Previous studies[17] have found that the decarboxylation radical is a common intermediate from the oxidation product and originates from the carboxyl cation. In DNA/histone complexes, existing evidence indicates that electrons transfer from histone to DNA, thereby inducing a significant increase in the proportion of DNA anions, and leaving the oxidation products in the histone side. Thus, the detection and study of the mechanisms of decarboxylation radicals can be helpful for understanding the role of histone on the radiation damage mechanisms for DNA in vivo. In addition, the carboxyl oxygen atoms are general intermolecular hydrogen bond acceptors in amino acids. Thus, the direct result of decarboxylation is the breakage of the hydrogen bond. If the carboxyl oxygen of lysine in chromatin acts as hydrogen bond acceptors between DNA and histone, then it is reasonable to predict that decarboxylation in lysine (or in histone) can induce weakening of the DNA-histone association following irradiation. This effect was reported by Lloyd and Peacocke in 1965 [29]. However, this prediction needs to be verified by more studies on the irradiation damage to DNA in vivo to show that the decarboxylation radical can be formed in chromatin and can induce the hydrogen bond breakage between histone and DNA.

[III] In the modeling calculations, full optimization plus frequency calculation were performed on the molecules H_2O and NH_4^+. The initial coordinates of H_2O came from cluster D in Fig. 5.2a and those of NH_4^+ came from cluster A in Fig.5.2a by substituting an H for the methyl group. Then H4' and H1' (see Fig. 5.2a) were removed from H_2O and from NH_4^+ respectively, followed by full optimization and frequency calculations on the two structures. Single point energy calculations were performed for each optimized geometry. The energies for deprotonation were given by $DPE(H_2O) = E(OH^-)-E(H_2O)$ and by $DPE(NH_4^+) = E(NH_3)-E(NH_4^+)$. The results show that the energy for deprotonation from H_2O is higher than that from NH_4^+ by 897.68kJmol^{-1}.

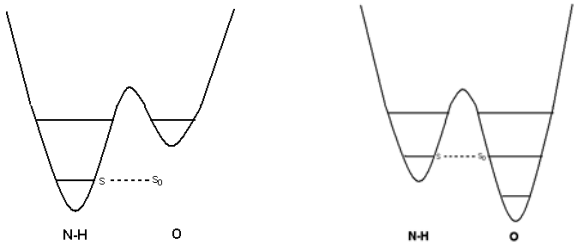

Fig. 5.7 *The sketch of energy curves for the proton in hydrogen bond N-H…O before the irradiation damage* ***(a)*** *and after the irradiation and the carboxyl anion formed* ***(b)****.*

References

1. M. Fujimoto, W. A. Seddon and D. R. Smith, Electron Spin Resonance Studies of Free Radicals in γ-Irradiated Amino Acid Crystals: α-Amino Isobutyric Acid and L-Lysine·HCl·$2H_2O$. *J. Chem. Phys.* **48,** 3345-3350 (1968).

2. R. G. Parr and W. Yang, *Density-Functional Theory of atoms and molecules*. Oxford University Press, New York, (1989).

3. T. F. Koetzle, M. S. Lehmann, J. J. Verbist, et al., Precision neutron diffraction structure determination of protein and nucleic acid components VII. The crystal and molecular structure of the amino acid L-lysine monohydrochloride dihydrate. *Acta crystallographica. Section B* **28,** 3207-3214 (1972).

4. R. R. Bugayong, A. Sequeira and R. Chidambaram, A neutron diffraction study of the structure of L-lysine monohydrochloride dihydrate. *Acta crystallographica. Section B* **28,** 3214-3219 (1972).

5. D. A. Wright and R. E. Marsh, The crystal structure of L-lysine monohydrochloride dihydrate. *Acta crystallographica* **15,** 54-64 (1962).

6. W. H. Nelson, Estimation of Errors in Eigenvalues and Eigenvectors from Magnetic Resonance Results by Use of Linear Data - Fitting Techniques. *Journal of magnetic resonance* **38,** 71-78 (1980).

7. D. R. Duling, A. G. Motten and R. P. Mason, Generation and evaluation of isotropic ESR spectrum simulations. *Journal of magnetic resonance* **77,** 504-511 (1988).

8. D. R. Duling, Simulation of multiple isotropic spin-trap EPR spectra. *Journal of magnetic resonance. Series B* **104,** 105-110 (1994).

9. M. J. Frisch, G. W. Trucks, H. B. Schlegel, et al., **Gaussian 03,** (Gaussian Inc., Wallingford CT, 2004)

10. B. Mennucci and J. Tomasi, Continuum solvation models: A new approach to the problem of solute's charge distribution and cavity boundaries. *J. Chem. Phys.* **106,** 5151-5158 (1997).

11. B. Mennucci, E. Cancès and J. Tomasi, Evaluation of Solvent Effects in Isotropic and Anisotropic Dielectrics and in Ionic Solutions with a Unified Integral Equation Method:

Theoretical Bases, Computational Implementation, and Numerical Applications. *The journal of physical chemistry. B* **101,** 10506-10517 (1997).

12. R. Cammi, B. Mennucci and J. Tomasi, Second-Order Møller-Plesset Analytical Derivatives for the Polarizable Continuum Model Using the Relaxed Density Approach. *The journal of physical chemistry. A* **103,** 9100-9108 (1999).

13. R. Cammi, B. Mennucci and J. Tomasi, Fast Evaluation of Geometries and Properties of Excited Molecules in Solution: A Tamm-Dancoff Model with Application to 4-Dimethylaminobenzonitrile. *The journal of physical chemistry. A* **104,** 5631-5637 (2000).

14. A. D. Becke, Density-functional thermochemistry. IV. A new dynamical correlation functional and implications for exact-exchange mixing. *J. Chem. Phys.* **104,** 1040-1046 (1996).

15. G. C. A. M. Vanhaelewyn, B. Jansen, E. Pauwels, et al., Experimental and Theoretical Electron Magnetic Resonance Study on Radiation-Induced Radicals in α-L-Sorbose Single Crystals. *The journal of physical chemistry. A* **108,** 3308-3314 (2004).

16. E. Pauwels, V. Van Speybroeck and M. Waroquier, Evaluation of Different Model Space Approaches Based on DFT to Examine the EPR Parameters of a Radiation-Induced Radical in Solid-State α-Glycine. *The journal of physical chemistry. A* **108,** 11321-11332 (2004).

17. E. Sagstuen, A. Sanderud and E. O. Hole, The Solid-State Radiation Chemistry of Simple Amino Acids, Revisited. *Radiation Research* **162,** 112-119 (2004).

18. C. Heller and H. M. McConnell, Radiation Damage in Organic Crystals. II. Electron Spin Resonance of $(CO_2H)CH_2CH(CO_2H)$ in β-Succinic Acid. *J. Chem. Phys.* **32,** 1535-1539 (1960).

19. H. Muto, *Trapped anions in organic crystals. Radical ionic systems: Properties in condensed phases A*. Lund, M. Shiotani, and Eds. Kluwer Academic Publishers, (1991).

20. H. Muto and M. Iwasaki, ENDOR studies of the superhyperfine couplings of hydrogen-bonded protons. I. Carboxyl radical anions in irradiated L-alanine single crystals. *J. Chem. Phys.* **59,** 4821-4829 (1973).

21. H. Muto, K. Nunome and M. Iwasaki, ENDOR studies of the superhyperfine couplings of hydrogen bonded protons. II. Protonated radical anion in irradiated succinic acid single crystals. *J. Chem. Phys.* **61,** 1075-1077 (1974).

22. H. Muto, K. Nunome and M. Iwasaki, ENDOR studies of the superhyperfine couplings of hydrogen-bonded protons. III. Protonated radical anions in irradiated L-valine hydrochloride monohydrate. *J. Chem. Phys.* **61,** 5311-5314 (1974).

23. M. Iwasaki and H. Muto, ENDOR studies of the superhyperfine couplings of hydrogen-bonded protons. IV. Carboxyl radical anions in irradiated glycine and α-amino isobutyric acid. *J. Chem. Phys.* **61,** 5315-5320 (1974).

24. K. T. Øhman, A. Sanderud, E. O. Hole, et al., Single Crystals of L-*O*-Serine Phosphate X-Irradiated at Low Temperatures: EPR, ENDOR, EIE, and DFT Studies. *The journal of physical chemistry. A* **110,** 9585-9596 (2006).

25. F. Ban, S. D. Wetmore and R. J. Boyd, A Density-Functional Theory Investigation of the Radiation Products of L-α-Alanine. *The journal of physical chemistry. A* **103,** 4303-4308 (1999).

26. F. Ban, J. W. Gauld and R. J. Boyd, A Density Functional Theory Study of the Radiation Products of Glycine. *The journal of physical chemistry. A* **104,** 5080-5086 (2000).

27. I. Miyagawa, N. Tamura and J. Cook, J. W., ESR Study of Stereospecific Proton Transfer in Irradiated Crystals of L-Alanine. *J. Chem. Phys.* **51,** 3520-3528 (1969).

28. M. Iwasaki, K. Minakata, K. Nunome, et al., ESR Study of OH Radicals Originating from Water of Crystallization of Carboxylic Acids. II. Role of Hydrogen Bonding in Selective Formation of OH Radicals. *J. Chem. Phys.* **57,** 3187-3193 (1972).

29. P. H. Lloyd and A. R. Peacocke, The Action of γ -rays on Deoxyribonucleohistone in Solution. *Proceedings of the Royal Society of London. B* **164,** 40-62 (1966).

CHAPTER 6.

L-LYSINE·HCl·2H_2O SINGLE CRYSTALS X-IRRADIATED AT 298K

Abstract

With K-band EPR (Electron Paramagnetic Resonance), ENDOR (Electron-Nuclear DOuble Resonance) and EIE (ENDOR-induced EPR) techniques, three free radicals (RI-RIII) in L-lys·HCl·2H_2O (L-lysine hydrochloride dihydrate) single crystals X-irradiated at 298K were detected at 298K, and six radical (R1, R1', R2-R5) were detected if the temperature was lowered to 66K from 298K. R1 and RI dominated the central portion of the EPR at 66K and at 298K respectively, and were identified as main chain deamination radical, $^{-}OOC\dot{C}H(CH_2)_4(NH_3)^{+}$. R1' was identified as a main chain deamination radical with the different configuration from R1 at 66K and it probably formed during cooling the temperature from 298K to 66K. The configurations of R1, R1' and RI were analyzed with their coupling tensors. DFT (Density Functional Theory) calculations reproduced the configurations of R1 and suggested that H14 (one of the side chain amino protons) was transferred to a neighboring carboxyl group through the intermolecular hydrogen bond following the main chain deamination. R2 and R3 each contain one α- and four β-proton couplings and have very similar EIEs at three crystallographic axes. The assignments of their couplings were based on a comparison of their coupling tensors to those from RII and RIII, whose EIE (B//~30° from <a>) were distinguishable. The comparison also indicated that R2 (66K) is the same radical as RII (298K), and R3 is the same as RIII. The two-layer ONIOM calculations (at B3LYP/6-31G(d,p):PM3) support that R2 and R3 are from different radicals: dehydrogenation at C4, $^{-}OOCCH(NH_3)^{+}CH_2\dot{C}H(CH_2)_2(NH_3)^{+}$, and dehydrogenation at C5, $^{-}OOCCH(NH_3)^{+}(CH_2)_2\dot{C}HCH_2(NH_3)^{+}$, respectively. Thus RII and RIII also are the radicals of C4 and C5 dehydrogenation. R4 and R5 are minority radicals, and were tentatively assigned as the side chain deamination radical, $^{-}OOCCH(NH_3)^{+}(CH_2)_3\dot{C}H_2$, and the radical dehydrogenation at C3, $^{-}OOCCH(NH_3)^{+}\dot{C}H(CH_2)_3(NH_3)^{+}$,

respectively, although the evidences were indirect. From simulation of the EPR (B//<a>, 66K), the concentration of R1, R1' and R2-R5 were estimated as: R1, 50%; R1', 11%; R2, 14%; R3, 16%; R4, 6%; R5, 3%. In the end, the radiation mechanisms in L-lysine were proposed and the possible effects of the stable radicals in lysine in chromatin were analyzed.

6.1 Introduction

Chapter 5 described the free radicals induced in L-lysine hydrochloride dihydrate (L-lys·HCl·2H_2O) single crystals irradiated at 66K; this chapter will focus on the studies on the stable radicals formed by irradiation at room temperature.

Earlier studies on radiation chemical mechanisms of lysine are mainly from Fujimoto et al. (1968) from EPR study of γ-irradiated L-lys·HCl·2H_2O (see Scheme 6.1) single crystals at 77K.[1] In controlled annealing experiments, at ~90K, they detected the radical from main chain deamination (see Scheme 6.2) transformed from the carboxyl anion radical (see Scheme 6.3), which formed immediately after the irradiation at 77K. When the temperature was increased subsequently to 130K, the deamination radical changed into a configuration with two unequal β-couplings and kept this configuration to 298K. When the temperature was lowered from 298K to 77K, the radical had a change in structure with two equal β-couplings. Because of the reversibility of the change in structures at 298K and at 77K, the deamination radical was believed to reach a chemically stable configuration at 298K and deformed by a structural change of its environment if cooled back to 77K. The authors mentioned that the two β-couplings at 298K (unequal couplings) and at 66K (equal couplings) are contrary to the expection that the molecules are undistorted at higher temperature, i.e., that the two β-couplings should be equal at higher temperature. Also, the side chain deamination radical was tentatively assigned using the EPR spectra at room temperature and the reaction mechanisms of the main chain deamination radical were analyzed.

In this work, with EPR, ENDOR and EIE techniques and theoretical calculations, additional stable free radicals were detected and identified. We detected the main chain deamination radical at 298K and its

two configurations as temperatures cooled from 298K to 66K. The configurations of these deamination radicals were analyzed based on their coupling tensors. We also detected two radicals with very similar EIE patterns and identified those as dehydrogenation at different sites of the side chain (at C4 and at C5, respectively) of lysine (see Schemes 6.4a and 6.4b). The side chain deamination radical was tentatively assigned to one of the minority radicals (see Scheme 6.5). Another minority radical was indirectly identified as dehydrogenation from C3. The radiation chemical mechanisms of L-Lys•HCl (see Scheme 6.6b) were analyzed based on these results.

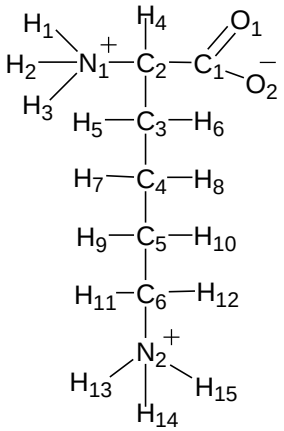

Scheme 6.1
Lysine molecule

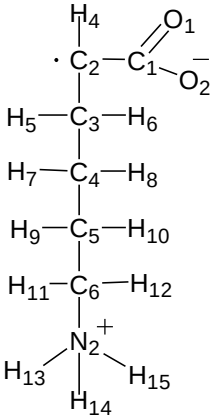

Scheme 6.2
The main-chain deamination

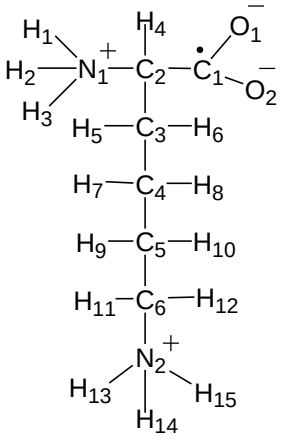

Scheme 6.3
Carboxyl anion radical

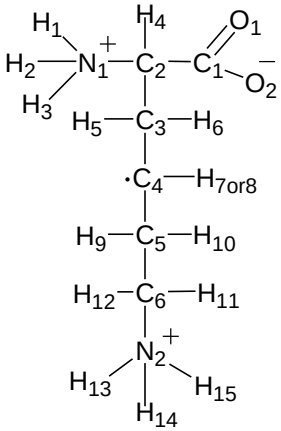

Scheme 6.4a
Dehydrogenation from C4

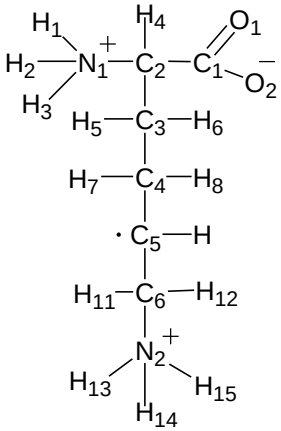

scheme 6.4b
Dehydrogenation from C5

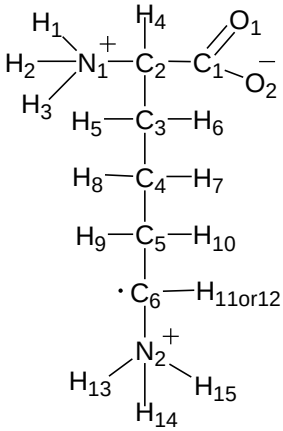

Scheme 6.4c
Dehydrogenation from C6

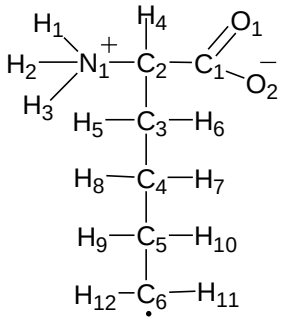

Scheme 6.5
Deamination from side chain

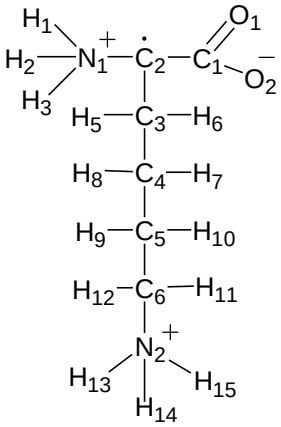

Scheme 6.6a
Dehydrogenation from C2

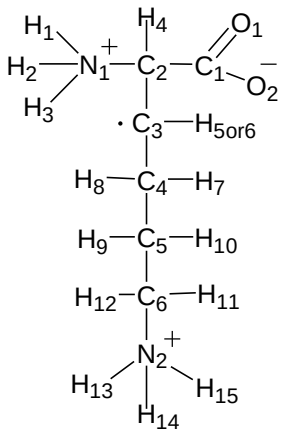

Scheme 6.6b
Dehydrogenation from C3

6.2 Experimental

Single crystals of L-Lys·HCl·2H_2O were X-ray irradiated at 298K and studied with K-band of EPR, ENDOR and EIE spectra at 298K and at 66K (by pumping the liquid nitrogen). The methods of crystal growth, data analysis, and spectra simulation were described in detail in Chapter 5.

To help identify the radicals and reproduce the reorientation of the radical, DFT (density functional theory) calculations were performed using the Gaussian03 program.[2] The coordinates for all the initial radical geometries were from the neutron diffraction studies.[3] Because the zwitterionic form is not a minimum energy configuration in gas phase, the full optimization carried out on the individual possible radical structures will lead to the fallacious proton transfer from the main chain amino group or from the side chain amino group to one of the oxygen atoms of the carboxyl group. Therefore to simulate the environmental effects three approaches were used for geometry optimizations on individual radical structures: one was to freeze some of the atom coordinates (generally those involved in the intermolecular hydrogen bonds) and the other was to use the PCM model by adding the keyword of "scrf=PCM".[4-6] In the PCM (Polarizable Continuum Model), the radical is embedded in a cavity surrounded by a continuum dielectric. (In this study, the solvent for all PCM optimizations was water with dielectric constant of 78.39.) In the third method, the neighboring molecules hydrogen bonded to the radical were added and the ONIOM calculations[7-11] were performed on the cluster model. For reproducing the magnetic

parameters, some parts of the optimized radical needed to be rotated or bent manually. All the radicals were optimized with the B3LYP functional and the 6-31G (d, p) basis set. The magnetic parameters were calculated subsequently on the final radical structure with single point calculations using the 6-311G (2d, p) basis set. The "NOSYMM" keyword was used for both the geometry optimization and the single point calculation and the Cl^- atom was omitted from all calculation models. When comparing the coupling tensors from experiments and modeling calculations, we still use two strategies: 1) the differences between isotropic values are <15MHz; 2) the angular differences between eigenvectors[I] are <25°. That is, only if all the tensors from one model satisfy the two strategies, is the model accepted as the one reproducing the structure (reorientation) of the radical.

6.3 Results and Analysis

6.3.1 Experiments at 66K

EPR and EIE

When the temperature was lowered to 66K after irradiation at room temperature, at least six distinct EIE patterns were detected and were assigned to five different radicals: R1-R5. Fig. 6.1 shows the EPR spectrum and the EIE patterns of R1, R1'-R5 with the magnetic field along <a>. For reasons discussed below, R1' is assigned to a different configuration of R1. The central dominant peaks of the EPR spectrum are due to radical R1. EPR from radicals R2 and R3 cover the full width of the spectrum and the outer most peaks on both sides are due to these two radicals, which give very similar EIE patterns. R4 and R5 are two minority radicals with EIE patterns that overlap in the central portion of EPR.

[I] The eigenvectors are those associated with maximum eigenvalues.

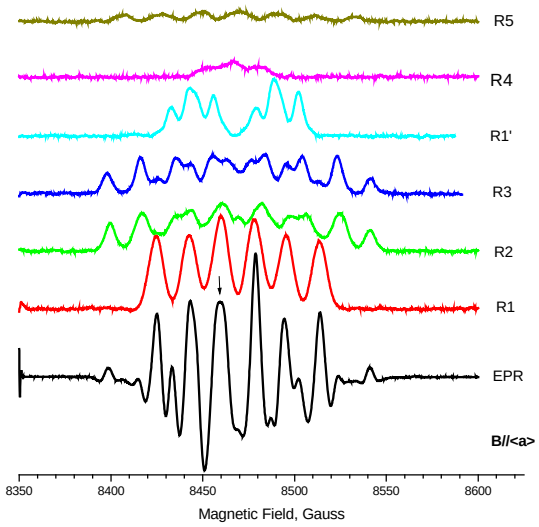

Fig. 6.1 *The second-derivative EPR spectrum and the EIE patterns of R1, R1'-R5 from single crystal L-lysine·HCl·2H_2O irradiated at room temperature and cooled down to 66K. The magnetic field is along <a>.*

ENDOR

Fig. 6.2 shows the ENDOR spectrum detected under the same conditions with the field locked to the center peak of the EPR spectrum as indicated by the arrow in Fig. 6.1. The ENDOR lines were assigned to radicals R1-R5 according to the EIE patterns shown in Fig. 6.1. The strong lines 1, 2, 2', 3, and 3' were assigned to the major radical R1. Lines 4-13 have indistinguishable EIE patterns at three crystallographic axes, and according to the analysis below, these ENDOR lines are from two very similar radicals R2 and R3. Lines 1, 4 and 5 overlap at 62.2MHz at this orientation and the EIE pattern from this ENDOR line shows characteristics of R1, R2 and R3, as is indicated in Fig. 6.3. Lines 14 and 15 were assigned to a different conformation of R1, and is denoted as R1'. Lines 16-18 are additional couplings of R4, and line 18 was only detected at this orientation. The two low-intensity lines 19 and 20 are from radical R5.

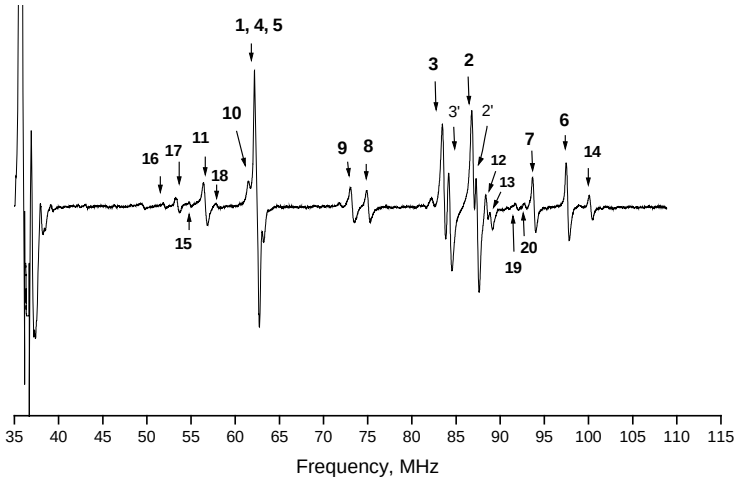

Fig. 6.2 *The first-derivative ENDOR spectrum of single crystal L-lysine·HCl·2H_2O detected at same conditions as those in Fig. 6.1 with B//<a>. The magnetic field is locked to one center peak of the EPR spectrum, asshown by the arrow in Fig. 6.1.*

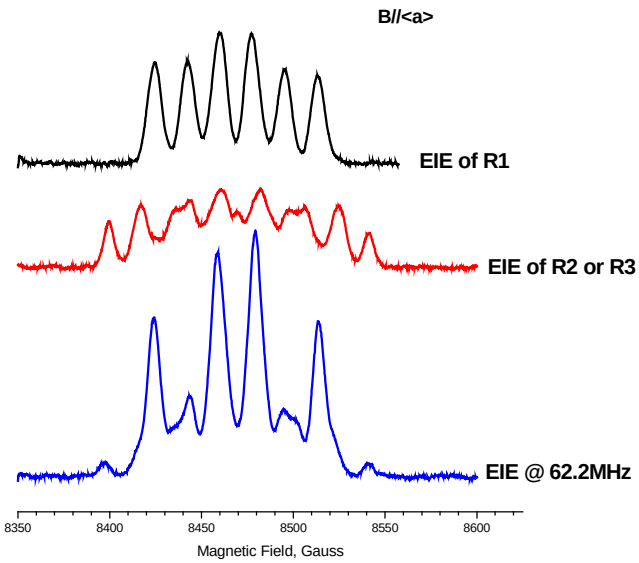

Fig. 6.3 *EIE pattern from ENDOR line at 62.2MHz in Fig. 6.2, where lines 1,4 and 5 are overlapped, EIE of R2 or R3, and EIE of R1. The magnetic field is along <a>.*

R1-deamination from main chain

As is mentioned above, five couplings, 1, 2, 2', 3 and 3' were assigned to R1, the hyperfine-coupling tensors of 1, 2, 3 and 3' were obtained and listed in Table 6.1. The tensor for line 2' could not be obtained

because it was not observed in <bc> plane. Angular dependence curves for lines 1, 2, 2', 3 and 3' are shown in Fig. 6.4. In the three rotation planes, the ENDOR curves for couplings 3 and 3' are very much alike. Moreover, principal values of 3 and 3'are different by less than 2MHz, and the angular differences between their three principal vectors are less than 6°. These parameters are quite different from those of 1 and 2, and these differences are listed in Table 6.2. Although the tensor for 2' could not be obtained, as is indicated in Fig. 6.4, in the <ac> and <ab> planes, the ENDOR from coupling 2' is very similar to that of coupling 2. At the same time, the EIE patterns of R1 at the three crystallographic axes indicate obviously that R1 has three main interactions. With tensor simulation and WINSIM simulation, the EIE patterns at the three crystallographic axes can be reproduced very well either with coupling 1, 2 and 3, or with couplings 1, 2' and 3', as shown in Fig. 6.5. Therefore couplings 2 and 2' have been assigned to the same proton; likewise, couplings 3 and 3' have been assigned to the same proton but different from those of 1, 2 and 2'. The observed differences between couplings 2 and 2', and between 3 and 3', could be due to the proton vibrations (motion). In the following discussion, couplings 2' and 3' are regarded as the same couplings as 2 and 3, respectively, and will not be mentioned for simplification.

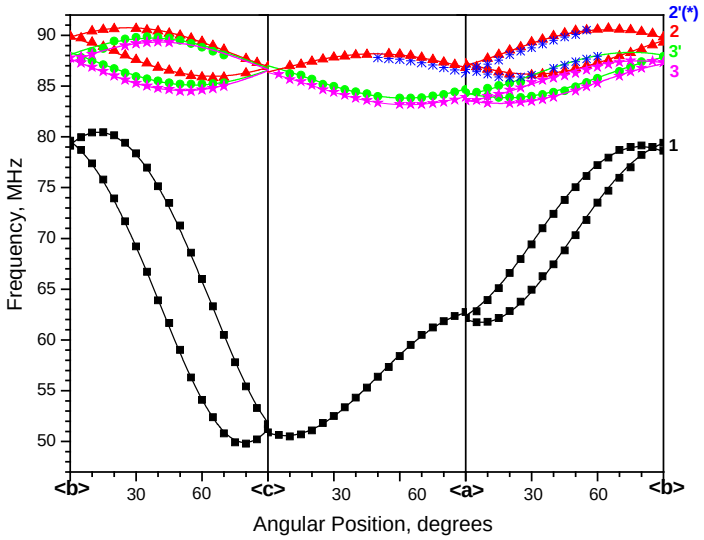

Fig. 6.4 *Angular dependent curves for couplings of R1of single crystal L-lys•HCl•2H_2O irradiated at 298K and detected at 66K.*

Table 6.1 *Hyperfine coupling tensors for radical R1 in single crystal L-lysine·HCl·2H$_2$O irradiated at 298K and detected at 66K.* [a-d]

				Eigenvectors[b]		
Tensor	Principal values[a,b]	Isotropic Values[a]	Anisotropic values[a]	<a>	<b>	<c*>
	-89.10(3)		-32.18	0.128(0)	0.975(0)	-0.180(1)
1	-54.54(3)	-56.92	2.39	0.957(0)	-0.074(1)	0.281(1)
	-27.14(3)		29.79	0.261(0)	-0.208(1)	-0.943(0)
	111.24(1)		7.63	0.481(1)	-0.789(2)	-0.382(2)
2	101.30(1)	103.61	-2.31	0.706(1)	0.607(1)	-0.364(2)
	98.30(1)		-5.31	0.519(1)	-0.094(2)	0.849(1)
	107.94(2)		7.97	0.229(1)	0.724(5)	0.651(1)
3	97.24(2)	99.97	-2.73	0.208(0)	-0.690(0)	0.693(4)
	94.74(2)		-5.23	0.951(0)	-0.023(2)	-0.309(4)
	109.51(2)		8.24	0.321(1)	0.726(7)	0.608(1)
3'	98.31(2)	101.27	-2.96	0.203(0)	-0.680(1)	0.705(5)
	96.00(2)		-5.27	0.925(1)	-0.103(3)	-0.365(5)

	Directions of Hx….C2[c]				
Proton	<a>	<b>	<c*>	:coupling	Angle diff (deg)[d]
H4	0.931	0.206	0.301	: 1	91.2
H5	-0.567	-0.795	-0.216	: 3	34.8
H6	0.242	-0.911	-0.334	: 2	15.7

[a]All these values are in units of MHz. [b]Numbers in parentheses are the estimated uncertainties in the last digit quoted as reported by the statistical analysis. [c] Hx are α and β-protons in main-chain deamination radical. [d]The angular differences are between eigenvectors associated with the maximum eigenvalue and the corresponding directions in the crystalline lattice.

Table 6.2 *The angular differences between eigenvectors of couplings 3 and 3', and between couplings 2 and 3. The anisotropic values are in MHz, and the angular differences are in degrees.*

Anisotropic Value	3 : 3'	2 : 3
~7.0	5.8	44.8
~-2.0	0.3	58.4
~-5.0	5.8	76.8

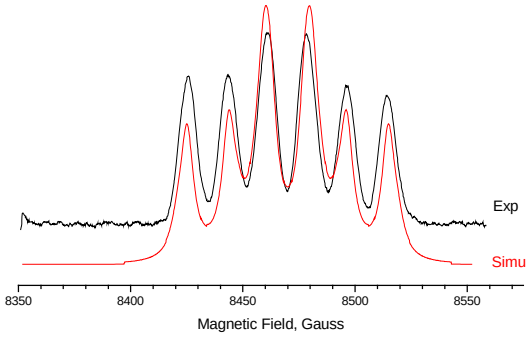

(a)

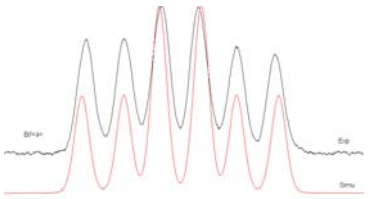

(b)

Fig. 6.5 (a) *EIE (B//<a>) simulation for R1 with coupling tensors 1, 2 and 3;* ***(b)*** *WINSIM simulation of EIE of R1 with coupling values of 1, 2' and 3' at <a>.*

From the hyperfine coupling tensors and angular dependence curves, coupling 1 shows typical characteristics of α-coupling, while couplings 2 and 3 are two typical β-couplings. Based on the annealing experiments, R1 was identified as the radical from deamination of the main chain (scheme 6.2). The spin, mainly located at C2, interacts with one α-proton (H4) and two β-protons (H5 and H6). In the work of M. Fujimoto, et al. the deamination radical was formed from the carboxyl radical anion after storing the crystal irradiated at 77K in a liquid-oxygen bath (90K) overnight. Upon controlled warming, it attained its stable configuration at 298K.[1] In this work, the carboxyl anion (see Scheme 6.3) was assigned as the primary radical for the crystal irradiated at 66K, and the EPR spectrum from the crystal irradiated at 66K and warming to 298K is comparable with the EPR from the crystal irradiated at room temperature, as is shown in Fig. 6.6. Therefore, major radical R1 is identified as the deamination radical.

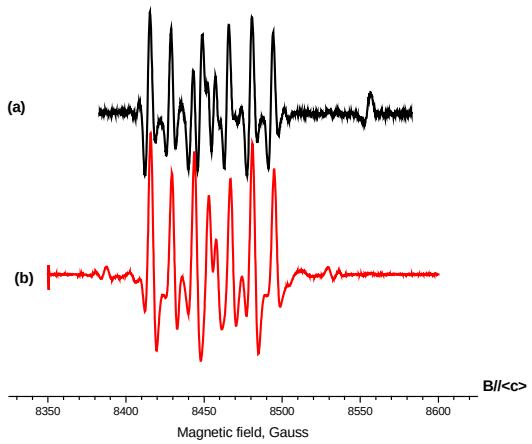

Fig. 6.6 (a) *EPR spectrum for single crystals of L-lysHCl H_2O irradiated at 66K and warming to 298K;* ***(b)*** *EPR spectrum for single crystals of L-lysHCl H_2O irradiated and detected at 298K. The magnetic field is along <c> in* ***(a)*** *and* ***(b)****.*

In the following the geometry characteristics of R1 obtained from the hyperfine-coupling tensors of 1-3 are described.

(I.) The rehybridization of the radical center from sp^3 to sp^2 conformation can be estimated with the coupling values of the α tensor. Using McConnell relation[12, 13]

$$a_{iso}(H_\alpha) = Q\rho, \qquad (1)$$

the isotropic value of coupling 1, $a_{iso}(H_\alpha)$ = -57.0MHz, and the proportionality constant, Q = -73.4 MHz[14], ρ, the spin density on C2, is estimated to be 0.78. Meanwhile, from the Gordy-Bernhard relation[15, 16],

$$a_z = Q^z_{dip}\rho \qquad (2)$$

and using the dipolar value of the α coupling, a_z = 31.43MHz, constant Q^z_{dip} = 38.7MHz, and spin density on C2 is 0.77. Then the almost complete rehybridization of sp^2 on the radical center can be expected because of the very close spin density calculated from (1) and (2).[17] (That is, there is little evidence for bending.)

(II) The β protons conformation can be derived from Heller-McConnell relation[18],

$$a_{iso}(H_\beta) = B_1\rho\cos^2\theta, \qquad (3)$$

where a_{iso} (H_β) is the isotropic value of the C- H β coupling, B_1 is a constant related to the geometry of the radical, ρ is spin density on the carbon atom of radical center, and θ is the dihedral angle between directions of H4-C2 bond and the spin orbital. Using a_{iso} of couplings 2 and 3, and $B_1\rho = 125MHz$[19] for the both couplings, the dihedral angles estimated for these two couplings are both ~25°. If both β protons are those bonded to C3, and assuming the bonds of C3 are purely tetrahedral, the possible configurations for the two β protons having similar coupling values are shown in Fig. 6.7a and 6.7b. The configuration in Fig. 6.7b with the dihedral angles $\theta_1 = \theta_2 = 30°$ is closer to the calculated results (~25°).

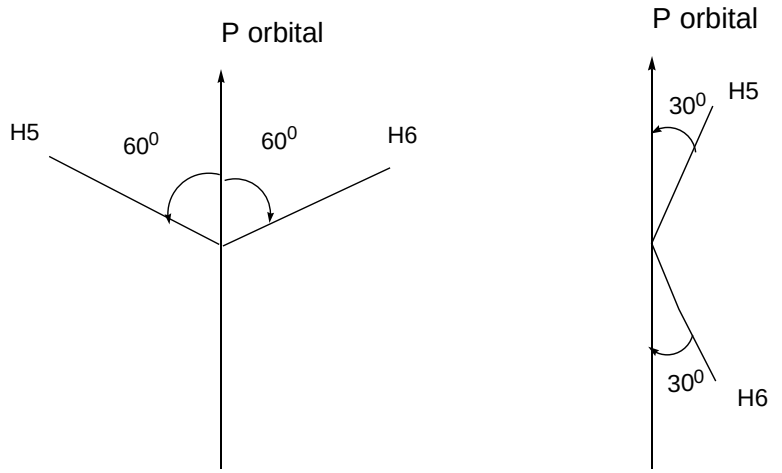

Fig. 6.7 *Two configurations for the β-protons bonded to a same carbon and with equal isotropic values. The arrow stands for the p orbital of the unpaired spin and the Cα-Cβ bond is normal to the page.*

(III) The reorientation of the radical can be estimated by comparing the principal axes of the coupling tensors with the expected directions in the crystal lattice. As listed in Table 6.1, the angle between the maximum dipolar vector of coupling 2 and the crystallographic direction of C2…H5 is ~16°; however the angle between the dipolar vector corresponding the positive component of coupling 1 and C2-H4 bond direction almost reaches to 90°, and the eigenvector[I] of coupling 3 is 30° from direction of C2…H6. These very large differences suggest that the radical experiences a large reorientation, which is consistent with previous results from deamination radicals in single crystals of serine and alanine.[20, 21] In

the next section, the configuration and reorientation of the deamination radical studied with modeling calculations will be discussed.

Modeling calculations on R1

The initial structure for the main-chain deamination radical was constructed by using the atomic coordinates from neutron diffraction studies on single crystal of L-lys·HCl·$2H_2O$[3] with the main-chain amino group removed. Then, the individual deamination radical was optimized using the PCM method and with the hydrogen bond related atoms frozen separately. However, the computed parameters from both models are quite different from those detected indicating that some other approach is necessary.

The next approach was to manually adjust the deamination structure. The analysis in (I.) above indicated the radical center (C2) to have a planar configuration. To accomplish this with the initial structure, the C2-H4 bond was bent to become coplanar with C1C2C3 (by rotating the C2-H4 bond about C1…C3 until the torsion angle C1-C3-H14-C2 = 0°). Then, the C2-C1 bond and the whole carboxyl group were rotated ~10° about the direction normal to the C1C2C3 plane to make the bond angle C1-C2-C3 ~120°. After these adjustments, the angular difference between the computed eigenvectors of the α-coupling and those of coupling 1 were reduced to 18.2°, 29.2° and 33.6° (for the initial structure, the differences are 24.3°, 101.1° and 96.0°). By bending the C3-H14 bond to 30° (i.e rotating the C3-H14 bond about C2-C4 direction), followed by rotating the carboxyl group to keep the radical center planar, all the angular differences for eigenvectors of the α-coupling are <18°: 17.2°, 7.3° and 15.7°. In addition, the isotropic value of –46.5MHz for the α-coupling is near the experimental value of -56.9MHz. However, this structure has two unequal β-couplings: 82.9MHz and 20.1MHz, and based on the results in (II.), the two β-proton couplings should be nearly the same as shown in Fig. 6.7b. In the next step, the whole side chain was rotated about the C2C3 bond axis by ~15°, with the result that the two β-coupling values are comparable: 62.02MHz and 57.63MHz (this structure is denoted as (0)). However, these couplings are less than the experimental values by ~40MHz. Also, the calculation showed a large isotropic coupling (86.03MHz) to N2 and this was also inconsistent with our experiments. Therefore, to

decrease the N2 coupling and increase the two β-couplings, three procedures were carried out separately: (1) H14 dehydrogenation: ONIOM calculations described below showed that H14 dehydrogenation computed hyperfine couplings like to those from experiment. Thus, deamination could be followed by H14 dehydrogenation. (2) Neighboring hydrogen atom added to O1: Proton transfer to the carboxyl group (O1 atom) has been identified for carboxyl anions in L-lys·HCl·H2O crystal, and carboxyl anion radicals are precursors to the deamination (identified from the experiments of Fujimoto et. al.[1]). Thus, the deamination radical possibly contains the transferred proton. In the structure for the model calculation, the bond length for O1-H' is 1Å, and the bond angle of H'-O1-C1 is 108.3°, which is the angle between the O1C1 bond and the hydrogen bond of O1…H'-N2' in the crystal. (3) Both of these: this structure was constructed because the above two cases can be concurrent for the radical.

Tensors from the three resulting structures, (1), (2) and (3) are listed in Table 6.3b-d; (Table 6.3a shows the tensors calculated from structure (0), the one before the last adjustments.) The eigenvectors from (1), (2) and (3) are very close to those from structure (0) and have very similar angular differences with those from experiment. However, the isotropic values from the three structures are quite different from those of structure (0): the isotropic coupling to N2 is reduced to ~0MHz; the absolute α-coupling values are increased ~6MHz in (1), and ~14MHz for (2) and (3); the two β-couplings are increased ~13MHz in (1), and are increased more than 20MHz in (2) and (3); the β-couplings in (3) are ~5MHz larger than those in (2). There is still ~20MHz different between the calculated β-coupling of H6 and experimental coupling 2. From the single point calculation on the structure (3) by means of the basis set of EPR-II, the two β-couplings are increased by ~6MHz, while the eigenvectors are very similar as those from calculation with 6-311G(2d,p), as are shown in Table 6.3e. This demonstrates that there is a deamination structure (3) with couplings like those measured experimentally and this final structure is shown in Fig. 6.8a.

Table 6.3(a) *The coupling tensors calculated on the structure (0).*[a, b]

			Eigenvectors				
Proton	Isotropic value[a]	Anisotropic value[a]	<a>	<b>	<c*>	:Coupling	Angle Diff (deg)[b]
		-30.76	0.331	0.863	-0.383		17.7
H4	-49.73	-0.40	0.922	-0.208	0.328	: 1	8.4
		31.16	-0.204	0.461	0.864		15.6
		7.14	0.275	0.896	0.348	: 3	20.3
H5	62.02	-3.18	-0.546	-0.153	0.824		
		-3.96	0.792	-0.417	0.447		
		8.18	-0.195	0.974	0.114	: 2	25.0
H6	57.63	-3.27	0.949	0.217	-0.231		
		-4.90	0.250	-0.063	0.966		
		1.80					
N2	86.03	-0.68					
		-1.12					

[a]All the values are in units of MHz. [b]The angular differences are between eigenvectors from the experimental and from the calculations. For β-couplings, the eigenvectors are those associated with maximum eigenvalues.

Table 6.3 (b) *The coupling tensors calculated on the structure (1).* [a, b]

			Eigenvectors				
Proton	Isotropic value[a]	Anisotropic value[a]	<a>	<b>	<c*>	:Coupling	Angle Diff (deg)[b]
		-36.84	0.327	0.865	-0.380		17.4
H4	-55.76	-0.42	0.929	-0.222	0.295	: 1	8.7
		37.27	-0.171	0.449	0.877		15.3
		8.73	0.278	0.894	0.351	: 3	20.1
H5	75.15	-3.90	0.711	0.054	-0.701		
		-4.83	0.646	-0.445	0.620		
		9.84	-0.200	0.974	0.108	: 2	25.1
H6	69.50	-4.11	0.953	0.219	-0.211		
		-5.73	0.229	-0.061	0.972		
N2	-0.04						

[a]All the values are in units of MHz. [b]The angular differences are between eigenvectors from the experimental and from the calculations. For β-couplings, the eigenvectors are those associated with maximum eigenvalues.

Table 6.3 (c) *The coupling tensors calculated on the structure of (2).* [a, b]

			Eigenvectors				
Proton	Isotropic value[a]	Anisotropic value[a]	<a>	<b>	<c*>	:Coupling	Angle Diff (deg)[b]
		-37.89	0.350	0.867	-0.354		17.4
H4	-63.50	-2.03	0.919	-0.246	0.307	: 1	10.2
		39.92	-0.179	0.433	0.884		14.2
		9.12	0.291	0.877	0.382		15.5
H5	83.18	-4.13	-0.352	-0.273	0.895	: 3	
		-5.00	0.890	-0.395	0.229		
		9.60	-0.245	0.964	0.102		23.9
H6	76.98	-3.37	0.924	0.264	-0.276	: 2	
		-6.23	0.293	-0.027	0.956		
N2	-0.03						

[a]All the values are in units of MHz. [b]The angular differences are between eigenvectors from the experimental and from the calculations. For β-couplings, the eigenvectors are those associated with maximum eigenvalues.

Table 6.3 (d) *The coupling tensors calculated on the structure (3).* [a, b]

			Eigenvectors				
Proton	Isotropic value[a]	Anisotropic value[a]	<a>	<b>	<c*>	: Coupling	Angle Diff (deg)[b]
		-37.87	0.346	0.871	-0.349		17.0
H4	-63.32	-1.92	0.921	-0.244	0.305	: 1	10.1
		39.79	-0.181	0.427	0.886		13.8
		9.13	0.299	0.865	0.403	: 3	17.0
H5	86.20	-4.11	-0.274	-0.326	0.905		
		-5.03	0.914	-0.381	0.139		
		9.33	-0.271	0.957	0.109	: 2	22.1
H6	83.03	-2.97	0.910	0.291	-0.297		
		-6.37	0.315	-0.019	0.949		
N2	-0.02						

[a]All the values are in units of MHz. [b]The angular differences are between eigenvectors from the experimental and from the calculations. For β-couplings, the eigenvectors are those associated with maximum eigenvalues.

Table 6.3 (e) *The coupling tensors calculated on the structure (3) with basis set of EPR-II.* [a, b]

			Eigenvectors				
Proton	Isotropic value[a]	Anisotropic value[a]	<a>	<b>	<c*>:	Coupling	Angle Diff (deg)[b]
		-37.74	0.343	0.872	-0.349		16.8
H4	-65.60	-2.09	0.923	-0.243	0.300	: 1	10.0
		39.82	-0.177	0.425	0.888		13.7
		9.18	0.300	0.858	0.418	: 3	16.0
H5	92.97	-4.03	-0.102	-0.407	0.908		
		-5.15	0.949	-0.315	-0.034		
		9.04	-0.267	0.957	0.113	: 2	22.1
H6	89.41	-2.67	0.910	0.289	-0.298		
		-6.38	0.318	-0.023	0.948		
N2	-0.02						

[a]All the values are in units of MHz. [b]The angular differences are between eigenvectors from the experimental and from the calculations. For β-couplings, the eigenvectors are those associated with maximum eigenvalues.

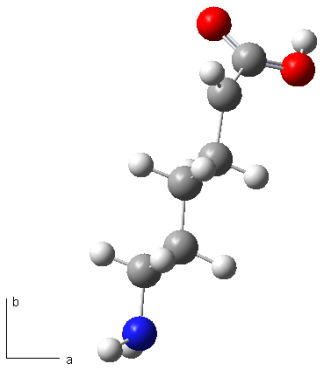

Fig. 6.8 *The final structure of single molecule calculation for main chain deamination radical of lysine.*

Cluster calculations

Because the results from individual radical optimizations (PCM and partial optimization) are not in agreement with experimental results and required significant manual adjustment before the computed values approximated the experimental results, the two-layer ONIOM method was used to optimize the radical's geometry within the model clusters. The optimizations on several cluster models including six or seven lysine and two or more water molecules neighboring to the center radical failed due to serious convergence problem. The intermediate structure in some optimizations using HF/3-21g or HF/6-31g for

the low level shows the side chain amino proton H14 in the center radical transferred to the neighboring carboxyl group, and these structures are generally close to an energy minimum point (one or two "items" converged)[22]. Thus we suppose this transfer was followed by the deamination, and construct the initial cluster (TrH14) as shown in Fig. 6.9: move the H14 from the center radical to bond to the neighboring oxygen atom with bond length H14-O1' = 1.0A (indicated by an arrow in Fig. 6.9), and the model included six lysine and seven water molecules neighboring the center radical (modeled all the hydrogen bonds to the center radical except those to Cl^-). The center radical was fully optimized and calculated using uB3LYP/6-31G(d,p), while the neighboring molecules were frozen at the original crystalline lattice positions during optimization and calculated using semiempirical methods (PM3 or AM1), or HF functional (at 3-21g or 6-31g), separately. These calculations were notated according to the low level method as (TrH14): AM1, (TrH14): PM3, (TrH14): HF/3-21G and (TrH14): HF/6-31G, respectively.

The calculations of (TrH14): AM1 and (TrH14): PM3 ran out of computational steps, and in the intermediate structures close to an energetic minimum point, the α-proton was rotated to be almost coplanar with carboxyl group and the two β-protons are quite unequal, which are different from the structures described below (the one in good agreement with the experiment). Thus the calculations were not continued to find the corresponding energetic stable structure.

The calculations of (TrH14): HF/3-21G and (TrH14): HF/6-31G were completed, and especially, the optimized structure in (TrH14): HF/3-21G (see Fig. 6.10a) has the two characteristics that agree with those derived from experiment: (I.) the radical center is almost planar, with only ~-5.9° of the torsion angle <C1-C3-H4-C2, and (II.) the two β-protons are almost symmetrically separated by C1-C2-C3 plane (~the nodal plane of the radical) with -67.1° and 65.1° for the torsion angles <H5-C3-H4-C2 and <H6-C3-H4-C2, respectively; and this structure for β-protons is similar as that derived for R1 (see Fig. 6.7b). The single-point calculation was performed on this optimized structure using B3LYP/6-311G(2d,p). The calculated coupling for H4 is -54.28MHz that is in good agreement with experimental value -56.92MHz. Also, the angular differences between principal vectors from coupling 1 and H4 are reduced to 33.8°,

19.0°, and 30.9° (before optimization, the differences are 24.3°, 101.1°, and 96.0°). For the two β-couplings, the two calculated isotropic couplings are almost equal: 77.99MHz (H5) and 80.54MHz (H6), although both of them are less than the experimental β-couplings (99.97MHz and 103.61MHz) by ~20MHz. The differences between eigenvectors[I] from experiments and from calculation are 33.0º for coupling 3 and H5, and 22.6º for coupling 2 and H6. We noticed that for α-couplings, the angular difference between the principal vectors with the intermediate component is acceptable (19.0º), and the

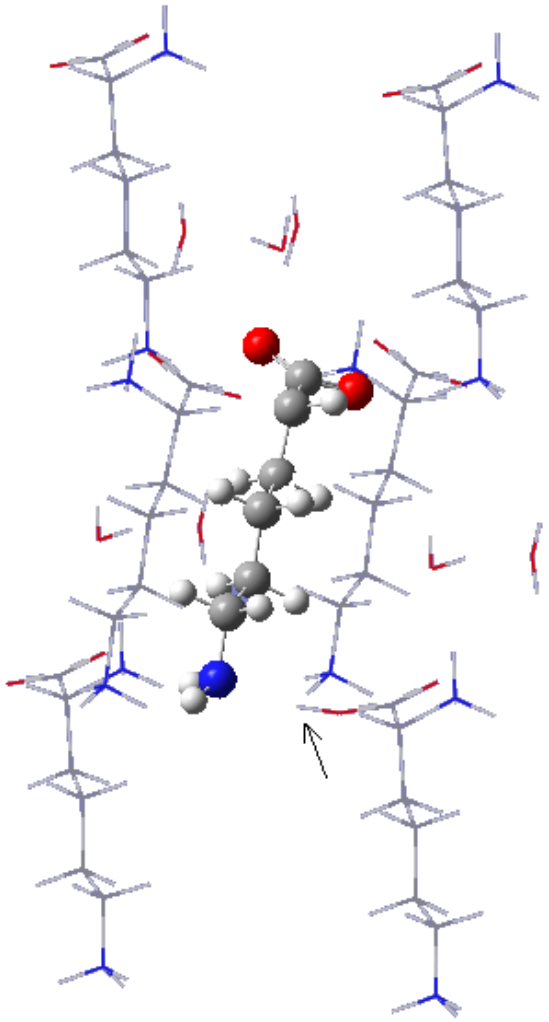

Fig.6.9 *The initial model cluster (TrH14): the H14 in center radical was transferred to the neighboring O1' (as indicated by the arrow).*

other two angular differences are both close to 30º. Considering for the complete sp^2 hybridization structure, the principal vector with the intermediate component of α-coupling is expected to be along the direction of the spin orbital. By rotating the radical with the spin orbital (or with the principal vector with the intermediate principle value of α-coupling) to ~30° (see Fig. 6.10b), all the angular differences for principal vectors of α-couplings are acceptable: 13.5°, 20.9°, and 15.9° respectively, and the differences between the eigenvectors[l] of the two β-couplings are also reduced to 6.2° and 16.6°. Meanwhile, the coupling values are almost same as those before rotation. For the single-point calculation performed on this structure using basis set of EPR-II, the β-coupling values can be increased by ~8MHz, which make the couplings more close to the experimental values: ~14MHz less than the experimental, while the principle vectors are very similar to those from calculation using 6-311G(2d, p). These results from calculation with 6-311G(2d, p) and with EPR-II are listed in Tables 6.4a-b, respectively.

The optimized structure from (TrH14): HF/6-31G (see Fig. 6.11a) is similar as that from (TrH14): HF/3-31G, except the two β-proton couplings are unequal: 94.41MHz for H5 and 62.31MHz for H6 (from single point energy calculation with 6-311G(2d,p) on the optimized structure.) By rotating the side chain about C2C3 axis to ~12º followed by rotating the molecule around the spin orbital to ~30º, the coupling tensors computed with EPR-II are very close to those from experiments as illustrated in Table 6.4c and the final structure (Fig. 6.11b) is almost same as that shown in Fig. 6.10b.

The calculations were also performed on the clusters with H13 transferred to O1' (another side chain amino proton to its neighboring O atom), or with H3' transferred to O1 (this transfer was identified in the carboxyl anion radical of L-lys·HCl·H2O), or with both transferred for the same model cluster (i.e., by transferring a neighboring proton to the center carboxyl group and transfering the center side chain amino proton to the neighboring carboxyl group at same time). However, for the calculations completed, the optimized structures are in no better agreement with experiment than that from (TrH14): HF/3-21G. Thus the structure from (TrH14): HF/3-21G followed by rotation with spin to 30º can be considered as the final structure of R1, and the H14 transferal may be followed by the main chain deamination.

(a) **(b)**

Fig. 6.10(a) *The optimized structure of main chain deamination radical from (TrH14):HF/3-21G* ***(b)*** *The structure from (a) rotated around spin orbital by ~30°.*

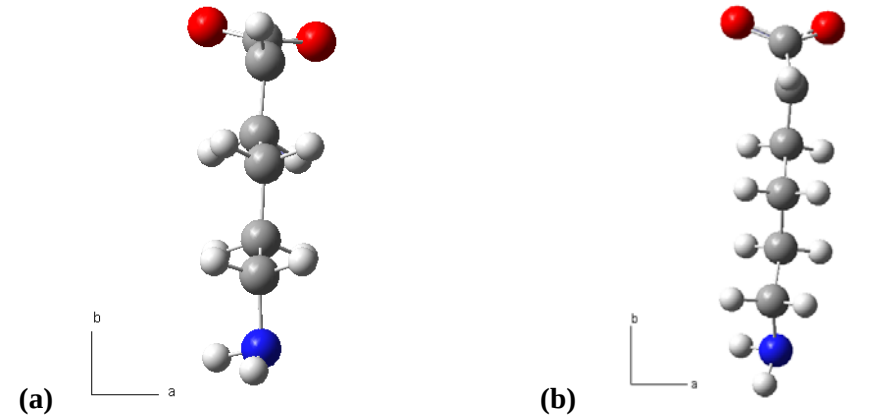

(a) **(b)**

Fig. 6.11(a) *The optimized structure of main chain deamination radical from (TrH14):HF/6-31G* ***(b)*** *The structure from (a) rotated around spin orbital by ~30° with the side chain with C2C3 axis rotated by 12°.*

Table 6.4(a) *The coupling tensors calculated with 6-311G(2d,p) on structure shown in Fig.6.10(b).* [a, b]

			Eigenvectors				
Proton	Isotropic value[a]	Anisotropic value[a]	<a>	<b>	<c*>:	Coupling	Angle Diff (deg)[b]
		-35.65	-0.104	0.972	-0.210		13.5
H4	-54.25	-0.10	0.995	0.098	-0.037	: 1	20.9
		35.75	0.015	0.213	0.977		15.9
		8.25	0.281	0.773	0.568	: 3	6.2
H5	77.99	-3.81	-0.008	-0.591	0.807		
		-4.44	0.960	-0.231	-0.160		
		8.36	-0.255	0.788	0.561	: 2	16.6
H6	80.53	-4.63	0.967	0.224	0.125		
		-3.73	0.028	-0.574	0.819		

[a]All the values are in units of MHz. [b]The angular differences are between eigenvectors from the experimental and from the calculations. For β-couplings, the eigenvectors are those associated with maximum eigenvalues.

Table 6.4(b) *The coupling tensors calculated with EPR-II on the structure shown in Fig. 6.10(b).*[a, b]

			Eigenvectors				
Proton	Isotropic value[a]	Anisotropic value[a]	<a>	<b>	<c*>	: Coupling	Angle Diff (deg)[b]
		-35.74	-0.101	0.973	-0.207		13.3
H4	-56.55	-0.28	0.995	0.095	-0.042	: 1	21.1
		36.02	0.021	0.210	0.978		16.3
		8.15	0.287	0.766	0.576	: 3	5.8
H5	85.95	-3.62	0.311	-0.643	0.700		
		-4.53	0.906	-0.022	-0.423		
		8.25	-0.260	0.780	0.569	: 2	16.7
H6	89.85	-3.54	-0.233	-0.622	0.747		
		-4.71	0.937	0.061	0.344		

[a]All the values are in units of MHz. [b]The angular differences are between eigenvectors from the experimental and from the calculations. For β-couplings, the eigenvectors are those associated with maximum eigenvalues.

Table 6.4(c) *The coupling tensors calculated with EPR-II on the structure shown in Fig. 6.11(b).*[a, b]

			Eigenvectors				
Proton	Isotropic value[a]	Anisotropic value[a]	<a>	<b>	<c*>	: Coupling	Angle Diff (deg)[b]
		-36.10	-0.003	0.982	-0.191		7.7
H4	-54.14	-0.26	0.999	0.009	0.032	: 1	15.3
		36.36	-0.033	0.191	0.981		13.2
		7.79	0.363	0.742	0.564	: 3	9.1
H5	87.92	-3.3	0.253	-0.661	0.707		
		-4.49	0.897	-0.114	-0.427		
		8.92	-0.186	0.787	0.588	: 2	20.8
H6	89.92	-4.07	-0.411	-0.606	0.681		
		-4.86	0.892	-0.115	0.436		

[a]All the values are in units of MHz. [b]The angular differences are between eigenvectors from the experimental and from the calculations. For β-couplings, the eigenvectors are those associated with maximum eigenvalues.

Radical R1'- another conformation of deamination from main chain

Couplings 14 and 15 were detected for radical R1' in the ENDOR experiment, as is shown in Fig. 6.2, and their tensors are listed in Table 6.5. The angular dependence curves are shown in Fig. 6.12. Coupling 14 is characteristic of a β-coupling while coupling 15 has the characteristic of an α-coupling. The EIE patterns of radical R1' at all three axes indicate R1' contains three major couplings. WINSIM

simulations indicate that the 3rd coupling, not detected in the ENDOR experiments, has very little anisotropy and evidently is from one β-proton with a coupling value around 30MHz (see Fig. 6.13). This coupling was denoted as "β-3rd".

With one α-coupling and two β-couplings, there are two possible structures for R1': deamination from the main chain (Scheme 6.2) or dehydrogenation at C3 (Scheme 6.6a). As is described in the following, R1' was assigned as a deamination radical with a conformation different from R1.

Comparison of the coupling tensors of R1, R1' and RI are indicated in Table 6.6, where RI is from irradiation and detection at 298K, R1 and R1' were detected at 66K after irradiation at 298K. The tensor of coupling 15 is quite similar as those of couplings 1 and α1. Especially for couplings 15 and α1, the differences between the eigenvectors are less than 6°, and the difference for principal values are within 2MHz. Since R1 and RI have been identified as the result of deamination from the main chain, the similarity of R1' to R1 and RI suggest that it is another configuration of R1, and the orientation of the α-proton for R1' is almost unchanged during the cooling to 66K.

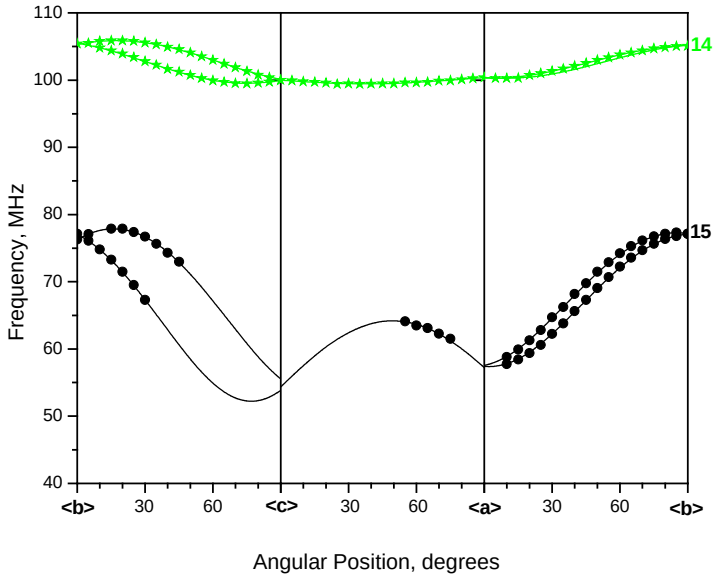

Fig. 6.12 *Angular dependent curves for couplings 14 and 15 from single crystal of L-lys·HCl·2H$_2$O irradiated at 298K and detected at 66K.*

Table 6.5 *Hyperfine coupling tensors for radical R1' in L-lys·HCl·2H$_2$O single crystal irradiated at 298K and detected at 66K.*[a, b]

Tensor	Principal values[a,b]	Isotropic Values[a,b]	Anisotropic values[a]	Eigenvectors[b] <a>	<b>	<c*>
	-84.49(5)		-31.75	0.057(1)	-0.965(1)	0.254(2)
15	-53.88(13)	-52.74	-1.14	0.853(1)	0.180(2)	0.490(2)
	-19.86(28)		32.88	0.519(3)	-0.189(2)	-0.834(2)
	139.78(2)		7.67	0.064(1)	-0.954(1)	0.294(3)
14	129.83(2)	132.11	-2.28	0.928(0)	0.165(1)	0.334(1)
	126.74(2)		-5.37	0.367(1)	-0.252(3)	-0.896(1)
			~7.00			
β-3rd		~30.00	~3.50			
			~3.50			

[a]All these values are in units of MHz. [b]Numbers in parentheses are the estimated uncertainties in the last digit quoted as reported by the statistical analysis.

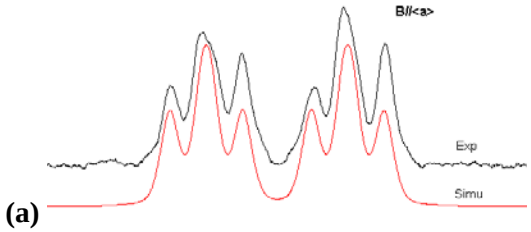

(a)

Set	Coupling*	Spin	Number
1	125.02	0.5	1
2	36.32	0.5	1
3	28.22	0.5	1

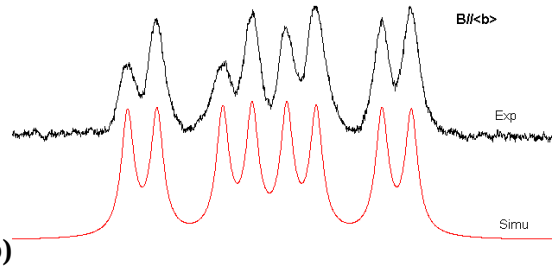

(b)

Set	Coupling*	Spin	Number
1	135.8	0.5	1
2	80.89	0.5	1
3	25.17	0.5	1

Fig. 6.13 *WINSIM simulation for EIE patterns of R1' at <a> and at <b>. The output coupling values are listed on the right side of* ***(a)*** *and* ***(b)****. * The coupling values are in MHz.*

Table 6.6 *Tensors comparison between couplings of R1 and R1' and between couplings of R1' and RI.*[a,b]

R1'			Eigenvectors			**R1**	
Tensor	Isotropic value[a]	Anisotropic value[a]	<a>	<b>	<c*>:	Tensor	Angle diff (deg)[b]
		-31.75	0.057	-0.965	0.254		11.7
15	-52.74	-1.14	0.853	0.180	0.490	:1	19.8
		32.88	0.519	-0.189	-0.834		16.0
14	132.11	7.67	0.064	-0.954	0.294	:2	47.8
14	132.11	7.67	0.064	-0.954	0.294	:3	61.0
R1'						**RI**	
		-31.75	0.057	-0.965	0.254		2.8
15	-52.74	-1.14	0.853	0.180	0.490	: α1	5.9
		32.88	0.519	-0.189	-0.834		5.8
14	132.11	7.67	0.064	-0.954	0.294	: β1	15.4
14	132.11	7.67	0.064	-0.954	0.294	: β2	41.2

[a]All these values are in units of MHz. [b]"Angle Diff (°)" are the angular differences between the experimental eigenvectors in units of degrees. For β couplings, the angular differences are between the corresponding maximum dipolar vectors.

On the other hand, the parameters of β-couplings for R1' are quite different from those for R1. The isotropic values of coupling 2 and 3 are almost equal, while the values of coupling 14 and "β-3rd" are different by more than 100MHz. Also, the angular difference between the maximum dipolar vectors of couplings 14 and 2 is 47.8°, and that between couplings 14 and 3 is ~61°. However, these differences can be explained by the conformational characteristics. According to the analysis on β-proton conformation of R1, the dihedral angles for coupling 2 and 3 are both close to 30° as shown in Fig. 6.7b. Using this method, for coupling 14 the estimated dihedral angle is 0°. Assuming purely tetrahedral bonding to C3, the dihedral angle for the 2nd β-proton should be ~60°. Using formula (3), the isotropic value of 30MHz and $B_1\rho$ = 125MHz, the calculated dihedral angle for coupling "β-3rd" is 61°, which agrees very well with the expected angle for the 2nd β-proton (~60°). The conformation is sketched in Fig. 6.14.

Thus R1' is assigned as another configuration of the main chain deamination radical at 66K; the major configuration difference of R1 and R1' are in β-protons configurations as shown in Fig. 7b and Fig. 6.14, respectively.

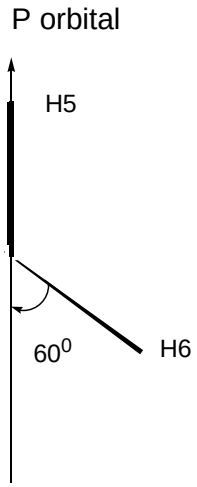

Fig. 6.14 *Conformation of two β-protons for radical R1'.*

R2 and R3-dehydrogenation from C4 (R2) and from C5 (R3)

As is mentioned above and shown in Fig. 6.2, ENDOR lines 4-13 are associated with EIE patterns having similar appearance. The spectral width of the EIE at <a> is about 143.6 Gauss and the sum of coupling values for ENDOR lines 4-13 at <a> is 287.0 Gauss, as indicated in Fig. 6.15. Since the total of all ENDOR couplings is about twice of EIE spectral width, the similar EIE patterns must come from more than one radical.

Hyperfine tensors for couplings 4-12 were obtained from ENDOR spectra (Table 6.7) but it was not possible to calculate the tensor for coupling 13 because its ENDOR lines were undetectable at most orientations. The angular dependence curves for couplings 4-13 are shown in Fig. 6.16. Tensors 4 and 5 exhibit large anisotropic coupling values characteristic of α-couplings. Tensors 6–12 exhibit the nearly axial symmetry and small anisotropies characteristic of β-couplings. Coupling 13 is assumed to be a β-coupling on the basis of the moderate anisotropy exhibited by ENDOR lines in the <ac> crystallographic plane (see Fig. 6.16b).

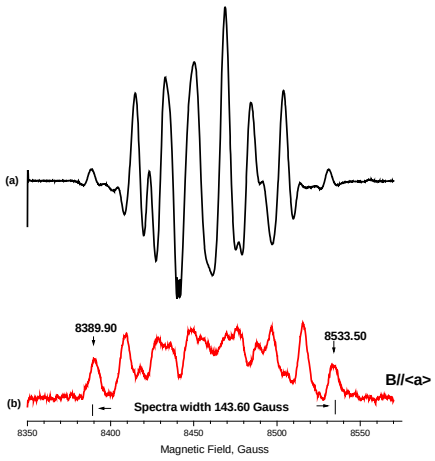

ENDOR Line	Resonant Frequency (MHz)	Coupling (Gauss)
4	62.50	18.93
5	62.50	18.93
6	97.60	44.00
7	93.90	41.36
8	75.10	27.93
9	73.12	26.51
10	61.66	18.33
11	56.63	14.74
12	88.55	37.54
13	89.00	37.86
	Sum	286.13

Fig. 6.15 (a) *EPR spectrum (B//<a>) taken from irradiated normal crystal L-lys·HCl·2H_2O irradiated at 298K and measured at 66K.* ***(b)*** *EIE spectrum of R2 and R3 (B//<a>), which gives the width of the spectra of 143.60Gauss. The table at the right side indicates the resonant frequencies and the corresponding coupling values at B//<a> for couplings 4-13. See text for the description.*

From examination of Table 6.9, it can be seen that pairs of couplings have similar isotropic values: 4 (-60.65MHz) and 5 (-58.58MHz), 6 (124.36MHz) and 7 (119.05MHz), 8 (80.14MHz) and 9 (75.77MHz), 10 (53.67MHz) and 11 (44.94MHz). Lines 12 and 13 are in the similar frequency range in the <ac> plane (see Fig. 6.16b); thus these two couplings most likely have similar isotropic values, which are close to 100MHz. These relationships suggest that there are two sets of couplings related to the EIE pattern, and that each set contains one α-coupling and four β-couplings (with isotropic values of ~120MHz, ~100MHz, ~80MHz and ~50MHz, respectively, for the β-couplings). This hypothesis is supported by use of WINSIM simulations (see Fig. 6.17).

Table 6.7 *Hyperfine coupling tensors for radical R2 and R3 in single crystal of L-lysine HCl $2H_2O$ irradiated at 298K and detected at 66K.* [a,b]

Tensor	Principal values[a,b]	Isotropic Values[a]	Anisotropic values[a]	Eigenvectors[b] <a>	<b>	<c*>
	-97.50(3)		-36.86	0.002(0)	0.869(0)	0.495(1)
4	-54.82(3)	-60.64	5.82	0.922(0)	0.191(1)	-0.338(0)
	-29.61(3)		31.03	0.388(0)	-0.457(1)	0.800(0)
	-97.76(3)		-39.18	0.229(0)	0.837(0)	-0.497(1)
5	-50.47(3)	-58.58	8.11	0.969(0)	-0.247(1)	0.031(0)
	-27.50(3)		31.08	0.096(0)	0.489(1)	0.867(0)
	132.37(2)		8.01	0.413(1)	-0.893(2)	0.180(2)
6	121.51(2)	124.36	-2.85	0.697(0)	0.437(1)	0.569(1)
	119.2(2)		-5.16	0.587(1)	0.109(2)	-0.803(2)
	127.20(2)		8.15	0.230(1)	0.954(2)	-0.192(2)
7	115.86(2)	119.05	-3.19	0.761(0)	-0.299(1)	-0.576(2)
	114.10(2)		-4.95	0.607(1)	0.014(2)	0.795(2)
	88.84(2)		8.70	0.448(1)	-0.251(9)	0.858(4)
8	76.20(2)	80.14	-3.94	0.378(1)	0.923(3)	0.072(10)
	75.37(2)		-4.77	0.810(5)	-0.292(5)	-0.508(1)
	84.74(2)		8.97	0.511(1)	-0.182(16)	-0.840(3)
9	71.56(2)	75.77	-4.21	0.154(1)	0.981(1)	-0.118(19)
	71.02(2)		-4.75	0.846(1)	-0.069(10)	0.529(2)
	61.26(2)		7.59	0.441(1)	-0.893(2)	-0.093(1)
10	52.33(2)	53.67	-1.34	0.560(0)	0.192(1)	0.806(1)
	47.42(2)		-6.25	0.701(2)	0.408(1)	-0.585(1)
	53.93(2)		8.99	0.238(1)	-0.928(2)	0.287(2)
11	42.58(2)	44.94	-2.36	0.611(0)	-0.087(2)	-0.787(1)
	38.30(2)		-6.64	0.755(1)	0.363(1)	0.547(2)
	116.28(2)		7.57	0.150(3)	-0.281(2)	0.948(2)
12	106.62(4)	108.71	-2.09	0.749(2)	0.659(2)	0.076(2)
	103.22(4)		-5.49	0.646(2)	-0.698(4)	-0.310(1)

[a]All these values are in units of MHz. [b]Numbers in parentheses are the estimated uncertainties in the last digit quoted as reported by the statistical analysis.

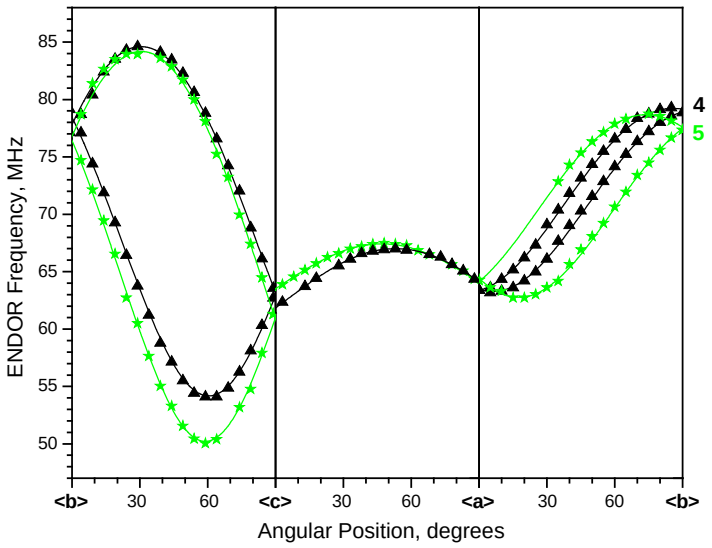

(a)

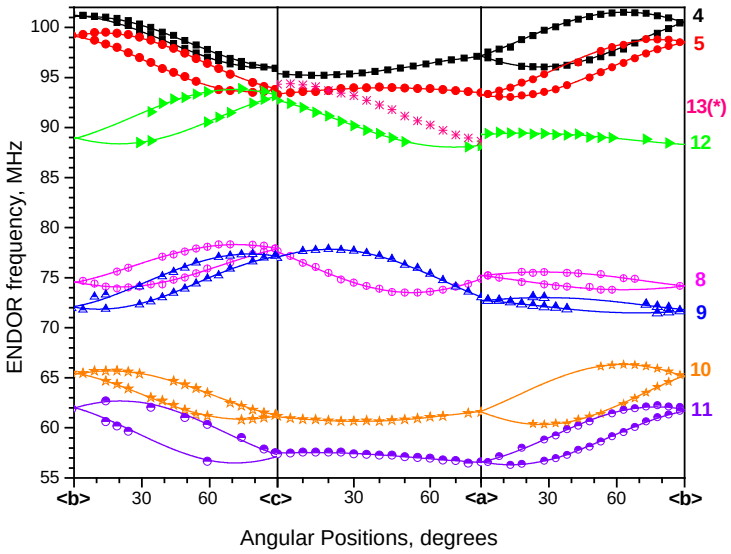

(b)

Fig. 6.16 *Angular dependence curves of couplings from R2* ***(a)*** *and R3* ***(b)***.

The structure of lysine is such that this set of couplings (one α and four β) could arise from these different radical forms: dehydrogenated at C4 (Scheme 6.4a), at C5 (Scheme 6.4b) and at C6 (Scheme 6.4c). In addition, the close similarity of the couplings within each pair suggests that the couplings might arise from one radical form trapped in different configurations. Because EIE patterns from the two sets of couplings are very similar, it was not possible to assign the couplings with EIE only.

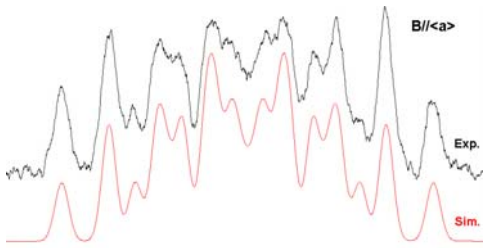

Fig. 6.17 *WINSIM simulation of EIE pattern of R2 and R3 with magnetic field along <a> axis. The WINSIM optimized coupling values are 38.85G, 34.99G, 27.27G, 17.96G and 17.0G.*

Eigenvectors[I] from α-couplings 4 and 5 have angular differences within 22°, and for each pair of β-couplings, 6 and 11, 7 and 10, 8 and 12, the eigenvectors[I] with maximum anisotropic values have angle differences never larger than 18°, as is indicated in Table 6.8. Although tensor 13 cannot be calculated, however this coupling has an ENDOR angular dependence curve similar to that of coupling 9 in the <ac> plane (see Fig. 6.16b). Thus it is reasonable to estimate that the eigenvector[I] of coupling 13 is close to that of coupling 9. In the crystalline lattice of lysine, for radical spin located on C4, C5, or C6, respectively, the angles between the dipolar directions of the β-protons in the same radical as shown in Fig. 6.18 are never less than 45° (see Table 6.9a-c). On that basis, couplings were separated into different groups if the difference of their eigenvectors[I] were less than 20°. With this procedure and the simulation results that each set of couplings contains one α and four β-protons with values of ~-58MHz, ~120MHz, ~100MHz, ~80MHz and ~50MHz, respectively, four possibilities of the β-coupling groupings (6, 10, 12, and 9; 6, 10, 13, and 8; 7, 11, 12 and 9; 7, 11, 13 and 8) were obtained. (The α-couplings cannot be assigned to any group affirmatively in this step.)

At the same time, results from RII and RIII (detected at room temperature) were analyzed. EIE patterns of RII and RIII obtained at ~20° from <a> and ~60° from <c> were distinguishable (see Fig. 6.31 in section of "Experiment at room temperature"), and based on the EIEs, room temperature couplings α2, β3, β5, β7, and β9 were ascribed to RII, while couplings α3, β4, β6, β8 and β10 were ascribed to RIII. The comparisons between tensors detected at 298K and at 66K indicated that tensors α2, β5, β7, and β9 are most similar to tensors 4, 7, 11 and 8, respectively, while tensors α3, β4, β6 and β8 are most similar

to tensors 5, 12, 6, 10 and 9, respectively. Although tensor 13 was not available, it could be similar to the remaining coupling β3, since the estimated coupling value of ~100MHz for 13 is close to coupling value of 99.36MHz from β3. These tensor comparisons are described in detail in the section of "Experiments at Room Temperature", and the differences between the tensors are listed in Table 6.15 of that section. RII and R2, RIII and R3 were assigned as the same radical detected at temperatures 298K and 66K, respectively, and the two sets of couplings at 66K can be grouped as 4, 7, 8, 11, 13 (R2) and 5, 6, 9, 10 12 (R3) based on the tensor comparisons. The grouping of the β-protons is satisfied with two possibilities above.

Table 6.8 *Comparison for the eigenvectors of couplings of radicals R2 and R3.*[a, b]

		Eigenvectors[b]					Eigenvectors[b]			
Coupling	Isotropic value[a]	<a>	<b>	<c*>	Coupling	Isotropic value[a]	<a>	<b>	<c*>	Angle Diff(°)[c]
4	-60.64	0.002	-0.869	0.495	5	-58.58	0.229	0.837	-0.497	13.4
4	-60.64	0.922	-0.191	-0.338	5	-58.58	0.969	-0.247	0.031	21.5
4	-60.64	0.388	0.457	0.800	5	-58.58	0.096	0.489	0.867	17.4
6	124.36	0.413	-0.893	0.180	11	44.94	0.238	-0.928	0.287	15.7
7	119.05	0.230	-0.954	-0.192	10	53.67	0.441	-0.893	-0.093	13.8
12	108.71	0.150	-0.281	0.948	8	80.14	0.448	-0.251	0.858	18.0

[a]The anisotropic values are in MHz. [b]Eigenvectors for α-couplings are the vectors with absolute maximum, median, and minimum principal values, respectively; for β-couplings, the vectors are associated with maximum principal values only. [c]"Angle diff (°)" is the angular difference between eigenvectors in units of degrees.

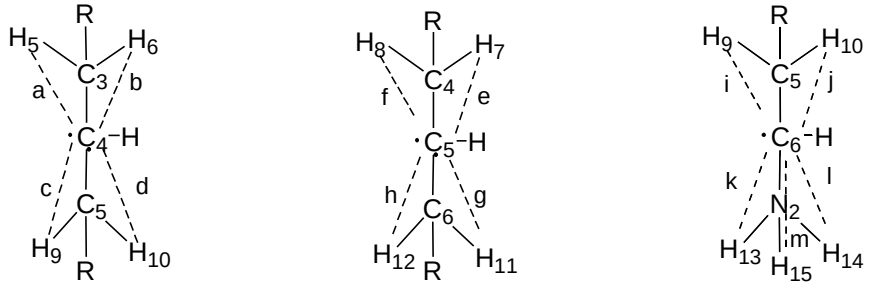

Fig. 6.18 *The crystallographic angle between the directions from the β-proton to radical center, assuming the spin is located on C4* ***(a),*** *C5* ***(b)*** *and C6* ***(c),*** *respectively.*

Table 6.9(a)-(c) *Angles between the directions denoted in Fig. 6.18(a-c), respectively.*

(a)		**(b)**		**(c)**	
Directions Comparison	Angle (°)	Directions Comparison	Angle (°)	Directions Comparison	Angle (°)
a:b	48.1	e:f	50.4	I:j	46.1
a:c	70.1	e:g	75.4	I:k	70.4
a:d	94.6	e:h	96.8	I:l	95.3
b:c	86.7	f:g	88.6	I:m	117.4
b:d	74.1	f:h	70.3	j:k	84.4
c:d	46.5	g:h	47.9	j:l	74.5
				j:m	120.0
				k:l	45.6
				k:m	47.3
				l:m	47.2

Table 6.9(d) *Angles between the directions denoted in Fig. 6.18(a-b).*

Directions Comparison	Angle (°)	Directions Comparison	Angle (°)	Directions Comparison	Angle (°)	Directions Comparison	Angle (°)
a:e	71.4	b:e	88.4	c:e	5.7	d:e	51.1
a:f	88.1	b:f	71.6	c:f	45.7	d:f	2.8
a:g	8.9	b:g	39.3	c:g	73.3	d:g	88.6
a:h	56.7	b:h	8.7	c:h	88.4	d:h	72.5

Next, the eigenvectors^{I} of couplings 4-12 were compared with the corresponding directions in the crystalline lattice. As listed in Table 6.10, all angular differences are less than 22.5°, which suggests that the reorientation is not large for these β-couplings. (Eigenvector^{I} of 13 is not shown in the table, but it should be similar to that of 9 from analysis above.) Also, we noticed the similarity of the crystallographic directions for β protons in radicals centered at C4, at C5 and at C6. All these crystallographic directions denoted in Fig 6.18a-b were compared, and the angles between the directions are listed in Table 6.9d: each difference between directions a and g, b and h, c and e, d and f is less than ~9°, and the other differences are larger than ~40°. Directions in Fig. 6.18c were also compared to those in Fig 6.18a-b separately (angles not shown here), and indicated i//a//g, j//b//h, k//c//e, and l//d//f. Therefore, we cannot assign the couplings to any possible radical based on the comparisons shown in Table 6.10, due to the parallelism of the crystallographic directions for the side chain hydrogen atoms. On the other hand, the similarities for the dipolar directions of the β-protons suggests that if the radicals are centered at C4 and at C5 (or at C6), the eigenvectors^{I} of the β-couplings from one radical (such as C4 dehydrogenation) should

Table 6.10 *Comparison the eigenvectors of the couplings of R2 andR3 and the corresponding directions in crystalline lattice for three possible radicals.*[a, b]

Direction	<a>	<b>	<c*>	Coupling	Angle Diff(°)[a]
Radical Center: C4					
C4-H7	0.895	0.221	0.388	: 4	40.6
				: 5	57.9
C4-H8	-0.717	0.346	0.605	: 4	68.7
				: 5	51.4
C4…H5	-0.51	0.205	-0.835	: 8	4.6
				: 12	22.2
C4…H6	0.242	-0.911	-0.334	: 9	14.0
C4…H9	-0.463	-0.824	-0.326	: 6	9.7
				: 11	14.4
C4…H10	0.324	-0.89	-0.32	: 7	9.9
				: 10	14.7
Radical Center: C5					
C5-H9	-0.807	-0.208	-0.552	: 4	31.7
				: 5	48.8
C5-H10	0.755	-0.392	-0.526	: 4	72.1
				: 5	54.9
C5…H7	0.532	0.808	0.255	: 6	9.5
				: 11	18.3
C5…H8	-0.31	0.878	0.366	: 7	11.9
				: 10	17.4
C5…H11	0.372	-0.218	0.903	: 8	5.4
				: 12	13.5
C5…H12	-0.436	-0.141	0.889	: 9	5.7
Radical Center: C6					
C6-H11	0.813	0.163	0.558	: 4	33.2
				: 5	50
C6-H12	-0.792	0.346	0.504	: 4	75.3
				: 5	58.0
C6…H9	-0.346	0.214	-0.914	: 8	7.0
				: 12	12.0
C6…H10	0.429	0.106	-0.897	: 9	17.5
C6…H13	-0.411	-0.818	-0.403	: 6	13.5
				: 11	13.5
C6…H14	0.342	-0.908	-0.242	: 7	7.5
				: 10	10.3
C6…H15	-0.186	-0.914	0.361	**: 7**[b]	10.3
				: 10[b]	21.3

[a]"Angle Diff(°)" stands for the angular difference between the crystallographic direction and the experimental eigenvector associated with maximum coupling component. [b]The sign of the y component is changed due to the group symmetry of $P2_1$.

be very similar as those from another radical (such as C5 dehydrogenation), like the case of R2 and R3. However, this is only one possibility, and the assignments need to be confirmed by more information.

In the following, based on the results from DFT calculations, the couplings are assigned to the radicals dehydrogenated from C4 and from C5, tentatively.

DFT calculations for radicals R2 and R3

In order to arrive at the assignment and distinguish if R2 and R3 are from two different radicals or from two different configurations of one radical, two-layer ONIOM optimizations were performed. In the two-layer ONIOM models, the six center radicals were formed by dehydrogenation from H7-H12 respectively and treated with DFT-B3LYP functional and with basis set of 6-31G (d, p). There are two surrounding cluster models: six neighboring lysine molecules and two water molecules (see Fig. 6.19), which were hydrogen bonded to the center radical; the second is a larger cluster model including seven neighboring lysine molecules and sixteen water molecules (see Fig. 6.20). Both surrounding models were calculated with semiempirical PM3 Hamiltonian. The center radicals were fully optimized among the frozen surrounding clusters. We denoted "DeH6-I" for center radical of H6 dehydrogenation among the first surrounding cluster model, and "DeH6-II" for the same radical surrounded with second neighboring model; the other two-layer ONIOM models use similar methodology.

Although the optimization for DeH7-I, DeH8-II, DeH9-I, DeH10-I, DeH11-II and DeH12-II did not converge, however, as described in the following, the completed calculation results still provided useful information to help reach the assignment. Firstly, the energy for the optimized models within the first and the second surrounding models were compared, respectively, and are indicated in Fig.6.21a-b. Next, the single point energy calculations were performed on the fully optimized center radicals using B3LYP functional and basis set of 6-311G (2d, p). The calculated parameters were compared with the experimental ones and Table 6.11 lists the closest coupling comparisons. In Fig. 6.21a, DeH11-I with highest energy is least stable. Meanwhile, the calculated parameters for the α-proton (H12) and β-proton (H9) in DeH11-I are quite different from the experimental ones, not only for the isotropic value but also

for the eigenvectors (see Table 6.11 h). Therefore, the possible radical from H11 dehydrogenation was rejected. In Fig.6.21b, DeH10-II has much higher energy than the others. As indicated in Table 6.11g, the eigenvector[I] of the β-proton H8 in DeH10-II is different from that of coupling 10 by ~72° (the difference from other experimental β-couplings is even larger). It is very unlikely that these couplings are from H10 dehydrogenation. On the other hand, DeH7-II and DeH8-I are the most stable structures with two lowest energies shown in Fig. 6.21b and 6.21a, respectively. Moreover, DeH7-II and DeH8-I have similar optimized structures and the coupling tensors from both of them are close to the experimental tensors 4, 7, 8, 11 and 13 (See Tables 6.11a and 6.11d). Especially for the eigenvectors, there is no difference over 21°. Thus dehydrogenation at C4 (DeH7 or DeH8) is one of the radicals giving the couplings 4, 7, 8, 11, 13: from energy comparisons, DeH7-II is more stable, and from coupling comparison, the coupling values from DeH8-I are closer to the experimental ones. The remaining couplings 6, 9, 10, and 12 are close to the calculated tensors from DeH9-II (see Table 6.11e), and the energy from DeH9-II is larger than energy from DeH7-II but lower than that from DeH8-I (see Fig. 6.21). For these reasons, H9 dehydrogenation could be the radical giving the second set of experimental couplings. Although the eigenvectors[I] of α-proton H10 in DeH9-II differ from experimental α-coupling 5 vector by a large amount (~60°), the differences are reduced to ~20° by bending H9 by -20° (see Table 6.11f). The parameters from DeH12-I are closer to couplings 4, 7, 8, 11, 13 than to couplings 5, 6, 9, 10, 12, but they are not in better agreement than those from comparisons for DeH7-II and DeH8-I (see Table 6.10a, 6.10d and 6.10i) and DeH12-I has higher energy than DeH8-I (Fig.6.21a), thus H12 dehydrogenation was rejected.

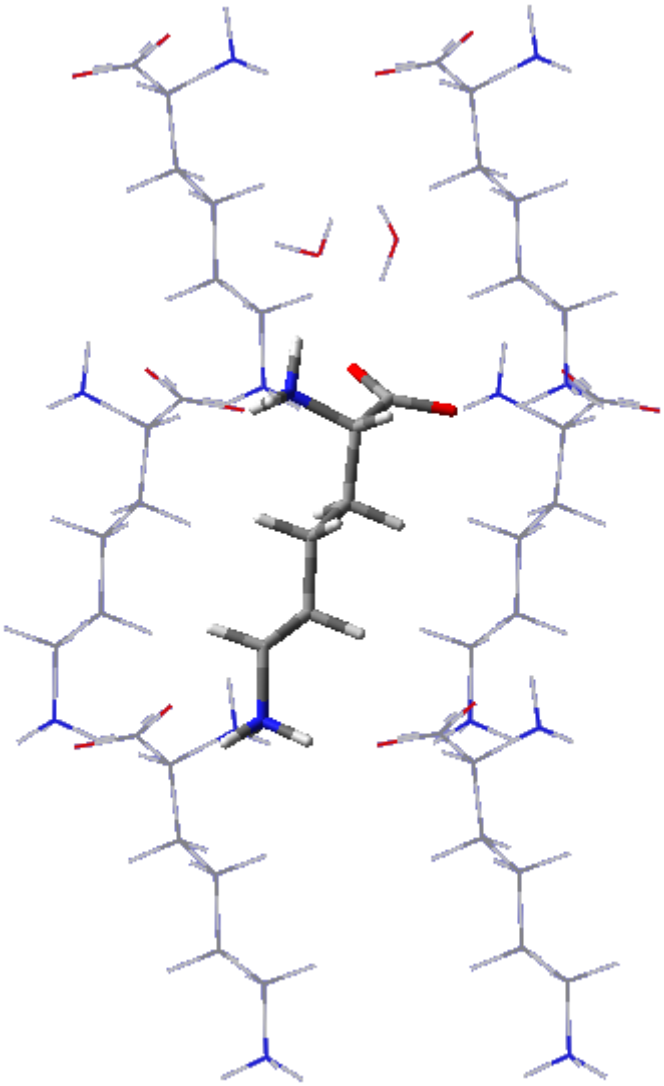

Fig. 6.19 *Two-layer ONIOM optimization model with the "first" surrounding cluster model (six lysine molecules and two water molecules) for radicals dehydrogenation from the side chain (see text).*

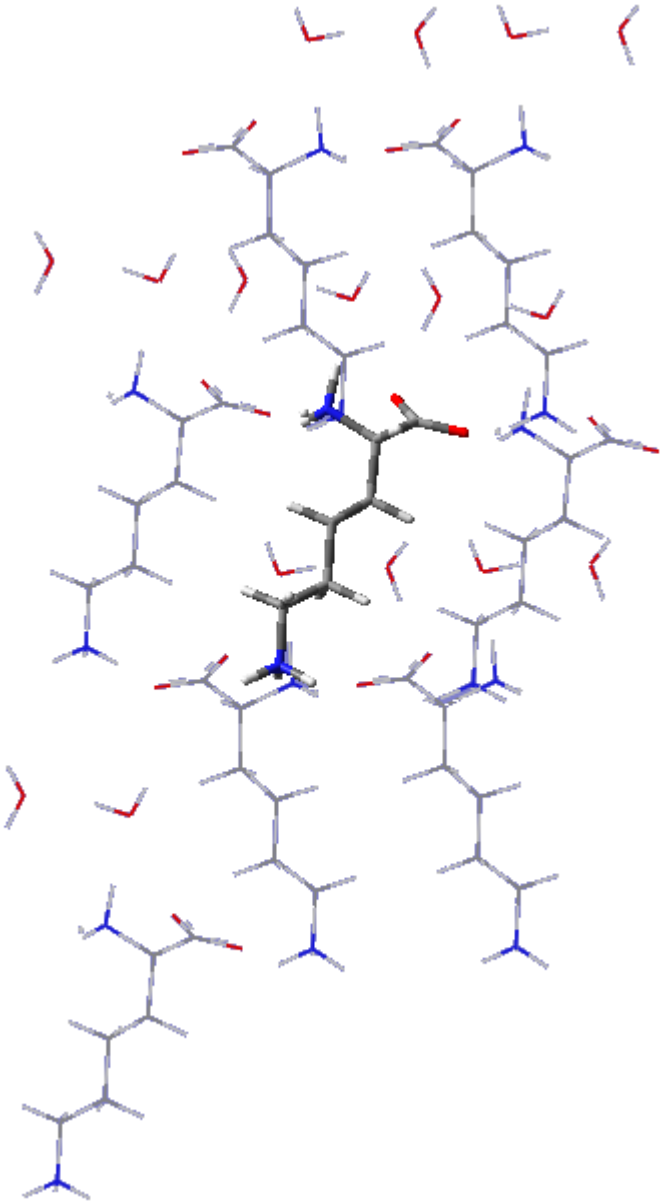

Fig. 6.20 *Two-layer ONIOM optimization model with the "second" surrounding cluster model (seven lysine molecules and sixteen water molecules) for radicals dehydrogenation from the side chain (see text).*

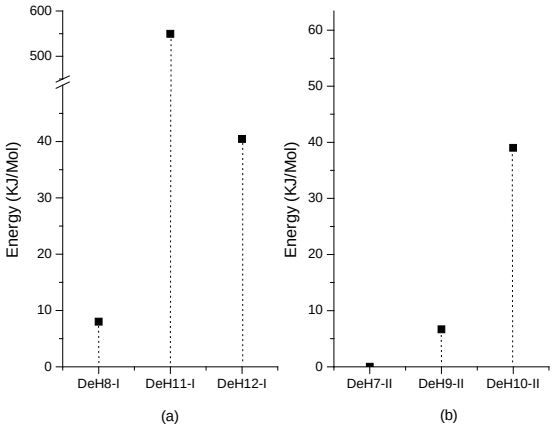

Fig. 6.21 *Energies for dehydrogenation radicals calculated with the "first" surrounding cluster models* ***(a)*** *and with the "second" surrounding cluster models* ***(b)***.

Table 6.11(a) *The coupling tensors calculated on the structure optimized from the "DeH7-II" model.*[a-c]

			Eigenvector				
Proton	Isotropic value[a]	Anisotropic value[a]	<a>	<b>	<c*>	Coupling	Angle Diff (°)[b]
		9.16	0.522	-0.145	0.841	: 8	7.3
H5	77.60	-3.96	0.321	0.947	-0.035		
		-5.21	0.791	-0.288	-0.54		
		8.10	-0.279	-0.069	0.958	: 13[c]	16.3
H6	142.04	-2.25	-0.573	0.813	-0.109		
		-5.85	0.771	0.579	0.266		
		-36.62	-0.055	0.868	-0.493	: 4	3.2
H8	-51.50	-0.78	0.902	-0.169	-0.398		3.2
		37.39	0.429	0.466	0.774		3
		8.66	0.271	0.889	0.37	: 11	5.3
H9	9.39	-3.69	0.909	-0.11	-0.401		
		-4.98	0.316	-0.445	0.838		
		8.52	-0.24	0.971	0.016	: 7	10
H10	101.50	-3.55	0.95	0.238	-0.204		
		-4.97	0.201	0.034	0.979		

[a]All these values are in unit of MHz. [b]"Angle Diff (°)" stands for the angular differences between the eigenvectors in units of degrees; For β couplings, the eigenvectors are those associated with maximum eigenvalues. [c]The eigenvectors of coupling 13 were considered the same as those of coupling 9.

Table 6.11(b) *The coupling tensors calculated on the intermediate structure from the "DeH7-II" optimization.* [a, b]

			Eigenvector				
Proton	Isotropic value[a]	Anisotropic value[a]	<a>	<b>	<c*>	Coupling	Angle Diff (°)[b]
		7.95	0.483	-0.300	0.823	: 12	20.5
H5	131.98	-2.71	0.702	0.694	-0.159		
		-5.24	-0.524	0.655	0.546		
		8.91	-0.185	-0.100	0.978	: 9	20.9
H6	65.06	-3.81	-0.036	0.995	0.095		
		-5.09	0.982	0.018	0.187		
		-38.21	-0.006	0.878	-0.479	: 5	13.7
H8	-58.17	-0.09	0.993	0.063	0.103		18.3
		38.30	-0.120	0.475	0.872		12.5
		8.23	0.333	0.924	0.189	: 6	4.9
H9	93.89	-3.51	0.390	-0.318	0.865		
		-4.72	0.859	-0.215	-0.466		
		9.32	-0.214	0.941	0.264	: 10	16.5
H10	74.24	-4.44	0.311	-0.190	0.931		
		-4.87	0.926	0.282	-0.252		

[a]All these values are in unit of MHz. [b]"Angle Diff (°)" stands for the angular differences between the eigenvectors in units of degrees; For β couplings, the eigenvectors are those associated with maximum eigenvalues.

Table 6.11(c) *The coupling tensors calculated on the structure from ONIOM optimization with the intermediate cluster in the "DeH7-II" optimization as the initial cluster model.* [a, b, c]

			Eigenvector				
Proton	Isotropic value[a]	Anisotropic value[a]	<a>	<b>	<c*>	Coupling	Angle Diff (°)[b]
		-5.17	0.800	-0.276	-0.532	: 8	6.4
H5	77.49	-3.91	0.318	0.948	-0.014		
		9.08	0.508	-0.158	0.847		
		-5.81	0.774	0.570	0.276	: 13[c]	15.8
H6	141.26	-2.30	-0.565	0.818	-0.107		
		8.11	-0.287	-0.073	0.955		
		-36.74	-0.038	0.869	-0.493		2.1
H8	-52.63	-0.63	0.909	-0.175	-0.379	: 4	2.6
		37.36	0.416	0.462	0.783		2.0
		-4.96	0.386	-0.454	0.803	: 11	5.8
H9	13.65	-3.71	0.873	-0.102	-0.477		
		8.67	0.298	0.885	0.357		
		-4.96	0.295	0.029	0.955	: 7	8.9
H10	105.52	-3.56	0.930	0.219	-0.294		
		8.54	-0.218	0.975	0.038		

[a]All these values are in unit of MHz. [b]"Angle Diff (°)" stands for the angular differences between the eigenvectors in units of degrees; For β couplings, the eigenvectors are those associated with maximum eigenvalues. [c]The eigenvectors of coupling 13 were considered the same as those of coupling 9.

Table 6.11(d) *The coupling tensors calculated on the structure optimized from the "DeH8-I" model.* [a, b, c]

Proton	Isotropic value[a]	Anisotropic value[a]	Eigenvector <a>	<b>	<c*>	:Coupling	Angle Diff (°)[b]
		8.64	0.523	-0.175	0.834	: 8	6.4
H5	57.77	-3.86	0.219	0.973	0.067		
		-4.79	0.824	-0.148	-0.547		
		8.00	-0.269	-0.051	0.962	: 13[c]	17.3
H6	146.43	-2.34	-0.591	0.798	-0.123		
		-5.66	0.761	0.601	0.245		
		-36.68	0.062	0.829	-0.556	: 4	5.4
H7	-54.87	-0.22	0.815	-0.363	-0.451		13.3
		36.91	0.576	0.425	0.698		12.5
		8.70	0.556	0.816	0.158	: 11	20.8
H9	40.38	-3.86	-0.483	0.163	0.86		
		-4.83	0.676	-0.554	0.485		
		8.34	0.022	0.996	0.091	: 7	15.7
H10	112.36	-3.52	-0.632	-0.057	0.773		
		-4.82	0.775	-0.074	0.628		

[a]All these values are in unit of MHz. [b]"Angle Diff (°)" stands for the angular differences between the eigenvectors in units of degrees; For β couplings, the eigenvectors are those associated with maximum eigenvalues. [c]The eigenvectors of coupling 13 were considered the same as those of coupling 9.

Table 6.11(e) *The coupling tensors calculated on the structure optimized from the "DeH9-II" model.* [a, b]

Proton	Isotropic value[a]	Anisotropic value[a]	Eigenvector <a>	<b>	<c*>	:Coupling	Angle Diff (°)[b]
		7.73	0.342	0.931	0.127	:6	5.4
H7	103.86	-2.67	0.914	-0.361	0.187		
		-5.06	-0.22	-0.052	0.974		
		8.17	-0.424	0.856	0.295	: 10	12.1
H8	2.79	-3.72	0.805	0.207	0.555		
		-4.45	-0.414	-0.473	0.778		
		-34.85	0.199	0.884	-0.422	: 5	5.6
H10	-41.90	-2.47	0.526	0.267	0.808		62.0
		37.32	0.827	-0.383	-0.412		62.3
		7.26	-0.196	-0.408	0.892	: 12	21.4
H11	112.35	-1.61	0.614	0.658	0.436		
		-5.65	0.765	-0.633	-0.121		
		9.55	0.76	0.231	-0.608	: 9	19.8
H12	30.77	-3.97	0.527	0.331	0.783		
		-5.58	-0.382	0.915	-0.13		

[a]All these values are in units of MHz. [b]"Angle Diff (°)" stands for the angular differences between the eigenvectors in units of degrees; For β couplings, the eigenvectors are those associated with maximum eigenvalues.

Table 6.11(f) *The coupling tensors calculated on the structure made by bending the α-proton by -20° relative to the radical optimized from the "DeH9-II" model.* [a, b]

			Eigenvector				
Proton	Isotropic value[a]	Anisotropic value[a]	<a>	<b>	<c*>	:Coupling	Angle Diff (°)[b]
		9.94	0.283	0.951	0.129	:6	8.7
H7	121.27	-4.08	0.886	-0.310	0.345		
		-5.86	-0.368	-0.017	0.930		
		7.91	-0.451	0.857	0.251	: 10	9.3
H8	30.17	-3.32	-0.002	-0.282	0.960		
		-4.59	0.893	0.432	0.129		
		-37.26	0.201	0.885	-0.421		5.4
H10	-56.53	-1.14	0.945	-0.062	0.321	: 5	19.8
		38.40	-0.258	0.462	0.849		20.5
		9.26	-0.227	-0.388	0.893	: 12	22.8
H11	99.49	-3.92	0.492	0.746	0.449		
		-5.34	0.841	-0.541	-0.021		
		8.10	0.741	0.269	-0.615	: 9	19.2
H12	76.25	-3.75	-0.155	0.960	0.233		
		-4.35	0.654	-0.078	0.753		

[a]All these values are in units of MHz. [b]"Angle Diff (°)" stands for the angular differences between the eigenvectors in units of degrees; For β couplings, the eigenvectors are those associated with maximum eigenvalues.

Table 6.11(g) *The coupling tensors calculated on the structure optimized from the "DeH10-II" model.* [a, b]

Proton	Isotropic value[a]	Anisotropic value[a]	Eigenvector <a>	<b>	<c*>	:Coupling	Angle Diff (°)[b]
		-5.29	-0.562	0.424	0.711		
H7	79.27	-3.77	0.416	-0.598	0.685	: 10	
		9.05	0.715	0.68	0.1594		72.2
		-5.46	0.921	-0.205	0.332		
H8	125.54	-2.62	-0.382	-0.299	0.875	: 7	
		8.07	0.08	0.932	0.353		20.2
		-35.96	0.199	0.822	-0.534		12
H9	-43.31	-2.12	0.696	-0.502	-0.513	: 4	24.4
		38.07	0.69	0.269	0.672		21.8
		-5.43	0.519	0.855	0		9.8
H11	11.74	-4.11	0.77	-0.468	-0.434	: 8	11.2
		9.54	0.371	-0.225	0.901		5.3
		-5.98	0.656	0.589	0.473		
H12	93.8	-1.88	-0.695	0.716	0.072	: 13	
		7.86	-0.296	-0.376	0.878		16.8

[a]All these values are in units of MHz. [b]"Angle Diff (°)" stands for the angular differences between the eigenvectors in units of degrees; For β couplings, the eigenvectors are those associated with maximum eigenvalues.

Table* 6.11*(h) *The coupling tensors calculated on the structure optimized from the "DeH11-I" model.* [a, b]

Proton	Isotropic value[a]	Anisotropic value[a]	Eigenvector <a>	<b>	<c*>	Coupling	Angle Diff (°)[b]
		3.27	0.393	0.195	0.899	:12	31.1
H9	60.63	-0.43	0.615	0.671	-0.415		
		-2.84	-0.684	0.716	0.144		
		5.55	-0.51	0.077	0.857	: 9	14.9
H10	6.09	-2.64	0.858	-0.024	0.513		
		-2.90	0.06	0.997	-0.054		
		-15.85	0.001	0.84	-0.543		13.3
H12	15.556	-5.56	0.101	0.54	0.836	: 5	90.6
		21.41	0.995	-0.056	-0.084		90.3
		3.94	0.195	0.934	0.300	: 6	14.4
H13	49.27	-1.27	0.583	-0.357	0.730		
		-2.68	0.789	0.032	-0.614		
		6.98	-0.523	0.839	0.148	: 10	6.7
H14	8.33	-3.39	0.674	0.302	0.674		
		-3.59	-0.522	-0.452	0.724		
		7.21	0.095	0.904	-0.418		
H15	7.13	-3.38	0.346	0.364	0.865		
		-3.83	0.934	-0.227	-0.278		

[a]All these values are in units of MHz. [b]"Angle Diff (°)" stands for the angular differences between the eigenvectors in units of degrees; For β couplings, the eigenvectors are those associated with maximum eigenvalues.

Table* 6.11*(i) *The coupling tensors calculated on the structure optimized from the "DeH12-I" model.* [a, b, c]

Proton	Isotropic value[a]	Anisotropic value[a]	Eigenvector <a>	<b>	<c*>	Coupling	Angle Diff (°)[b]
		8.90	0.585	-0.1	0.805	: 8	12.1
H9	50.53	-4.18	0.442	0.871	-0.213		
		-4.72	0.68	-0.481	-0.554		
		5.74	-0.178	0.032	0.984	: 13[c]	24.3
H10	108.56	-1.12	-0.451	0.886	-0.11		
		-4.61	0.875	0.463	0.143		
		-29.37	-0.053	0.88	-0.472		3.0
H11	-23.17	-3.99	-0.571	0.361	0.737	: 4	32.4
		33.36	0.819	0.309	0.483		32.3
		9.85	0.424	0.885	0.193	: 11	12.2
H13	21.55	-4.62	-0.512	0.058	0.857		
		-5.23	0.747	-0.462	0.478		
		6.46	-0.19	0.959	0.212	: 7	2.2
H14	84.55	-2.50	-0.652	-0.285	0.703		
		-3.95	0.734	-0.005	0.679		
		9.81	-0.102	0.909	-0.403		
H15	8.84	-4.37	0.807	-0.161	-0.568		
		-5.45	0.581	0.384	0.718		

[a]All these values are in units of MHz. [b]"Angle Diff (°)" stands for the angular differences between the eigenvectors in units of degrees; For β couplings, the eigenvectors are those associated with maximum eigenvalues. [c]The eigenvectors of coupling 13 were considered the same as those of coupling 9.

The above results support that couplings 4, 7, 8, 11, 13 and 5, 6, 9, 10, 12 are from two different radicals: C4 dehydrogenation (DeH7 or DeH8) and C5 dehydrogenation (DeH9). However, it is still necessary to study the possibility of two conformations from same radical. There are several origins to induce this possibility: more than one molecule in the asymmetric unit; cutting the hydrogen atoms bonded to the same carbon or nitrogen atom (such as H9 dehydrogenation and H10 dehydrogenation); same dehydrogenation but trapped in different configurations (or in the different potential wells); different configurations formed during annealing or cooling the crystal, i.e., trapped in different potential wells by absorbing or losing thermal energy. In this case, the first two origins can be ruled out: there is

only one molecule in the asymmetric unit cell of L-lys·HCl·2H_2O single crystal. The calculations described above confirmed H7 or H8 dehydrogenation reproduced one set of couplings and H9 dehydrogenation reproduced another set, thus excluding the possibilities that H7 and H8 dehydrogenation induced the two sets of couplings, neither for H9 and H10 dehydrogenation. The last origin is also ruled out because two sets of couplings were detected at both 66K and 298K, and the couplings at 66K are very close to those at 298K (see Table 6.14 in section of "Experiments at Room Temperature").

In order to determine if the two sets of couplings were from same dehydrogenation radical trapped in different configurations (or with different potential wells), we tried to find if there is an energetically stable structure from H7 or H8 dehydrogenation which can reproduce couplings 5, 6, 9, 10, 12 (different from DeH7-II and DeH8-I). In first method, the intermediate radical structure (5^{th} step) in DeH7-II optimization was found to reproduce couplings 5, 6, 9, 10, 12 as shown in Table.6.11b, then the ONIOM optimization was performed on this intermediate cluster as the initial model cluster to check if there is a similar structure (reproducing couplings 5, 6, 9, 10, 12) that is energetically stable. However, the optimization led to a structure similar to the final structure from DeH7-II, so does its parameters (see Table 6.11c). The energies of the three structures (from DeH7-II, intermediate step, and from reoptimization) are illustrated in Fig. 6.22 and this indicates that the optimized structure from DeH7-II is still the most stable. (No intermediate structure in DeH8-I optimization can reproduce couplings 5, 6, 9, 10, 12.) In the second method, by manually rotating the side chain and bending the α-protons on the optimized structures from DeH7-II and DeH8-I, we make the structures that can reproduce couplings 5, 6, 9, 10, 12, and then we perform the ONIOM optimizations on the structures within the cluster to find the stable structure which can reproduce couplings 5, 6, 9, 10, 12. All these optimizations formed structures similar to those from DeH7-II or DeH8-I and still reproduce couplings 4, 7, 8, 11 and 13 (not shown here); i.e., there is not an energy stable structure from H7 or H8 dehydrogenation that can reproduce couplings 5, 6, 9, 10, 12. Using a similar method on the optimized structure from DeH9-II (results not shown here), no stable structure was found to be able to reproduce couplings 4, 7, 8, 11 and 13. The

above calculation results can tentatively doubt onthe possibility of the same dehydrogenation radical trapped in two different configurations. Thus the hypothesis of two sets of couplings from one radical trapped in different conformations can probably be ruled out.

From the analysis above, the optimized radicals from both DeH7-II and DeH8-I can reproduce couplings 4, 7, 8, 11, 13, and the optimized radical from DeH9-II and bending H9 to –20° can reproduce couplings 5, 6, 9, 10, 12; that is, R2 and R3 were very likely from two different radical forms: dehydrogenation at C4 (DeH7 or DeH8) and at C5 (DeH9), respectively.

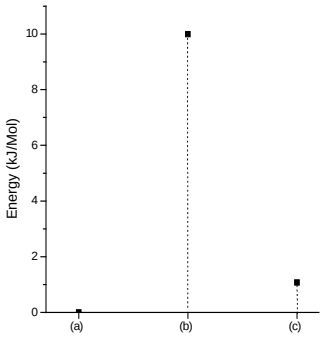

Fig. 6.22 *Energies for the three structures:* ***(a)*** *optimized structure from "DeH7-II";* ***(b)*** *the intermediate structure 9 (in 5th step) in optimization of "DeH7-II";* ***(c)*** *the initially structure optimized from (b).*

R4- radical of side chain deamination

Based on the EIE pattern (B//<a>) shown in Fig. 6.1, ENDOR lines 17 and 18 in Fig. 6.2 were assigned to R4. Although the EIE pattern of line 16 is not very clear, it is about same width as that of R4 in Fig. 6.1. Thus line 16 was tentatively assigned to R4. The coupling tensors of lines 16 and 17 are listed in Table 6.12 and the angular dependence curves are shown in Fig. 6.23. Line 18 was only observed at one orientation (B//<a>) and its tensor could not be calculated. Tensors 16 and 17 both are characteristic of α-couplings; therefore, R4 was assigned to the radical from side chain deamination (Scheme 6.5). This structure has unpaired spin located mainly on C6, thus leading to two α-couplings and two β-couplings.

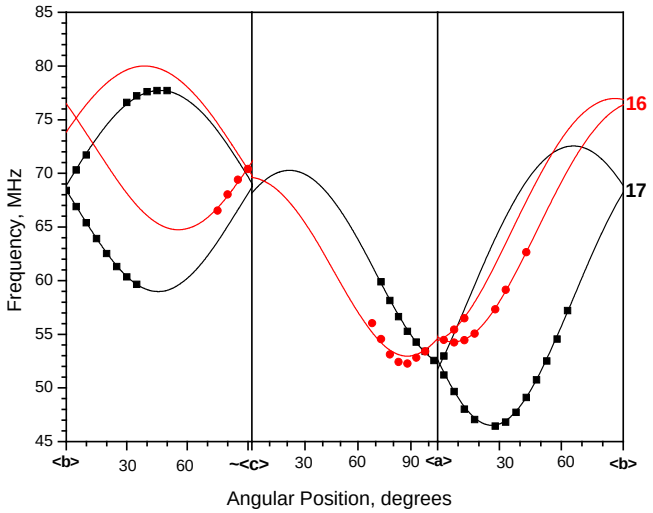

Fig. 6.23 *Angular dependent curves for couplings 16 and 17 of single crystal L-lys•HCl•2H$_2$O irradiated at 298K and detected at 66K.*

Table 6.12 *Hyperfine coupling tensors for radical R4 in single crystal L-lysine HCl 2H$_2$O irradiated at 298K and detected at 66K.*[a,b]

				Eigenvectors[b]		
Tensor	Principal values[a,b]	Isotropic Values[a]	Anisotropic values[a]	<a>	<b>	<c*>
	-86.83(11)		-34.13	0.369(1)	0.713(3)	-0.597(1)
17	-48.71(9)	-52.70	3.99	0.210(1)	0.562(2)	0.800(2)
	-22.56(7)		30.14	0.906(1)	-0.421(1)	0.058(3)
	-96.99(9)		-34.19	0.327(1)	0.736(1)	0.593(1)
16	-60.45(9)	-62.80	2.35	0.448(1)	-0.673(1)	0.589(2)
	-30.95(7)		31.85	0.833(1)	0.073(2)	-0.549(1)

[a]All these values are in units of MHz. [b]Numbers in parentheses are the estimated uncertainties in the last digit quoted as reported by the statistical analysis.

For DFT calculations on this structure the side chain amino group was simply deleted from the dataset, as shown in Fig. 6.24a. Geometry optimizations were performed with two methods as described before: freezing the atoms involved in the intermolecular hydrogen bonds (marked as "f" in Fig. 6.24a) and the PCM model by adding the key word of "scrf=PCM". The two approximations gave very similar optimized geometries and very similar magnetic parameters. As is shown in Fig. 6.24b, the optimized structure has a completely planar radical center. Also, the two β-protons are quite close to the nodal plane of the radical, so the β-couplings are not large, both about 30MHz. Changing the torsion angle of H11-C5-H12-C6 from ~6° into ~-11° by bending the two α-protons brings the calculated parameters into better agreement with the experimental parameters, as listed in Table 6.13. ENDOR line 18 located at 57.81MHz as shown in Fig. 6.2 is consistent with one of the predicted β-couplings. WINSIM simulations can reproduce the central three-peak of the EIE at <a> (see Fig. 6.25) using the three measured couplings 31.9MHz (line 16), 35.0MHz (line 17), 41.5MHz (line18) and the predicted β-coupling value ~35MHz. However, since there is some noise on the both sides of the experimental EIE pattern, the two shoulders of the simulated pattern cannot be easily compared to the experimental one. Therefore, R4 was only tentatively assigned, and more evidence is needed to confirm this identification.

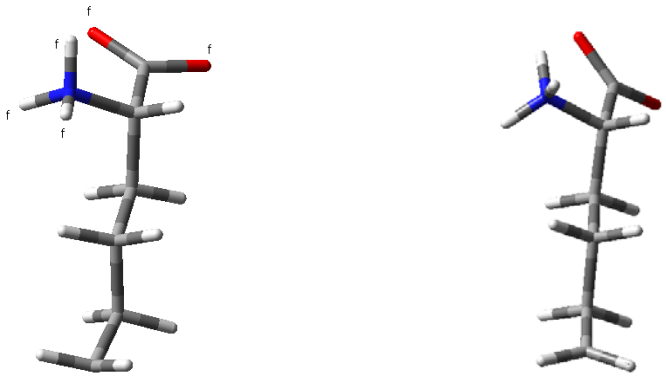

(a) **(b)**

Fig. 6.24(a) *The initial structure of deamination from side chain for energy optimization.* ***(b)*** *PCM optimized structure from deamination of the side chain.*

Table 6.13 *The parameters calculated on the side-chain deamination radical.*[a,b]

Proton	Isotropic Values[a]	Anisotropic values[a]	Eigenvectors <a>	<b>	<c*>	: Coupling Angle Diff (°)[b]
		-38.59	-0.425	-0.401	0.811	22.0
H11	-57.33	-1.1	0.291	0.786	0.542	:17 20.5
		39.69	0.857	-0.466	0.219	9.8
		-38.67	0.589	0.511	0.626	20.0
H12	-57.24	-1.01	0.089	-0.811	0.579	:16 22.1
		39.67	0.803	-0.285	-0.523	20.7
		-5.06	0.826	0.445	-0.346	
H9	28.78	-4.39	-0.242	0.834	0.496	
		9.45	0.510	-0.326	0.796	
		-5.00	0.773	-0.633	0.046	
H10	33.86	-4.49	0.584	0.737	0.340	
		9.49	-0.249	-0.236	0.940	

[a] All these values are in units of MHz. [b] The "Angle diff (°)" is the angular difference between the calculated and the experimental eigenvectors associated with the maximum eigenvalues in units of degrees.

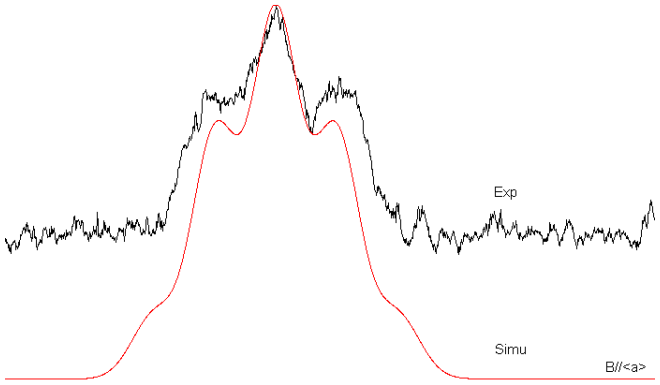

Fig. 6.25 *WINSIM simulation for EIE of R4 at B//<a>.*

R5-dehydrogenation from C3

According to the simulation of the EPR spectra, R5 is minority radical, (~3% concentration as estimated from EPR simulation). Its EIE patterns and ENDOR lines were only observed in the <ac> plane, thus no coupling tensors for R5 could be calculated.

As is shown in Fig. 6.2 (B//<a>), ENDOR lines 19 and 20 located at 91.7MHz and at 92.7MHz are ascribed to R5, and the ENDOR curves of these two couplings in <ac> plane are characteristics of β-couplings. Using the values of couplings 19 and 20 at <a> and estimating values of ~20G for the two unobserved proton couplings at <a>, the EIE patterns can be reproduced very well with WINSIM (see Fig. 6.26a). An EIE simulation with the 3rd coupling being 20G from nitrogen also can reproduce the 7-peak pattern with correct spacing, but the peak-ratio, 1:1:2:1:2:1:1, does not match that from experimental 1:1:2:2:2:1:1 (see Fig. 6.26b). Therefore, R5 is unlikely to exhibit nitrogen coupling, but the observed data are consistent with a radical having at least four proton couplings. Possible structures are dehydrogenation at C2 (four β-couplings, see scheme 6.6a); dehydrogenation at C3 (one α-coupling and three β-couplings, see scheme 6.6b); dehydrogenation at C4 or C5 (a different configuration of R2 or R3). From ENDOR and EIE measurements at <c>, an additional coupling denoted as 21 was tentatively assigned to R5 based on the EIE width. The WINSIM simulation of the EIE pattern at <c> is shown in Fig. 6.26c. The simulation used computed coupling values of 46.0G, 37.27G, 26.0G and 17.0G, which are comparable with the experimental values of couplings 19 (38.3G), 20 (44.1G), 21 (21.0G), and the estimated 4th (~20G) at <c>. Fitting the ENDOR data for line 21 in the <ac> plane indicates that the coupling value at <a> is also close to 20G (see Fig. 6.27). Moreover, coupling 21 shows characteristics of an α-coupling, and its available ENDOR data indicate a quite different angular dependent behavior from those of R2 and R3 in <ac> plane. Therefore the possible assignment of R5 to dehydrogenation from C2 (no α-coupling) or to the different conformation of R2 or R3 can be rejected, with the result that radical R5 best fits that from dehydrogenation of C3. In that structure, the unpaired spin, mainly located at C3, will interact with one α-proton (H5 or H6) and three β-protons (H4, H7 and H8).

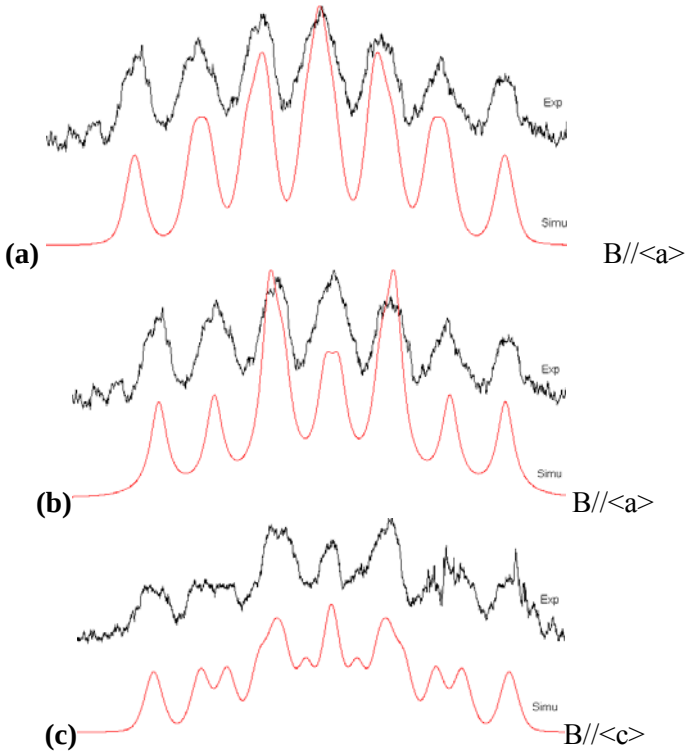

Fig. 6.26 *WINSIM simulation for EIE pattern of R5 at <a>:* ***(a)*** *with four proton couplings (spin = 0.5);* ***(b)*** *with two proton couplings (spin = 0.5) and one nitrogen coupling (spin = 1.0);* ***(c)*** *WINSIM simulation for EIE pattern of R5 at <c>.*

Computational models created by freezing the hydrogen bond-related atoms and deleting either H5 or H6 were optimized separately. As for R2 and R3, the two optimized geometries from H5 dehydrogenation or H6 dehydrogenation are quite similar, as are the magnetic parameters calculated from each. Thus, the following results describe only those with H5 deleted.

By comparison to the computed isotropic values listed in Table 6.12, couplings 19 and 20 can be assigned to β-protons H7 and H4, respectively. The 4th coupling used in the WIMSIM simulation can be attributed to a β-coupling from H8. The computed tensors for H5, H6 and H7 were used to simulate the ENDOR curves in the <ac> plane. As shown in Fig. 6.28a-c, the simulated curves exhibit angular dependent behavior similar to those detected for couplings 19-21 but with absolute frequency differences of 6MHz or less.

The above results support the identification of R5, however, confirmation of it will require additional data.

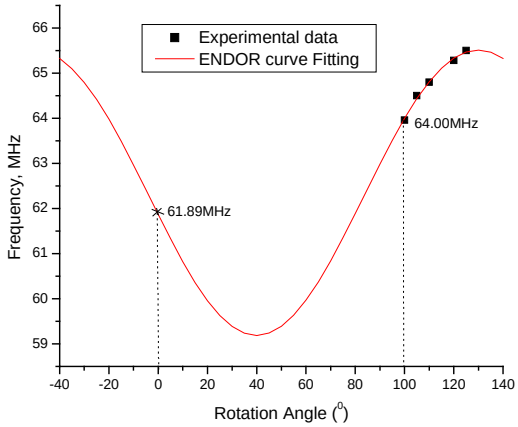

Fig. 6.27 *ENDOR curve fitting with "ORIGIN" program for coupling 21 of R4 in the <ac> plane.*

Table 6.14 *Comparison of the coupling values from WINSIM simulation of EIE pattern of R4 at <a> and the coupling values from DFT calculations on the structure of dehydrogenation of H5.* [a]

WINSIM Simulation (B//<a>)		**DeH5:**	
ENDOR line	Couplings (MHz)	Proton	Couplings (MHz)
19	111.40	H7	105.69
20	113.82	H4	122.36
21	56.00	H6[a]	56.40[a]
4th coupling	56.00	H8	40.96

[a]H6 is an α-proton with an isotropic value of –53.73MHz; 56.40MHz is the coupling value at <a> from the tensor simulation.

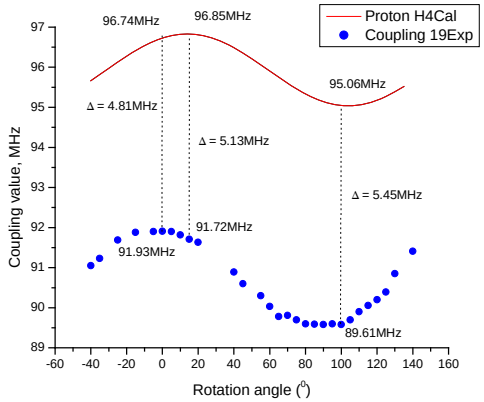

(a)

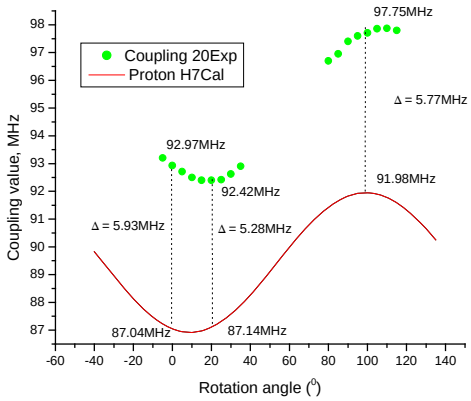

(b)

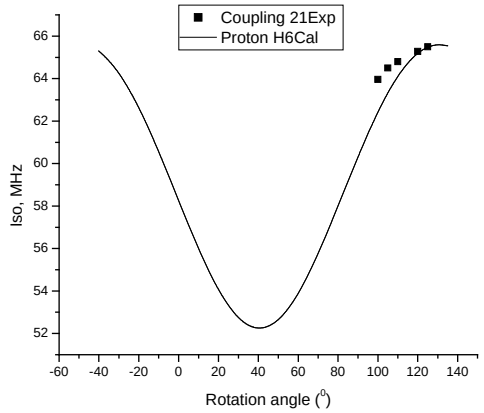

(c)

Fig. 6.28 *Comparison the ENDOR curves from experiment and from DFT calculations on the model of dehydrogenation of H5 in the <ac> plane.* ***(a)*** *ENDOR data of coupling 19 and simulated curve of H4;* ***(b)*** *ENDOR data of coupling 20 and simulated curve of H7;* ***(c)*** *ENDOR data of coupling 21 and the simulated curve of H6.*

EPR simulation

Because ENDOR from all five radicals R1-R5 was detected at <a>, this orientation was chosen for simulation of the EPR spectrum to estimate the relative yields of these five radicals. With WIMSIM, the EPR was well reproduced with the five radicals, in the ratios R1: R2: R3: R1': R4: R5 of about 50: 14: 16: 11: 6: 3, as is indicated in Fig. 6.29. All the couplings used are comparable with the corresponding experimental values or with the values expected from the analysis described above.

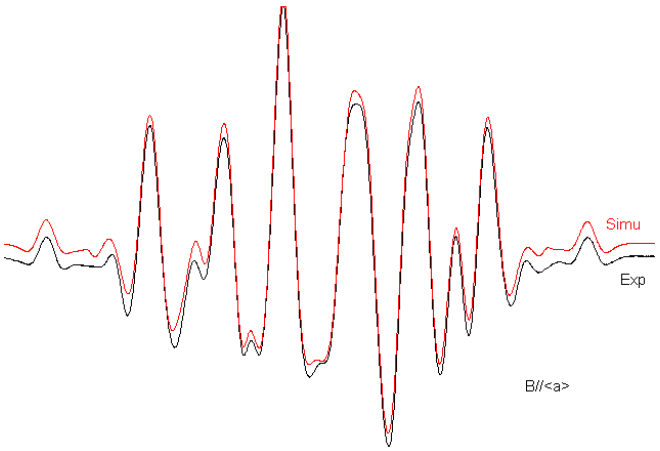

Fig. 6.29 *WINSIM simulation for EPR spectrum at <a> in L-lysHCl2H2O single crystal irradiated at 298K and detected at 66K.*

6.3.2 Experiments at 298K

Fig. 6.30 shows EPR spectra from the crystal irradiated at room temperature and measured (a) at room temperature and (b) cooled to 66K both with the magnetic fields along <b>, where the EPR spectra are mostly expended. The two EPRs are different and the change is reversible. These characteristics were also reported in the work of Fujimoto.M et al.[1]

Fig. 6.31 shows the EPR spectrum and three distinct EIE patterns from radicals RI-RIII from the crystal irradiated and measured at room temperature with the magnetic field ~30° from <a> and ~50° from <c>, where the EIE of RII and RIII are distinguishable. RI is the major radical and gives the main pattern of the EPR, while RII and RIII extend over the full length of the EPR and give the outermost

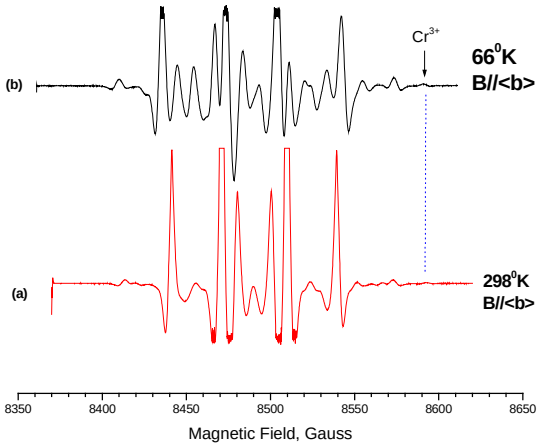

Fig. 6.30 *Second-derivative EPR spectrum for single crystal L-Lys · HCl · $2H_2O$ irradiated and measured at room temperature* ***(a)*** *and at a temperature lowered from room temperature to 66K* ***(b)*** *with the magnetic field along <b>.*

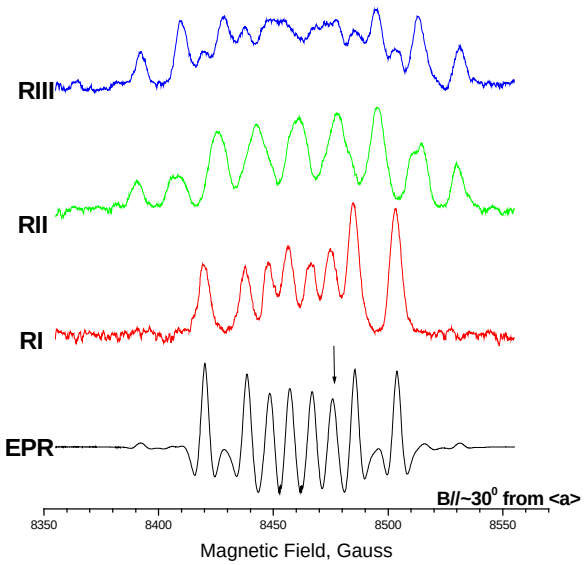

Fig. 6.31 *Second-derivative EPR spectrum, and EIE patterns from RI, RII and RIII in L-Lys·HCl·$2H_2O$ single crystal irradiated and measured at room temperature with magnetic field along ~30° from <a> and ~50° from <c>.*

peaks at both sides. Fig. 6.32 shows the corresponding ENDOR spectrum with the field locked to one of the center peaks of the EPR as indicated to by an arrow in Fig. 6.31, and the ENDOR lines were grouped

based on the EIE in Fig. 6.31. The coupling tensors, listed in Table 6.13, were attained from the angular dependence data for RI-RIII shown in Fig. 6.33a-c, respectively.

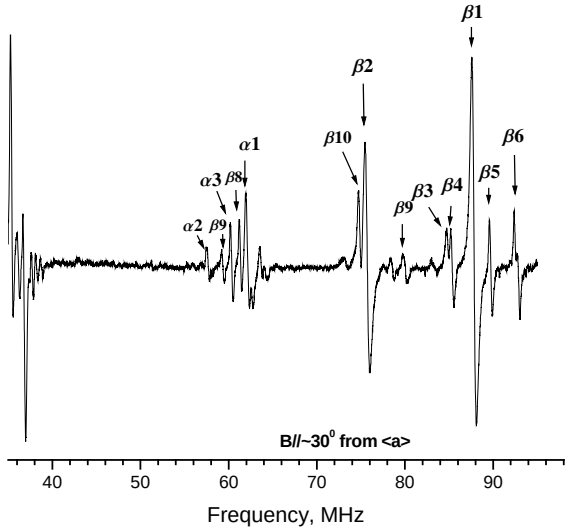

Fig. 6.32 *First-derivative ENDOR spectrum for L-Lys·HCl·2H_2O single crystal irradiated and measured at room temperature with the field locked to the EPR peak as indicated by an arrow in Fig. 6.31. The magnetic field is along ~30° from <a> and ~50° from <c>.*

Table 6.15 *Hyperfine coupling tensors for radicals RI-RIII from single crystal of L-Lys·HCl·2H_2O irradiated and measured at room temperature.* [a,b]

	Principal values[a,b]	Isotropic values[a]	Anisotropic values[a]	Eigenvectors[b] <a>	<b>	<c*>
RI						
	-84.03(12)		-32.42	0.041(2)	-0.955(1)	0.294(1)
α1	-49.64(5)	-51.61	1.97	0.861(0)	0.183(1)	0.474(1)
	-21.17(8)		30.44	0.507(1)	-0.234(1)	-0.830(1)
	110.89(2)		5.53	0.063(2)	-0.841(9)	0.537(6)
β1	103.74(2)	105.36	-1.62	0.514(0)	0.488(2)	0.705(6)
	101.44(4)		-3.92	0.856(5)	-0.232(5)	-0.463(8)
	86.53(2)		5.19	0.594(1)	0.714(3)	-0.370(4)
β2	80.26(2)	81.34	-1.08	0.741(1)	-0.307(2)	0.598(2)
	77.24(2)		-4.10	0.313(2)	-0.629(4)	-0.711(3)

	Principal values[a]	Isotropic Values[a]	Anisotropic values[a]	Eigenvectors <a>	<b>	<c*>
RII						
	-93.00(4)		-35.67	0.004(1)	0.853(0)	-0.522(1)
α2	-51.96(4)	-57.33	5.37	0.958(0)	-0.154(1)	-0.243(0)
	-27.02(4)		30.31	0.288(0)	0.499(1)	0.817(0)
	108.06(13)		8.70	0.169(5)	0.182(17)	-0.969(3)
β3	95.99(3)	99.36	-3.37	0.140(1)	-0.977(2)	-0.159(17)
	94.03(16)		-5.33	0.976(1)	0.108(4)	0.191(6)
	119.38(2)		7.66	0.197(1)	0.946(14)	-0.257(1)
β5	108.34(2)	111.72	-3.38	0.034(0)	0.256(3)	0.966(4)
	107.43(2)		-4.29	0.980(1)	-0.199(0)	0.018(13)
	91.39(2)		8.88	0.400(1)	-0.139(2)	0.906(1)
β9	80.76(3)	82.51	-1.75	0.576(2)	0.807(1)	-0.130(2)
	75.39(4)		-7.12	0.713(1)	-0.574(2)	-0.403(2)
	64.41(2)		8.04	0.122(2)	-0.926(4)	0.360(3)
β7	53.77(3)	56.37	-2.60	0.655(0)	-0.197(2)	-0.729(2)
	50.93(3)		-5.44	0.746(1)	0.325(3)	0.582(4)
RIII						
	-96.90(4)		-37.82	0.080(0)	0.833(0)	-0.548(1)
α3	-49.47(3)	-59.08	9.61	0.993(0)	-0.113(1)	-0.027(0)
	-30.86(4)		28.22	0.085(0)	0.542(1)	0.836(0)
	104.15(2)		7.96	0.189(1)	-0.299(10)	0.935(11)
β4	92.54(2)	96.19	-3.65	0.727(1)	0.684(10)	0.072(10)
	91.89(2)		-4.30	0.661(0)	-0.666(5)	-0.347(1)
	121.66(2)		7.67	0.470(1)	0.861(11)	0.193(9)
β6	110.45(2)	113.99	-3.54	0.592(1)	-0.470(4)	0.655(9)
	109.85(2)		-4.14	0.655(2)	-0.194(13)	-0.731(11)
	90.00(2)		8.15	0.431(1)	0.202(1)	-0.880(19)
β10	78.04(2)	81.85	-3.81	0.901(1)	-0.035(21)	0.433(1)
	77.50(2)		-4.35	0.057(0)	-0.979(4)	-0.197(9)
	63.87(2)		7.00	0.402(2)	0.899(4)	-0.176(3)
β8	54.42(2)	56.87	-2.45	0.657(1)	-0.149(1)	0.739(2)
	52.31(2)		-4.56	0.638(2)	-0.413(4)	-0.651(4)

[a]All these values are in units of MHz. [b]Numbers in parentheses are the estimated uncertainties in the last digit quoted as reported by the statistical analysis.

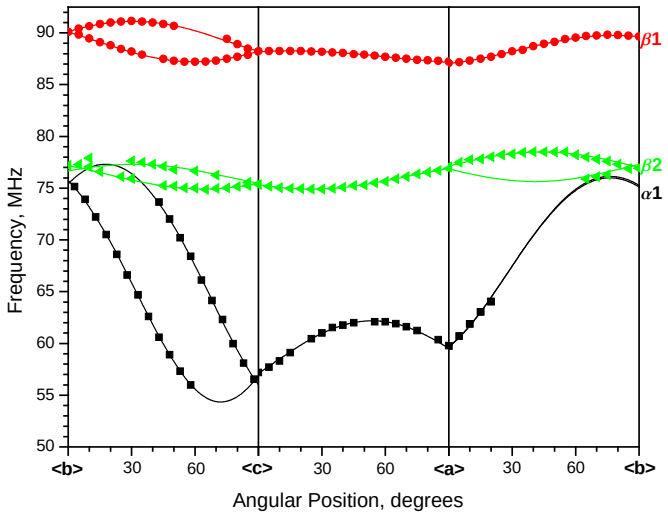

Fig. 6.33(a) *Angular dependence curves for couplings from RI.*

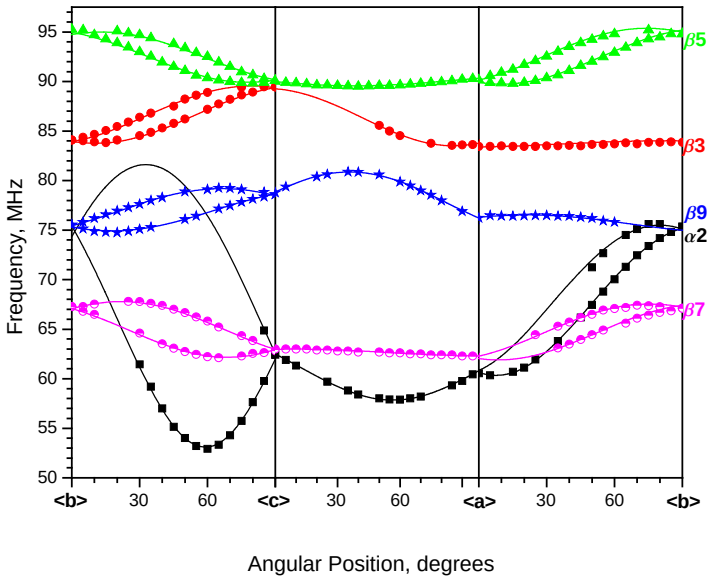

Fig. 6.33(b) *Angular dependence curves for couplings from RII.*

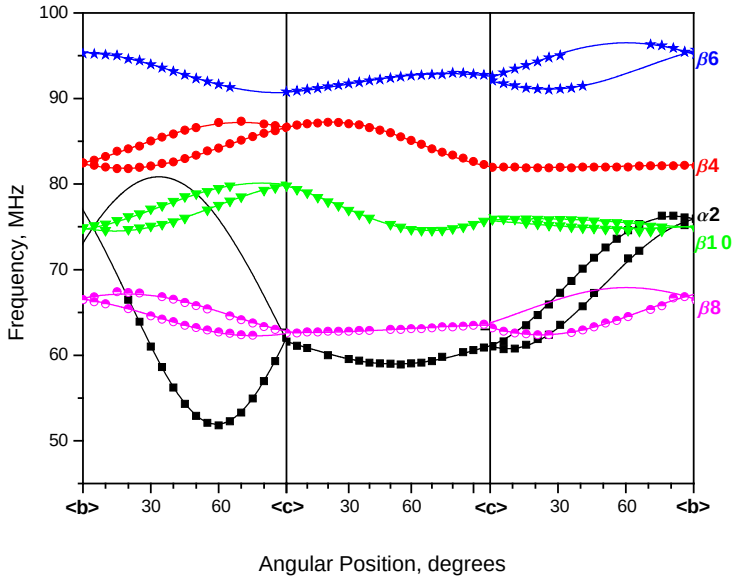

Fig. 6.33(c) *Angular dependence curves for couplings from RIII.*

With coupling tensors of α1, β1 and β2, the EIE pattern of RI (in Fig. 6.31b) can be reproduced as shown in Fig. 6.34. From comparison of the EIE and the EPR at 298K and at 66K, RI (at room temperature) and R1 (at 66K) are major radicals and give the main patterns of the EPR in each case. From the tensor comparisons between RI and R1 as listed in Table 6.14, α1 (RI) is similar to 1(R1): the difference in the isotropic values is only 5.48MHz, and the angular differences are within 17° between the principal vectors. For the β-coupling tensors, the maximum dipolar vector of β1 (RI) is close to that of 2 (R1) with differences of only 7.8°, while the maximum dipolar vector of β2 (RI) is close to that of 3 (R1) with difference of 13.4°. However, the coupling values from R1 and RI are different: isotropic values of 2 and 3 are almost equal to ~100MHz, while those of β2 and β3 are unequal with a_{iso}(β2)=105.36MHz and a_{iso}(β3)=81.34MHz. It is the β-coupling difference between R1 and RI that lead to the different main patterns of the EPR at 298K and 66K as shown in Fig. 6.30. From the analysis above and the annealing experiments[1], RI can be assigned as the same radical of R1 (main chain deamination) with different β-couplings from R1.

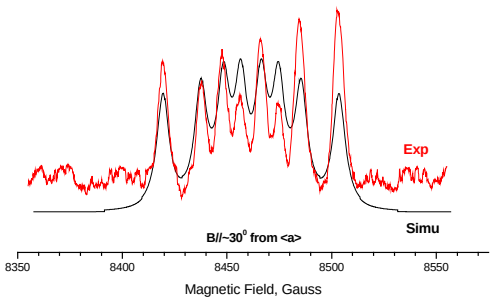

Fig. 6.34 *Simulation of EIE spectrum of RI at ~30° from <a> and ~50° from <c> with coupling tensors of α1, β1 and β2.*

Table 6.16 *Tensors comparison between RI and R1.*[a,b]

RI Coupling	Isotropic value[a]	Anisotropic value[a]	Eigenvectors <a>	<b>	<c*>	**R1** Coupling	Angle Diff (°)[b]
		-32.42	0.041	-0.955	0.294		11.8
α1	-51.61	1.97	0.861	0.183	0.474	: 1	19.2
		30.44	0.507	-0.234	-0.830		15.5
β1	105.36	5.53	0.063	-0.841	0.537	: 3	13.4
β2	81.34	5.19	0.594	0.714	-0.370	: 2	7.9

[a] All these values are in units of MHz. [b] "Angle diff (°)" is the angular difference between the eigenvectors in units of degrees. For β-couplings, the eigenvectors are those associated with the maximum eigenvalues.

The configuration for the β-protons of R1 has been studied and is shown in Fig. 6.7b. Using the same method, the β-protons configuration for RI can be calculated: θ (β2) = 36.2° from $\cos^2\theta$ (β2) = 81.34/125 and θ (β3) =23.3° from $\cos^2\theta$ (β2) = 105.36/125. Based on these results, the configuration for the β-protons is illustrated in Fig. 6.35. Compared to the configuration of R1, the two β-protons of RI were rotated ~7° around the C2-C3 axis. This small rotation angle should not induce the large difference between the maximum dipolar vector of the corresponding β-couplings, and this conclusion is in

agreement with comparison results as described above: the maximum dipolar vector of coupling 2 is close to that of β1, as well as for coupling 3 and β2.

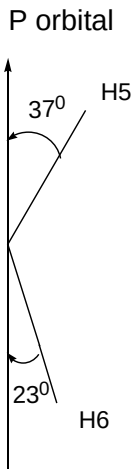

Fig. 6.35 *Schematic representation for the configuration of β-protons H5 and H6 at room temperature. The line with arrow stands for the p orbital of the unpaired spin, and the C2-C3 axis is perpendicular to the page.*

Furthermore, we noticed that the maximum anisotropic values of the β-couplings 2 and 3 are larger than that of β1 and β2 by ~2.5MHz as shown in Tables 6.1 and 6.16. Because this value depends on C2…H_β separation, it can be deduced that the β protons in RI are a little more close to C2 than those in R1 as a result of the temperature change.

The assignment of the couplings for RII and RIII are based on the EIE patterns shown in Fig. 6.31. At the same orientation in Fig. 6.31, the EIEs of RII and RIII were reproduced as shown in Fig. 6.36a and 6.36b, respectively, with the tensors of α2, β3, β5, β7, and β9 for RII, and with the tensors of α3, β4, β6, β8 and β10 for RIII. At 66K, the EIE for R2 and R3 were virtually the same making it difficult to assign the ENDOR tensors. The tensors from RII and RIII (at room temperature) that are closest to those from R2 and R3 (at 66K) are listed in Table 6.17. The comparisons show all the coupling tensors from RII and RIII are very similar to the corresponding tensors from R2 and R3: the angular differences between the eigenvectors[I] are less than 8°, and the differences of couplings are within 8MHz, except for β6 and 6 (difference: 10.4MHz), β7 and 11 (difference: 11.4MHz), β4 and 12 (difference: 12.5MHz). Although

tensor 13 was not detected, it could be similar to the remaining coupling β3, since the coupling value ~100MHz estimated for 13 is similar to 99.36MHz for β3. Using the tensor comparisons, the couplings from R2 and R3 can be grouped as 4, 7, 8, 11, 13 and 5, 6, 9, 10, 12, respectively. From the results above, RII can be assigned to the same radical as R2 (dehydrogenation at C4), and RIII is the same as R3 (dehydrogenation at C5). The assignments of R2 and R3 are described in section of "R2 and R3" in "Experiments at 66K".

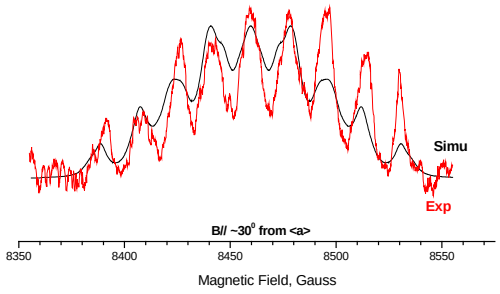

(a)

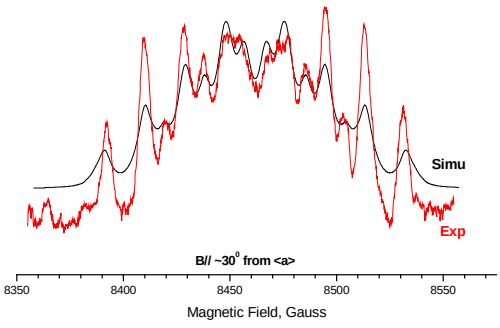

(b)

Fig. 6.36 *Simulation of EIE spectrum of* ***(a)*** *RII with tensors α2, β3, β5, β7, β9 and of* ***(b)*** *RIII with tensors of α3, β4, β6, β8, β10. For the EIE in* ***(a)*** *and* ***(b)****, the magnetic fields were aligned ~30° from <a> and ~50° from <c>.*

Table 6.17 *Tensor comparisons between RII and R2, RIII and R3.*[a,b,c]

RII Coupling	Isotropic value[a]	Anisotropic value[a]	Eigenvectors <a>	<b>	<c*>	**R2** Coupling	Angle Diff (°)[b]
		-35.67	0.004	0.853	-0.522		1.8
α2	-57.33	5.37	0.958	-0.154	-0.243	: 4	6.2
		30.31	0.288	0.499	0.817		6.3
β3	99.36	8.7	0.169	0.182	-0.969	: 13	(N/A)[c]
β5	111.72	7.66	0.197	0.946	-0.257	: 7	4.2
β7	56.37	8.04	0.122	-0.926	0.360	: 11	7.8
β9	82.51	8.88	0.400	-0.139	0.906	: 8	7.4

RIII Coupling	Isotropic value[a]	Anisotropic value[a]	Eigenvectors <a>	<b>	<c*>	**R3** Coupling	Angle Diff (°)[b]
		-37.82	0.080	0.833	-0.548		9.1
α3	-59.08	9.61	0.993	-0.113	-0.027	: 5	8.5
		28.22	0.085	0.542	0.836		3.6
β4	96.19	7.96	0.189	-0.299	0.935	: 12	2.6
β6	113.99	7.67	0.470	0.861	0.193	: 6	3.8
β8	56.87	7.00	0.402	0.899	-0.176	: 10	5.2
β10	81.85	8.15	0.431	0.202	-0.880	: 9	5.3

[a]All these values are in units of MHz. [b] "Angle diff (°)" is the angular difference between the eigenvectors in units of degrees. For β-couplings, the eigenvectors are those associated with the maximum eigenvalues. [c] The tensor of coupling 13 could not be obtained from the experiments, so it is not possible to compared the coupling 13 vector to that of β3.

6.4 Discussion

The reversibility of the EPR and ENDOR spectra at 298K and 66K after the crystal was irradiated at 298K suggests that the radicals formed in room temperature irradiation are chemically stable radicals. From above analysis, the major stable radicals were identified as the main chain deamination radical and the radicals from dehydrogenation at C4 and at C5, respectively. Combining the results from irradiation at

low temperature (66K), the annealing experiments before[1], and the review of the previous studies of radiation of amino acids[23, 24], the route of the free radicals formation can be analyzed as follows.

For the reduction process, the carboxyl anion was identified in the crystal irradiated at 66K and annealing experiments[1] indicated that the main chain deamination radical is the secondary radical of the anion. Thus, the reduction reaction route was considered as that shown in Fig. 6.34.

For the oxidation process, in the crystal irradiated at 66K, the decarboxylation radical was identified, while no dehydrogenation radical was detected. From previous studies on the oxidation process in irradiated amino acids[23], the dehydrogenation radicals are most probably formed from the decarboxylation radical following the oxidation reaction route as shown in Fig. 6.35.

In addition, since main chain amino groups of amino acids form the peptide bond in proteins, the secondary reduction reaction (main chain deamination) will induce the dissociation of the peptide linkage, which was already indicated in some peptides[24]. Accordingly, we can predict that the main chain deaminations of lysine in chromatin would dissociate the histone linkage. Furthermore, based on the studies of amino acid-bases interactions in 129 protein-DNA complexes, the main chain amino nitrogen atoms are acceptors of hydrogen bonds to DNA bases (especially to cytosine). Thus, we could also predict that the main chain deamination radicals formed in lysine of histone in vivo would weaken the association of histone from the DNA following the ionizing irradiation, a reaction which was reported by Lloyd and Peacocke in 1965[25].

The side chain amino group of lysine, as the important donor of hydrogen bonds to DNA basis, will promote the association of the DNA-histone. However, the side chain deamination radical was only partially identified; and from EPR simulations, the concentration of this radical (R4) is only 6%. The side chain deamination in lysine might be not one of the main reasons for the dissociation of DNA-histone following irradiation.

However, these predictions are from the preliminary results on irradiated lysine hydrochloride only, and more investigations on the irradiation damage in DNA in vivo are needed.

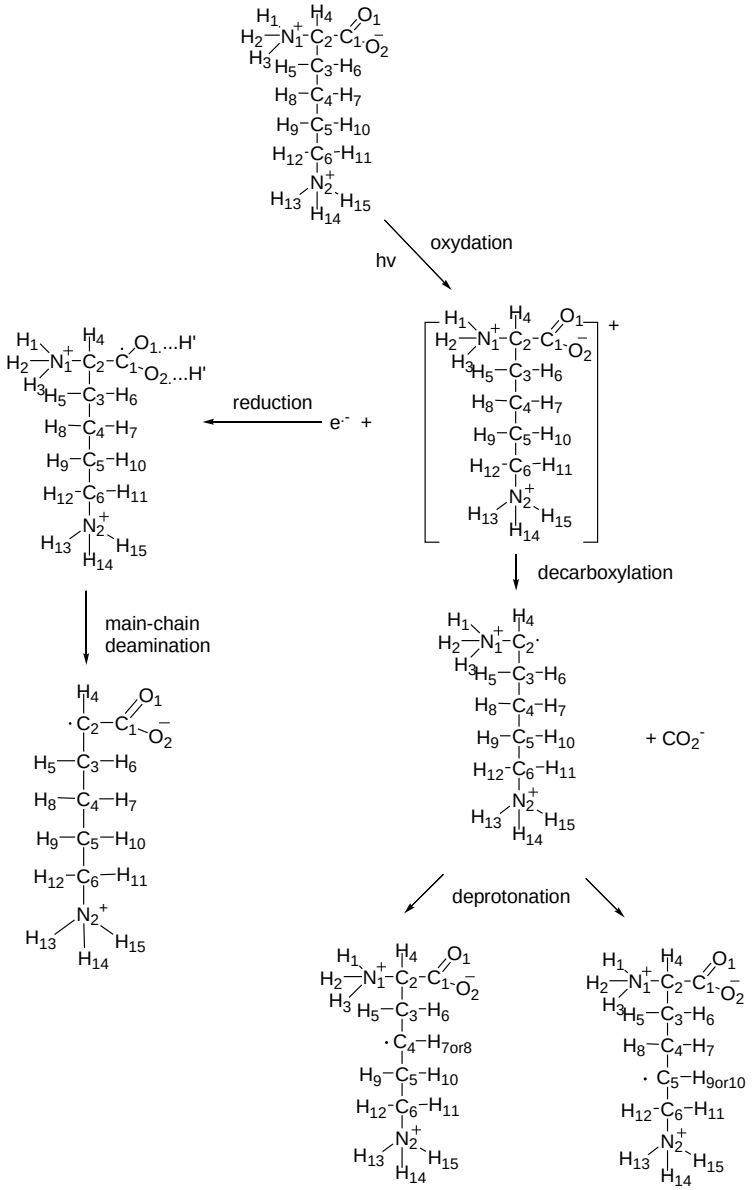

Fig. 6.37 *Proposed reduction and oxidation effects in irradiated L-lysine·HCl.*

References

1. M. Fujimoto, W. A. Seddon and D. R. Smith, Electron Spin Resonance Studies of Free Radicals in γ-Irradiated Amino Acid Crystals: α-Amino Isobutyric Acid and L-Lysine·HCl·2H_2O. *J. Chem. Phys.* **48,** 3345-3350 (1968).

2. M. J. Frisch, G. W. Trucks, H. B. Schlegel, et al., **Gaussian 03,** (Gaussian Inc., Wallingford CT, 2004)

3. T. F. Koetzle, M. S. Lehmann, J. J. Verbist, et al., Precision neutron diffraction structure determination of protein and nucleic acid components VII. The crystal and molecular structure of

the amino acid L-lysine monohydrochloride dihydrate. *Acta crystallographica. Section B* **28,** 3207-3214 (1972).

4. B. Mennucci and J. Tomasi, Continuum solvation models: A new approach to the problem of solute's charge distribution and cavity boundaries. *J. Chem. Phys.* **106,** 5151-5158 (1997).

5. B. Mennucci, E. Cancès and J. Tomasi, Evaluation of Solvent Effects in Isotropic and Anisotropic Dielectrics and in Ionic Solutions with a Unified Integral Equation Method: Theoretical Bases, Computational Implementation, and Numerical Applications. *The journal of physical chemistry. B* **101,** 10506-10517 (1997).

6. R. Cammi, B. Mennucci and J. Tomasi, Fast Evaluation of Geometries and Properties of Excited Molecules in Solution: A Tamm-Dancoff Model with Application to 4-Dimethylaminobenzonitrile. *The journal of physical chemistry. A* **104,** 5631-5637 (2000).

7. M. Svensson, S. Humbel, R. D. J. Froese, et al., ONIOM: A Multilayered Integrated MO + MM Method for Geometry Optimizations and Single Point Energy Predictions. A Test for Diels-Alder Reactions and $Pt(P(t\text{-}Bu)_3)_2 + H_2$ Oxidative Addition. *The Journal of Physical Chemistry* **100,** 19357-19363 (1996).

8. S. Humbel, S. Sieber and K. Morokuma, The IMOMO method: Integration of different levels of molecular orbital approximations for geometry optimization of large systems: Test for n-butane conformation and S_N2 reaction: $RCl+Cl^-$. *J. Chem. Phys.* **105,** 1959-1967 (1996).

9. T. Vreven, K. S. Byun, I. Komaromi, et al., Combining Quantum Mechanics Methods with Molecular Mechanics Methods in ONIOM. *Journal of Chemical Theory and Computation* **2,** 815-826 (2006).

10. H. P. Hratchian, P. V. Parandekar, K. Raghavachari, et al., QM:QM electronic embedding using Mulliken atomic charges: Energies and analytic gradients in an ONIOM framework. *J. Chem. Phys.* **128,** 034107-034111 (2008).

11. R. Declerck, E. Pauwels, V. V. Speybroeck, et al., First-principles calculations of hyperfine parameters with the Gaussian and augmented-plane-wave method: Application to radicals embedded in a crystalline environment. *Physical Review B (Condensed Matter and Materials Physics)* **74,** 245103 (2006).

12. H. M. McConnell, Indirect Hyperfine Interactions in the Paramagnetic Resonance Spectra of Aromatic Free Radicals. *J. Chem. Phys.* **24,** 764-766 (1956).

13. H. M. McConnell and D. B. Chesnut, Theory of isotropic hyperfine interactions in π-electron radicals. *J. Chem. Phys.* **28,** 107-117 (1958).

14. R. W. Fessenden and R. H. Schuler, Electron Spin Resonance Studies of Transient Alkyl Radicals. *J. Chem. Phys.* **39,** 2147-2195 (1963).

15. W. Gordy, *Theory and Application of Electron Spin Resonance*. Johe Wiley & Sons, Inc, New York, NY, (1980).

16. W. A. Bernhard, The use of alpha hyperfine coupling tensors as a measure of unpaired spin density and free radical geometry. *J. Chem. Phys.* **81,** 5928-5936 (1984).

17. P. A. Erling and W. H. Nelson, Dependence of α-Proton Hyperfine Couplings on Free Radical Geometry. *The Journal of Physical Chemistry A* **108,** 7591-7595 (2004).

18. C. Heller and H. M. McConnell, Radiation Damage in Organic Crystals. II. Electron Spin Resonance of $(CO_2H)CH_2CH(CO_2H)$ in β-Succinic Acid. *J. Chem. Phys.* **32,** 1535-1539 (1960).

19. J. R. Morton, Electron Spin Resonance Spectra of Oriented Radicals. *Chemical Reviews* **64,** 453-471 (1964).

20. K. T. Øhman, A. Sanderud, E. O. Hole, et al., Single Crystals of L-*O*-Serine Phosphate X-Irradiated at Low Temperatures: EPR, ENDOR, EIE, and DFT Studies. *The journal of physical chemistry. A* **110,** 9585-9596 (2006).

21. S.-i. Kuroda and I. Miyagawa, ENDOR study of an irradiated crystal of L-alanine: Environment of the stable $CH_3CHCO_2^-$ radical. *J. Chem. Phys.* **76,** 3933-3944 (1982).

22. J. B. Foresman and A. Frisch, *Exploring Chemistry with Electronic Structure Methods*. Gaussian, Inc., Pittsburgh, PA, (1993).

23. E. Sagstuen, A. Sanderud and E. O. Hole, The Solid-State Radiation Chemistry of Simple Amino Acids, Revisited. *Radiation Research* **162,** 112-119 (2004).

24. H. C. Box, *Radiation effects-ESR and ENDOR analysis*. Academic Press, Inc., New York, NY, (1977).

25. P. H. Lloyd and A. R. Peacocke, The Action of γ -rays on Deoxyribonucleohistone in Solution. *Proceedings of the Royal Society of London. B* **164,** 40-62 (1966).

CHAPTER 7.

L-ARGININE · HCl · H_2O SINGLE CRYSTALS IRRADIATED AT 66K

Abstract:

With K-band EPR (Electron Paramagnetic Resonance), ENDOR (Electron-Nuclear DOuble Resonance) and EIE (ENDOR-induced EPR) techniques, at least five radicals were detected in single crystals of L-arginine hydrochloride monohydrate X-irradiated at 66K. Radicals R1a and R1b were identified as the two different geometry conformations of the carboxyl anion radical, $(H_2OO\dot{C})CH(NH_3)^+(CH_2)_3NHC(NH_2)_2^+$. The main geometry difference in R1a and R1b is that the β-proton in R1b is much closer to the nodal plane of the radical than that in R1a, and this makes the C-H β-coupling in R1b smaller than that of R1a by ~40MHz. The two geometrically distinct molecules of the asymmetric unit in the crystal are believed to be the origins of R1a and R1b, because the main-chain proton in one molecule is much closer to the carboxyl plane (giving R1b), than in the other molecule (giving R1a). DFT (Density-Functional Theory) calculations on cluster models constructed separately for each molecule of the asymmetric unit support the assignments. These also indicated that the additional exchangeable dipolar couplings in R1a and R1b were from the protons involved in intermolecular hydrogen-bonds to the carboxyl group. Radical R2 was identified as the decarboxylation radical, $\dot{C}H(NH_3)^+(CH_2)_3NHC(NH_2)_2^+$. Experimental results and DFT calculations indicated that the radical center of R2 is not in a completely sp^2 configuration and the β-protons experienced a small reorientation. Radical R3, with two proton couplings and one nitrogen coupling (estimated from the WINSIM simulations), was identified as the anion radical with an electron localized on the guanidyl group, $^-(OOC)CH(NH_3)^+(CH_2)_3NH\dot{C}(NH_2)_2^+$. DFT calculations on the cluster models reproduced the experimental values very well and thus supported the assignments. The geometry optimization indicated that the guanidyl group transformed from a planar to a pyramidal structure after the electron was trapped. Radical R4 exhibited one α- and three β-couplings, and one of the β-couplings was exchangeable. Thus R4 was assigned as a side chain

dehydrogenation radical, $^{-}(OOC)CH(NH_3)^{+}(CH_2)_2\dot{C}HNHC(NH_2)_2^{+}$. Although it was not possible to obtain sufficient data to calculate the β-coupling tensors, the similarity of the α-tensor in R4 and that in the same dehydrogenation radical detected at room temperature supported the assignment. Radical R5, with one nonexchangeable β-coupling, could not be identified.

7.1 Introduction

In the general case, arginine (see Scheme 7.1) is the amino acid most often in contact, usually through hydrogen bonds to guanine, and backbone (phosphate).[1] In the nucleosome core, arginine side chains from histone penetrate the minor grooves at every turn of the DNA double helix. Also, arginine side chains participate in frequent hydrogen bonds to DNA phosphate oxygen atoms and pyrimidine O2 atoms.[2] Thus in order to predict the DNA damage from ionizing radiation within the chromatin structure, it is important to characterize the radiation chemistry of arginine independently and in association with DNA constituents.

However, there are few previous studies on irradiated arginine. Joshi and Johnsen examined the kinetics of radical decay in crystalline amino acids and proposed that the radical dehydrogenated from C5 (see Scheme 7.2) was the stable radical in single crystal of L-arginine·HCl·H_2O X-irradiated at room temperature, but it was not definitely characterized.[3, 4] M. Aydin, et al. detected the same dehydrogenation radical using EPR techniques in L-arginine powder γ-irradiated at room temperature.[5] In addition, Hård Olsen used X-band EPR, ENDOR techniques, and DFT calculations to study L-arginine phosphate single crystals X-irradiated at 295K and 77K.[6] In his work, the carboxyl radical anion (see scheme 7.3), the decarboxylation radical (see scheme 7.4) and the side-chain dehydrogenation radical (see scheme 7.2) were identified in the crystals X-irradiated at 77K, and the carboxyl anion radical and the decarboxylation radical were proposed to be the precursors of the main-chain deamination radical (see scheme 7.5) and the side-chain dehydrogenation radicals (see scheme 7.2), respectively, which were the stable radicals detected in crystals irradiated at 295K.

This work focuses on K-band EPR, ENDOR and DFT studies of the L-arginine·HCl·H_2O single crystals X-irradiated at 66K and at 298K. This chapter describes the free radicals detected in the crystal irradiated at 66K. In addition to the carboxyl radical anion (see scheme 7.3), the decarboxylation radical (see scheme 7.4) and the side-chain dehydrogenation radical, the guanidyl anion radical (see scheme 7.6) also was identified. Hyperfine tensors from DFT geometry optimized structures compared well with experiment, indicating that the computations reproduced the radical structures.

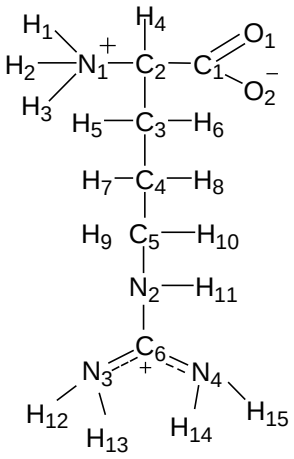

Scheme 7.1 *Arginine molecule in L-arginine HCl H2O single crystal*

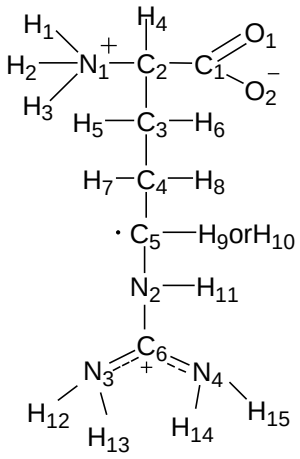

Scheme 7.2 *The radical from dehydrogenation at C5*

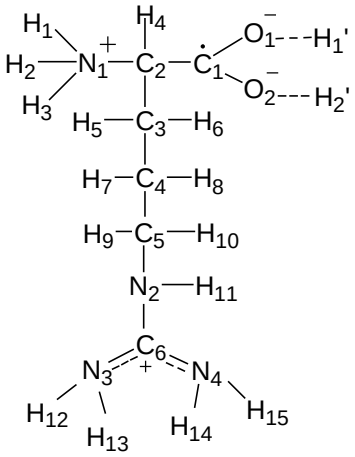

Scheme 7.3
The carboxyl radical anion

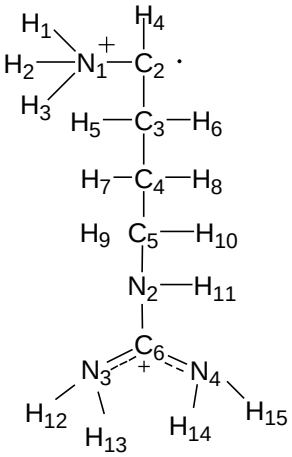

Scheme 7.4
The decarboxylation radical

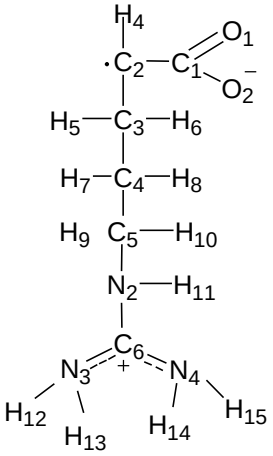

Scheme 7.5

The main-chain deamination radical

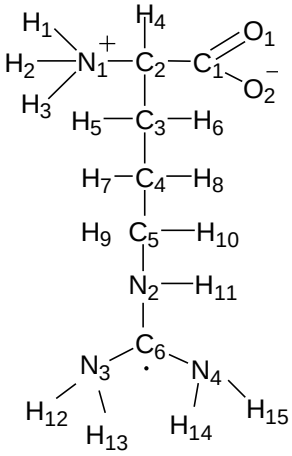

Scheme 7.6

The Guanidyl anion radical

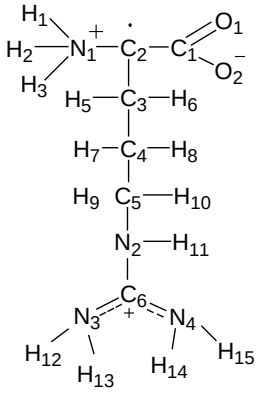

Scheme 7.7

The radical from dehydrogenation at C2

7.2 Experimental

L-arginine hydrochloride monohydrate (L-arginine·HCl·H_2O, Sigma Chem. Co.) single crystals were obtained from the saturated aqueous solution by slow evaporation at room temperature. Partially deuterated crystals were prepared from material recrystallized at least three times from a saturated solution of deuterium oxide (D_2O, Sigma Chem. Co.) by slow evaporation in the desiccator at room temperature. Dow and Jensen (1972) studied the crystal structure with X-ray diffraction.[7] The crystal is monoclinic ($P2_1$), with two molecules in the asymmetric unit, denoted as molecules A and B respectively, and with four molecules (two from molecule A and two from molecule B) per unit cell.

In the crystals, the arginine molecule is a zwitterionic cation with positive charges on both the main chain amino group and the side chain guanidyl group, and with a single negative charge on the main chain carboxyl group. (See Scheme 7.1) The geometries of molecules A and B are closely similar except for their carboxyl group. Although the O1O2C2C1 groups (see Scheme 7.1) of both molecules A and B are planar with similar torsion angles ∠O1-O2-C2-C1 < ~2°, the deviation of H4 from the carboxyl plane in molecule A is larger than that in molecule B by ~20°. Both guanidyl groups in molecules A and B are planar.

The arginine molecule is anchored in an extensive system of hydrogen bonds. The two carboxyl oxygen atoms and all the N-H hydrogen atoms in molecules A and B participate in hydrogen bonds to atoms in neighboring molecules, and there are no intramolecular hydrogen bonds reported. The arrangements of hydrogen bonds to the main chain amino protons and the guanidyl protons are similar for molecules A and B. However, the arrangements are different for hydrogen bonds to the carboxyl oxygen atoms: for molecule A, O1 is hydrogen bonded to two main chain amino protons from two different neighboring molecules both with lengths H'…O1 of ~1.8Å, and O2 is hydrogen bonded to a guanidyl proton from the third neighboring molecule and to a neighboring water proton both with lengths H'…O2 of ~2.2Å. For molecule B, O1 is hydrogen bonded to a main chain amino proton and a guanidyl proton from the same neighboring molecule with respective lengths H'…O1 of 2.0Å and 2.5Å, and O2 is hydrogen bonded to a main chain amino proton from a second neighboring molecule and to a neighboring water proton with respective lengths H'…O2 of 2.0Å and 2.4Å. These differences in the arrangement of hydrogen bonds to the carboxyl groups and in the carboxyl groups' geometry of molecule A and B will lead to the two different configurations of the carboxyl radical anion as described below.

Both normal and deuterated forms of crystals were X-irradiated at 66K (pumped liquid nitrogen) for about three hours to a dose of 100-200kGy. Subsequently, the K-band EPR, ENDOR and EIE were recorded at 66K. The methods of crystal orientation, temperature control and monitoring, data analysis,

and spectrum simulations were described above (see Chapter 4). In this work, the crystallographic <a>, <b> and <c*> were chosen as the orthogonal reference system.

The theoretical computations were performed to help with identifying the radicals and to investigate the reorientation of the radical. All the initial atomic coordinates of the radicals were from the crystallographic studies.[7] These initial radical geometries were optimized using Density Functional Theory (DFT) methods with Becke's three parameter hybrid functional B3LYP in combination with Pople and coworker's 6-31G(d,p) basis set. Single point calculations for hyperfine coupling constants of the radicals were performed using DFT and a higher basis set 6-311G(2d,f). The keyword "NOSYMM" was used for both the optimization and the single point calculations to prevent the Cartesian coordinates of the radical model from rotating or shifting with respect to the reference frame. In this work, the cluster models and single molecule models were constructed for studying different radicals as described below. The final models chosen were those giving computational results with 1) no single coupling values >15MHz, and 2) no single eigenvectors[I] >25° from experimental values.[8] To achieve the assignment it sometimes was necessary to adjust manually the atomic coordinates as described in the discussion below.

7.3 Results and Analysis

EPR and EIE

As is shown in Fig. 7.1(a), the EPR spectrum recorded from L-arginine · HCl single crystal immediately after X-ray irradiation at 66K with the magnetic field along <c> consists of a dominant four-line hyperfine pattern in the center with some weak lines on both sides. The EPR from the partially deuterated L-arg·HCl single crystal taken under the same conditions and at the same orientation as shown in Fig. 7.1(b) consists of a strong two-line pattern at the center, with weak lines on both sides that are quite different from those in Fig. 7.1(a). These differences indicate that at least one coupling contributing to the four-line pattern comes from an exchangeable proton, and that some couplings of the weak lines also are due to exchangeable protons.

[I] The maximum dipolar vector is the eigenvector associated with the maximum eigenvalue.

Moreover, the four-line hyperfine pattern is resolved in the EPR spectra only when the magnetic field is near <c>. With magnetic field along <a> (B//<a>) the EPR from the normal crystal is a wide two-line pattern with slight shoulders as shown in Fig. 7.1(c). This pattern is nearly the same as that from the partially deuterated crystal for B//<a> as shown in Fig. 7.1(d). These characteristics indicate that one coupling in the center pattern becomes irresolvable by EPR at <a>, and that other coupling in the center pattern is from a nonexchangeable proton.

At least five distinct EIE patterns were detected from the normal crystals with the magnetic field along <c> as is shown in Fig. 7.2. From the analysis described latter, they can be assigned to four different radicals, denoted as R1a, R1b, R2, R3, and R4. (R1a and R1b are the same radical in different configurations as will be discussed below.) The comparison of the EPR spectrum and the EIE patterns for B//<c> as shown in Fig. 7.2 indicates that the dominant four-line pattern in the center of the EPR is mainly from radical R1a, and that some weak lines on both sides are from radicals R2-R4; the EPR from R1b overlaps one of the center four peaks at this orientation.

One additional distinct EIE pattern was detected for B//<a> (see Fig. 7.26a in section of "R5-unknown radical"), and it was assigned to a radical denoted as R5.

ENDOR

Fig. 7.3(a) shows the ENDOR spectrum for B//<c> from the normal crystal with the magnetic field locked to the EPR peak as indicated by the arrow in Fig. 7.1(a). Assignment of the ENDOR lines in Fig. 7.3(a) was based on the EIE patterns shown in Fig. 7.2 as follows: as labeled in Fig. 7.3(a), lines a1 and a2 gave the dominant four-line pattern in the center of the EPR for B//<c> and were assigned to radical R1a; lines b1-b3 gave strong one-peak EIE patterns as shown in Fig. 7.2 and were assigned to radical R1b; the weak lines A-D gave six-line EIE patterns in peak ratio of 1:2:2:2:2:1 as shown in Fig. 7.2 and were assigned to radical R2; lines 1 and 2 gave five-line EIE patterns in ratio of 1:1:2:1:1 as shown in Fig. 7.2 and were assigned to R3; only the weak ENDOR line "R4-I" gave the four-line EIE pattern in ratio of ~1:1:2:2:2:2:1:1 as shown in Fig. 7.2 and was assigned to R4. Fig. 7.3(c) shows the ENDOR spectrum for

B//<a> from the normal crystal with the magnetic fields locked to the peak of the EPR as indicated by the arrow in Fig. 7.1(c). One additional ENDOR line was detected at <a> for R1 and denoted a3; this coupling was difficult to detect at <c>, since it almost overlaps with the free proton line at this orientation.

Fig. 7.3 (b) and (d) show the ENDOR spectra from the partially deuterated crystals for B//<c> and for B//<a>, under same conditions as those in Fig. 7.3(a) and (c), with the magnetic field locked to the EPR peaks indicated by the arrows in Fig. 7.1(b) and (d). As are shown in Fig. 7.3(a)-(b) and (c)-(d), respectively, comparisons of the ENDOR spectra from the normal and partially deuterated crystals at the same orientations indicate that lines a1, b1, B, and R4-1 can be observed in ENDOR from both types of the crystals. Thus, these lines are from nonexchangeable protons. Lines a2, a3, b2, b3, 1 and 2 are strong in ENDOR from the normal crystal but become unobservable in ENDOR from the partially deuterated crystal, and these lines are due to exchangeable protons. Lines A, C and D are always very weak in the ENDOR spectra from both types of crystals, and it is difficult to estimate if they are exchangeable or not.

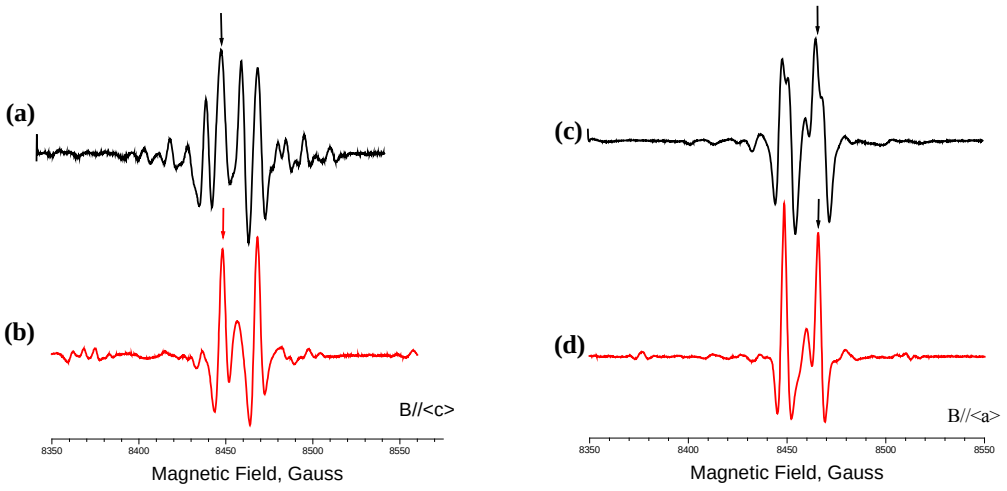

Fig. 7.1 *The 2nd-derivative EPR spectra detected at 66K immediately after the crystals irradiated at 66K. The magnetic fields are along <c> in* ***(a)*** *and* ***(b)*** *and along <a> in* ***(c)*** *and* ***(d)****. The spectra in* ***(a)*** *and* ***(c)*** *are from L-arginine· HCl· H_2O normal crystals, and the spectra in* ***(b)*** *and* ***(d)*** *are from the partially deuterated crystals.*

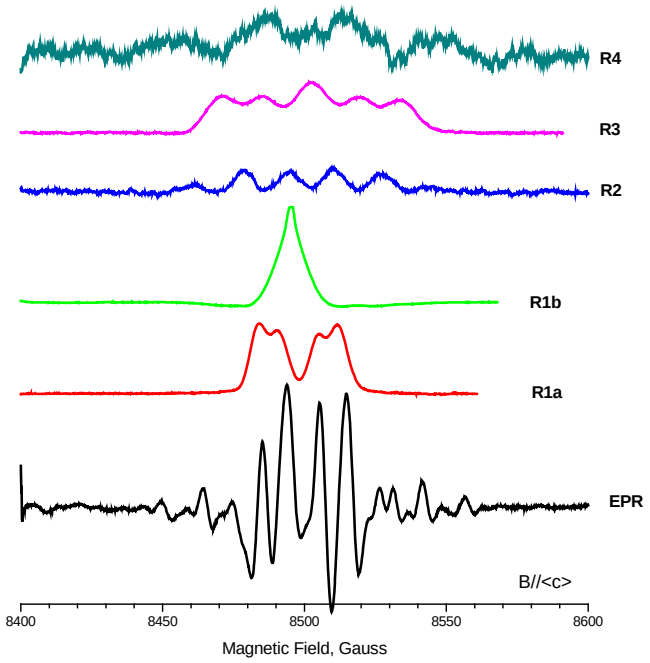

Fig. 7.2 *The EPR and the EIE for R1a, R1b, R2-R4 detected from the normal crystal of L-arginine· HCl· H_2O at <c> under same conditions as in Fig. 7.1.*

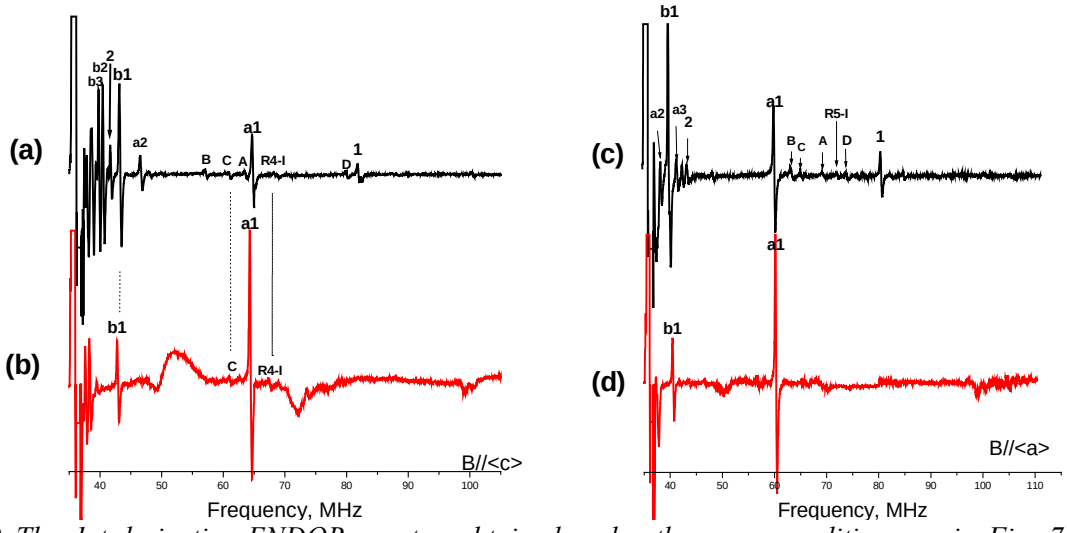

Fig. 7.3 *The 1st-derivative ENDOR spectra obtained under the same conditions as in Fig. 7.1. The magnetic fields are along <c> in* ***(a)*** *and* ***(b)*** *and along <a> in* ***(c)*** *and* ***(d).*** *The spectra in* ***(a)*** *and* ***(c)*** *are from L-arginine· HCl· H_2O normal crystals, and the spectra in* ***(b)*** *and* ***(d)*** *are from the partially deuterated crystals.*

Radical R1a-the carboxyl radical anion from molecule A

As mentioned above, at least three couplings (a1, a2 and a3) were assigned to R1a as labeled in Fig. 7.3. EIE simulations for B//<a> and for B//<c> based on couplings a1, a2 and a3 are shown in Fig. 7.4a and 7.4b. Couplings a1 and a2 were sufficient to simulate the dominant four-line hyperfine pattern in the EPR spectrum for B near <c>; at orientations farther from <c>, coupling a2 became small enough that only a1 was resolvable in the EPR. The result was a strong two-line pattern at the center. Coupling a3 always was very small and was unresolvable in the EPR at all orientations. For B near <c>, ENDOR lines from coupling a3 overlap with the free proton lines and were difficult to detect.

From comparison of the ENDOR spectra shown in Fig. 7.3, it can be seen that coupling a1 is nonexchangeable, while couplings a2 and a3 are both exchangeable. Also, the four-line EIE pattern from the normal crystal (Fig. 7.5a) for B//<c> becomes a two-line EIE pattern from the partially deuterated crystal EIE (Fig. 7.5b) at the same orientation. The EIEs at <a> from both crystal types are two-line patterns as shown in Fig. 7.5c and 7.5d. Moreover, the EIE patterns for B//<a> and for B//<c> from the partially deuterated crystal can be reproduced by coupling a1alone (see Fig. 7.4c and 7.4d). These results are further evidence that the larger coupling a1 is from a nonexchangeable hydrogen while the smaller coupling a2 is from an exchangeable hydrogen.

The angular dependence curves of couplings a1-a3 are illustrated in Fig. 7.6. Analysis of these data gave the hyperfine coupling tensors for a1-a3 as listed in Table 7.1. Tensor a1, with moderate anisotropy, was assigned as a β-coupling; since it is nonexchangeable, it must be from a C-H β-proton. Tensors a2 and a3 show characteristics of O-H β-couplings, which have greater anisotropy than typical C-H or N-H β-couplings. This also is consistent with the evidence that a2 and a3 are from exchangeable protons. Thus, the only possibility for R1a is the carboxyl radical anion (see Scheme 7.3), in which the spin is mainly located on C1. For this radical structure, H4 provides the C-H β-coupling a1, while H1’ and H2’ will give the two O-H dipolar couplings a2 and a3. (H1’ and H2’ are protons from other molecules

hydrogen bonded to O1 and O2 of molecule A in the crystal. H1' is from the main-chain amino group of a nearby molecule, and H2' is from an adjacent water molecule.)

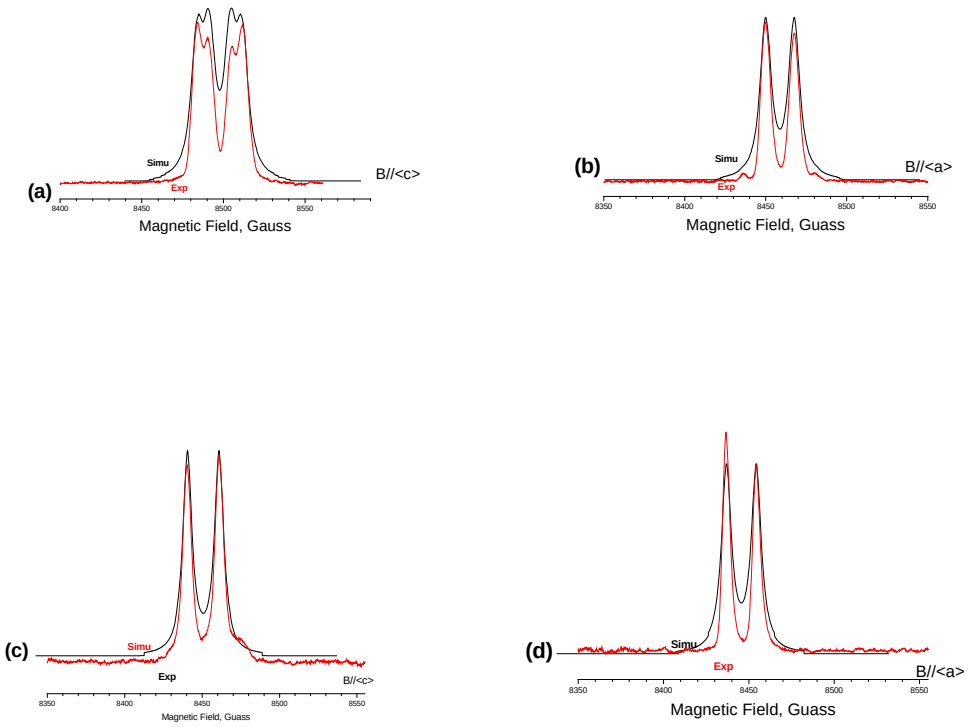

Fig. 7.4 (a) *and* ***(b)*** *EIE simulations for R1a from the normal crystals with couplings a1-a3;* ***(c)*** *and* ***(d)*** *EIE simulations for R1a from the deuterated crystals with couplings a1only; in* ***(a)*** *and* ***(c),*** *B//<c>, in* ***(b)*** *and* ***(d)****, B//<a>.*

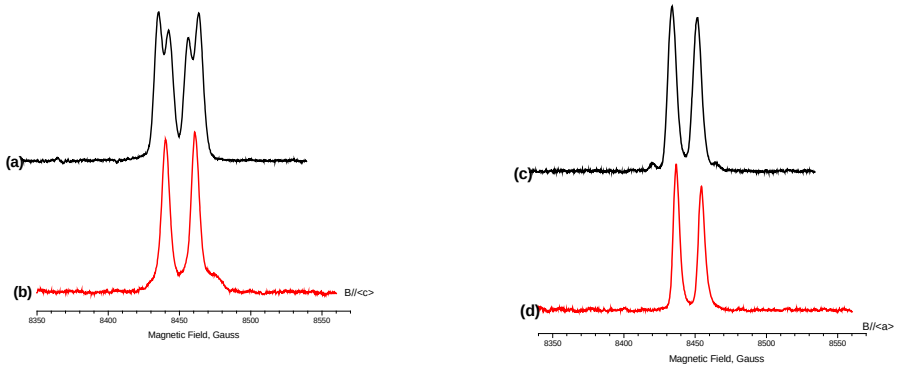

Fig. 7.5 (a) *and* ***(b)*** *The comparisons of the EIE patterns from the normal crystal and from the partially deuterated crystal at <c>;* ***(c)*** *and* ***(d)*** *The similar comparison at <a>. The EIEs in* ***(a)*** *and* ***(c)*** *are from the normal crystals and the EIEs in* ***(b)*** *and* ***(d)*** *are from the partially deuterated crystals.*

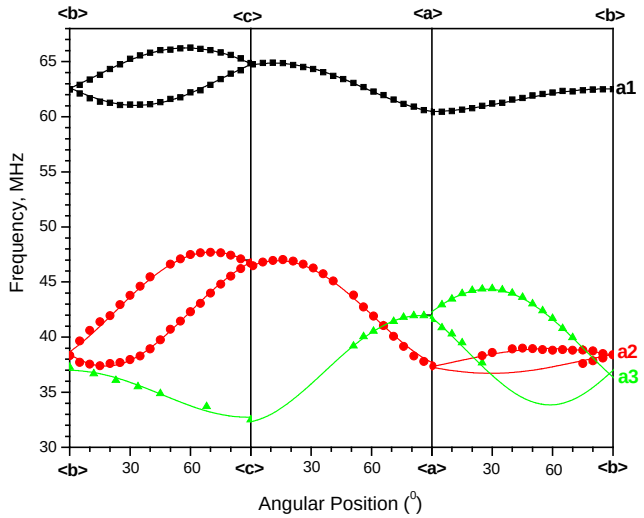

Fig. 7.6 *The angular dependent curves for couplings a1, a2 and a3 of radical R1a.*

Table 7.1 *Hyperfine coupling tensors for radical R1 in L-arginine·HCl·H_2O single crystals irradiated at 66K.*[a,b]

Tensors	Principal values[a,b]	Isotropic Values[a]	Anisotropic values[a]	Eigenvectors[b] <a>	<b>	<c*>
	60.28(2)		7.36	0.093(1)	0.527(3)	-0.845(2)
a1	50.69(2)	52.92	-2.23	0.575(1)	-0.721(2)	-0.387(3)
	47.80(2)		-5.12	0.813(1)	0.450(2)	0.370(2)
	23.62(3)		14.32	0.198(1)	-0.320(7)	-0.927(5)
a2	3.03(3)	9.30	-6.27	0.599(1)	-0.709(6)	0.372(6)
	1.24(4)		-8.06	0.776(0)	0.629(1)	-0.051(4)
	16.90(5)		15.21	0.874(1)	-0.483(5)	-0.058(8)
a3	-3.71(10)	1.69	-5.40	0.426(2)	0.817(6)	-0.388(17)
	-8.11(11)		-9.80	0.235(4)	0.314(18)	0.920(8)

[a]All these values are in units of MHz. [b]Numbers in parentheses are the estimated uncertainties in the last digit quoted as reported by the statistical analysis.

The maximum dipolar vectors[I] of tensors a1-a3 were compared to the corresponding crystallographic directions as listed in Table 7.2. The assignment of coupling a1 to proton H4 is supported by the difference of only 7.2° between the maximum dipolar vector[I] of a1 and the direction of C1…H4 in

molecule A. Similarly, a2 and a3 can be assigned to H1' and H2', respectively, because the directions of H1'…C1 and H2'…C1 are closest to the maximum dipolar vectors of a2 and a3; the respective angular differences are 14.6° and 26.2°. The four neighboring protons H1'-H4', hydrogen bonded to the carboxyl group of molecule A in the crystal, are shown in Fig. 7.7(b). From the modeling calculation described later, proton H1' will transfer from the neighboring molecule to O1 and give coupling a2, after the electron is trapped by the carboxyl group; also, proton H2' becomes much closer to O2 and gives dipolar coupling a3. Although the proceeding discussion indicated that R1a is the carboxyl anion, and that protons H1' and H2' move closer following electron capture; the analysis does not provide a distinction between molecules A and B. However, the following geometry-based analysis indicates that R1a is the carboxyl anion from molecule A.

Table 7.2 *The comparison between the maximum engenvectors[a] of tensors a1-a3 and the corresponding crystallographic directions in molecule A.[a,b]*

	Eigenvectors[a]			Directions of Hx'….C1[b]				
Coupling	<a>	<b>	<c*>	Proton[b]	<a>	<b>	<c*>	Angle Diff (°)[c]
a1	0.093	0.527	-0.845	H4	0.202	0.466	-0.862	6.9
a2	0.198	-0.320	-0.927	H1'	0.138	-0.546	-0.826	14.6
				H2'	0.998	-0.049	-0.028	76.2
				H3'	0.672	-0.504	-0.543	37.1
				H4'	-0.433	-0.868	-0.244	65.3
a3	0.874	-0.483	-0.058	H1'	0.138	-0.546	-0.826	64.4
				H2'	0.998	-0.049	-0.028	26.2
				H3'	0.672	-0.504	-0.543	30.4
				H4'	-0.433	-0.868	-0.244	86.8

[a]The eigenvectors are the principal directions associated with the largest coupling components. [b] Hx' are the neighboring protons hydrogen bonded to the carboxyl group of lysine molecule, H1'- H4', as denoted in Fig. 7.7. [c]"Angle Diff (°)" are the angular differences between the experimental eigenvectors and the crystallographic directions in units of degrees.

From the Heller-McConnell equation,[9]

$$a_{C\text{-}H} = B_1\rho\cos^2\theta \text{ [II]} . \qquad (1)$$

With the standard $B_1\rho$ value of 77.3MHz for the carboxyl anion radical[10], and the measured isotropic value for a1 of 52.92MHz, the angle θ is evaluated as $\theta_{C\text{-}H}$ = 34.2°. For the undamaged molecule, the torsion angle <H4-C2-C1-O1 is 57.8° in the molecule A; if the spin orbital is normal to the carboxyl plane, the configuration angle will be 32.2°. This is very close to the configuration angle of 34.2° calculated above for a1. However, the torsion angle < H4-C2-C1-O1 in molecule B is 36.3°, and gives the configuration angle is 53.7°, which is quite different from the above calculated angle of a1. From the analysis shown and given later, the geometry of the carboxyl anion radical from molecule B is more consistent with radical R1b.

The $B_1\rho$ value in the Hellen-McConnell equation above is 40.32MHz for O-H dipolar coupling in the carboxyl anion radical[11]. From this and the isotropic values for a2 and a3, their configuration angles for a2 and a3 are 61.3° and 78.2°, respectively. That is, the two neighboring protons giving a2 and a3 are very close to the nodal plane of the radical. Similarly, from the crystallographic torsion angles <H1'-O1-C1-O2 and <H2'-O1-C1-O2 of 21.7° and 79.1°, and by assuming that the nodal plane is the carboxyl plane in the crystal, the configuration angles for H1' and H2' are 68.3° and 10.9°, respectively. The crystallographic configuration angle for H1' (68.3°) is very close to the configuration angle calculated for a2 (61.3°); while the crystallographic configuration angle for H2' (10.9°) is quite different from the configuration angle calculated for a3 (78.2°). However, from the computational modeling discussed below, in the optimized structure for the carboxyl anion radical of molecule A, H2' moves closer to O2, after the anion is formed. Also, the carboxyl group becomes a tetrahedral structure with O2 bending toward H2'. These two geometric changes in the anion lead to H2' being much closer to the nodal plane, (see Fig. 7.7d), and thereby giving a small isotropic value.

[II] In equation (1), $a_{C\text{-}H}$ is the isotropic value from a C-H β-coupling, B_1 is the constant, ρ is the spin density, and θ is the configuration angle between the C-H_β bond and the spin orbital. In equation (2), $a_{O\text{-}H}$ is the isotropic value from O-H dipolar coupling, and the other characters have similar meaning as those in equation (1).

Modeling Calculations of R1a: In order to reproduce the geometry and the magnetic parameters of R1a, a cluster model was constructed as shown in Fig. 7.7a: molecule A is the neighbor to four clusters I-IV. Almost all the atomic coordinates in the cluster model are from the X-ray crystallographic study.[7] Clusters I and IV are the main chain amino groups in two different neighboring aginine molecules, cluster III is the side chain guanidyl group in a third neighboring arginine molecule, and cluster II is a neighboring water molecule. The remainders of the molecules in clusters I, III and IV are simplified by three methyl groups. In these four neighboring clusters, H1'in I and H4' in IV are hydrogen bonded to O1; H2' in II and H3' in III are hydrogen bonded to O2. To obtain an anion radical model, one electron was added to the whole cluster, and the environmental effects were simulated by freezing some of the atoms in the cluster model during the geometry optimization, as indicated by the atoms labeled "f" in Fig. 7.7a. The optimization was performed using B3LYP/6-31G(d,p) followed by the single point energy calculation using B3LYP/6-311G(2d,p).

The partially optimized clusters are shown in Fig. 7.7c and 7.7d. The carboxyl group of molecule A shows a tetrahedral structure with torsion angle <C2-O2-O1-C1 of 29.2°, a significant rearrangement from the planar structure with torsion angle <C2-O2-O1-C1 of only -0.3° before the optimization. Also, protons H1'-H4' are closer to the carboxyl group than before the anion is formed. Especially, the distance O1…H1' shortened to 1.04Å from 1.83Å, while the distance N'(I)…H1' lengthened to 1.53Å from 0.95Å. These indicate that H1' was transferred to O2 through the hydrogen bond from the neighboring molecule after the electron was captured by the carboxyl group of molecule A. The single point energy calculation indicates that the spin density is mainly located on atoms of the carboxyl group, C1 (0.66), O1 (0.04), and O2 (0.19). As are listed in Table 7.3, the calculated hyperfine tensors from protons H4, H1' and H2' reproduce the experimental tensors a1, a2 and a3 very well: the angular differences of the maximum dipolar vectors[I] are less than 6°, the differences of isotropic values are less than 8MHz, and the differences of the anisotropic components are less than 2MHz. These small differences confirm the assignments of R1a as the carboxyl anion radical from molecule A, and also confirm the assignments of

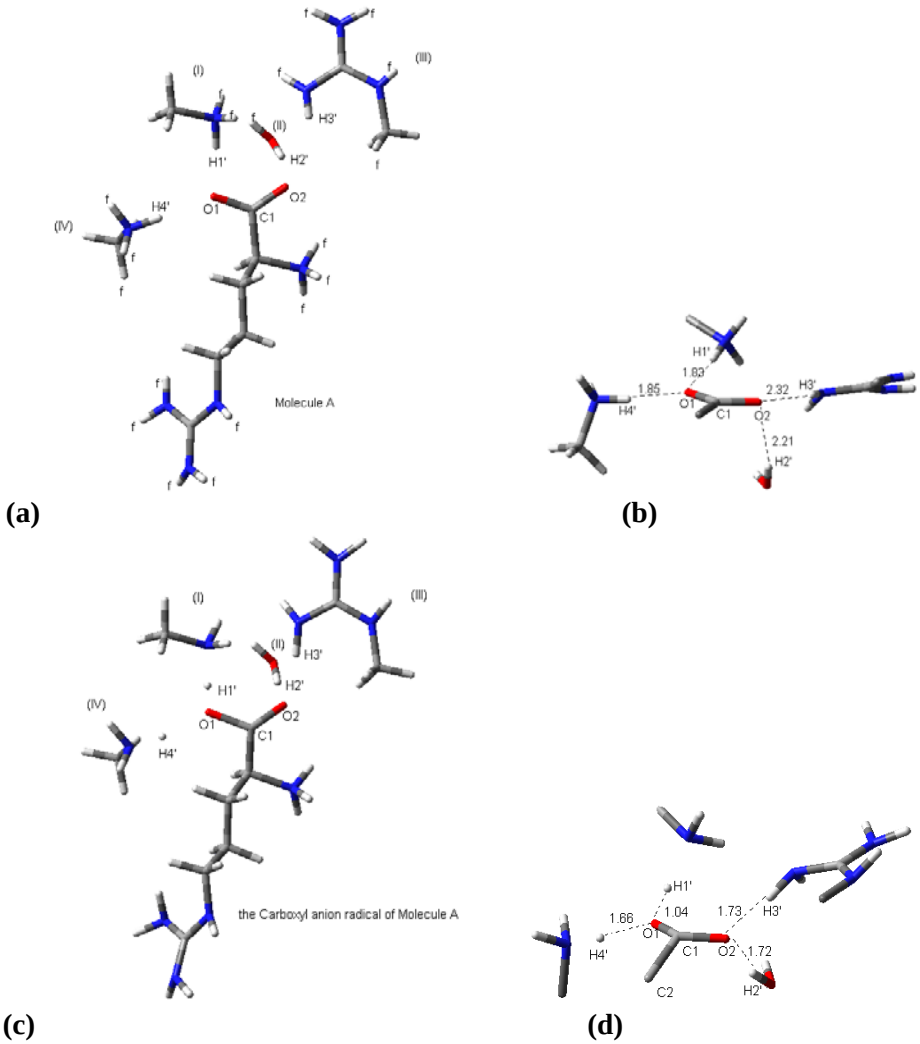

Fig. 7.7 *The cluster model for the carboxyl anion radical before* ***(a)*** *and after* ***(c)*** *the geometry optimization, and the carboxyl group and its neighboring clusters before* ***(b)*** *and after* ***(d)*** *the geometry optimization. The numbers in* ***(b)*** *and* ***(d)*** *are the corresponding distances in units of angstroms.*

a1→H4, a2→H1', and a3→H2'. (Protons H1' and H2' form the dipolar coupling with O1 and O2.) The optimized geometry shown in Fig. 7.7c and 7.7d indicates that H1' is the transferred proton from the neighboring molecule; however, H2' is still kept in the neighboring water (cluster II) with bond length O2'-H2' of 0.97Å, although H2' moved closer to the carboxyl group and formed a dipolar coupling to O2 after the electron was trapped. From the geometry optimization, protons H3' and H4' also moved closer to the carboxyl group (~0.6Å for H3'…O2 and ~0.2Å for H4'…O1). However, the calculated tensors for H3' and H4' show small anisotropy (see Table 7.3) and indicate that these two protons did not form

dipolar O-H couplings. The calculated nitrogen β-coupling from N1 has very small isotropic value of ~3.34MHz and also has very small anisotropic components (0.51, -0.22, -0.29) as listed in Table 7.3.

Table 7.3 *The calculated hyperfine coupling tensors from the optimized cluster model of the carboxyl anion radical of molecule A.* [a,b]

				Eigenvectors				
Proton	Principal Value[a]	Isotropic value[a]	Anisotropic value[a]	<a>	<b>	<c*>	Coupling	Angle diff (°)[b]
	53.64		8.54	0.075	0.525	-0.848	: a1	1.1
H4	41.06	45.10	-4.04	-0.043	0.851	0.523		
	40.61		-4.49	0.996	-0.003	0.086		
	25.5		15.22	0.153	-0.234	-0.96	: a2	5.9
H1'	4.43	10.28	-5.85	0.257	0.948	-0.19		
	0.84		-9.44	0.954	-0.218	0.205		
	11.76		16.66	0.861	-0.504	-0.07	: a3	1.5
H2'	-12.76	-4.90	-7.86	0.496	0.801	0.335		
	-13.7		-8.80	-0.113	-0.324	0.94		
	9.47		8.88	-0.663	-0.311	0.681		
H3'	-3.51	0.59	-4.10	0.732	-0.460	0.502		
	-4.19		-4.78	0.160	0.831	0.533		
	6.5		5.83	0.528	0.846	0.072		
H4'	-1.88	0.67	-2.55	0.803	-0.470	-0.367		
	-2.61		-3.28	0.277	-0.251	0.928		
	3.85		0.51					
N1	3.12	3.34	-0.22					
	3.05		-0.29					

[a] All these values are in units of MHz. [b] The "Angle diff (°)" is the angular difference between the calculated and the experimental eigenvectors associated with the maximum eigenvalues in units of degrees.

From the above results, radical R1a can be assigned to the carboxyl anion radical from molecule A with a C-H β-coupling a1 from H4 and two O-H dipolar couplings a2 and a3 from H1' and H2'. The other couplings from H3', H4' and N1, etc., are too small to be detected in the experiments.

Radical R1b-the carboxyl radical anion from molecule B

The EIEs of R1b at three crystallographic axes are one-line patterns, as is shown in Fig. 7.2 for B//<c>. At least three couplings b1, b2 and b3 labeled in Fig. 7.3 were assigned to R1b. The WINSIM simulation of R1b EIE pattern for B//<c> with couplings b1-b3 is shown in Fig. 7.8. All the couplings in R1b are small and unresolvable by the EIE. The comparions of the ENDOR spectra from the normal and partially deuterated crystals at the same orientation indicate that coupling b1 is nonexchangeable, while b2 and b3 are exchangeable, as are shown in Fig. 7.3. The EIE pattern (B//<c>) for ENDOR line b1 from the partially deuterated crystal (Fig. 7.3b) is also a strong one-line pattern. This is similar to the EIE (B//<c>) from the normal crystal, as shown in Fig. 7.9. This evidence confirms that coupling b1 is from a nonexchangeable proton. The angular dependence curves of b1-b3 are shown in Fig. 7.10. The hyperfine coupling tensor of b1 is listed in Table 7.4; the coupling tensors for b2 and b3 cannot be obtained since their ENDOR lines overlap with the free proton lines at most orientations. Coupling b1 shows moderate anisotropy, and because it is nonexchangeable, coupling b1 was assigned to a C-H β-coupling.

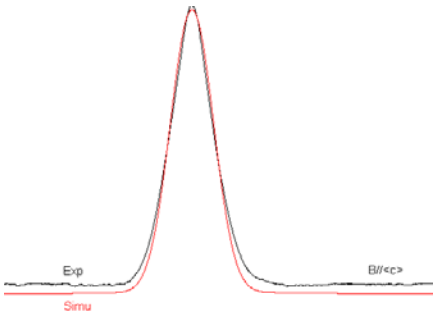

Fig. 7.8 *WINSIM simulation for the EIE pattern of R1b (B//<c>) with couplings b1-b3 at <c>.*

From the above characteristics, R1b can be assigned to the carboxyl radical anion (see Scheme 7.3) in a different configuration from R1a. The isotropic value of C-H β-coupling b1 is only 10.59MHz, which is much smaller than that of coupling a1 (52.92MHz) in R1a. From the Heller-McConnell equation (1) for C-H β-couplings, the configuration angle for b1 will be 68.3° (with $B_1\rho$ = 77.3MHz). This configuration angle is almost twice that of a1 (34.2°), which indicates that the β-proton giving b1 is much

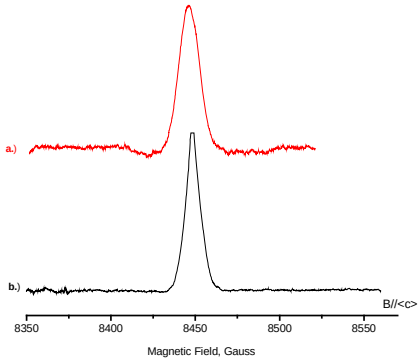

Fig. 7.9 *EIE patterns (B//<c>) of R1b from the normal crystal* ***(a)*** *and from the partially deuterated crystal* ***(b).***

closer to the nodal plane of the anion radical than that giving a1. From the crystallographic studies[7], the main difference in the configuations of molecule A and B is that H4 in molecule B is closer to the carboxyl plane with the torsion angle <H4-C2-C1-O2 of 36.3°, which is smaller than that of 57.8° in molecule A by ~22°. Assuming the spin orbital is normal to the carboxyl plane of molecule B, the configuration angle of H4 will be 53.7°. This angle is close to the calculated configuration angle of 68.3° for coupling b1. Moreover, the maximum dipolar vector[I] of b1 is almost parallel with the crystallographic direction C1… H4 in molecule B with the angular difference of only 11.2°, as is shown in Table 7.4. Therefore, it is reasonable to assign b1 to proton H4 in molecule B. Couplings b2 and b3 are exchangeable, thus they can be assigned to the protons coupling to the carboxyl oxygen atoms. Since b1 and b2 are small, we can estimate from equation (2) that their configuration angles should be large, i.e., the two protons are both very closest to the nodal plane of the spin orbital. Protons H1'- H4' which form intermolecular hydrogen bonds to the carboxyl group of molecule B in the crystal, are shown in Fig. 7.12(b). Protons H1' (hydrogen bonded to O1) and H2' (hydrogen bonded to O2) are closet to the carboxyl plane with the torsion angles < H1'-O1-C1-O2 of 1.5° and < H2'-O2-C1-O1 of 31.1°; protons H3' (hydrogen bonded to O2) and H4' (hydrogen bonded to O1) are more out of the carboxyl plane with the torsion angles < H3'-O2-C1-O1 of 86.7° and < H4'-O1-C1-O2 of 40.1°. From the modeling

calculation for the carboxyl anion radical of molecule B as described below, H1' and H2' are protons transferred to O1 and O2 and lead to the O-H dipolar couplings of the anion. By using the calculated tensors from H1' and H2', the ENDOR curves of b2 and b3 in <ac> plane can be reproduced. Based on these results, we can assign couplings b2 and b3 to protons H1' and H2', although it was not possible to obtain tensors for b2 and b3.

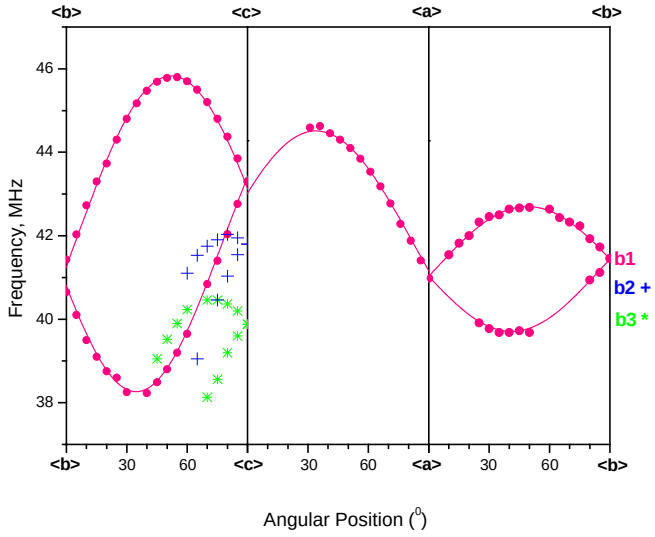

Fig. 7.10 *Angular dependence curves for couplings b1-b3 of radical R1b.*

Table 7.4 *Hyperfine coupling tensors for radical R1b in L-arginine·HCl·H_2O single crystals irradiated at 66K.*[a,b,c]

				Eigenvectors[b]		
Tensors	Principal values[a,b]	Isotropic Values[a]	Anisotropic values[a]	<a>	<b>	<c*>
	21.66(2)		11.06	0.416(1)	0.531(2)	-0.738(10)
b1	6.10(2)	10.60	-4.50	0.897(1)	-0.375(9)	0.235(4)
	4.04(2)		-6.56	0.152(1)	0.760(7)	0.632(3)
$H4_b$…C1 direction in Molecule B				0.268	0.464	-0.844
Angular difference of 11.3° with eigenvector[c] of coupling b1						

[a]All these values are in units of MHz. [b]Numbers in parentheses are the estimated uncertainties in the respective values as reported by the statistical analysis. [c]This eigenvector is the principal direction associated with the largest coupling component.

Modeling calculations of R1b: A cluster model was built for the carboxyl radical anion of molecule B. As is shown in Fig. 7.11a, molecule B has three neighboring clusters: cluster I is almost from an arginine molecule, except that the main chain carboxyl group is simplified by a hydrogen atom; cluster II is the main chain amino group of a different neighboring arginine molecule, and the remainders of each molecule were replaced by a methyl group for simplification; cluster III is a neighboring water molecule. H1' and H4' in cluster I are hydrogen bonded to O1, H2' in II and H3' in III are hydrogen bonded to O2. Similar to the carboxyl radical anion model of molecule A, one electron was added to the whole cluster, and some of the atoms were fixed during the optimization to simulate the environmental effects. (These fixed atoms are marked "f" in Fig. 7.11a.)

The whole cluster was partially optimized by using B3LYP/6-31G(d,p). The geometry optimization indicates that the planar carboxyl group of molecule B became a tetrahedral with torsion angle <O1-C2-O2-C1 of 22.6° after the electron was trapped by the carboxyl group. Meanwhile, protons H1' in cluster I and H2' in II moved closer to O1 and O2 with distances H1'…O1 of 1.02Å and H2'…O2 of 1.05Å; as a result, they became farther from their original clusters: distance N1'(I)…H1' is lengthened to 1.71Å from 0.89Å, and N'(II)…H2' is lengthened to 1.62Å from 0.91Å. These indicate that protons H1' and H2' transferred to O1 and O2 after the anion formed.

The single point energy calculation was performed on the optimized cluster model with B3LYP/6-311G(2d,p). The calculation shows that the spin density is mainly on the carboxyl group: 0.71 on C1, 0.07 on O1 and 0.15 on O2. The calculated coupling tensor from H4 is close to that of b1. However, the calculated coupling from H1' is 16.60MHz, which is too large for coupling b2 or b3. Thus the computed coupling for H1' appears to be overestimated. To investigate this further, the carboxyl group was rotated manually about the C1-C2 axis by 10°.

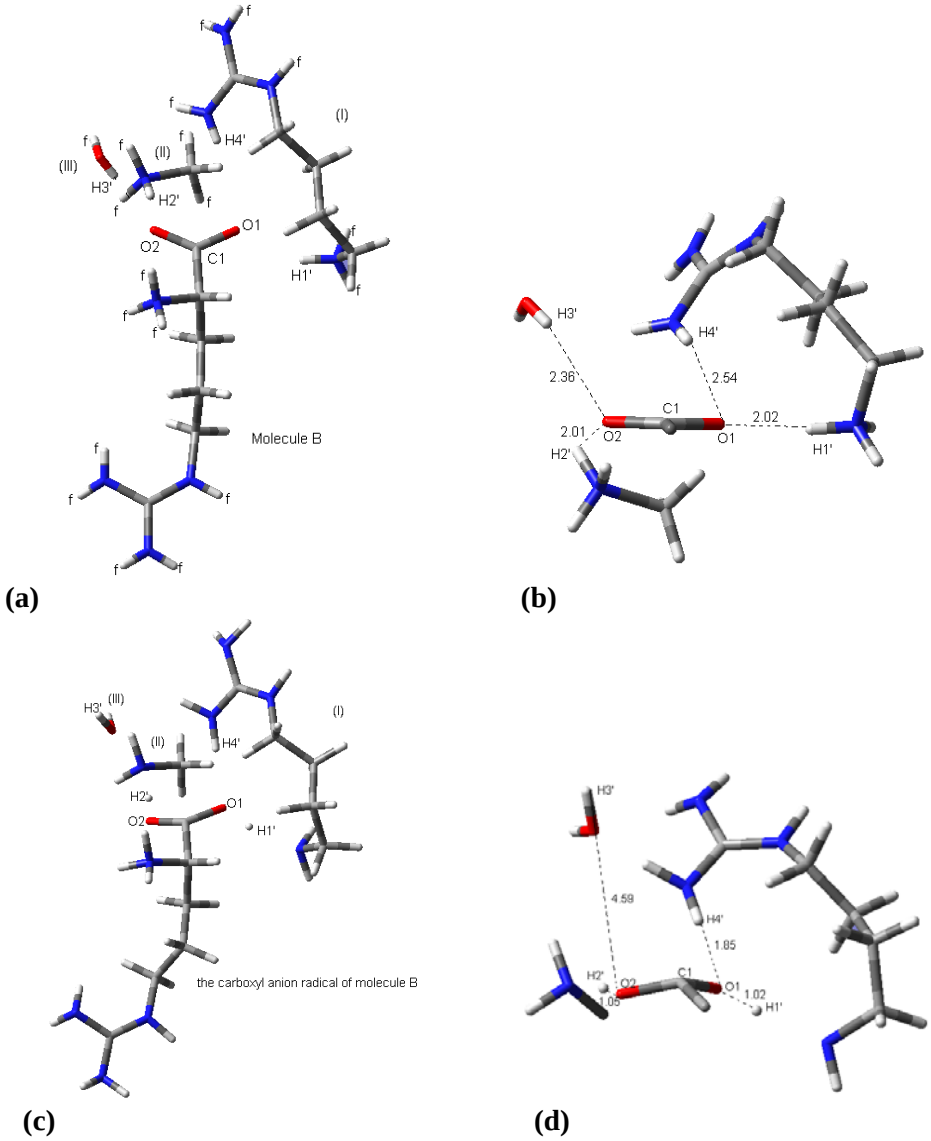

Fig. 7.11 *The cluster model for the carboxyl anion radical before* ***(a)*** *and after* ***(c)*** *the geometry optimization, and the carboxyl group and its neighboring clusters before* ***(b)*** *and after* ***(d)*** *the geometry optimization. The numbers in (b) and (d) are the corresponding distances in units of angstroms.*

The hyperfine coupling tensors from the adjusted structure, listed in Table 7.5, are in better agreement with the experimental results. From the adjusted structure, the calculated coupling tensor from H4 has the isotropic value of 11.83MHz and anisotropic values of 10.95MHz, -4.29MHz and -6.65MHz; the corresponding values measured for tensor b1 are 10.59MHz (isotropic), 11.06MHz, -4.50MHz and -6.56MHz (anisotropic). In addition, the angular differences for the three eigenvectors are 10.9°, 16.6° and 12.7°. The coupling from H1' is -4.53MHz from the adjusted structure and is also reasonable for an

O-H dipolar coupling of R1b. Although it was not possible to measure tensors b2 and b3, the indications were that they are small and consistent with the calculated tensors from H1' and H2' in the adjusted structure. As well, the calculated tensors from H1' and H2' can reproduce the angular dependence curves of b2 and b3 detected in <ac> plane as shown in Fig. 7.12. Based on these results, we assigned coupling b2 to proton H1' and coupling b3 to H2'. By using the calculated couplings for proton H4, H1' and H2' at <c>, and 14.19MHz as the coupling for N1 listed in Table 7.5, the EIE pattern of R1b for B//<c> can be reproduced well, as is shown in Fig. 7.13.

Table 7.5 *The DFT calculated hyperfine-coupling tensors from the optimized cluster model of the carboxyl anion followed by rotating the carboxyl group with C1-C2 axis to 10° of the carboxyl anion radical of molecule B, and the angular differences between the calculated and experimental eigenvectors.*[a, b]

				Eigenvectors				
Proton	Principal Value[a]	Isotropic value[a]	Anisotropic value[a]	<a>	<b>	<c*>	Coupling	Angle diff (°)[b]
	22.78		10.95	0.236	0.550	-0.801	: b1	11.0
H4	7.54	11.83	-4.29	0.971	-0.168	0.171		
	5.18		-6.65	0.041	0.818	0.574		
	10.41		14.94	0.392	0.913	-0.111		
H1'	-9.72	-4.53	-5.19	0.65	-0.19	0.736		
	-14.28		-9.75	-0.651	0.361	0.668		
	16.43		16.43	0.015	-0.307	0.952		
H2'	-6.47	-7.27	-6.47	0.831	-0.526	-0.183		
	-9.96		-9.96	0.556	0.793	0.248		
	1.64		1.67	0.899	0.432	0.076		
H3'	-0.81	-0.03	-0.81	-0.318	0.76	-0.567		
	-0.86		-0.86	-0.303	0.486	0.82		
	9.07		8.18	-0.561	0.306	0.769		
H4'	-3.21	0.89	-3.21	0.773	0.525	0.355		
	-4.97		-4.97	-0.295	0.794	-0.531		
	15.26		1.06	-0.205	0.424	0.882		
N1	-0.45	14.19	-0.45	-0.414	0.779	-0.471		
	-0.62		-0.62	0.887	0.461	-0.016		

[a] All these values are in units of MHz. [b] The "Angle diff (°)" is the angular difference between the calculated and the experimental eigenvectors associated with the maximum eigenvalues in units of degrees.

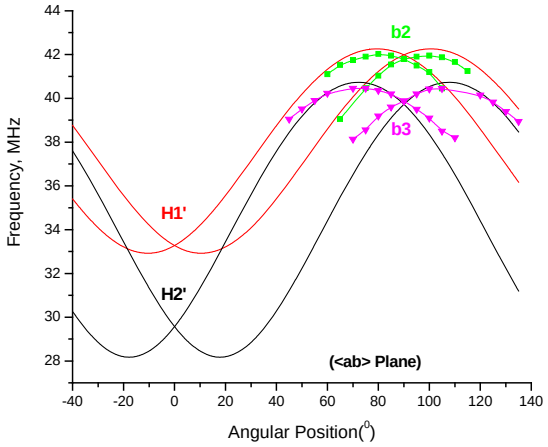

Fig. 7.12 *The measured angular dependence curves of couplings b2 and b3 in <ac> plane were simulated with the calculated tensors from protons H1' and H2'.*

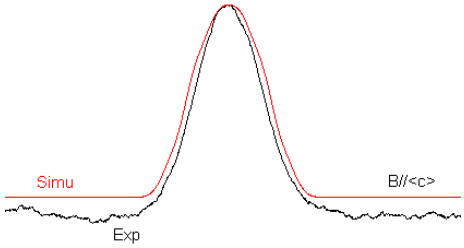

Fig. 7.13 *WINSIM simulation for the EIE pattern (B//<c>) of R1b by using the calculated couplings b1-b2 at <c>.*

Therefore, the model calculations supported the assignment of R1b to the carboxyl anion radical from molecule B with coupling b1 from proton H4, b2 from H1' and b3 from H2'. (H4 is in molecule B, while H1' and H2' transferred to the carboxyl group of molecule B from the neighboring molecules.) The major difference in configurations R1a (the carboxyl anion radical from molecule A) and R1b is that the C-H β-coupling in R1b is much closer to the nodal plane than that in R1a so that the C-H β-coupling in R1b is small and unresolvable in the EPR at any orientation. Also, from the above analysis, the O-H dipolar couplings in R1a and R1b are different: in R1a they are from one main chain amino proton in a neighboring molecule and one water proton; while these in R1b are from main chain amino protons in two different neighboring molecules. We believe that the differences in R1a and R1b are related to their

initial structural difference, and also to the different arrangements of intermolecular hydrogen bonds to their carboxyl groups.

Radical R2-The decarboxylation radical

Four couplings A-D (as labeled in Fig. 7.3a and 7.3c) were assigned to R2. The angular dependence curves of these couplings are shown in Fig. 7.14 and their hyperfine coupling tensors are listed in Table 7.6. The anisotropic components of tensor A are typical for a C-H α-coupling, and tensors B-D are β-couplings with small anisotropy. As shown in Fig. 7.15, the EIE patterns of R2 at three crystallographic axes can be reproduced very well by using tensors A-D. The ENDOR spectrum for B//<c> from the partially deuterated crystal (see Fig. 7.3b) shows that coupling C is from a nonexchangeable proton. (Couplings A, B and D are very weak in the ENDOR spectra from both types of crystal and it is difficult to estimate if they are from exchangeable or nonexchangeable protons.) By choosing ENDOR line C in Fig. 7.3b (from the partially deuterated crystal), the EIE is three-line pattern with peak ratio of 1:2:1 (see Fig. 7.16a), and the EIE of R2 at the same orientation (B//<c>) from the normal crystal is a six-line pattern with peak ratio of 1:2:2:2:2:1 (see Fig. 7.2). These indicate that at least one of couplings A-D is exchangeable.

From these results, there are two possibilities for R2: the radical from dehydrogenation at C5 (Scheme 7.2) and the decarboxylation radical (Scheme 7.4). For the first possibility, the spin is mainly located on C5, and then H9 or H10 provides the α-coupling, while H7, H8 and H11 provide the β-couplings. For this case, H11 is exchangeable. The radical from dehydrogenation at C5 has been identified as one of the stable radicals in the crystal irradiated at 298K. However, tensors A-D are quite different from the tensors of this stable radical detected at 66K and at 298K: as shown in Table 7.7, the angular differences between the eigenvectors of tensor A and tensors α(66K) and α(298K) are more than ~40°; although the maximum eigenvectors[I] of tensors B and C are both close to those of tensors β1(66K)

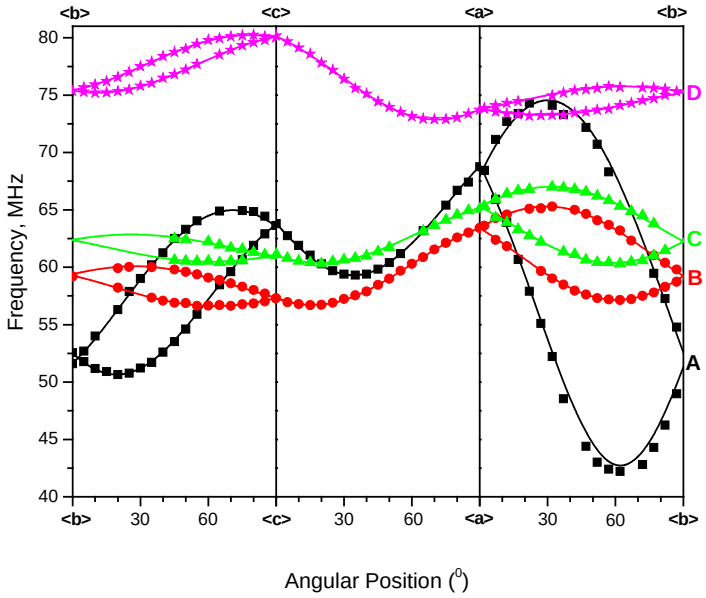

Fig. 7.14 *The angular dependence curves of couplings A-D.*

Table 7.6 *Hyperfine coupling tensors for radical R2 detected in L-arginine·HCl·2H$_2$O single crystals irradiated at 66K.*[a, b]

Coupling	Principal value[a b]	Isotropic value[a b]	Anisotropic value[a b]	Eigenvector[b] <a>	<b>	<c*>
	-82.99(3)		-35.04	0.776(1)	0.445(0)	0.447(0)
A	-47.84(3)	-47.95	0.11	0.419(0)	0.166(1)	-0.893(0)
	-13.02(3)		34.93	0.472(1)	-0.880(0)	0.058(1)
	59.73(2)		12.05	0.835(0)	0.483(1)	0.264(5)
B	42.43(2)	47.68	-5.25	0.550(0)	-0.736(4)	-0.394(6)
	40.89(2)		-6.79	0.005(1)	0.474(8)	-0.880(3)
	62.59(2)		9.29	0.811(1)	0.511(12)	0.286(25)
C	48.80(2)	53.30	-4.50	0.531(1)	-0.436(36)	-0.727(21)
	48.51(2)		-4.79	0.246(1)	-0.741(30)	0.624(35)
	89.84(2)		9.64	-0.301(1)	-0.097(1)	-0.949(0)
D	79.36(2)	80.20	-0.84	0.377(1)	-0.926(0)	-0.025(1)
	71.41(2)		-8.79	0.876(0)	0.365(1)	-0.315(1)

[a.] All of the values are in units of MHz. [b]Numbers in parentheses are the estimated uncertainties in the respective values as reported by the statistical analysis.

and β1(298K) with the angular differences < 10°, the differences for the isotropic values are more than 45MHz; coupling D of 80.20MHz is close to β2(66K) of 83.06MHz and β2(298K) of 89.48MHz, but the angular differences between the eigenvectors of D and those of β2(66K) and β2(298K) are larger than 40°; β3(66K) and β3(298K) of ~22MHz are different from β-couplings B-D. Therefore, the assignment of R2 to the radical of dehydrogenation from C5 can be rejected.

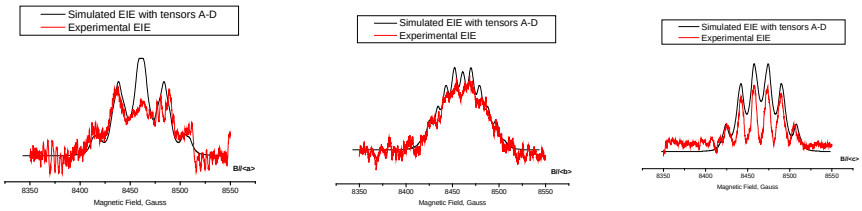

Fig. 7.15 *EIE simulations for radical R2 at crystallographic axes <a>, <b> and <c> with tensors A-D.*

For the decarboxylation radical, the spin is mainly on C2, and H4 is a C-H α-proton, H1-H3 are exchangeable β-protons, and H5 and H6 are nonexchangeable protons. As shown in Table 7.8, the maximum eigenvectors[I] of couplings B-D are close to the corresponding crystallographic directions of a decarboxylated structure in molecules A and B: the maximum eigenvector[I] of tensor D is < 16° from H2…C2; the maximum eigenvectors[I] of tensor B and C are different by 2.5°, thus both the maximum eigenvectors[I] of B and C are close to the directions H1…C2, H5…C2, and H6…C2. Since coupling C is nonexchangeable, it can be ascribed to H5 or H6, and coupling B is ascribed to the exchangeable proton H1. The eigenvector with positive anisotropic component of α-coupling A is ~30° different from H4-C2 in molecules A and B. Using the nonexchangeable couplings A and C at <c>, the EIE pattern for B//<c> from the partially deuterated crystal can be reproduced very well as shown in Fig. 7.16b. From these results, R2 can be assigned to the decarboxylation radical; also, these indicate that there was not much reorientation when the radical was formed. After decarboxylation, the hydrogen bonds of the main chain amino protons and the guanidyl protons fix the radical and make it less moveable. Thus the main

reorientation is the rehybridization of the radical center C2 from sp^3 to sp^2, with the consequence that the direction H4-C2 is significant reoriented (from the comparison above, by ~30°). The characteristic of small reorientation for β-protons has also been found in the decarboxylation radical of irradiated L-lysine monohydrochloride (chapter 5) and L-*O*-serine phosphate single crystals[12].

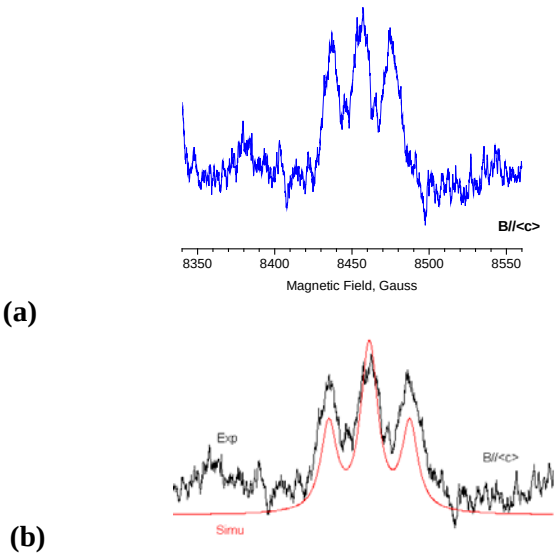

Fig. 7.16(a) *EIE pattern of R2 from the partially deuterated crystal with the magnetic field along <c>;* ***(b)*** *Simulation with couplings A and C at <c> for EIE in (a).*

The rehybridization of the radical center can be studied with McConnell relation[13]

$$a_{iso}(H_\alpha) = Q\rho^{**} \qquad (3)$$

and Gordy-Bernhard relation,[14, 15]

$$a_z = Q^z_{dip}\,\rho^{**}. \qquad (4)$$

Using the isotropic value of coupling A, $a_{iso}(H_\alpha)$ = -47.95MHz, and Q = -73.4MHz[16], then from (3), ρ= 0.65; using the maximum dipolar value of α-coupling A, a_z = 34.93MHz, and Q^z_{dip} = 38.7MHz, then from (4), ρ= 0.90. The evident difference of ρ obtained from (3) and (4) indicates that the radical center did not completely rehybridized to sp^2 configuration, and there is still a bending in C2-H4-N3-C3.[17] This result will be supported by the modeling computations described as follows.

Table 7.7(a) *The comparisons of tensors A-D and the tensors from the radical of dehydrogenation at C5 detected at 66K in the crystal irradiated at 298K.*[a,b]

			Eigenvectors				
Coupling	Isotropic value[a]	Anisotropic value[a]	<a>	<b>	<c*>	:Coupling	Angle diff(°)[b]
		-30.81	0.688	0.408	-0.601		63.5
α(66K)	-59.81	-0.85	-0.726	0.389	-0.567	: A	74.5
		31.66	0.002	0.826	0.564		46.1
		7.51	0.846	0.481	0.229		2.3
β1(66K)	106.60	-5.26	0.533	-0.751	-0.391	: B	0.6
		-2.25	-0.016	0.453	-0.892		1.6
		7.51	0.846	0.481	0.229		4.1
β1(66K)	106.60	-5.26	0.533	-0.751	-0.391	: C	26.5
		-2.25	0.016	-0.453	0.892		26.3
		8.93	-0.352	-0.936	-0.013		77.9
β2(66K)	83.06	-4.15	0.337	-0.14	0.931	: D	76.5
		-4.78	0.873	-0.324	-0.364		40.4
		9.42	0.206	0.571	-0.795		
β3(66K)	24.97	-2.62	0.726	-0.634	-0.266		
		-6.80	0.656	0.522	0.545		

[a]All the values are in units of MHz. [b] "Angle differ(°)" is the angular difference between the calculated and the experimental eigenvectors associated with the maximum eigenvalues.

Table 7.7(b) *The comparisons of tensors A-D and the tensors from the radical of dehydrogenation at C5 detected at 298K in the crystal irradiated at 298K.*[a,b]

			Eigenvectors				
Coupling	Isotropic value[a]	Anisotropic value[a]	<a>	<b>	<c*>	:Coupling	Angle diff(°)[b]
		-32.76	0.695	0.421	-0.582		62.2
α(298K)	-56.76	1.26	-0.717	0.355	-0.600	: A	72.9
		31.50	0.046	-0.835	-0.549		43.6
		6.62	0.752	0.612	0.245		8.8
β1(298K)	98.876	-4.31	0.641	-0.592	-0.489	: B	11.2
		-2.30	-0.155	0.524	-0.837		10.2
		6.62	0.752	0.612	0.245		6.9
β1(298K)	98.876	-4.31	0.641	-0.592	-0.489	: C	17.4
		-2.30	0.155	-0.524	0.837		18.4
		7.51	-0.279	-0.96	-0.036		77.8
β2(298K)	89.48	-3.58	0.959	0.276	-0.067	: D	83.8
		-3.93	-0.055	-0.053	-0.997		75.7
		8.71	0.345	0.592	-0.728		
β3(298K)	22.38	-2.65	0.776	-0.616	-0.133		
		-6.06	0.528	0.519	0.672		

[a] All the values are in units of MHz. [b] "Angle differ(°)" is the angular difference between the calculated and the experimental eigenvectors associated with the maximum eigenvalues.

In addition, the configuration of β-protons can be estimated with Heller-McConnell relation (1)[9]. Using the isotropic values of couplings B-D, and $B_1\rho$ = 125MHz for the decarboxylation radical[18], the configuration angles for B-D are 51.9°, 49.2°, 36.8°, respectively. In the undamaged crystal, assuming the spin orbital is along the former C2-C1 bond of molecules A and B, configuration angles for the β-protons are ~38°(H1), ~25°(H2), ~85°(H3), ~53°(H5), ~62°(H6). The configuration angle of H2 is smallest and suggests H2 would have the largest coupling. The larger configuration angles of H3 and H6 indicate that these two protons are closer to the nodal plane and should have much smaller couplings. H1 and H5 with moderate configuration angle should have moderate couplings. These results are consistent with the above directional comparisons: coupling D of 80.2MHz is largest and its eigenvector[I] is most parallel with direction of H2…C2; couplings B (47.68MHz) and C (53.30MHz) are moderate, and their eigenvectors[I]

are most parallel with directions H1…C2 and H5…C2, respectively. Couplings from H3 and H6 could not be observed, which is consistent with their larger configuration angles and too small couplings. Therefore, these analyses further support the assignment of R2 to the decarboxylation radical.

Table 7.8 *The comparison of the eigenvectors[a] of couplings A-D to the corresponding crystallographic directions in the decarboxylation radicals from molecules A and B.[b,c]*

	Eigenvectors[a]				Directions of Hx….C2 in MA			
Couplings	<a>	<b>	<c*>	protons	<a>	<b>	<c*>	Angle Diff (°)[b]
A	0.472	-0.88	0.058	H4	0.203	-0.89	0.408	25.5
B	0.835	0.483	0.264	H1	0.760	0.557	0.336	7.1
C	0.811	0.511	0.286	H1	0.760	0.557	0.336	4.4
B	0.835	0.483	0.264	H5	0.823	0.512[c]	0.245	2.3
C	0.811	0.511	0.286	H5	0.823	0.512[c]	0.245	2.4
B	0.835	0.483	0.264	H6	0.912	0.262	0.316	13.7
C	0.811	0.511	0.286	H6	0.912	0.262	0.316	15.4
D	0.301	0.097	0.949	H2	0.326	0.363	0.873	15.9

	Eigenvectors[a]				Directions of Hx….C2 in MB			
Couplings	<a>	<b>	<c*>	protons	<a>	<b>	<c*>	Angle Diff (°)[b]
A	0.472	-0.880	0.058	H4	0.069	-0.93	0.362	29.3
B	0.835	0.483	0.264	H1	0.842	0.360	0.402	10.6
C	0.811	0.511	0.286	H1	0.842	0.360	0.402	10.9
B	0.835	0.483	0.264	H5	0.720	0.641[c]	0.266	11.2
C	0.811	0.511	0.286	H5	0.720	0.641[c]	0.266	9.1
B	0.835	0.483	0.264	H6	0.956	0.089	0.279	23.8
C	0.811	0.511	0.286	H6	0.956	0.089	0.279	25.8
D	0.301	0.097	0.949	H2	0.301	0.301	0.905	11.9

[a]The eigenvectors are the principal directions associated with the largest coupling components. [b]"Angle Diff (°)" are the angular differences between the experimental eigenvectors and the crystallographic directions in units of degrees. [c]The sign of the y component is changed due to the symmetry of the monoclinic system.

Modelling calculations for R2: The single molecule models for the decarboxylation radical in molecules A and B were constructed by taking the atomic coordinates of molecules A and B from the crystallographic studies[7], and removing the carboxyl group from molecules A and B. To simulate the envirormental effects on the radical, the PCM model was used in the geometry optimization by adding the keyword "scrf=PCM". In this method, the radical was surrounded with a dielectric medium with the dielectric constant of water (78.39).[19-22] In addition, the above results indicate that the β-protons had little

reorientation, thus the three main chain amino protons were frozen during the PCM optimizations. The optimizations for molecule A and B were performed using B3LYP/6-31G(d,p) followed by the single point calculations on the corresponding optimized structures using B3LYP/6-311G(2d,p). The calculations show that: the spins are 0.99 located on C2 of molecule A and B; the eigenvectors of the calculated tensors from H4 in molecule A and B are close to those of tensor A with angular differences for the eigenvectors < 15°; the maximum eigenvectors[l] of the calculated β-couplings from H1, H2 and H5 in molecule A and B are close to those of couplings B, D and C, respectively, with the angular differences < 20°. However, the calculations also show that some of the results are inconsistent with the experimental results: the computed radical centers were completely rehybridized to sp^2 and became purely planar configurations with the torsion angle <C3-N1-H4-C2 of ~10° for molecules A and B, and thus the differences for α-coupling from H4 and coupling A is larger than 15MHz. Also, the calculated β-coupling values are ~30MHz (H1), ~120MHz (H2), ~24MHz (H3), ~34MHz (H5) and ~30MHz (H6), and are quite different from the experimental ones: coupling B of 47.68MHz (H1), C of 53.30MHz (H5) and D of 80.20MHz (H2). To improve the calculated couplings, three adjustments were performed manually on the optimized radical structure from molecules A and B: 1) bending H4 by 20°, (then torsion angle <C3-N1-H4-C2 still are ~15° less than that in the undamaged molecules A and B); 2) rotating the main chain amino protons about N1C2 axis by ~15°; 3) rotating the whole side chain about the C2C3 axis by 20°. The final radical structures from molecules A and B are shown in Fig. 7.17. The single point calculations on the final structures from molecules A and B are listed in Table 7.9. All the calculated tensors agree very well with the experimental tensors. Therefore, the modeling calculations not only support the assigment of R2 to the decarboxylation radical, they also confirm the characteristics from the above analysis: the radical center was not completely rehybridized to sp^2 with a bending structure and all the β-protons experienced small reorientation.

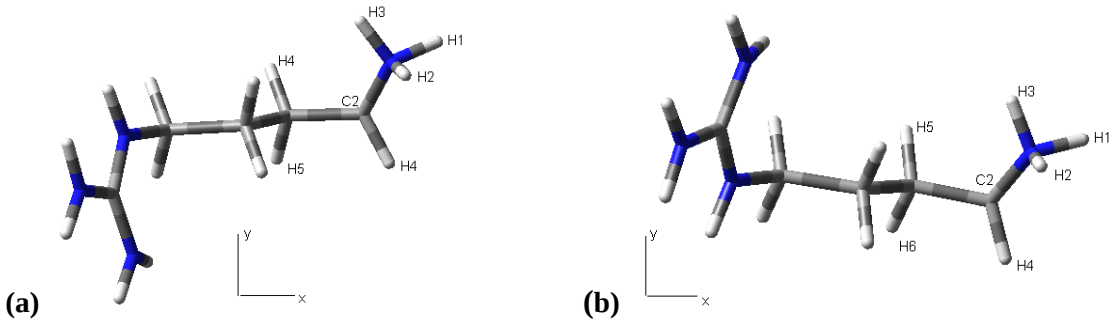

(a) **(b)**

Fig.7.17 *The final models for the decarboxylation radical from molecules A* ***(a)*** *and B* ***(b)****.*

Table 7.9 (a) *The calculated hyperfine coupling tensors from the final models for the decarboxylation radical of molecule A.*[a, b]

			Eigenvectors				
Proton	Isotropic value[a]	Anisotropic value[a]	<a>	<b>	<c*>	: Coupling	Angle diff (°)[b]
		12.50	0.692	0.597	0.407	:B	13.2
H1	62.61	-5.92	0.721	-0.535	-0.441		
		-6.58	-0.045	0.598	-0.800		
		8.61	-0.411	-0.324	-0.852	:D	15.5
H2	88.26	-3.22	0.396	-0.905	0.153		
		-5.39	0.821	0.275	-0.500		
		9.32	-0.050	0.791	0.609		
H3	0.83	-3.89	0.218	-0.587	0.780		
		-5.43	0.975	0.172	-0.143		
		-36.67	0.760	0.420	0.496		3.3
H4	-41.43	-4.70	0.480	0.151	-0.864	:A	3.9
		41.37	0.438	-0.895	0.087		2.0
		10.76	0.879	-0.406	0.250	:C	7.3
H5	63.4	-5.11	0.466	0.842	-0.271		
		-5.65	-0.100	0.355	0.930		
		10.06	0.822	0.460	0.336		
H6	5.46	-4.50	-0.216	-0.294	0.931		
		-5.56	-0.527	0.838	0.143		

[a] All these values are in units of MHz. [b] The "Angle diff (°)" is the angular difference between the calculated and the experimental eigenvectors associated with the maximum eigenvalues in units of degrees.

Table 7.9 (b) *The calculated hyperfine coupling tensors from the final models for the decarboxylation radical of molecule B.*[a, b]

			Eigenvectors				
Proton	Isotropic value[a]	Anisotropic value[a]	<a>	<b>	<c*>	: Coupling	Angle diff (°)[b]
		12.61	0.774	0.493	0.397	:B	8.4
H1	62.37	-6.06	0.627	-0.507	-0.592		
		-6.55	-0.091	0.707	-0.702		
		8.43	-0.442	-0.271	-0.855	:D	13.9
H2	86.60	-3.17	0.158	-0.962	0.223		
		-5.26	0.883	0.036	-0.468		
		9.32	0.125	0.811	0.572		
H3	1.09	-3.91	-0.064	-0.568	0.820		
		-5.41	0.990	-0.139	-0.019		
		-36.52	0.820	0.260	0.510		11.5
H4	-42.41	-4.87	0.528	0.002	-0.850	:A	11.3
		41.39	0.222	-0.966	0.135		15.7
		10.64	0.766	-0.591	0.253	:C	5.4
H5	52.35	-5.15	0.636	0.755	-0.161		
		-5.49	-0.095	0.284	0.954		
		10.25	0.885	0.270	0.380		
H6	10.01	-4.69	-0.301	-0.292	0.908		
		-5.56	-0.356	0.918	0.177		

[a] All these values are in units of MHz. [b] The "Angle diff (°)" is the angular difference between the calculated and the experimental eigenvectors associated with the maximum eigenvalues in units of degrees.

Radical R3-one electron trapped by the guanidyl group

From the EIE patterns at three crystallographic axes, ENDOR lines 1 and 2 were assigned to R3. However, couplings in addition to 1 and 2 are necessary to reproduce these EIE patterns. The differences of the EIE widths at three crystallographic axes and the corresponding sums of couplings 1 and 2 are ~25G. These differences indicate that R3 includes at least one additional coupling, which was not observed in the ENDOR experiments. From the WINSIM simulations, as is shown in Fig. 7.18a, the EIE pattern for B//<c> was reproduced very well when the missing coupling was taken to be 13.35G (37.38MHz) from spin = 1 (a nitrogen atom). An aulternative possibility is to set the miss couplings as

two from protons (spin = 1/2) of ~13G (36.40MHz), but the simulated pattern has quite different peak ratio from the experimental EIE for B//<c>, although the two patterns are in very similar width, as is shown in Fig. 7.18b. Moreover, the EIE patterns for B//<a> and for B//<b> can also be reproduced very well by using the missing coupling of ~13G from a nitrogen atom (see Fig. 7.18c and 7.18d). Therefore, the WINSIM simulations indicate that the missing coupling, denoted as coupling 3, is a nitrogen coupling of ~13G at three axes; while the nitrogen coupling is generally difficult to detect in the ENDOR experiment.

The angular dependence curves of couplings 1 and 2 are shown in Fig. 7.19, and the corresponding hyperfine coupling tensors are listed in Table 7.10. Both couplings 1 and 2 are β-couplings with small anisotropy. As are shown in Fig. 7.3b and 7.3d, couplings 1 and 2 were not observed in the ENDOR spectra from the partially deuterated crystals. This indicates that both couplings are from exchangeable protons, i.e., protons bonded to nitrogen or oxygen atoms. However, coupling 1 is very unlikely to be from an O-H β-proton: its anisotropic values are smaller than those of typical O-H dipolar couplings (only 6.72MHz, -2.21MHz, and -4.51MHz); also its isotropic value of 93.26MHz is much larger than those of the O-H dipolar couplings in R1a and R1b (<10MHz); moreover, its maximum eigenvector[I] is very different from the crystallographic directions C1…Hx' in molecules A and B. (The smallest angular difference is 30.2°, as listed in Table 7.11.) Hx' are the protons H1'-H4' that are hydrogen bonded to O1 and O2 in molecule A and B, as shown in Fig. 7.7b and Fig. 7.11b. Therefore, coupling 1 must be from a N-H β-proton, and not from an O-H β-proton. In arginine molecular (Scheme 7.1), the nitrogen atoms are at least three bonds away from oxygen, thus coupling 2 could not be from an O-H β-proton, if coupling 1 is from a N-H β-proton. In summary, both couplings are from N-H β-protons.

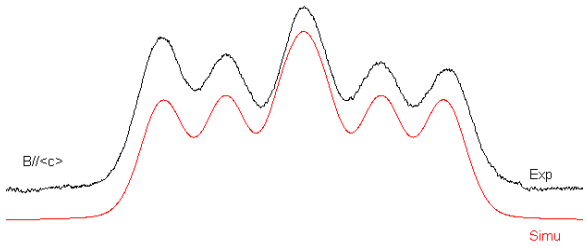

(a)

Coupling	Value(G)	Spin
1	3.70	0.5
2	32.89	0.5
3	13.35	1.0

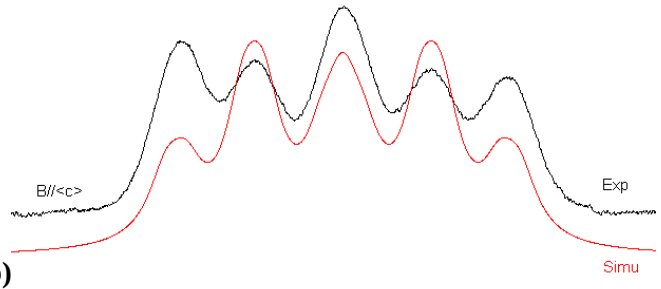

(b)

Coupling	Value(G)	Spin
1	3.70	0.5
2	32.90	0.5
3	14.85	0.5
4	13.96	0.5

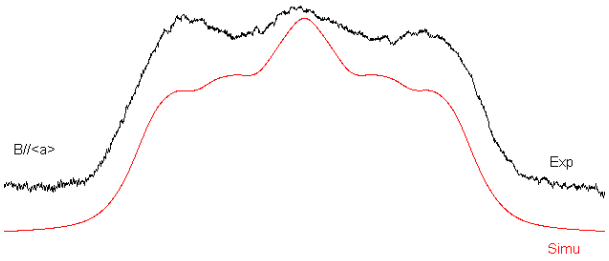

(c)

Coupling	Value(G)	Spin
1	5.04	0.5
2	31.86	0.5
3	12.52	1.0

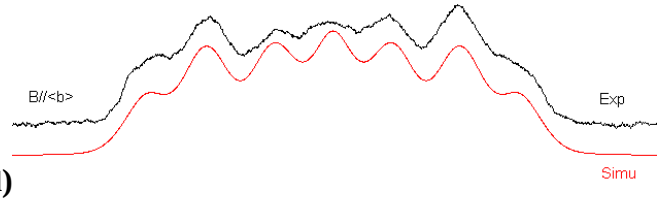

(d)

Coupling	Value(G)	Spin
1	9.90	0.5
2	35.20	0.5
3	12.87	1.0

Fig. 7.18 *WINSIM simulations of the R3 EIE patterns for B//<c>* ***(a)*** *and* ***(b)*** *for B//<a>* ***(c)*** *and for B//<b>* ***(d)****. In (a), one nitrogen coupling was set the missing coupling and in (b), two proton couplings were set as the missing couplings. The tables on the right side show the couplings used in the simulations.*

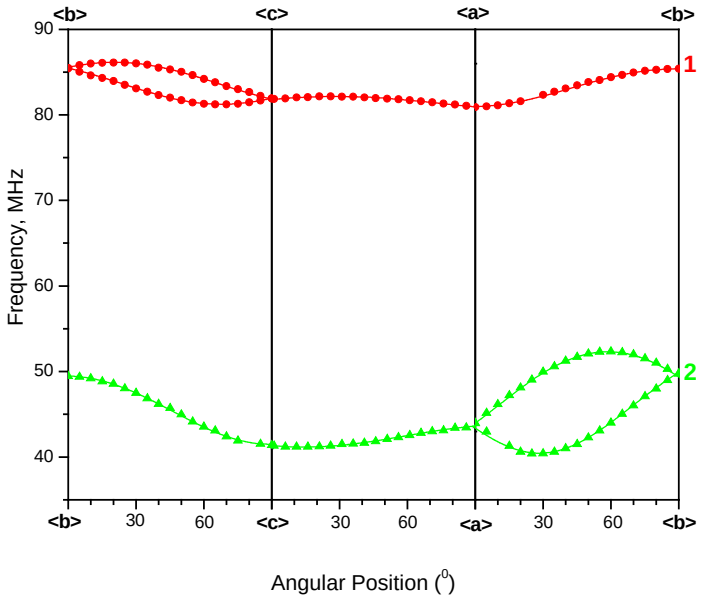

Fig. 7.19 *Angular dependence curves for R3 couplings 1 and 2.*

Table 7.10 *Hyperfine coupling tensors for radical R3 in L-arginine·HCl·H_2O single crystals irradiated at 66K .*[a, b]

Coupling	Principal value[a b]	Isotropic value[a b]	Anisotropic value[a b]	Eigenvector[b] <a>	<b>	<c*>
	99.98(2)		6.72	0.069(1)	-0.926(3)	-0.370(3)
1	91.05(2)	93.26	-2.21	0.654(0)	0.322(1)	-0.685(2)
	88.75(2)		-4.51	0.754(1)	-0.195(2)	0.628(3)
	32.65(2)		15.27	0.502(1)	-0.864(4)	0.025(2)
2	11.13(3)	17.38	-6.25	0.376(0)	0.244(2)	0.894(2)
	8.36(2)		-9.02	0.779(1)	0.440(2)	-0.448(5)

[a]All of the values are in units of MHz. [b]Numbers in parentheses are the estimated uncertainties in the last digit quoted as reported by the statistical analysis.

Based on these characteristics, there are two possibilities for R3. One is from dehydrogenation of H4 (see Scheme 7.7) with the spin mainly located on C2; thus two of three main-chain amino β-protons and the α-nitrogen in this radical could provide couplings 1-3, and the remaining couplings could be too small to be detected if the corresponding protons are very close to the nodal plane of the radical. The H4 dehydrogenation radical has been identified as one of stable radicals in L-arg·HCl crystals irradiated at

room temperature. As listed in Table 7.12, the isotropic couplings of this stable radical are 136.36MHz (C-H β-coupling), 70.01MHz and 55.96MHz (N-H β-couplings) detected at 66K, and are 117.54MHz (C-H β-coupling), 71.48MHz and 52.19MHz (N-H β-couplings) detected at room temperature, and the nitrogen coupling is only -4.65MHz from the modeling calculation. These couplings are quite different from those measured for R3: N-H β-couplings of 93.26MHz (coupling 1) and 17.38MHz (coupling 2), nitrogen coupling of 39.2MHz (coupling 2), and no C-H coupling were detected. Therefore, it's unlikely that R3 is the radical from H4 dehydrogenation.

Table 7.11 *The comparison of the maximum eigenvector[a] of coupling 1 and the crystallographic directions of Hx'…C1 in molecule A and B.[b,c]*

	Eigenvectors[a]				Directions of Hx'….C1 in MA[b]			
Coupling	<a>	<b>	<c*>	proton	<a>	<b>	<c*>	Angle Diff (°)[c]
1	0.069	-0.926	-0.370	H1'	0.138	-0.546	-0.826	34.8
				H2'	0.998	-0.049	-0.028	82.8
				H3'	0.672	-0.504	-0.543	44.4
				H4'	-0.433	-0.868	-0.244	30.2
	Eigenvectors[a]				Directions of Hx'….C1 in MB[b]			
Couplings	<a>	<b>	<c*>	proton	<a>	<b>	<c*>	Angle Diff (°)[c]
1	0.069	-0.926	-0.370	H1'	0.422	-0.902	0.096	34.0
				H2'	-0.037	-0.120	-0.992	61.6
				H3'	0.901	-0.434	0.014	62.7
				H4'	0.69	-0.339	-0.639	53.2

[a] The eigenvectors are those associated with the maximum coupling components. [b] Hx' are the neighboring protons H1'-H4' hydrogen bonded to the carboxyl group in molecule A (see Fig. 7.7b) and molecule B (see Fig. 7.11b) [c] "Angle Diff (°)" are the angular differences between the experimental eigenvectors and the crystallographic directions in units of degrees.

The other possibility for R3 is the "guanidyl anion" radical (see scheme 7.6). This radical is the result of electron trapped by the guanidyl center atom C6, and can exhibit five N-H β-couplings and three α nitrogen couplings. Table 7.13 lists the comparison between the maximum dipolar vectors[I] of couplings 1 and 2 and the crystallographic directions of Hx…C6 (x = 11, 12…15, respectively) in both molecules A and B. Both the maximum dipolar vectors[I] of coupling 1 and 2 are close to the direction H11…C6 and also to H13…C6 in molecule A and B with similar angular differences. These results suggest that

coupling 1 is from H11 or H13, but since the directions H11…C6 and H13…C6 are very close, and coupling 1 cannot be definitely ascribed to H11 or to H13 just from this comparison related to the maximum eigenvector[l]; coupling 2 cannot be ascribed to H11 or H13 due to the same reason. Thus, these comparisons indicate that couplings 1 and 2 arise from N-H β-protons H11 and H13, but they do not allow assigning the couplings to specific protons. Similarly, the couplings might be from either molecule A, molecule B, or both. However, the modeling calculations described follows will support the assignment of R3 to the guanidyl anion and gives the assignments of coupling 1→H13, 2→H11, 3→N3 from the comparisons related to the isotropic and anisotropic values.

Table 7.12 *The comparisons of the couplings from R3 and the couplings from the radical of dehydrogenation at H4 detected at 66K and at 298K in the crystal irradiated at 298K.*[a-d]

Coupling[a]	Isotropic value[b]	Coupling[c]	Isotropic value[b]	Coupling[d]	Isotropic value[b]
		C-H β (298K/66K)	136.36	C-H β (298K/298K)	117.54
N-H β	93.26	N-H β (298K/66K)	70.01	N-H β (298K/298K)	71.48
N-H β	17.38	N-H β (298K/66K)	53.96	N-H β (298K/298K)	52.19
Nitrogen	~36.20	Calculated nitrogen coupling			-4.65

[a]The couplings were from R3 [b]All the values are in units of MHz. [c]The couplings from the radical of dihydrogenation at H4 detected at 66K in the crystal irradiated at 298K. [d] The couplings from the radical of dihydrogenation at H4 detected at 298K in the crystal irradiated at 298K.

Cluster modeling calculations for R3: Cluster models were constructed for the guanidyl anion by using the crystallographic coordinates from X-ray diffraction studies on L-arg·HCl single crystal. The cluster model for molecule A includes the center molecule A, two neighboring waters (I-III), and a protion of a neighboring molecule B. These contain atoms in intermolecular hydrogen bonds to the guanidyl group of the molecule A. As shown in Fig. 7.20a, I and II are neighboring water molecules, whose oxygen atoms are hydrogen bonded to H15 and H16; III contains the main chain groups (carboxyl group, amino group, carbon and hydrogen atoms) of a neighboring B molecule, the remainder of which is

reproduced by a hydrogen atom for simplification. In III, O1' and H3' are hydrogen bonded respectively to H12 and O1 of the center molecule. (H11 and H13 of molecule A in the crystal are hydrogen bonded to two different Cl^- atoms, which were omitted in our cluster model.) To simulate the anion radical, one electron was added to the whole cluster. The cluster model was optimized with DFT procedures using B3LYP/6-31G(d, p). During optimization, some atoms were frozen (marked "f" in Fig. 7.20a) to simulate the other crystallographic environmental effects, but the guanidyl group and side chain of the center molecule were fully optimized. The optimized clusters are shown in Fig. 7.20b. The most evident geometric change is that the planar guanidyl group became tetrahedral with the torsion angle <N2-N4-N3-C6 of 22.8°. Single point calculation performed on the optimized cluster model using B3LYP/6-311G(2d, p) indicates that the spin is mainly located on C6 (0.72). The coupling tensor calculated for H13 is very close to measured tensor 1. However, no calculated tensors compare well with measured tensor 2. Also, the calculation indicates two large nitrogen couplings (61.33MHz from N2 and 46.13MHz from N3), and these are inconsistent with the experimental results showing only one large nitrogen coupling (~36MHz). Since the hydrogen bond H11…Cl^- is omitted in the cluster model, and it was unconstrained in the optimization, H11 in the optimized model was bent manually toward the direction H11…Cl^- by ~30° (see Fig. 7.20c). With this change, the calculated tensors from H13 and H11 are in good agreement with experimental tensors 1 and 2. Also, from the adjusted structure, there is only one large nitrogen coupling of 40.29MHz from N3. This is in good agreement with experimental coupling 3 (~36MHz). The computed coupling of 25.91MHz from H14 in the adjusted model has no corresponding experimental one. Thus, in the next step, H14 and H15 were rotated manually about the C6-N4 axis by 15°. The calculated tensors from the final adjusted model are listed in Table 7.14. From comparisons of the isotropic and anisotropic values and the eigenvectors, it can be seen that couplings 1 and 2 are in very good agreement with calculated couplings from H13 and H11; also, coupling 3 is close to the calculated nitrogen coupling from N3; the couplings from H14 and H15 are 7.17MHz and 7.62MHz, respectively, and become acceptable. Therefore, the cluster modeling calculation for molecule A support the

assignment of R3 to the guanidyl radical anion, and we can ascribe coupling 1 to H13, 2 to H11, and 3 to N3. (Here H11, H13 and N3 are atoms in molecule A.)

Table 7.13 *The comparison between the eigenvectors[a] of couplings 1 and 2 and the corresponding crystallographic directions of the guanidyl anion radical in molecule A and B.[b,c,d]*

	Eigenvectors[a]				Directions of Hx….C6 in MA[b]			
Coupling	<a>	<b>	<c*>	proton	<a>	<b>	<c*>	Angle Diff (°)[c]
1	0.069	-0.926	-0.37	H11	-0.131	-0.956	-0.261	13.4
				H12	0.632	-0.561	-0.535	40.4
				H13	0.210	-0.978	-0.011	22.5
				H14	0.728	-0.342	-0.595	54.1
				H15	-0.374	-0.362	0.854	90.4
	Eigenvectors[a]				Directions of Hx….C6 in MB[b]			
Coupling	<a>	<b>	<c*>	proton	<a>	<b>	<c*>	Angle Diff (°)[c]
1	0.069	-0.926	-0.37	H11	-0.239	-0.944	-0.229	19.5
				H12	0.772	-0.482	-0.414	49.2
				H13	0.311	-0.948	-0.068	22.4
				H14	0.752	-0.233	-0.617	60.3
				H15	-0.400	-0.385	0.832	88.8
	Eigenvectors[a]				Directions of Hx….C6 in MA[b]			
Coupling	<a>	<b>	<c*>	proton	<a>	<b>	<c*>	Angle Diff (°)[c]
2	0.502	-0.864	0.025	H11	0.131	-0.956[d]	0.261	26.1
				H12	-0.632	0.561	0.535	79.6
				H13	0.210	-0.948	-0.011	18.2
				H14	0.728	-0.342	-0.595	54.1
				H15	-0.374	-0.362	0.854	90.4
	Eigenvectors[a]				Directions of Hx….C6 in MB[b]			
Coupling	<a>	<b>	<c*>	proton	<a>	<b>	<c*>	Angle Diff (°)[c]
2	0.502	-0.864	0.025	H11	0.239	-0.944[d]	0.229	19.7
				H12	0.772	-0.482	-0.414	92.2
				H13	0.311	-0.948	-0.068	13.2
				H14	0.752	-0.233	-0.617	80.7
				H15	0.400	0.385	-0.832	59.2

[a] The eigenvectors are those associated with the maximum coupling components.[b] Hx are H11-H15 in molecule A (MA) and molecule B (MB) [c] "Angle Diff (°)" are the angular differences between the experimental eigenvectors and the crystallographic directions in units of degrees.[d] The sign of this vector's y component is changed to "+" from "-" due to the symmetry of monoclinic crystal.

Similar cluster modeling calculations were performed for the guanidyl anion of molecule B (see Fig. 7.21) Also, the optimized cluster indicates that the planar guanidyl group of molecule B in the crystal became tetrahedral with torsion angle <N2-N4-N3-C6 of 25.5°. From the single point calculation on the

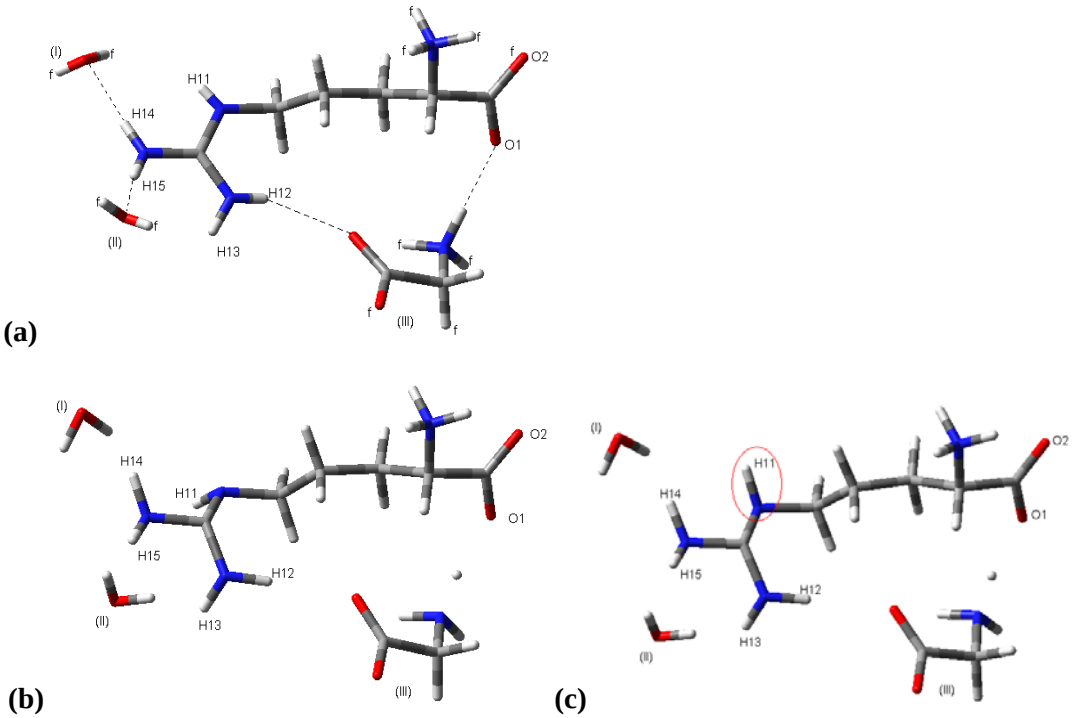

Fig. 7.20 *The cluster model for the guanidyl anion radical in molecule A.* ***(a)*** *The initial cluster model; the dash lines show the crystallographic hydrogen bonds;* ***(b)*** *the optimized cluster model;* ***(c)*** *the adjusted cluster model by bending H11.*

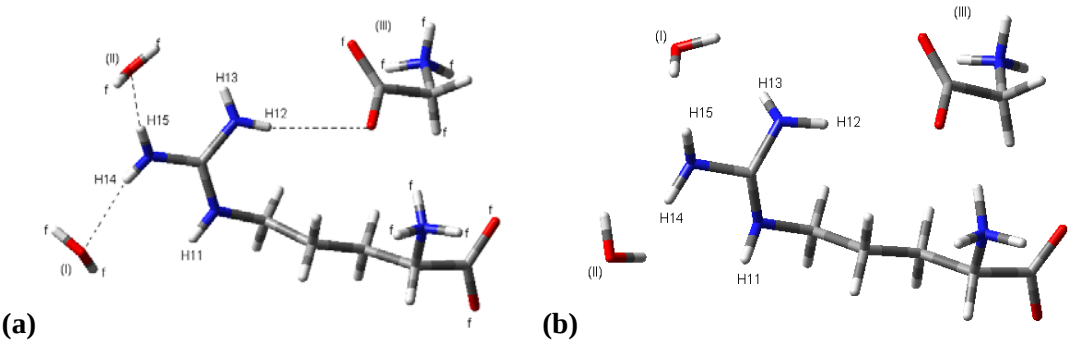

Fig. 7.21 *The cluster model for the guanidyl anion radical in molecule B.* ***(a)*** *The initial cluster model; the dash lines show the crystallographic hydrogen bonds;* ***(b)*** *H12 and H13 rotated with N3-C6 axis by 10°, H14 and H15 rotated with N4-C6 by 5° on the optimized cluster model.*

optimized structure, the spin is mainly on C6 (0.73). The calculated tensors from H11 and H13 are in good agreement with couplings 2 and 1; however, the couplings of 14.11MHz (from H12) and 13.90MHz (from H15) were not detected in the experiment. Thus to seek a structure compatible with these couplings, H12 and H13 were rotated manually about N3-C6 axis by 10°, H15 and H16 were rotated manually by 5°

about N4-C6 axis. The tensors calculated from the final structure are listed in Table 7.15. These from H11 and H13 agree very well with experimental tensors 2 and 1, respectively, and the nitrogen coupling from N3 (39.55MHz) is very close to the experimental coupling 3 (~36MHz). In addition, the couplings from H12 and H15 decreased to 4.17MHz and 8.61MHz. Thus, from the modeling calculation for molecule B, we can assign R3 to the guanidyl anion radical, and ascribe coupling 1 to H13, 2 to H11, and 3 to N3. (Here, H13, H11, and N3 are atoms in molecule B)

Table 7.14 *The calculated coupling tensors from the adjusted cluster model of the guanidyl radical anion in molecule A.*[a,b]

			Eigenvectors				
Proton	Isotropic value[a]	Anisotropic value[a]	<a>	<b>	<c*>	: Coupling	Angle diff (°)[b]
		15.1	0.321	-0.945	0.053		11.8
H11	11.64	-5.66	0.481	0.212	0.851	:2	6.6
		-9.45	0.816	0.248	-0.522		11.9
		10.07	-0.449	0.616	0.648		
H12	-1.41	-3.74	0.161	0.769	-0.619		
		-6.33	0.879	0.174	0.444		
		7.13	-0.183	-0.942	-0.280		15.6
H13	105.3	-2.63	0.641	0.102	-0.761	:1	13.3
		-4.50	0.745	-0.319	0.586		7.3
		13.18	-0.668	0.700	0.251		
H14	7.17	-5.07	0.738	0.666	0.108		
		-8.10	0.092	-0.257	0.962		
		12.59	-0.191	-0.477	0.858		
H15	7.62	-4.71	0.960	0.093	0.266		
		-7.88	-0.207	0.874	0.440		
		3.63	0.154	0.209	0.966		
N3	48.09	-1.19	-0.68	0.732	-0.05		
		-2.44	0.717	0.649	-0.255		
N1	0.55						
N2	-1.00						
N4	-1.94						

[a] All these values are in units of MHz. [b] The "Angle diff (°)" is the angular difference between the calculated and the experimental eigenvectors associated with the maximum eigenvalues in units of degrees.

Therefore, from the above results, R3 can be assigned to the guanidyl anion radical from molecules A and B, and couplings 1-3 can be assigned to H13, H11 and N3, respectively. The other β-protons in the anion radical are closer to the nodal plane and were not detected.

Table 7.15 *The calculated coupling tensors from the adjusted cluster model of the guanidyl radical anion in molecule B.*[a,b]

			Eigenvectors				
Proton	Isotropic value[a]	Anisotropic value[a]	<a>	<b>	<c*>	: Coupling	Angle diff (°)[b]
		15.96	0.263	-0.955	-0.136		17.5
H11	12.46	-6.08	0.555	0.035	0.832	:2	16.0
		-9.89	0.790	0.294	-0.539		9.5
		10.37	-0.490	-0.492	0.720		
H12	4.17	-3.41	-0.275	0.870	0.409		
		-6.95	0.827	-0.002	0.562		
		6.84	-0.169	-0.827	-0.536		17.7
H13	100.34	-2.58	0.589	0.351	-0.728	:1	4.5
		-4.26	0.791	-0.438	0.428		18.1
		13.56	0.649	0.624	-0.435		
H14	8.61	-5.04	0.757	-0.588	0.285		
		-8.52	0.078	0.514	0.854		
		13.05	-0.185	0.677	0.713		
H15	5.07	-4.69	0.975	0.034	0.222		
		-8.36	0.126	0.736	-0.666		
		2.71	0.022	0.032	0.999		
N3	39.55	-0.73	0.600	0.799	-0.039		
		-1.98	0.800	-0.600	0.002		
N1	0.09						
N2	-0.01						
N4	-2.65						

[a] All these values are in units of MHz. [b] The "Angle diff (°)" is the angular difference between the calculated and the experimental eigenvectors associated with the maximum eigenvalues in units of degrees.

Radical R4-the radical of dehydrogenation from C5

The EIE pattern of R4 was only observed for B//<c> and is shown in Fig. 7.2. The peak ratio in the EIE of ~1:1:2:2:2:2:1:1 suggested that there are more than two couplings contributed to the pattern. However, only one ENDOR line "R4-I" was assigned to R4 as shown in Fig. 7.3. Also, as shown in Fig. 7.3a and 7.3b, coupling R4-I has the same intensity in the ENDOR spectrum for B//<c> from the normal crystal and from the partially deuterated crystal. This indicates that coupling R4-I is from a nonexchangeable proton. The angular dependence curve of R4-I shows large anisotropy in all three rotation planes (see Fig. 7.22). The hyperfine coupling tensor R4-I listed in Table 7.16 confirmed that R4-I is a typical C-H α-coupling.

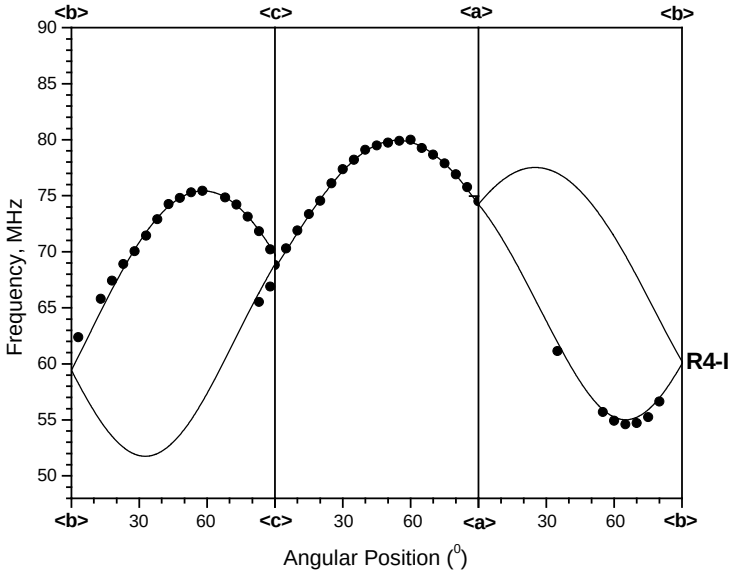

Fig. 7.22 *Angular dependence curve for coupling R4-I.*

WINSIM simulations indicate that the EIE pattern of R4, shown in Fig. 7.2, can be reproduced in two ways: (1) with coupling R4-I at <c> of 25.19G (70.53MHz) and three other proton couplings of 34.27G (95.96MHz), 29.57G (82.80MHz), 8.84G (24.75MHz) as shown in Fig. 7.23a;, (2) with R4-I along with one proton coupling of 7.73G (21.64MHz) and one nitrogen coupling of 29.40G (82.32MHz) in addition with the measured coupling R4-I at <c> (75.88MHz) as shown in Fig. 7.23b. However, it is

very unlikely that R4 is from the second group of couplings because the nitrogen coupling of 82.3MHz is too large for any reasonable structure. For example, the α nitrogen coupling in R3 (the guanidyl anion) is only ~14G (39.2MHz), and the α nitrogen couplings in R1a/R1b (the carboxyl radical anions) and in R2 (the decarboxylation radical) are smaller than 10MHz. If this large nitrogen coupling is due to the spin mainly located on a nitrogen atom, then it will be inconsistent with the result that coupling R4-I is from a C-H α proton. Based on these reasons, we can rule out the second possibility in the WINSIM simulation for R4, and conclude that the main couplings of R4 are from four protons.

Table 7.16 *Hyperfine coupling tensors for R4 in L-arginine hydrochloride monohydrate single crystal irradiated at 66K.* [a,b]

				Eigenvectors[b]		
Coupling	Principal value[a,b]	Isotropic value[a]	Anisotropic value[a]	<a>	<b>	<c*>
	-102.26(5)		-40.81	0.736(0)	0.423(1)	-0.529(1)
R4-I	-52.72(4)	-61.45	8.73	0.639(1)	-0.176(1)	0.749(0)
	-29.38(6)		32.07	-0.223(0)	0.889(1)	0.400(1)

[a]All these values are in the units of MHz. [b]Numbers in parentheses are the estimated uncertainties in the last digit quoted as reported by the statistical analysis.

As shown in Fig. 7.24, the EIE obtained by choosing ENDOR line R4-I for B//<c> from the partially deuterated crystal (Fig. 7.3b) has the similar pattern of 1:2:2:1 as that from the normal crystal. This indicates that the large couplings in R4, i.e., the couplings of 95.95MHz, 82.80MHz in the WINSIM simulation, and R4-I, are from nonexchangeable protons. Moreover, the width of the EIE pattern from the normal crystal is ~100G (~280MHz); while the width of the EIE pattern from the partially deuterated crystal is ~90G (~252MHz). The width difference of ~10G (~28MHz) suggests that the smallest coupling of 21.64MHz in the WINSIM simulation is from an exchangeable proton. Then we simulate the EIE pattern (B//<c>) from the partially deuterated crystal by using the couplings of 95.96MHz, 82.80MHz, and 70.53MHz only. The EIE pattern is reproduced and is shown in Fig. 7.23c. From these characteristics, and the structure of arginine molecule, R4 can be the radical from dehydrogenation of C5

(see scheme 7.2). This is the structure most likely to exhibit one exchangeable and three non-exchangeable couplings, with one of the non-exchangeable couplings from an α-proton.

The radical of dehydrogenation from C5 has been identified as one of the stable radicals in L-arg·HCl single crystals irradiated at room temperature. The hyperfine coupling tensors of this stable radical detected at room temperature and at 66K are listed in Table 7.17. The eigenvectors of α-coupling 1_L detected at 66K are quite similar to those of R4-I with angular differences of 5.5°, 16.9° and 16.4°, while the eigenvectors of α-coupling 1_R detected at room temperature is also similar to those of R4-I with the differences of 3.4°, 14.1° and 13.5°, although the maximum and the intermediate components of R4-I are ~8MHz larger than those of couplings 1_L and 1_R. The β-couplings from the stable radical formed by dehydrogenated from C5 are 106.60MHz, 83.06MHz, 24.97MHz detected at 66K, and are 98.87MHz, 89.48MHz, and 22.38MHz detected at room temperature. These couplings are very similar to the simulation β-couplings for R4: 95.96MHz, 70.53MHz, and 24.75MHz. In addition, the smallest β-coupling of ~25MHz in the stable radical was ascribed to H11, the exchangeable proton, which is consistent with the above result that smallest simulation coupling of 24.75MHz is from an exchangeable proton.

Therefore, the above results confirm the assignment that R4 is from the dehydrogenation at C5. In this structure, the spin is mainly on C5, the α-coupling R4-I is from H9 or H10, the nonexchangeable β-couplings are from H7 and H8, and the exchangeable coupling of ~25MHz is from H11. Since the experimental EIE pattern and ENDOR line R4-I are weak, it is possible that the other ENDOR couplings of R4 are too weak to be detectable.

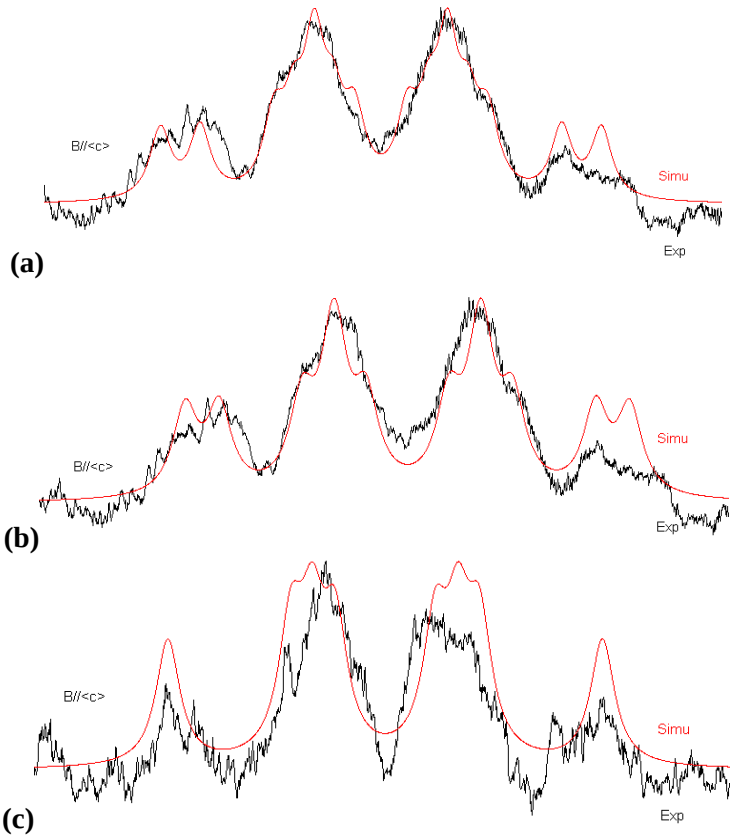

Fig. 7.23 *WINSIM simulations for the EIE pattern (B//<c>) of R4 from the normal crystal by using four proton couplings* ***(a)*** *or by using two proton couplings and one nitrogen coupling* ***(b)****, and for the EIE pattern (B//<c>) of R4 from the partially deuterated crystal by using three proton couplings* ***(c)****.*

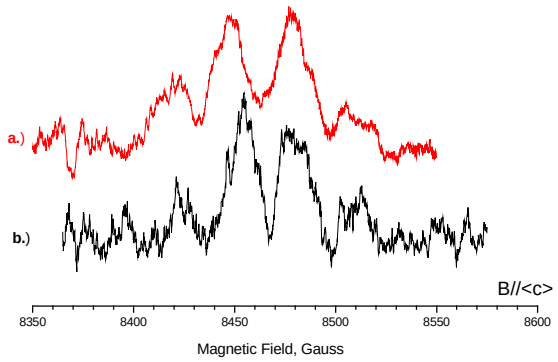

Fig. 7.24 *The EIE patterns of R4 for B//<c> from the normal crystal* ***(a)*** *and from the partially deuterated crystal* ***(b)****.*

Table 7.17 *The comparison of tensor R4-I and the coupling tensors from the radical of dehydrogenation from C5 detected at 66K* ***(a)*** *and at 298K* ***(b)*** *in L-arginine·HCl·H_2O single crystals irradiated at 298K.*[a,b]

(a)			Engenvetor				
Tensor	Isotropic value[a]	Anisotropic value[a]	<a>	<b>	<c*>	:Tensor	Ang Diff (^{0})[b]
		-30.81	0.686	0.408	-0.601		5.5
1_L	-59.81	-0.85	0.726	-0.389	0.567		16.9
		31.66	0.002	0.826	0.564		16.4
		7.51	0.846	-0.481	0.229		
2_L	106.60	-2.25	0.016	0.453	0.892		
		-5.26	0.533	0.751	-0.391		
		8.93	0.352	0.936	0.013		
3_L	83.06	-4.78	0.873	-0.324	-0.365		
		-4.15	0.337	-0.140	0.931		
		9.42	0.206	0.571	-0.795		
4_L	24.97	-2.62	0.726	-0.634	-0.266		
		-6.80	0.656	0.522	0.545		
(b)							
		-32.76	0.696	0.421	-0.582		3.4
1_R	-56.76	1.26	0.717	-0.355	0.600		14.1
		31.50	-0.046	0.835	0.549		13.5
		6.62	0.752	0.612	0.245		
2_R	98.87	-2.30	0.155	-0.524	0.837		
		-4.31	0.641	-0.592	-0.489		
		7.51	0.279	0.960	0.036		
3_R	89.48	-3.58	0.959	-0.276	-0.067		
		-3.93	0.055	-0.053	0.997		
		8.70	0.345	0.592	-0.728		
4_R	22.38	-2.65	0.776	-0.616	-0.133		
		-6.06	0.528	0.519	0.672		

[a]These values are in unit of MHz. [b]The "Ang Diff (°)" stands for the angular difference in degree between the eigenvectors of α-coupling tensor R4-I and those of α-coupling tensors 1_L (66K) and 1_R (298K).

Radical R5-unknown radical

As mentioned above, one additional EIE pattern was detected for B//<a> as shown in Fig. 7.25a and was assigned as radical R5. The only observed ENDOR line for R5 was labeled as "R5-I" in Fig. 7.3c. The angular dependence curve of R5-I is shown in Fig. 7.26, and the tensor R5-I is listed in Table 7.18.

R5-I is characteristic of a β-coupling. As is shown in Fig. 7.25b, the WINSIM simulation indicates that the EIE for B//<c> involves two proton couplings: R5-I and one coupling of 1.91G (5.35MHz). The second coupling was not observed in the experiments. Since R5-I is very weak in the ENDOR (B//<a>) from the normal crystal, it was difficult to estimate whether or not coupling R5-I is exchangeable by comparing the ENDOR spectra to that from the normal and partially deuterated crystals.

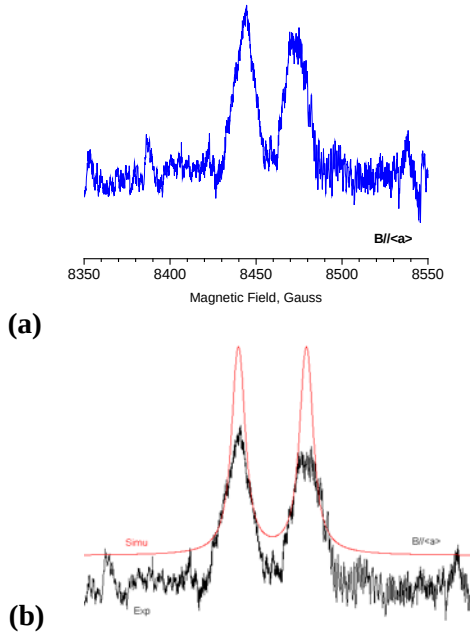

Fig. 7.25(a) *The EIE pattern of R5 for B//<a>;* ***(b)*** *the WINSIM simulation for the EIE in (a).*

Since the EIE of R5 is similar as that of R1a at same orientation as shown in Fig. 7.27, and from the above results, R5 could be the carboxyl anion radical (see Scheme 7.2) with a configuration different from R1a and R1b. If so, then R5-I can be ascribed to H4. However, the tensor comparisons listed in Table 7.19 show that tensor R5-I is quite different from tensors a1 and b1 (the tensors from H4 in R1a and R1b): the angular differences between the eigenvectors are > 45°. Thus R5 is very unlikely the carboxyl anion radical. Then it was not possible to identify R5.

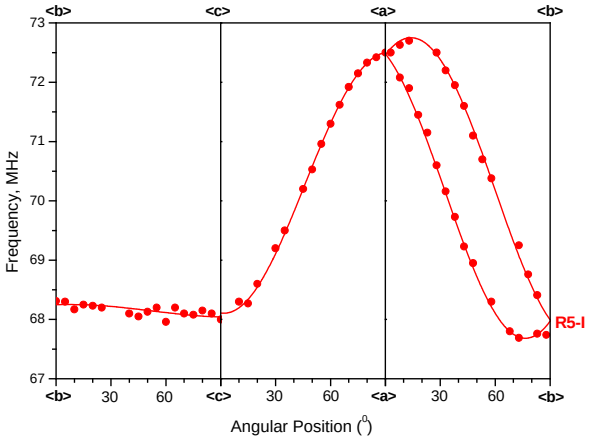

Fig.7.26 *The angular dependence curve for coupling R5-I.*

Table 7.18 *Hyperfine coupling tensor of R5-I detected in L-arginine·HCl·H_2O single crystals irradiated at 66K.*[a,b]

				Eigenvectors[b]		
Coupling	Principal value[a,b]	Isotropic value[a]	Anisotropic value[a]	<a>	<b>	<c*>
	73.47(2)		6.52	0.971(0)	0.238(3)	0.033(1)
R5-I	64.13(2)	66.95	-2.82	0.027(1)	0.026(12)	-0.999(0)
	63.24(2)		-3.71	0.239(2)	-0.971(0)	-0.019(12)

[a]These values are in the unit of MHz. [b]Numbers in parentheses are the estimated uncertainties in the last digit quoted as reported by the statistical analysis

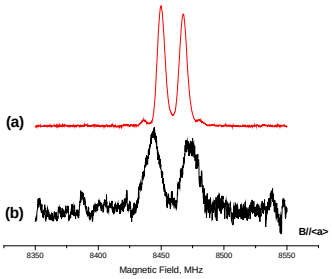

Fig. 7.27 *Comparison of EIE patterns from R1a* ***(a)*** *and R5* ***(b)*** *for B//<a>.*

Table 7.19 *The comparisons of tensors a1 and b1 to tensor R5-I*[a,b]

Coupling	Isotropic value[a]	Anisotropic value[a]	Eigenvectors <a>	<b>	<c*>	:Coupling	Angle diff (°)[b]
		7.35	0.093	0.527	-0.845		79.2
a1	52.92	-2.23	0.575	-0.721	-0.387	R5-I	67.5
		-5.12	-0.813	-0.450	-0.37		75.5
		11.06	0.416	0.531	-0.738		59.6
b1	10.60	-4.50	-0.897	0.375	-0.235	R5-I	77.3
		-6.56	-0.152	-0.760	-0.632		44.5

[a]These values are in the unit of MHz. [b]The "Angle diff (°)" is the angular difference between the eigenvectors in units of degrees.

7.4 Summary and Discussion:

Chapter 5 discusses proton transfer mechanisms in the carboxyl anion radicals with quantum tunneling theory. The comparison in Table 5.5 shows that small couplings a2 and a3 detected in R1a, b2 and b3 in R1b have anisotropy typical of O-H dipolar couplings. Radical R2, the decarboxylation radical, is a common oxidation product in amino acids irradiated at low temperature. Room temperature irradiation results and annealing experiments with 66K irradiation indicated that the carboxyl anion radical and the decarboxylation radical were precursors to the main chain deamination and dehydrogenation radicals (from C5 and from C2), respectively, as discussed in Chapter 8.

Radical R3, the anion radical from electron trapped by the guanidyl group, is unusual in irradiated amino acids. Formation of the guanidyl radical anion can be due to the electron affinity of the guanidyl group being sufficient to trap an electron. Our modeling calculations gave indirect support to this explanation[III]. In addition, the geometry optimizations on cluster models of R3 indicated that the guanidyl group transformed from a planar to a tetrahedral structure after the electron was trapped, with the result that the distances of intermolecular hydrogen bonds related to the guanidyl group increased by 0.1-0.4Å. These increases can weaken, or even break, the hydrogen bonds. From studies of the nucleosome core particle, the side-chain of arginine is inserted into the minor grooves of DNA, and commonly involves

[III]The cluster models (see Fig. 7.21 and 7.22) of R3 were optimized partially (some atoms were frozen during the optimizations) and cannot be used to calculate the electron affinity. However, after the geometry optimization, the electron added initially to the whole cluster was localized on the carbon atom of the guanidyl group supports our estimate indirectly that the guanidyl group has enough electron affinity to produce the guanidyl radical anion (R3).

hydrogen bonds to phosphate oxygen atoms and pyrimidine O2 atoms.[2] Thus, if the guanidyl anion radical forms in arginines, the related hydrogen bonds will be weakened or broken, thereby affecting the histone-DNA association and the stability of the nucleosome core.

Radical R4, the radical from dehydrogenation at C5, also was detected in crystals irradiated at room temperature. The α-tensors and β-couplings of this radical from irradiation at low and room temperatures were very similar indicating the radical experienced very little reorientation. Also, R4 is a common oxidation product, and could be either a secondary product of decarboxylation radical, or a product of the radical losing one electron oxidation and deprotonation at C5 (see discussion in Chapter 8). Radical R5 exhibited very weak ENDOR lines and could not be identified.

References

1. N. M. Luscombe, R. A. Laskowski and J. M. Thornton, Amino acid-base interactions: a three-dimensional analysis of protein-DNA interactions at an atomic level. *Nucl. Acids Res.* **29,** 2860-2874 (2001).

2. K. Luger, A. W. Mader, R. K. Richmond, et al., Crystal structure of the nucleosome core particle at 2.8Å resolution. *Nature.* **389,** 251-260 (1997).

3. A. Joshi and R. H. Johnsen, Kinetics of radical decay in crystalline amino acids. II. High-temperature study. *The Journal of Physical Chemistry* **80,** 46-51 (1976).

4. J. J. Tria, D. Hoel and R. H. Johnsen, The kinetics of radical decay in crystalline amino acids. 7. Monohydrates. *The Journal of Physical Chemistry* **83,** 3174-3179 (1979).

5. M. Aydin, M. H. Baskan, S. Yakar, et al., EPR studies of gamma-irradiated L-alanine ethyl ester hydrochloride, L-arginine and alanyl-L-glutamine. *Radiation Effects and Defects in Solids* **163,** 41-46 (2008).

6. B. Olsen, *Study of free radicals in single crystals of L-arginine monophosphate monohydrate at 295K and 77K*. (Master thesis in physics) Physics Institue, University of Oslo, (2008).

7. J. Dow and L. H. Jensen, Refinement of structure of arginine hydrochloride monohydrate. *Acta cryst. B* **26,** 1662-1671 (1969).

8. E. Pauwels, V. Van Speybroeck and M. Waroquier, Evaluation of Different Model Space Approaches Based on DFT to Examine the EPR Parameters of a Radiation-Induced Radical in Solid-State α-Glycine. *The journal of physical chemistry. A* **108,** 11321-11332 (2004).

9. C. Heller and H. M. McConnell, Radiation Damage in Organic Crystals. II. Electron Spin Resonance of $(CO_2H)CH_2CH(CO_2H)$ in β-Succinic Acid. *J. Chem. Phys.* **32,** 1535-1539 (1960).

10. H. Muto, Trapped anions in organic crystals. Radical ionic systems: Properties in condensed phases A. Lund, M. Shiotani, and Eds. Kluwer Academic Publishers, (1991).

11. H. Muto and M. Iwasaki, ENDOR studies of the superhyperfine couplings of hydrogen-bonded protons. I. Carboxyl radical anions in irradiated L-alanine single crystals. *J. Chem. Phys.* **59,** 4821-4829 (1973).

12. K. T. Øhman, A. Sanderud, E. O. Hole, et al., Single Crystals of L-*O*-Serine Phosphate X-Irradiated at Low Temperatures: EPR, ENDOR, EIE, and DFT Studies. *The journal of physical chemistry. A* **110,** 9585-9596 (2006).

13. H. M. McConnell, Indirect Hyperfine Interactions in the Paramagnetic Resonance Spectra of Aromatic Free Radicals. *J. Chem. Phys.* **24,** 764-766 (1956).

14. W. Gordy, Theory and Application of Electron Spin Resonance. John Wiley & Sons, Inc, New York, NY, (1980).

15. W. A. Bernhard, The use of alpha hyperfine coupling tensors as a measure of unpaired spin density and free radical geometry. *J. Chem. Phys.* **81,** 5928-5936 (1984).

16. R. W. Fessenden and R. H. Schuler, Electron Spin Resonance Studies of Transient Alkyl Radicals. *J. Chem. Phys.* **39,** 2147-2195 (1963).

17. P. A. Erling and W. H. Nelson, Dependence of α-Proton Hyperfine Couplings on Free Radical Geometry. *The Journal of Physical Chemistry A* **108,** 7591-7595 (2004).

18. J. R. Morton, Electron Spin Resonance Spectra of Oriented Radicals. *Chemical Reviews* **64,** 453-471 (1964).

19. B. Mennucci and J. Tomasi, Continuum solvation models: A new approach to the problem of solute's charge distribution and cavity boundaries. *J. Chem. Phys.* **106,** 5151-5158 (1997).

20. B. Mennucci, E. Cancès and J. Tomasi, Evaluation of Solvent Effects in Isotropic and Anisotropic Dielectrics and in Ionic Solutions with a Unified Integral Equation Method: Theoretical Bases, Computational Implementation, and Numerical Applications. *The journal of physical chemistry. B* **101,** 10506-10517 (1997).

21. R. Cammi, B. Mennucci and J. Tomasi, Second-Order Møller-Plesset Analytical Derivatives for the Polarizable Continuum Model Using the Relaxed Density Approach. *The journal of physical chemistry. A* **103,** 9100-9108 (1999).

22. R. Cammi, B. Mennucci and J. Tomasi, Fast Evaluation of Geometries and Properties of Excited Molecules in Solution: A Tamm-Dancoff Model with Application to 4-Dimethylaminobenzonitrile. *The journal of physical chemistry. A* **104,** 5631-5637 (2000).

CHAPTER 8.

L-ARGININE · HCl · H_2O SINGLE CRYSTALS IRRADIATED AT 298K

Abstract:

K-band EPR, ENDOR, EIE and DFT studies identified three radicals in single crystals of L-arginine hydrochloride monodyhidrate irradiated at 298K: the main-chain deamination radical, (R1a-c, and RI), $^{-}$(OOC)ĊH$(CH_2)_3$NHC$(NH_2)_2^{+}$, the radical dehydrogenated at C5, (R2 and RIIa, RIIb), $^{-}$(OOC)CH$(NH_3)^{+}$ $(CH_2)_2$ĊHNHC$(NH_2)_2^{+}$, and the radical dehydrogenated at C2, (R3 and RIII), $^{-}$(OOC)ĊH$(NH_3)^{+}$ $(CH_2)_3$NHC$(NH_2)_2^{+}$. Three conformations of deamination radical, R1a, R1b and R1c were detected at 66K. DFT calculations indicated that R1b and R1c were from the deamination radical with two O-H dipolar couplings, $(H_2…$OOC)ĊH$(CH_2)_3$NHC$(NH_2)_2^{+}$, while R1a does not have an O-H dipolar coupling. DFT geometry optimizations also indicated that R1a-R1c were significantly reoriented from parent structure. Only one conformation of the deamination radical, RI was detected at 298K. No DFT model was found to reproduce the parameters of RI. However, comparison of the crystallographic directions to eigenvectors of the measured couplings in RI indicates that RI experienced little reorientation. Based on the comparison between R1a-R1c and RI, RI can be assigned as the deamination radical with two O-H dipolar couplings. Two conformations of the radical dehydrogenated from C5, RIIa and RIIb were detected at 298K. The relative intensity of ENDOR lines from RIIa and RIIb indicated that the yield of RIIa was much larger than that of RIIb. Only one conformation of this radical, labeled R2, was detected at 66K. The coupling tensors in RIIa, RIIb and R2 are very similar and this indicated that the radical had little reorientation during the temperature dropped to 66K. R3 and RIII detected at 66K and 298K, respectively, are from the radical dehydrogenated at C2. The conformation of this radical also changed very little during cooling to 66K. Radical R4 could not be identified.

8.1 Introduction:

Previous studies of X-irradiated L-arginine· HCl· H_2O single crystal (see Scheme 8.1) and in the γ-irradiated L-arginine powder at room temperature reported the radical dehydrogenated at C5 (see Scheme 8.2).[1-3] Using X-band EPR, ENDOR and theoretical calculations in L-arginine·phosphate·H_2O single crystals X-irradiated at room temperature, Hård Olsen described the main-chain deamination radical (see Scheme 8.3a), and the radical dehydrogenated from side chain (see Scheme 8.2) were identified. [4]

This chapter describes the free radicals detected at 298K and 66K in L-arginine·HCl·H_2O single crystals irradiated at 298K. Using K-band EPR, ENDOR and DFT calculations, it was possible to study the different conformations of the main-chain deamination radicals at 66K and 298K (see Schemes 8.3a and 8.3b), and to identify the radical dehydrogenated at C5 (see Scheme 8.2). Furthermore, this work identified the radical from dehydrogenation of the main chain carbon (see Scheme 8.4). This radical is a common stable radical in irradiated amino acids, but has not previously been reported in previous work of irradiated arginine. Combining the results from the low temperature irradiation and the annealing experiments, the mechanisms of irradiation damage in L-arginine are proposed.

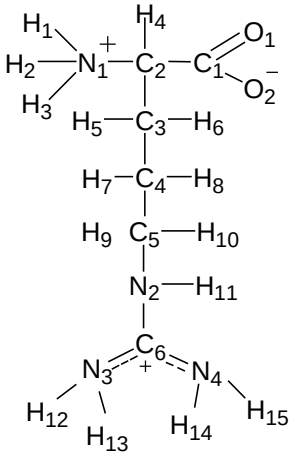

Scheme 8.1 *Arginine molecule in L-arginine HCl H2O single crystal*

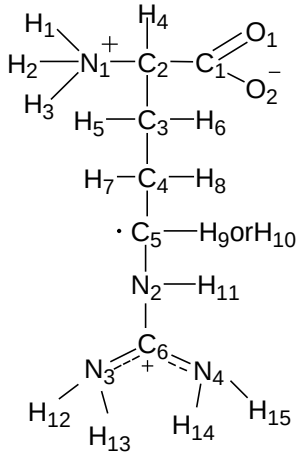

Scheme 8.2 *The radical from dehydrogenation at C5*

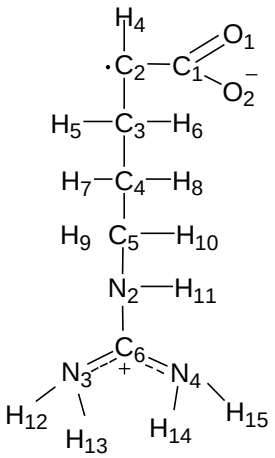

Scheme 8.3a

The main chain deamination radical

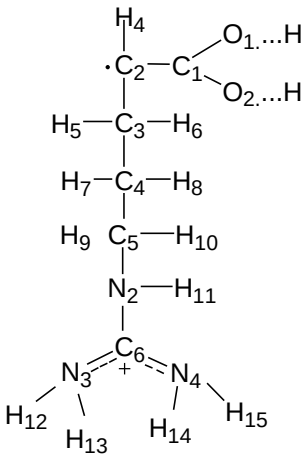

Scheme 8.3b

The main chain deamination radical with two O-H dipolar protons

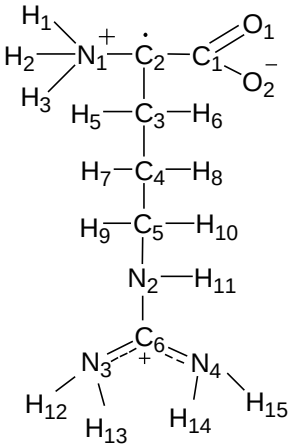

Scheme 8.4

The radical dehydrogenated at C2

8.2 Experimental

Using K-band of EPR, ENDOR and EIE techniques, free radicals in single crystals of L-arginine monohydrochloride monohydrate (L-arginine·HCl·H_2O; Sigma Chem. Co.) X-ray irradiated at 298K were studied at 298K and at 66K (by pumping the liquid nitrogen). The methods of crystal growth, data analysis, and spectra simulation were described in detail in Chapter 7.

DFT (density functional theory) calculations were performed in the Gaussian03[5] program to reproduce the magnetic parameters and the conformations of the radicals. The coordinates for all the initial radical geometries were from the neutron diffraction studies.[6] To simulate the environmental

effects, the DFT calculations with single molecule used the PCM model in geometry optimizations by adding the keyword of "scrf=PCM" (see Chapter 5 and 6). In addition to that, some of the atoms were frozen to simulate the effects of intermolecular hydrogen bonds. In the calculation with the cluster model, some parts of the neighboring molecules that involved hydrogen bonds to the radical were added. During optimization, some atoms were frozen to simulate the environmental effects. All the radicals were optimized with the B3LYP functional and the 6-31G(d,p) basis set. The magnetic parameters were calculated subsequently on the final radical structure with single point calculations using the 6-311G(2d, p) basis set. The "NOSYMM"[7] keyword was used for both the geometry optimization and the single point calculation and the Cl^- atom was omitted from all calculation models.

8.3 Results and Analysis

8.3.1 Experiments at 66K

EPR and EIE

Fig. 8.1 shows the EPR spectra (B//<b>) from the normal crystal (a.) and the partially deuterated crystal (b.) of L-arg·HCl·H_2O irradiated at room temperature and measured after the temperature was lowered to 66K. The EPR spectrum from the normal crystal is dominated by a strong four-line pattern accompanied with some weaker lines in the center and on both sides; the EPR from the partially deuterated crystal is a more complicated pattern with additional lines. These characteristics indicated that both EPR spectra contained conponents from several radicals. In addition, the differences between the EPR spectra indicated that one or more couplings are from exchangeable protons.

Fig. 8.2 shows ENDOR spectra (B//<b>) from the two types of crystals with the magnetic field set to one of the central EPR peaks as indicated by arrows in Fig. 8.1. The absence of lines 15 and 18 in the ENDOR spectrum from the partially deuterated crystals indicated that these couplings are from exchangeable protons.[i] Lines 10, 11 and 17 are weaker in both types of crystals and it was impossible to

[i] The two peaks of 15 in Fig. 2a.) are from its two sites and that indicate there is a small misorientation.

attribute them to exchangeable or nonexchangeable protons from the ENDOR spectra comparison. The ENDOR lines were grouped based on the EIE patterns as described in the following.

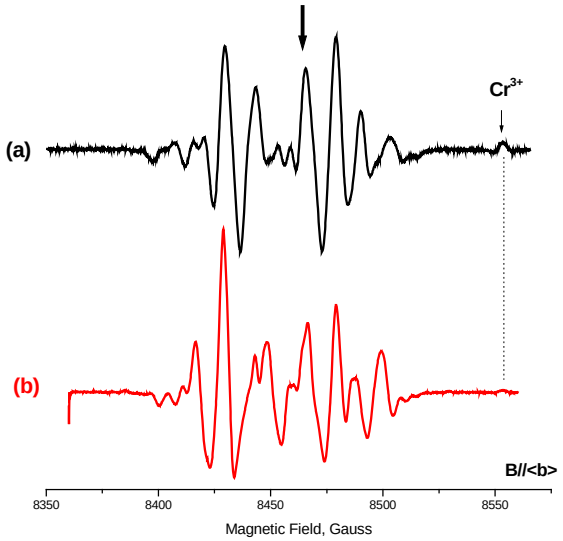

Fig. 8.1 *EPR spectra from the normal crystal* ***(a)*** *and the partially deuterated crystal* ***(b)*** *of L-arg·HCl·H_2O with magnetic field along <b>.*

Six distinct EIE patterns were detected from the two types of crystals and were ascribed to radicals R1a-c, R2-R4, respectively. From our analysis, radicals R1a-R1c are the same radical with different conformations, and R1a-c, R2-R4 are different radicals. Fig. 8.3 shows the EIE patterns (B//<b>) from the normal crystals that are compared to the EPR (B//<b>), and the comparison indicates that the strong four lines are associated with R1a. The weak lines on both sides are from R1c, R2 and R3. From these EIE patterns, ENDOR lines 1-5 (see Fig. 8.2) were ascribed to R1a, lines 6-8 were ascribed to R1b, lines 10-11 were ascribed to R1c, lines 12-15 were ascribed to R2, lines 16-18 were ascribed to R3, and line 19 was ascribed to R4. (Line 9 was also ascribed to R1b, but it was not detected in the ENDOR spectrum shown in Fig. 8.2)

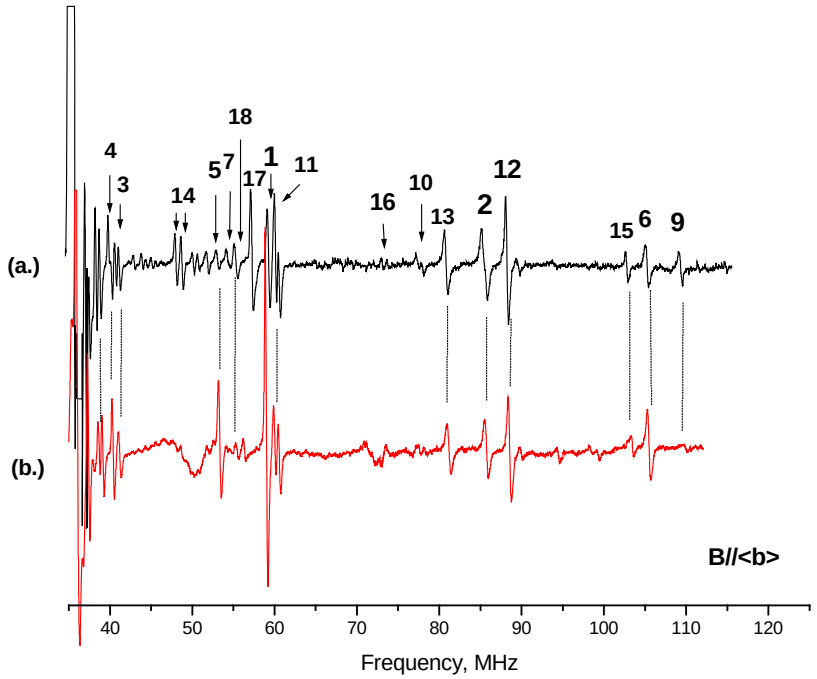

Fig. 8.2 *The ENDOR spectra from the normal* ***(a)*** *and the partially deuterated crystals* ***(b)*** *of L-arg·HCl·H_2O with the magnetic field locked to one of the center EPR peaks as indicated by the arrows in Fig. 8.1.*

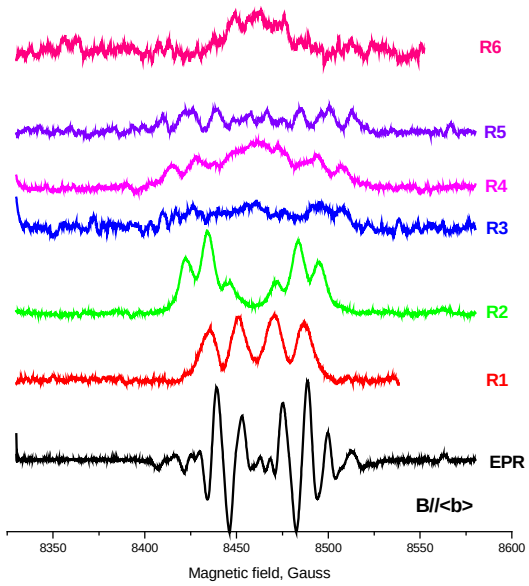

Fig. 8.3 *EPR and EIE patterns obtained from the normal crystal L-arg·HCl·H_2O with the magnetic field along <b>.*

Radical R1a: main-chain deamination radical

Radical R1a is one of the main radicals detected at 66K from the crystal irradiated at room temperature. From the WINSIM simulations for the EPR spectra as described later, the concentration of R1a is ~30%. ENDOR lines 1-4 were assigned to R1a (see Fig. 8.2). The angular dependence curves of these couplings are shown in Fig. 8.4, and based on these data, their tensors were obtained and are listed in Table 8.1. Tensor 1 is typical of an α-coupling with large anisotropy; tensors 2 and 3 are typical of β-couplings with small anisotropy and axial symmetry; tensor 4 has a very small and negative isotropic value, thus it was assigned as a distant coupling. With tensors 1-4, EIE patterns of R1a at three axes can be reproduced very well as shown in Fig. 8.5. Therefore, R1a has one α- and two β-couplings (one β-coupling is larger, ~97.08MHz; the other is much smaller, only ~5.07MHz.) Moreover, the comparison between the ENDOR spectra from the normal and the partially deuterated crystals (see Fig. 8.2) indicates that couplings 1-4 are from nonexchangeable protons.

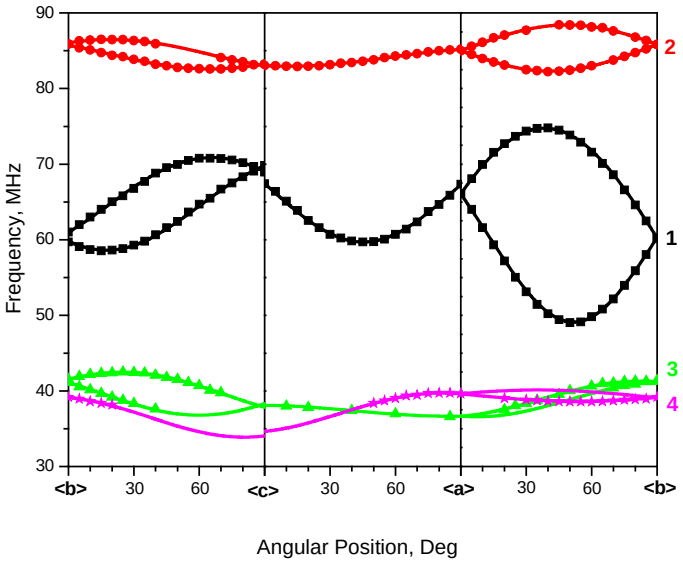

Fig. 8.4 *Angular dependence curves of couplings 1-4.*

Table 8.1 *Hyperfine coupling tensors for radical R1a in single crystal of L-arginine·HCl·H_2O irradiated at 298K and detected at 66K.*[a, b]

Tensors	Principal values[a,b]	Isotropic Values[a]	Anisotropic values[a]	Eigenvectors[b] <a>	<b>	<c*>
	-86.06(2)		-30.27	0.670(0)	-0.494(1)	-0.555(0)
1	-55.81(2)	-55.79	-0.02	0.370(0)	-0.426(1)	0.826(0)
	-25.49(3)		30.30	0.644(1)	0.758(0)	0.103(0)
	12.90(3)		7.81	0.098(4)	0.881(6)	0.462(4)
2	1.46(8)	5.09	-3.63	0.564(1)	0.333(25)	-0.755(24)
	0.92(8)		-4.17	0.820(2)	-0.335(4)	0.465(6)
	105.40(1)		8.31	0.630(1)	0.742(3)	-0.228(2)
3	93.86(2)	97.09	-3.23	0.525(1)	-0.191(3)	0.829(1)
	92.00(1)		-5.09	0.572(1)	-0.642(3)	-0.510(4)
	4.48(21)		7.50	0.114(6)	-0.130(7)	-0.985(1)
4	-5.33(3)	-3.02	-2.31	0.570(5)	-0.804(4)	0.172(8)
	-8.20(2)		-5.18	0.814(3)	0.581(5)	0.017(4)

[a]All these values are in units of MHz. [b]Numbers in parentheses are the estimated uncertainties in the last digit quoted as reported by the statistical analysis.

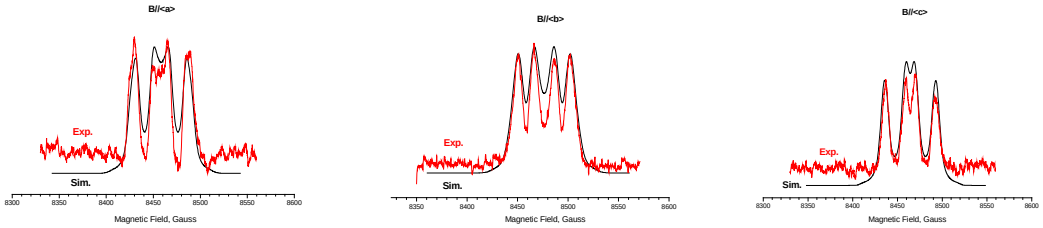

Fig. 8.5 *EIE simulations for R1a at <a>, <b> and <c> with tensors 1-4.*

From the above results, radical R1a can be assigned to the main chain deamination radical with the spin mainly on C2 leading to one α-proton coupling (from H4), and two β-proton couplings (from H5 and H6). (See Scheme 8.3a) Thus, coupling 1 can be ascribed to H4, couplings 2 and 3 can be ascribed to H5 or H6, and coupling 4 can be ascribed to a distant proton to the radical center. However, as listed in Table 8.2, the eigenvectors[I] of couplings 1-3 are quite different from their corresponding crystallographic

[I] The eigenvectors are those associated with the maximum eigenvalue for β-couplings.

directions in molecules A and B. Based on a distance estimate, as described below, coupling 4 appears to come from a γ-proton in the radical (either H7 or H8). Also, the eigenvectors[I] of coupling 4 are very different from any crystallographic directions of H_γ ... C2 in molecules A and B. These comparisons indicate that radical R1a reoriented in large degree.

Table 8.2 *Comparison the eigenvectors[a] of couplings 1-4 of radical R1a detected at 66K from L-arginine·HCl·H_2O single crystals irradiated at 298K and the corresponding crystallographic directions.*[b, c]

	Eigenvectors[a]				Directions of Hx….C2 in MA[b]			
Couplings	<a>	<b>	<c*>	protons	<a>	<b>	<c*>	Angle Diff (°)[c]
1	0.644	-0.758	0.103	H4	0.203	-0.89	0.408	32.1
2	0.098	0.881	0.462	H5	0.823	0.512	0.245	49.8
				H6	0.912	-0.262	0.316	89.7
3	0.63	-0.742	-0.229	H5	0.823	0.512	0.245	85.3
				H6	0.912	-0.262	0.316	45.8
4	0.114	-0.13	-0.985	H7	0.724	-0.269	-0.635	42
				H8	0.689	0.281	-0.668	45.6

	Eigenvectors[a]				Directions of Hx….C2 in MB[b]			
Couplings	<a>	<b>	<c*>	protons	<a>	<b>	<c*>	Angle Diff (°)[c]
1	0.644	-0.758	0.103	H4	0.069	-0.93	0.362	38.1
2	0.098	0.881	0.462	H5	0.72	0.641	0.266	40.7
				H6	0.956	-0.089	0.279	81.7
3	0.63	-0.742	-0.229	H5	0.72	0.641	0.266	94.8
				H6	0.956	-0.089	0.279	52.8
4	0.114	-0.13	-0.985	H7	0.575	-0.387	-0.721	34.3
				H8	0.765	0.117	-0.633	45.9

[a]The eigenvectors are the principal directions associated with the largest coupling components. [b] Hx are protons in molecule A (MA) and in molecule B (MB). [c]"Angle Diff (°)" are the angular differences between the experimental eigenvectors and the crystallographic directions in units of degrees.

Using the isotropic value of the coupling tensors 1-3, the geometry of R1a can be derived. With McConnell relation[8],

$$a_{iso}(H_\alpha) = Q\rho \quad [II] \qquad (1)$$

[II]In equation (1), $a_{iso}(H_\alpha)$ is the isotropic value of an α-coupling tensor, Q is constant related with the structure of the radical, and ρ is spin density on the radical center. In equation (2), $a_z(H_\alpha)$ is the positive anisotropic value of the α-coupling tensor, Q^z_{dip} is a constant, and ρ is spin density on the radical center. In equation (3), $a_{iso}(H_\beta)$ is the isotropic value of a β-coupling tensor, B_0 and B_1 are constants, θ is the dihedral angle between the C-H b-bond and the spin orbital, and ρ is spin density on the radical center. In equation (4), a_d is the dipolar coupling, ρ is spin density on the radical center, and r is the disance from the γ proton to the radical center.

and constant Q = -73.4MHz[9], the spin density on C2 can be estimated as ρ= (-55.78) / (-73.4) = 0.76. From the Gordy-Bernhard relation[10, 11],

$$a_z = Q^z_{dip}\rho \quad (2)$$

and Q^z_{dip} = 38.7MHz, the spin density on C2 can be estimated as =30.3 / 38.7 = 0.78. The similarity of the spin densities obtained from (1) and (2) indicates that the radical center C2 is in a purely sp^2 configuration.[12]

Also, the conformation of β-protons can be estimated with Heller-McConnell relation for β-coupling[13]:

$$a_{iso}(H_\beta) = B_1\rho \cos^2\theta. \quad (3)$$

Using $B_1\rho$ = 125MHz[14] and the isotropic values of tensors 2 and 3, the dihedral angles for the protons having couplings 2 and 3 are 28.2° and 78.4°, respectively. Considering the sum of the two dihedral angles is close to 120°, the possible conformation for the two β-protons is sketched in Fig. 8.6. From the distant coupling tensor 4, the distances from the radical center to the distant protons can be estimated from the relation[15, 16]

$$a_d = 160\ \rho / r^3. \quad (4)$$

Using the spin density (ρ) of 0.78, and a_d = 7.50MHz for tensor 4, then the distance from the distant proton to C2 is 2.55Å. This distance is near to that from γ-protons on C2 (H7 and H8) in the crystal (~2.7Å), and considering coupling 4 is nonexchangeable, thus coupling 4 could only be ascribed to a γ-proton in the radical.

The large reorientation of the radical makes it impossible to assign couplings 2-4 to the corresponding protons. The modeling calculations described as follow, will reproduce the reorientation of the radical R1a and help to assign these couplings.

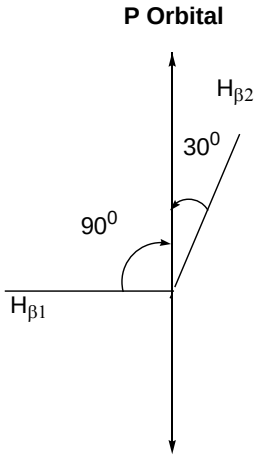

Fig. 8.6 *The possible conformation for the two β-protons of radical R1a.*

Modeling Calculation of R1a: The main chain deamination radical models were constructed by removing the main chain amino groups from the molecules A and B, denoted as Deamin-MA and Deamin-MB, repectively. The atomic coordinates of molecules A and B are from the crystallographic studies.[6] To simulate the environmental effects on the radical, two approximations were performed on the models. The PCM method, by adding the key word of "scrf=PCM", was used to simulate the effects from the crystal lattice; also, the effects of the intermolecular hydrogen bonds on the carboxyl group were simulated by freezing the two carboxyl oxygen atoms during geometry optimizations. The single point calculations following the geometry optimization were performed with two basis sets, 6-31G(d, p) and 6-311G(2d,p). As are listed in Table 8.3b and 8.3d, using the 6-311G(2d,p) basis, the calculated coupling tensors from α-proton H4, β-proton H5, and γ-proton H7 in optimized models Deamin-MA and Deamin-MB agree well with experimental tensors 1, 2 and 4, respectively. However, the calculated coupling tensor from β-proton H6 in model Deamin-MA has the eigenvector[I] much different from that of experimental tensor 3; the angular difference is ~27°. Also, the calculated tensor from H6 in model Deamin-MB has a much smaller isotropic value than that of experimental tensor 3 (smaller by 17.69MHz). Comparing to those from 6-311G(2d, p), the calculated parameters from 6-31G (d, p) are in very good agreement with the experimental values listed in Table 8.3a and 8.3c. Therefore, the

calculations support the identification that radical R1a is from main chain deamination, and that the unpaired spin is mainly on C2. The computations indicate ρ(C2) ~0.9 in Deamin-MA and Deamin-MB. At the same time, the optimized conformations of Deamin-MA and Deamin-MB agree with the results analyzed above: 1.) the side chain of the radical is reoriented to a large degree; 2.) torsional angles of <C1-C3-H4-C2 in Deamin-MA and Deamin-MB are close to 0°, indicating that the radical centers are almost planar, thereby having a purely sp^2 configuration on C2; 3.) the geometries for β-protons in Deamin-MA and Deamin-MB are close to those shown in Fig. 8.6; 4.) the distances between γ-proton H7 and C2 in Deamin-MA and Deamin-MB are both ~2.7Å, which is near the distance estimated above (~2.55Å).

Table 8.3(a) *The DFT calculated hyperfine-coupling tensors from deamination radical model of Deamin-MA with basis set of 6-31G (d,p), and the angular differences between the calculated and experimental eigenvectors.*[a, b]

			Engenvetor				
Coupling	Isotropic value[a]	Anisotropic value[a]	<a>	<b>	<c*>:	Coupling	Angle diff (°)[b]
		-33.77	-0.409	0.635	0.656		18
H4	-60.04	-1.35	0.388	-0.53	0.755	:1	7.3
		35.12	0.826	0.563	-0.03		17.1
		8.70	0.447	0.812	0.376	:2	21.1
H5	4.88	-4.02	0.251	-0.517	0.818		
		-4.68	0.859	-0.271	-0.435		
		8.65	0.303	-0.906	-0.297	:3	21.4
H6	101.91	-3.28	0.622	-0.048	0.782		
		-5.37	0.722	0.421	-0.548		
		6.60	-0.184	-0.006	-0.983	:4	18.5
H7	-2.75	-2.03	-0.404	0.912	0.071		
		-4.57	0.896	0.41	-0.17		

Table 8.3(b) *The DFT calculated hyperfine-coupling tensors from deamination radical model of Deamin-MA with basis set of 6-311G (2d,p), and the angular differences between the calculated and experimental eigenvectors.*[a, b]

			Engenvetor				
Coupling	Isotropic value[a]	Anisotropic value[a]	<a>	<b>	<c*>:	Coupling	Angle diff (º)[b]
		-34.2	-0.424	0.623	0.657		17
H4	-53.95	-1.3	0.394	-0.527	0.753	:1	7.3
		35.51	0.816	0.578	-0.022		16
		8.77	0.443	0.808	0.389	:2	20.8
H5	5.35	-3.84	0.368	-0.559	0.743		
		-4.93	0.818	-0.186	-0.545		
		8.99	0.214	-0.896	-0.389	:3	27.3
H6	89.57	-4.03	0.259	-0.332	0.907		
		-4.96	0.942	0.295	-0.161		
		6.42	-0.186	-0.013	-0.983	:4	18.4
H7	-2.6	-1.8	-0.329	0.943	0.05		
		-4.62	0.926	0.333	-0.18		

Table 8.3(c) *The DFT calculated hyperfine-coupling tensors from deamination radical model of Deamin-MB with basis set of 6-31G (d,p), and the angular differences between the calculated and experimental eigenvectors.*[a, b]

			Engenvetor				
Coupling	Isotropic value[a]	Anisotropic value[a]	<a>	<b>	<c*>:	Coupling	Angle diff (º)[b]
		-33.77	0.634	-0.705	-0.318		18.4
H4	-59.95	-1.38	0.196	-0.251	0.948	:1	15.8
		35.15	0.748	0.664	0.021		9.3
		8.71	0.239	0.949	0.206	:2	17.3
H5	2.57	-4.03	0.285	-0.271	0.919		
		-4.68	0.928	-0.161	-0.335		
		8.70	0.495	-0.869	0.024	:3	18.0
H6	88.59	-3.48	0.475	0.294	0.83		
		-5.22	0.728	0.399	-0.558		
		6.72	-0.018	-0.279	-0.96	:4	11.5
H7	-3.01	-1.96	-0.549	0.805	-0.223		
		-4.76	0.835	0.523	-0.168		

Table 8.3(d) *The DFT calculated hyperfine-coupling tensors from deamination radical model of Deamin-MB with basis set of 6-311G (2d,p), and the angular differences between the calculated and experimental eigenvectors.*[a, b]

			Engenvetor				
Coupling	Isotropic value[a]	Anisotropic value[a]	<a>	<b>	<c*>:	Coupling	Angle diff (°)[b]
		-34.25	0.648	-0.69	-0.322		17.6
H4	-53.88	-1.38	0.21	-0.245	0.947	:1	15.5
		35.62	0.733	0.681	0.014		8.2
		8.76	0.233	0.949	0.214	:2	16.7
H5	3.26	-3.84	0.275	-0.276	0.921		
		-4.93	0.933	-0.156	-0.325		
		8.91	0.429	-0.901	-0.063	:3	17.6
H6	79.39	-4.03	0.185	0.02	0.983		
		-4.88	0.884	0.434	-0.175		
		6.53	-0.017	-0.29	-0.957	:4	11.9
H7	-2.73	-1.77	-0.47	0.847	-0.249		
		-4.76	0.883	0.445	-0.151		

[a] All these values are in units of MHz. [b] The "Angle diff (°)" is the angular difference between the calculated and the experimental eigenvectors associated with the maximum eigenvalues in units of degrees.

Radicals R1b and R1c- different conformations of the main-chain deamination radical

As mentioned above, ENDOR lines 5-7 were assigned to R1b, 8-10 were assigned to R1c (see Fig. 8.2; line 8 was only detected in <ac> plane and is not shown Fig. 8.2). The angular dependence curves of these couplings are shown in Fig. 8.7a and 8.7b, and their tensors are listed in Table 8.4a and 8.4b. For R1b, tensor 5 is typical of an α-coupling with large anisotropy; tensors 6 and 7 are typical of β-couplings with smaller anisotropy and axial symmetry. For R1c, tensors 9 and 10 are typical of β-couplings; tensor 8 could not be obtained because ENDOR line 8 was only detected in <ac> plane. However, the angular dependence of line 8 in the <ac> plane shows large anisotropy, and line 8 was assigned as an α-coupling. With tensors 5-7, EIE patterns from R1b at three axes can be reproduced very well as shown in Fig. 8.8a for B//<b>. Although line 8 was not detected at <b>, coupling 8 at <b> was estimated as ~13G from the width of the EIE (~95G) and couplings 9 (52.60G) and 10 (29.75G) at the same orientation. With these couplings, WINSIM simulations also reproduced the EIE patterns of R1c at <b>, as shown in Fig. 8.8b.

Therefore, the above results indicate that radicals R1b and R1c each have one α- and two β-couplings. In addition, the comparisons of EIE patterns from the normal and the partially deuterated crystals, as shown in Fig. 8.9a and 8.9b, indicated that the major couplings in R1b and R1c are from nonexchangeable protons.

From the above analysis and the structure of arginine molecules, it is possible that R1b and R1c result from the main-chain deamination radical with conformations different from R1a (see Scheme II). The eigenvectors[I] of tensors 5-7 in R1b, 9 and 10 in R1c were compared to the corresponding crystallographic directions. As shown in Table 8.5, the eigenvector[I] of tensor 5 is near the directions of C2-H4 in molecules A and B, and that of tensor 6 also is very close to the directions of C2…H5 in molecules A and B; however, the eigenvector[I] of tensors 7, 9 and 10 are quite different from the directions of C2…H6 in molecules A and B. The modeling calculations described as follows indicated that both R1b and R1c were reoriented significantly from the parent.

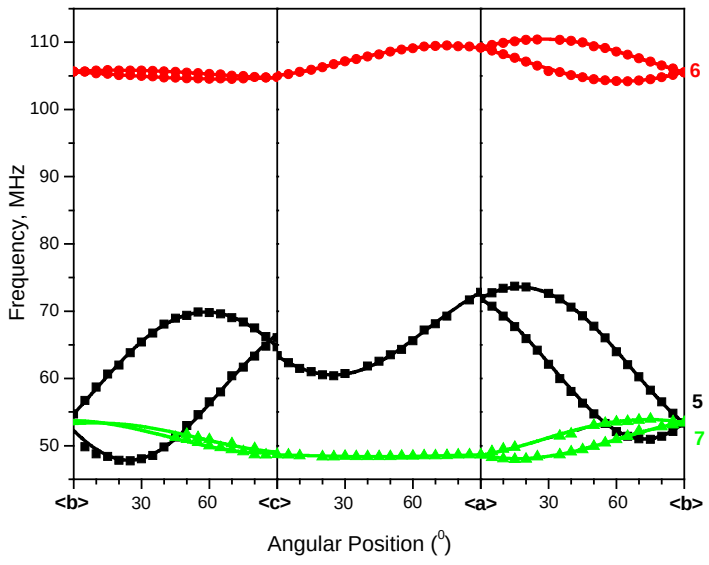

Fig. 8.7(a) *Angular dependence curves of couplings 5-7 (couplings of R1b).*

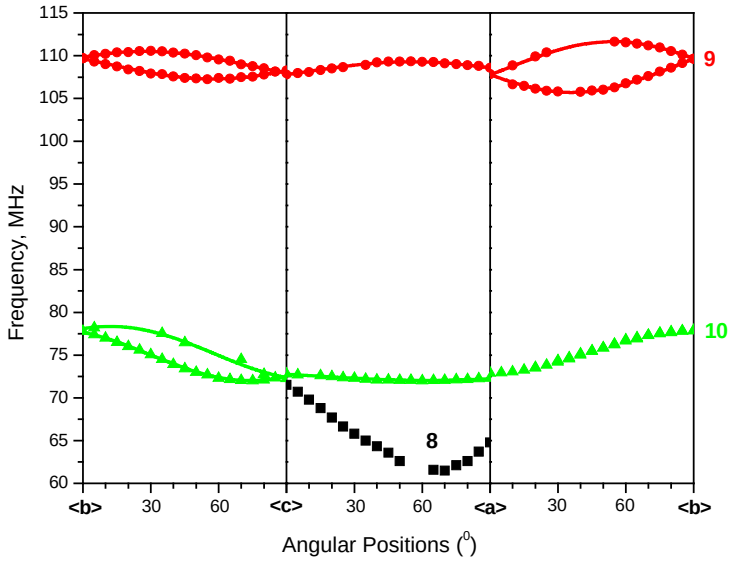

Fig. 8.7(b) *Angular dependence curves of couplings 8-10 (couplings of R1c).*

Table 8.4(a) *Hyperfine coupling tensors for radical R1b detected at 66K in L-arginine·HCl·H_2O single crystals irradiated at 298K.*[a,b]

Tensors	Principal values[a,b]	Isotropic values[a]	Anisotropic values[a]	Eigenvectors[b] <a>	<b>	<c*>
	-84.62(3)		-31.45	0.764(0)	-0.356(0)	-0.538(1)
5	-52.12(3)	-53.17	1.05	0.633(0)	0.252(1)	0.732(0)
	-22.76(3)		30.41	0.125(0)	0.900(1)	-0.418(1)
	149.07(2)		8.20	0.889(1)	-0.444(2)	0.112(1)
6	138.21(1)	140.87	-2.66	0.183(1)	0.568(3)	0.802(2)
	135.33(1)		-5.54	0.420(1)	0.693(2)	-0.586(3)
	35.86(2)		7.39	0.28(1)	-0.952(9)	-0.101(2)
7	25.58(2)	28.47	-2.89	0.224(2)	0.169(2)	-0.960(2)
	23.98(2)		-4.49	0.931(2)	0.254(3)	0.262(9)

Table 8.4(b) *Hyperfine coupling tensors for radical R1c detected at 66K in L-arginine·HCl·H_2O single crystals irradiated at 298K.*[a,b,c,d]

Tensors	Principal values[a,b]	Isotropic values[a]	Anisotropic values[a]	Eigenvectors[b] <a>	<b>	<c*>
		25.30[c]		B//<a>		
8		21.29[c]		B//<c>		
		36.40[d]		B//<b>		
	151.68(1)		7.10	0.461(1)	0.787(2)	0.411(1)
9	142.80(2)	144.58	-1.78	0.388(1)	0.238(2)	-0.891(0)
	139.27(2)		-5.31	0.798(1)	-0.570(1)	0.196(3)
	84.52(2)		8.05	0.034(1)	0.969(2)	0.247(5)
10	73.70(3)	76.47	-2.77	0.947(0)	0.048(2)	-0.318(1)
	71.21(2)		-5.26	0.320(1)	-0.244(5)	0.915(2)

[a]All these values are in units of MHz. [b]Numbers in parentheses are the estimated uncertainties in the last digit quoted as reported by the statistical analysis. [c]The coupling of line 8 detected in <ac> plane. [d]The coupling of line 8 estimated from the WINSIM simulation.

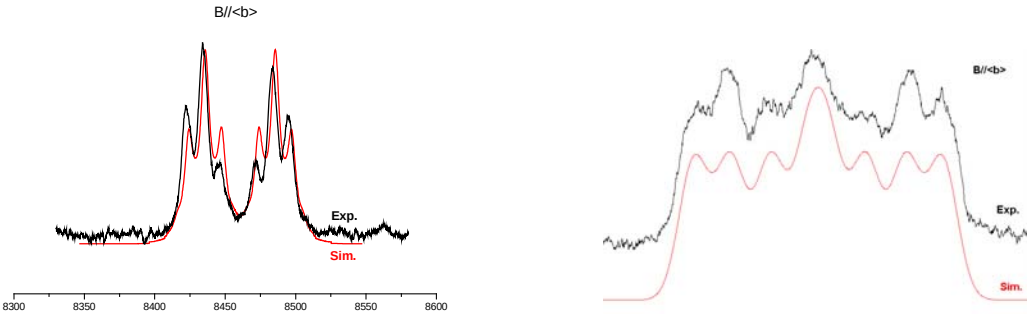

(a) **(b)**

Fig. 8.8(a) *Simulation of EIE at <b> (R1b) with tensors 5-7;* ***(b)*** *WINSIM simulation of EIE at <b> (R1c) with couplings 8-10.*

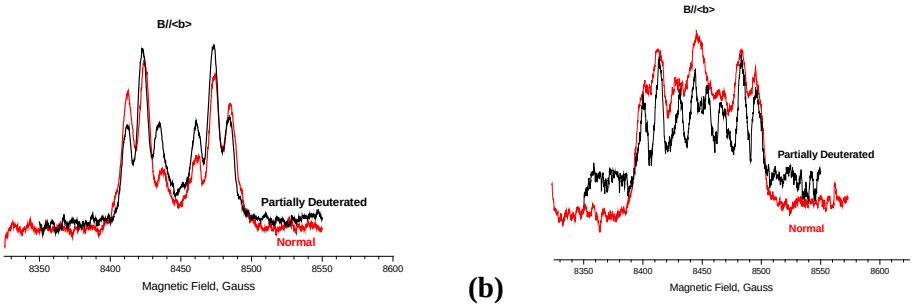

(a) **(b)**

Fig. 8.9 *The comparison of the EIE patterns from the normal and the partially deuterated crystals for R1b* ***(a)*** *and R1c* ***(b)***.

Table 8.5 *The comparison between the eigenvectors[a] of coupling tensor in R1b* ***(a.)*** *and R1c* ***(b.)*** *and the corresponding crystallographic directions.*[b,c]

(a)	Eigenvectors[a]			Protons[b]	Directions of Hx….C2 in MA[b]			
Coupling	<a>	<b>	<c*>		<a>	<b>	<c*>	Angle Diff (º)[c]
5	0.125	0.900	-0.418	H4	0.203	-0.890	0.408	18.9
6	0.889	-0.444	0.112	H6	0.912	-0.262	0.316	15.7
7	0.288	-0.952	-0.101	H5	0.823	0.512	0.245	106.0

Coupling	Eigenvectors[a]			Protons[b]	Directions of Hx….C2 in MB[b]			Angle Diff (º)[c]
	<a>	<b>	<c*>		<a>	<b>	<c*>	
5	0.125	0.900	-0.418	H4	0.069	-0.930	0.362	11.6
6	0.889	-0.444	0.112	H6	0.956	-0.089	0.279	23.0
7	0.288	-0.952	-0.101	H5	0.720	0.641	0.266	115.5

(b)	Eigenvectors[a]			Protons[b]	Directions of Hx….C2 in MA[b]			
Coupling	<a>	<b>	<c*>		<a>	<b>	<c*>	Angle Diff (º)[c]
9	0.461	0.787	0.411	H6	0.912	-0.262	0.316	69.9
10	0.034	0.969	0.247	H5	0.823	0.512	0.245	54.2

Coupling	Eigenvectors[a]			Protons[b]	Directions of Hx….C2 in MA[b]			
	<a>	<b>	<c*>		<a>	<b>	<c*>	Angle Diff (º)[c]
9	0.461	0.787	0.411	H6	0.956	-0.089	0.279	61.0
10	0.034	0.969	0.247	H5	0.720	0.641	0.266	44.7

[a]The eigenvectors are the principal directions associated with the largest coupling components. [b] Hx are protons in molecule A (MA) and in molecule B (MB). [c]"Angle Diff (°)" are the angular differences between the experimental eigenvectors and the crystallographic directions in units of degrees.

In addition, the geometries of R1b and R1c can be analyzed with the coupling tensors. Using the isotropic value of coupling 5 (-53.17MHz) and constant Q of -73.4MHz, the spin density on C2 is 0.72 from McConnell relation (1); using the dipolar value of coupling 5 (30.41MHz) and the constant Q^{z}_{dip} = 38.7MHz, the spin density on C2 is 0.78 from the Gordy-Bernhard relation (2). The similarity of the spin densities obtained from the two methods indicated that the radical center of R1b is in a purely sp^2 configuration. Because the α-coupling tensor in R1c could not be obtained, the geometry of the radical center for R1c could not be analyzed with these methods. (That will be analyzed in the modeling calculations below.) For β-couplings, the isotropic value of coupling 6 (140.87MHz) is much larger than that of β-coupling 7 (28.47MHz) in R1b. We used the Heller-McConnell relation (3) to get

$$a_{iso}\text{ (coupling 9)}/a_{iso}\text{(coupling 10)} = \cos^2\theta_{\beta 1}/\cos^2\theta_{\beta 2},$$

and used the relation of $(\theta_{\beta 1} + \theta_{\beta 1}) = 60°$ by assuming C3 in purely sp^3, and we can obtain that $\theta_{\beta 1}$ = ~15.0° and $\theta_{\beta 2}$ = ~45.0°. The corresponding configuration for the β-protons is shown in Fig. 8.10.

Moreover, the smaller and the larger β-couplings in R1a (5.09MHz and 97.09MHz) are much smaller than those of R1b (28.47MHz and 140.87MHz) and R1c (76.47MHz and 144.58MHz). The modeling calculations described in the following indicate that R1b and R1c are different conformations of the main-chain deamination radical with two O-H dipolar protons (see Scheme 8.3b).

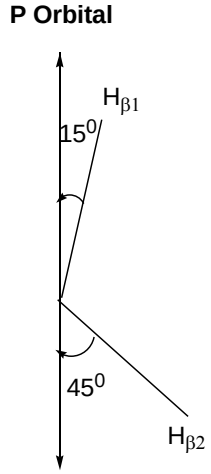

Fig. 8.10 *The configuration of β-protons in R1c.*

Modeling Calculations

In the modeling calculations for R1b and R1c, the main-chain deamination radical models, constructed from molecule B with two dipolar O-H protons, can reproduce the experimental values very well. (The deamination radical models with two dipolar O-H protons were also constructed from molecule A; however, none of these models reproduced the experimental coupling tensors.) For computations, the deamination radical was created by removing the main chain amino group from molecule B. In the model best reproducing the parameters of R1b, which was denoted as model "Deamin-R1b", the two O-H dipolar protons are from two different neighboring molecules: one is from the main chain amino group (transferred to O1) and the other is from the guanidyl group (transferred to O2) in the 2nd neighbor with O-H lengths of both 1.01Å, as shown in Fig. 8.11a. Effects from the environments were simulated with the PCM model, and two O-H protons were frozen during the optimization to approximate the effects of the intermolecular hydrogen bonds. The geometry optimization indicated that the radical experienced complicated reorientations: the radical center bent and became planar in a purely sp^2 configuration, the whole side chain rotated so that one β-proton was in the plane of the radical center, and the other was almost normal to it. In the optimized geometry as shown in Fig. 8.12a, dihedral angle <H4-C1-C3-C2 (= 0.8°) indicates that the radical center is planar, while dihedral angles <H5-C3-C2-H4 (= 13.1°) and <H6-C3-C2-H4 (= 78.0°) indicate that H5 is near the plane of the radical center, while H6 is almost normal to it. The magnetic parameters from the single point calculation on the optimized structure agree with the experimental values very well, as shown in Table 8.6a.

In the model best reproducing the parameters of R1c, denoted as model "Deamin-R1c", one of the O-H dipolar protons is from the water (transferred to O1), the other is from the main-chain amino group in a neighboring molecule (transferred to O2). O-H lengths of both are 1.01Å, as shown in Fig. 8.11b. The effects from the intermolecular hydrogen bonds were simulated by freezing the two O-H protons and the guanidyl protons during the optimization. The geometry optimization indicated that the radical center also bent to be planar in a purely sp^2 configuration, and the two β-protons rotated to a larger degree than

that in the optimization for R1b. In the optimized structure as shown in Fig. 8.12b, dihedral angle <H4-C1-C3-C2 (= 0.9°) indicates the radical center is planar, <H5-C3-C2-H4 (= 64.8°) and <H6-C3-C2-H4 (= 47.0°) indicate the two β-protons are in a conformation similar as that shown Fig. 8.10. The magnetic parameters from the single point calculation on the optimized structure agree well with the experimental values of R1c, as shown in Table 8.6b. The experimental α-coupling tensor 8 could not be obtained, making it impossible to compare the calculated α-coupling tensor to the experimental one. However, the EIE patterns of R1c can be reproduced very well with the calculated tensors as shown in Fig. 8.13. Therefore the EIE simulations indicated that the calculated α-coupling tensors are close to the experimental ones.

Another model, very similar to "Deamin-R1b", produced parameters that are very close to those of R1c (denoted as "Deamin-R1c♦"). The only difference is that, in "Deamin-R1c♦" the guanidyl protons also were frozen during the geometry optimization in addition to the two O-H dipolar protons, as shown in Fig. 8.11c. The optimized radical is in a similar conformation to that in "Deamin-R1c" (see Fig. 8.12c). The calculated parameters from this model, as listed in Table 8.6c, are very close to the experimental values of R1c. The main difference between the experimental and calculated values is that the calculated coupling from H6, only 44.46MHz, is smaller than the experimental one by ~32MHz.

The models described above led to computer results reproducing the experimental values, and support the assignment of R1b and R1c as the main-chain deamination radical with two O-H dipolar protons. Also, in optimizations of "Deamin-R1c" and "Deamin-R1c♦", the guanidyl groups were frozen, while in that of "Deamin-R1b", the guanidyl group was set free. This difference suggests that, in the formation of R1c, the guanidyl group was limited by the surroundings, and the reorientation focused on the side chain from C2 to C5, while for R1b, the whole side-chain joined the radical reorientation. Thus, for this reason, the deamination radical formed with the different conformations of R1b and R1c.

The conformations of R1a-c and RI, the deamination radical detected at room temperature were compared and will be discussed in detail in the sections on room temperature experiments.

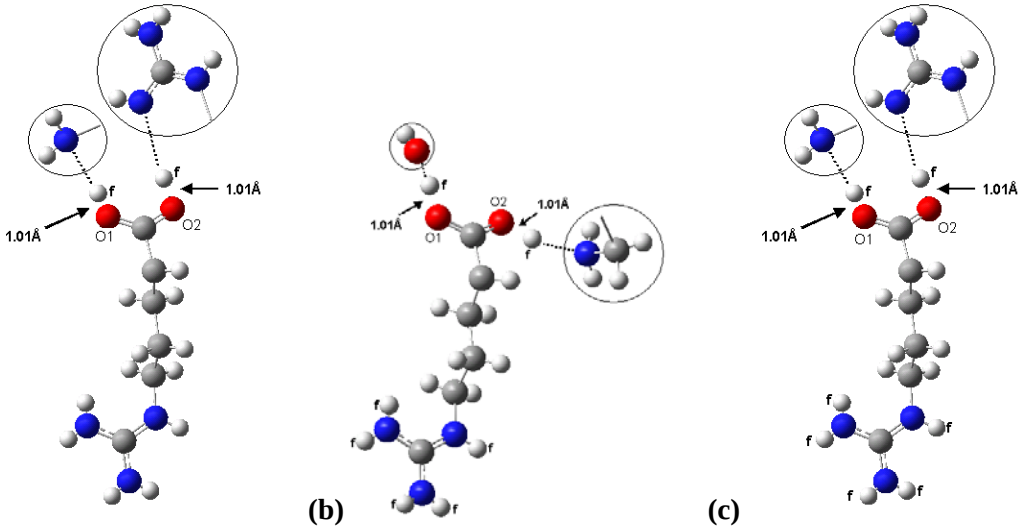

(a) **(b)** **(c)**

Fig. 8.11 *The initial structures of models "Deamin-R1b"* ***(a),*** *"Deamin-R1c"* ***(b)*** *and "Deamin-R1c♦"* ***(c.)****. The two groups in the circles were the parent group of the O-H dipolar protons and were omitted during the calculations; "f" marks the atom frozen in the geometry optimization.*

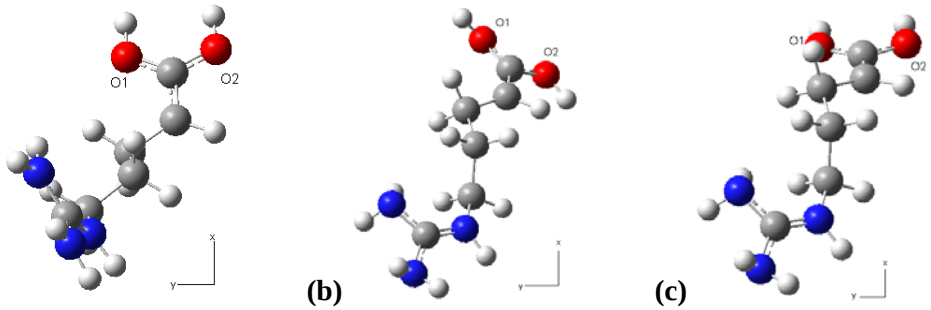

(a) **(b)** **(c)**

Fig. 8.12 *The optimized structures of the models "Deamin-R1b"* ***(a),*** *"Deamin-R1c"* ***(b)*** *and "Deamin-R1c♦"* ***(c)****.*

Table 8.6 *DFT calculated hyperfine-coupling tensors from models "Deamin-R1b"* ***(a)****, "Deamin-R1c"* ***(b)****, and "Deamin-R1c♦"* ***(c)****, and the angular differences between the calculated and experimental eigenvectors.*[a,b]

(a)				Eigenvectors				
Protons	Principal Value[a]	Isotropic value[a]	Anisotropic value[a]	<a>	<b>	<c*>	:Coupling	Angle diff (°)[b]
	-73.41		-26.7	0.777	-0.441	-0.450		6.9
H4	-50.68	-46.71	-3.97	0.529	0.070	0.846	:5	13.6
	-16.04		30.67	0.341	0.895	-0.288		14.4
	21.33		6.82	0.184	-0.975	-0.122		6.5
H5	11.99	14.51	-2.52	-0.627	-0.212	0.750	:7	
	10.22		-4.29	0.757	0.062	0.650		
	139.24		7.95	0.871	-0.453	0.190		4.6
H6	128.95	131.29	-2.34	0.152	0.616	0.773	:6	
	125.68		-5.61	0.467	0.645	-0.606		
(b)				Eigenvectors				
Protons	Principal Value[a]	Isotropic value[a]	Anisotropic value[a]	<a>	<b>	<c*>	:Coupling	Angle diff (°)[b]
	-78.36		-29.14	-0.456	0.494	0.740		
H4	-52.44	-49.22	-3.22	0.823	-0.084	0.562		
	-16.87		32.35	0.340	0.865	-0.368		
	141.51		7.65	0.386	0.734	0.559		10.1
H5	132.36	133.86	-1.50	0.909	-0.198	-0.367	:9	
	127.71		-6.15	0.159	-0.649	0.744		
	87.94		8.30	-0.293	0.956	0.021		22.8
H6	76.87	79.64	-2.77	-0.412	-0.146	0.899	:10	
	74.11		-5.53	0.863	0.255	0.437		

(c)				Eigenvectors				
Protons	Principal Value[a]	Isotropic value[a]	Anisotropic value[a]	<a>	<b>	<c*>	:Coupling	Angle diff (°)[b]
	-73.31		-27.03	-0.349	0.422	0.837		
H1C2	-50.09	-46.28	-3.81	0.914	-0.046	0.404		
	-15.44		30.84	0.209	0.906	-0.37		
	161.42		8.15	0.477	0.574	0.666		19.1
H1C3	151.4	153.27	-1.87	0.877	-0.362	-0.316	:9	
	146.99		-6.28	0.06	0.735	-0.676		
	51.54		7.08	-0.203	0.968	0.146		14.7
H2C3	42.29	44.46	-2.17	-0.465	-0.226	0.856	:10	
	39.54		-4.92	0.862	0.106	0.496		

[a] All these values are in units of MHz. [b] The "Angle diff (°)" is the angular difference between the calculated and the experimental eigenvectors in units of degrees. For β- coupling tensors, only the eigenvectors associated with the maximum eigenvalues were compared.

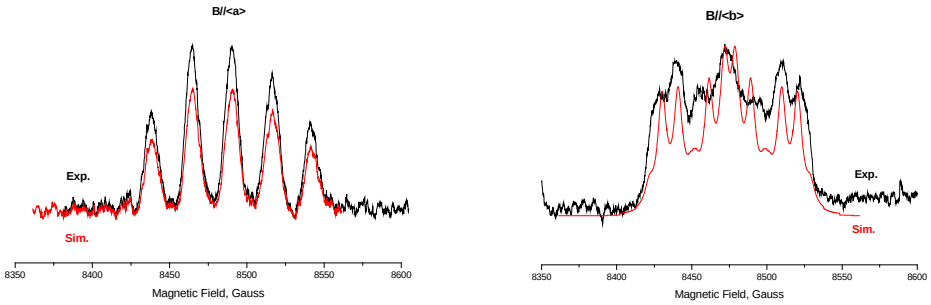

Fig. 8.13 *Simulations for EIE patterns of R1c at <a> and <b> with tensors calculated from the model "Deamin-R1c".*

Radical R2-dehydrogenation from C5

From ENDOR and EIE of the normal crystals, couplings 11-14 are ascribed to R2 (see Fig. 8.2). Based on the angular dependence curves of these couplings as shown in Fig. 8.14, the coupling tensors were obtained and are listed in Table 8.7. Coupling 11 shows large anisotropy and was assigned as an α-coupling; couplings 12-14 show small anisotropy and axial symmetry characteristics and were assigned as β-couplings. With coupling tensors 11-14, the EIE patterns of R2 at three crystallographic axes are reproduced very well as shown in Fig. 8.15. Comparisons of the ENDOR spectra from the normal and the

partially deuterated crystals (see Fig. 8.2) indicated that couplings 11-13 are from the nonexchangeable protons, while coupling 14 is from an exchangeable proton. With tensors of 11-13, the EIE patterns from the partially deuterated crystals can be reproduced very well as shown in Fig. 8.16. Thus the EIE simulations support that coupling 14 is exchangeable. From the characteristics of R2 and the structure of arginine molecule, the only possibility of R2 is dehydrogenation from C5 (see Scheme 8.2): the spin is mainly located at C5, then coupling 11 is from proton H9 or H10; coupling 14 is from exchangeable proton H11; couplings 12 and 13 are from nonexchangeable protons H7 and H8.

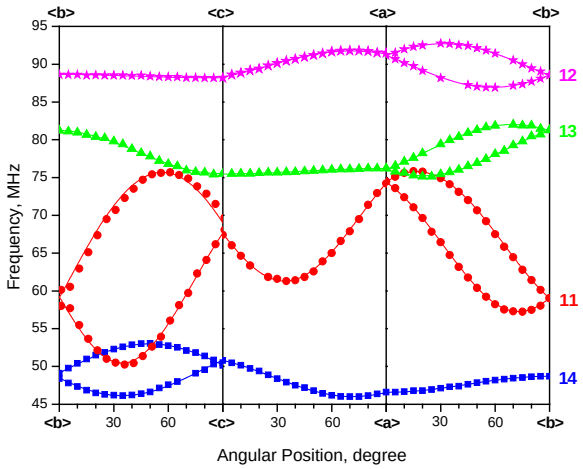

Fig.8.14 *Angular dependence curves of couplings 11-14.*

The maximum eigenvectors[I] of couplings 11-14 were compared to the corresponding crystallographic directions in molecules A and B. As listed in Table 8.8, the eigenvector[I] of coupling 11 is very close to the directions C5-H9 in molecule A and C5-H10 in molecule B; the eigenvector[I] of coupling 12 is very close to C5…H8 in molecules A and B; while the eigenvector[I] of couplings 13 is quite different from directions C5…H7, C5…H8 in molecules A and B, and the eigenvector[I] of coupling 14 is quite different from direction C5…H11 in molecules A and B. These differences suggest that the β-protons of R2 experienced reorientation in large degree, which is supported by DFT optimizations described as follows.

Table 8.7 *Hyperfine coupling tensors for radical R2 in L-arginine·HCl·H_2O single crystals irradiated at 298K and detected at 66K.*[a,b]

Tensors	Principal values[a,b]	Isotropic Values[a]	Anisotropic values[a]	Eigenvectors[b] <a>	<b>	<c*>
	-90.62(3)		-30.81	0.688(0)	0.408(0)	-0.601(1)
11	-60.66(3)	-59.81	-0.85	0.726(0)	-0.389(1)	0.567(0)
	-28.15(3)		31.66	0.002(0)	0.826(1)	0.564(0)
	114.11(2)		7.51	0.846(0)	-0.481(2)	0.229(1)
12	104.35(2)	106.60	-2.25	0.016(0)	0.453(3)	0.892(2)
	101.34(2)		-5.26	0.533(1)	0.751(2)	-0.391(4)
	91.99(2)		8.93	0.352(1)	0.936(14)	0.013(5)
13	78.91(2)	83.06	-4.15	0.337(0)	-0.140(5)	0.931(3)
	78.28(2)		-4.78	0.873(1)	-0.324(6)	-0.364(15)
	34.39(2)		9.42	0.206(1)	0.571(2)	-0.795(2)
14	22.35(2)	24.97	-2.62	0.726(2)	-0.634(2)	-0.267(2)
	18.17(2)		-6.80	0.656(0)	0.522(2)	0.545(1)

[a]All these values are in units of MHz. [b]Numbers in parentheses are the estimated uncertainties in the last digit quoted as reported by the statistical analysis.

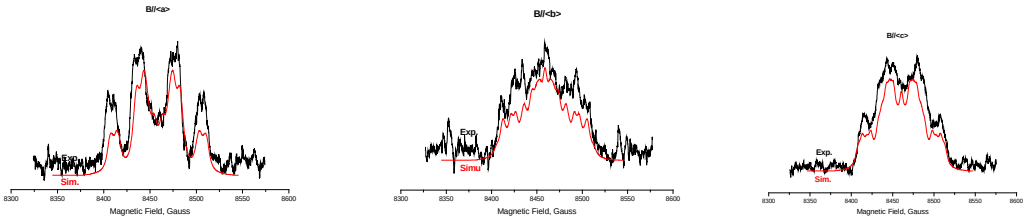

Fig. 8.15 *EIE patterns of R2 at <a>, <b> and <c> from the normal crystal L-arginine·HCl·H_2O simulated with tensors 11-14.*

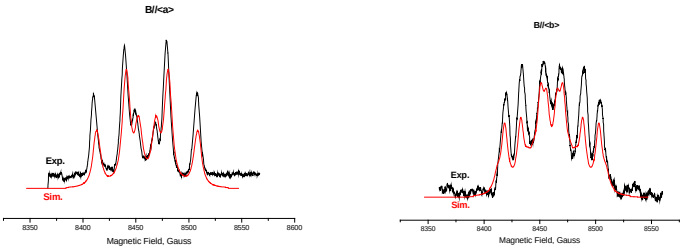

Fig. 8.16 *EIE patterns of R2 at <a>, <b> and <c> from the partially deuterated crystal L-arg·HCl·H_2O simulated with tensors 11-13.*

The geometry of the radical center can be estimated with Heller-McConnell relation (1) and Gordy-Bernhard relation (2). With $a_{iso}(H_\alpha)$ = -59.81MHz of coupling 11, the spin density on C5, ρ = 0.81 from equation (1); with $a_z(H_\alpha)$ = 31.66MHz, the spin density on C5, ρ = 0.82 from equation (2). The very close spin densities from (1) and (2) indicated the radical center is in purely sp^2 hybridization, i.e, atoms C4, C5, C6, and H9 or H10 are almost coplanar.

For the β-couplings, with Heller-McConnell relation (3) and the isotropic values of couplings 12, 13 and 14, the dihedral angle θ_d for the β-protons can be obtained as 22.6°, 32.9° and 63.6°, respectively. According to this, the β-protons configurations are sketched in Fig. 8.17. These geometry characteristics of α and β-couplings estimated from the relations (1)-(3) are also supported by the DFT calculations.

Table 8.8 *Comparison the eigenvectors[a] of couplings 11-14 from radical R2 in L-arginine·HCl·H_2O single crystals irradiated at 298K and detected at 66K and the corresponding crystallographic directions.[b, c]*

	Eigenvectors[a]				Directions of H□….C5[b]			
Coupling	<a>	<b>	<c*>	Protons[b]	<a>	<b>	<c*>	Angle Diff (°)[c]
12	0.002	0.826	0.564	H9(MA)	-0.439	0.743	-0.506	70.8
				H10(MA)	0.207	0.816	0.54	11.8
				H9(MB)	-0.154	0.87	0.468	10.8
				H10(MB)	0.579	0.599	0.553	36.1
13	0.846	-0.481	0.229	H8(MA)	0.896	-0.287	0.339	13.2
				H8(MB)	0.672	-0.693	0.262	15.9
14	0.352	0.936	0.013	H7(MA)	0.809	0.459	0.367	44.0
				H7(MB)	0.924	-0.018	0.381	71.7
15	0.206	0.571	-0.795	H11(MA)	0.590	0.176	-0.788	32.0
				H11(MB)	0.573	0.249	-0.781	28.2

[a]The eigenvectors are the principal directions associated with the largest coupling components. [b]H_β are the β-protons of the radical dehydrogenation from C5; "MA" and "MB" stand for in molecule A and in molecule B, respectively. [c]"Angle Diff (°)" are the angular differences between the experimental eigenvectors and the crystallographic directions in units of degrees.

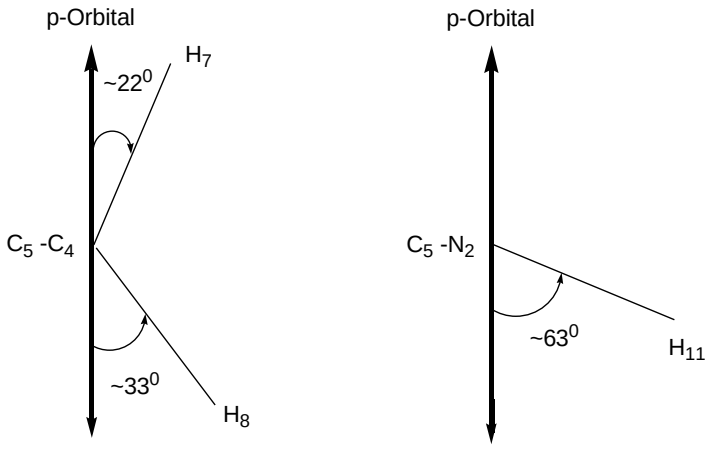

Fig. 8.17 *The sketches for the β-coupling configuarations of radical R2 estimated from the Heller-McConnell relation (3).*

Modeling calculations for radical R2: The single molecule models for radical R2 were obtained by removing H9 and H10 in molecules A and B, denoted as DeH9-MA, DeH10-MA, DeH9-MB and DeH10-MB, respectively. The initial coordinates of the atoms are from the crystallographic studies[6]. The geometry optimizations were performed with PCM model by adding the keyword "scrf = PCM" and followed by the single point calculations. The calculated results from DeH9-MA and DeH10-MB are in better agreement with the experimental values. However, there are still some unacceptable differences between the calculated and the experimental values. In DeH9-MA, the calculated coupling of H7 is ~60MHz less than that of coupling 13, and the coupling of H11 is ~20MHz less than that of coupling 14; also, the difference between the intermediate eigenvector of H10 and that of coupling 11 is >26°; in DeH10-MB, although all the differences between the eigenvectors are < 10°, the calculated coupling of H8 is ~50MHz less than that of coupling 13, and the coupling of H11 is ~20MHz less than that of coupling 14. To improve the calculated parameters, manual adjustments were performed on the two optimized models. For DeH9-MA, three steps were performed: 1) bending H10 by changing dihedral angle H10-N2-C4-C5 and freezing C5 by 5°, 2) rotating H7 and H8 about C4-C5 by changing dihedral angle H10- C4-C5-H7 and freezing H10 by 37°, 3) rotating the guanidyl group about C4-N2 by changing dihedral angle H10-C5-N2-H11 and freezing H10 by 20°. For DeH10-MB, H7 and H8 are rotated about C5-C4 by 25° and H11 is rotated about the C5-N2 by 20°. The calculated parameters from the adjusted

structures agree very well with the experimental values as listed in Table 8.9. Also, the adjusted structures (see Fig. 8.18a and 8.18b) supported the results estimated above: the dihedral angles C4-N2-H10-C5 are < 9° support that the radical center is almost planar; assuming the spin orbital is normal to the plane of the radical center, the dihedral angles of the β-protons H7, H8 and H11 are ~45°, ~20°, and ~68°, respectively, in DeH9-MA, and are ~22°, ~41°, and ~59°, respectively, in DeH10-MB, so these dihedral angles are very close to those estimates above for the β-couplings with association indicated in Table 8.9.

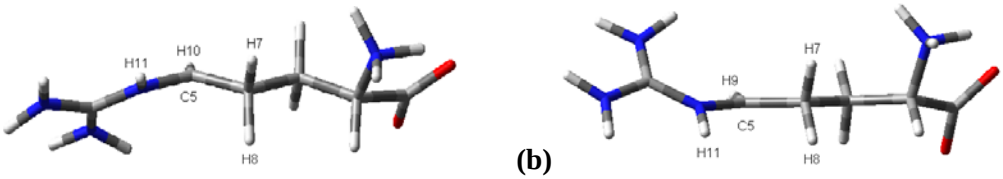

(a) **(b)**

Fig. 8.18 *The adjusted structures of the "DeH9-MA" model* ***(a)*** *and the "DeH10-MB"model* ***(b)***.

Table 8.9 *DFT calculated hyperfine-coupling tensors on adjusted structure of the radical dehydrogenation from C5 and the angular difference between the calculated and experimental maximum dipolar vectors.*[a, b, c]

DeH9-MA[c]

				Eigenvectors				
Protons	Principal Value[a]	Isotropic value[a]	Anisotropic value[a]	<a>	<b>	<c*>	:Coupling	Angle diff(°)[b]
	83.24		8.99	0.673	0.738	0.047	:13	21.8
H7	70.03	74.25	-4.22	-0.408	0.317	0.856		
	69.48		-4.77	0.617	-0.596	0.514		
	107.58		6.8	0.913	-0.197	0.357	:12	18.4
H8	98.65	100.78	-2.13	-0.293	0.293	0.910		
	96.12		-4.66	-0.284	-0.936	0.210		
	-94.33		-34.27	0.852	0.102	-0.513		20.6
H10	-61.05	-60.06	-0.99	0.465	-0.598	0.653	:11	19.9
	-24.8		35.26	0.241	0.795	0.557		13.8
	29.16		7.54	0.141	0.587	-0.797	:14	3.8
H11	19.73	21.62	-1.89	0.876	-0.449	-0.175		
	15.97		-5.65	-0.460	-0.674	-0.578		

DeH10-MB[c]

Protons	Principal Value[a]	Isotropic value[a]	Anisotropic value[a]	Eigenvectors <a>	<b>	<c*>	:Coupling	Angle diff(°)[b]
	108.4		7.34	0.796	-0.54	0.272	:13	5.5
H7	98.33	101.06	-2.73	-0.217	0.165	0.962		
	96.45		-4.61	0.565	0.825	-0.014		
	86.01		8.45	0.398	0.915	-0.060	:12	5.3
H8	73.76	77.56	-3.80	-0.652	0.328	0.683		
	72.9		-4.66	0.645	-0.233	0.728		
	-95.77		-34.97	0.832	0.260	-0.491		13.2
H9	-61.58	-60.8	-0.78	0.555	-0.403	0.728	:11	13.5
	-25.06		35.74	0.009	0.878	0.479		5.5
	37.14		7.41	0.415	0.645	-0.642	:14	15.4
H11	28.11	29.73	-1.62	0.731	-0.657	-0.188		
	23.94		-5.79	0.542	0.391	0.744		

[a]All the values are in units of MHz. [b]"Angle diff (°)" is the angular difference between the calculated and the experimental eigenvectors; for β-couplings only the eigenvectors associated with the maximum eigenvalues were compared. [c] "DeH9-MA" stands for the calculation model of dehydrogenation of H9 in molecule A; "DeH10-MB" stands for the calculation model of dehydrogenation of H10 in molecule B.

R3-dehydrogenation at C2

Based on the ENDOR and EIE from the normal crystals, couplings 15-17 were assigned to radical R3 (see Fig. 8.2). The angular dependence curves of these couplings are shown in Fig. 8.19 and their corresponding coupling tensors are listed in Table 8.10. Couplings 15-17 show characteristics typical of β-couplings. However, the EIE patterns of R3 from the normal crystal cannot be reproduced with couplings 15-17 only. The WINSIM simulations as shown in Fig. 8.20 indicate that R3 should include one additional proton coupling, which was not detected in the ENDOR experiments. This additional coupling, denoted as R3-I, was assigned as a β-coupling since the simulated couplings at three crystallographic axes are always close to 10G (28MHz). Moreover, from the comparison of ENDOR spectra from the normal and the partially deuterated crystals as shown in Fig. 8.2, coupling 16 is from an exchangeable proton, coupling 15 is from a nonexchangeable proton, and it is not possible to ascribe coupling 17 to a nonexchangeable or exchangeable proton because lines 17 in ENDOR spectra of both

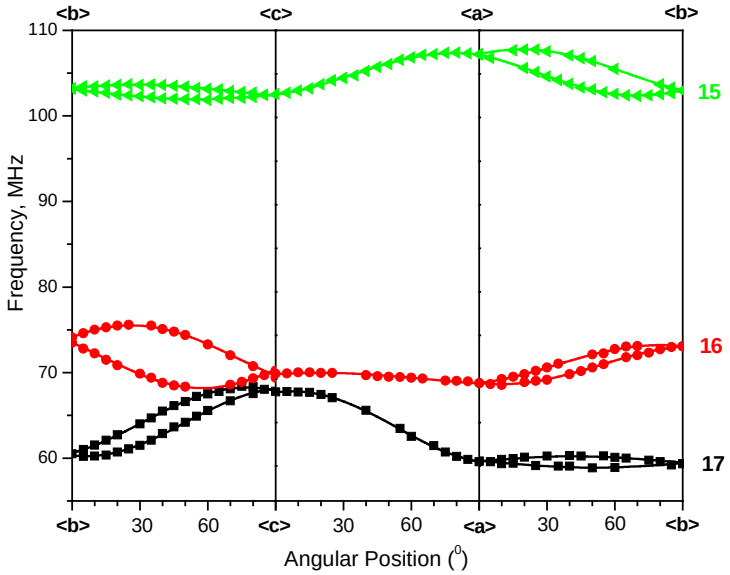

Fig. 8.19 *Angular dependence curves of couplings 15-17.*

Table 8.10 *Hyperfine coupling tensors for radical R3 detected at 66K in L-arginine·HCl·H_2O single crystals irradiated at 298K.*[a,b]

Tensors	Principal values[a,b]	Isotropic Values[a]	Anisotropic values[a]	Eigenvectors[b] <a>	<b>	<c*>
	143.72(2)		7.36	0.927(0)	-0.341(1)	0.154(2)
15	133.82(1)	136.36	-2.54	0.362(1)	0.713(3)	-0.600(4)
	131.54(1)		-4.82	0.095(1)	0.612(4)	0.785(3)
	79.24(2)		9.23	0.129(1)	0.858(0)	0.497(6)
16	66.71(2)	70.01	-3.30	0.990(0)	-0.139(3)	-0.016(1)
	64.09(2)		-5.92	0.055(0)	0.494(5)	-0.868(0)
	65.19(2)		11.23	0.195(1)	0.171(3)	0.966(3)
17	49.13(2)	53.96	-4.83	0.764(1)	0.591(3)	-0.259(2)
	47.55(2)		-6.41	0.615(0)	-0.788(1)	0.016(1)

[a]All these values are in units of MHz. [b]Numbers in parentheses are the estimated uncertainties in the last digit quoted as reported by the statistical analysis.

types of crystals are very weak. The WINSIM simulation of the EIE for B//<b> from the partially deuterated crystal as shown in Fig. 8.21 indicates that coupling 16 is from an exchangeable proton and coupling R3-I is from a nonexchangeable proton. Therefore, radical R3 with four β-couplings (two are

exchangeable and the other two are nonexchangeable) can be assigned to the radical of dehydrogenation from C2 (see Scheme 8.4) with the spin mainly located on C2.

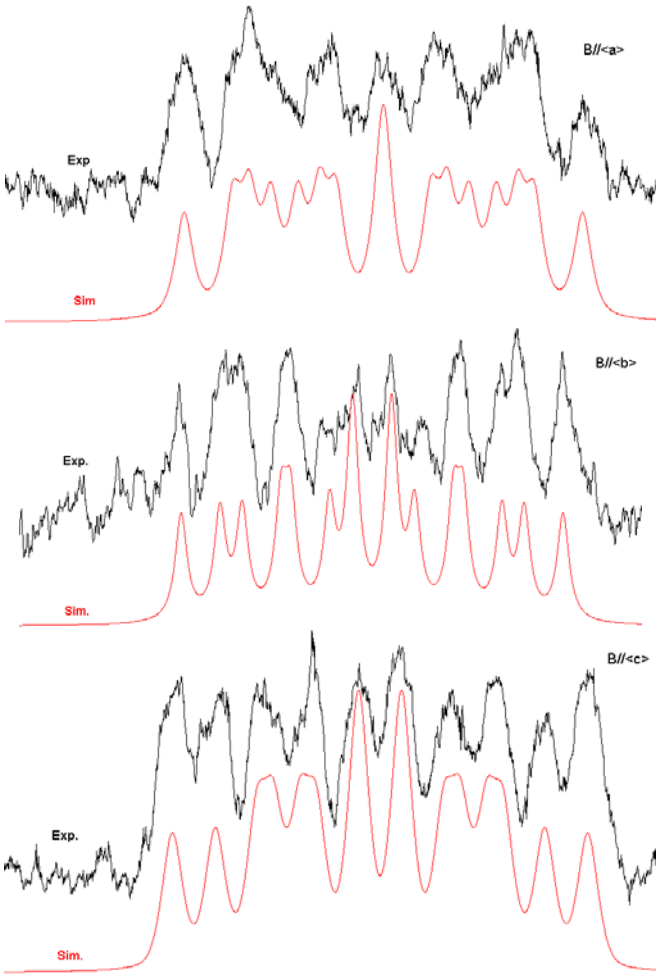

Fig. 8.20 *WINSIM simulations for EIE patterns of R3 from the normal crystals L-arg·HCl·H_2O with the magnetic field along <a>, <b> and <c>.*

In order to help assign the couplings to β-protons H1-H3, H5 and H6 in the radical, the eigenvectors[I] of couplings 15-17 were compared to the crystallographic directions in molecules A and B. As shown in Table 8.11, the eigenvectors[I] of couplings 15, 16 and 17 are very close to directions H1…C2, H3…C2, and H2…C2 (in molecules A and B), respectively, and thus 15, 16 and 17 can be assigned to H1, H3 and H2 (in molecules A and B). Thus coupling R3-I can be assigned to H4 (in molecules A and B), the other

nonexchangeable proton in the radical. The comparisons support the assignment of R2 to the radical dehydrogenation from C2, and also indicated that no large reorientation occurred after the radical formed.

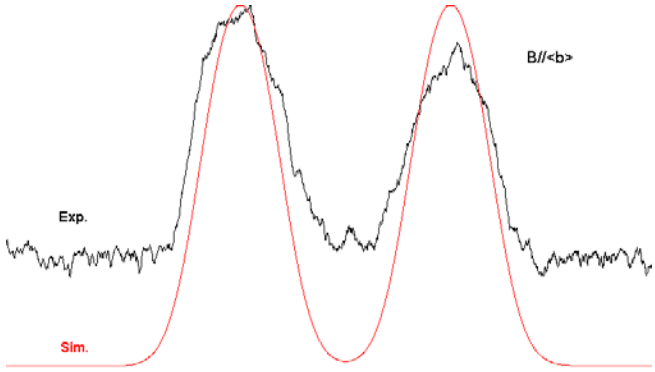

Fig. 8.21 *WINSIM simulation for EIE pattern of R3 from the partially deuterated crystal L-arg·HCl·H_2O with nonexchangeable couplings 15 and R3-I; the magnetic field is along <b>.*

Table 8.11 *The comparison between the maximum eigenvectors of tensors 15-17 and the corresponding crystallographic directions in molecules A and B.*[a,b]

	Eigenvectors[a]				Directions of H_β….C2[b]			
Coupling	<a>	<b>	<c*>	Protons[b]	<a>	<b>	<c*>	Angle Diff (°)[c]
15	0.927	-0.341	0.154	H1(MA)	0.823	-0.512	0.245	12.8
				H1(MB)	0.720	-0.641	0.266	22.0
16	0.129	0.858	0.497	H3(MA)	0.053	0.900	0.433	6.1
				H3(MB)	0.268	0.870	0.414	9.3
17	0.195	0.171	0.966	H2 (MA)	0.326	0.362	0.873	14.4
				H2 (MB)	0.301	0.301	0.905	10.1

[a]The eigenvectors are the principal directions associated with the largest coupling components. [b]H_β are the β-protons of the radical dehydrogenation from C2; "MA" and "MB" stand for in molecule A and in molecule B, respectively. [c]"Angle Diff (°)" are the angular differences between the experimental eigenvectors and the crystallographic directions in units of degrees.

Modeling calculation: The experimental coupling tensors of R3 were reproduced well from the calculations performed on the cluster models. As shown in Fig. 8.22a and 8.22b, the center radicals of the cluster models were constructed by removing H4 from molecules A and B, respectively. In addition to the center radical, the cluster model for R3 (molecule A) contains two amino groups I and II, one guanidyl group III in three neighboring molecules, respectively, and one neighboring water molecule IV. H1' and

H2’ in groups I and II involve the hydrogen bonds to O1; while H3’ and H4’ in groups III and IV involve the hydrogen bonds to O2. For calculation efficiency, the remainders of arginine molecules in groups I-III are simulated with methyl groups (see Fig. 8.22a). Similarly, the cluster model for R3 (molecule B) contains neighboring groups I-III: group I is from an arginine molecule with the carboxyl group replaced by a H atom; group II is an amino group from a second arginine neighbor, and the other parts of the molecule are simulated by a methyl group; group III is a neighboring water molecule. H1’ and H2’ in group I involve the hydrogen bonds to O1; while H3’ and H4’ in groups II and III involve the hydrogen bonds to O2 (see Fig. 8.22b). All the initial atom coordinates are from the crystallographic studies.[6] Considering the environmental effects on the clusters, some of the atoms were frozen during the geometry optimization, as marked “f” in Fig. 8.22a and 8.22b. The single point calculations performed on the optimized clusters for R3 (molecules A and B) indicated that the unpaired spin is mainly on C2 of the center radicals (~0.86). The optimized structures for R3 (molecules A and B), as shown in Fig. 8.22c and 8.22d, indicate that the radical centers are not completely planar, with dihedral angles <N1-C1-C3-C2 of 23.2° and 28.6°, respectively. The calculated coupling tensors from the optimized cluster for R3 (molecule A) reproduce the experimental coupling tensors very well, as are listed in Table 8.12a. The calculated coupling tensors from the optimized cluster of R3 (molecule B) also reproduce the experimental tensors well, except the coupling on H2 is smaller than that of coupling 17 by ~31MHz, as are listed in Table 8.22b. By rotating the amino protons by ~15° around N1-C2 axis of the center radical (molecule B), couplings on amino protons H1-H3 are 1.02MHz, 37.00MHz, and 59.81MHz, respectively; i.e., couplings on H2 and H3 are smaller than those of couplings 17 and 16 by ~16MHz and 10MHz, respectively. The single point calculation on the adjusted cluster using the basis set of EPR-II increases the couplings on H2 and H3 by ~5MHz, on H5 by ~10MHz, on H1 and on H6 by ~1MHz, and these couplings are much closer to the experimental couplings, as are listed in Table 8.22c. Thus, the cluster calculations supported the assignment of R3 to the radical dehydrogenation at C2.

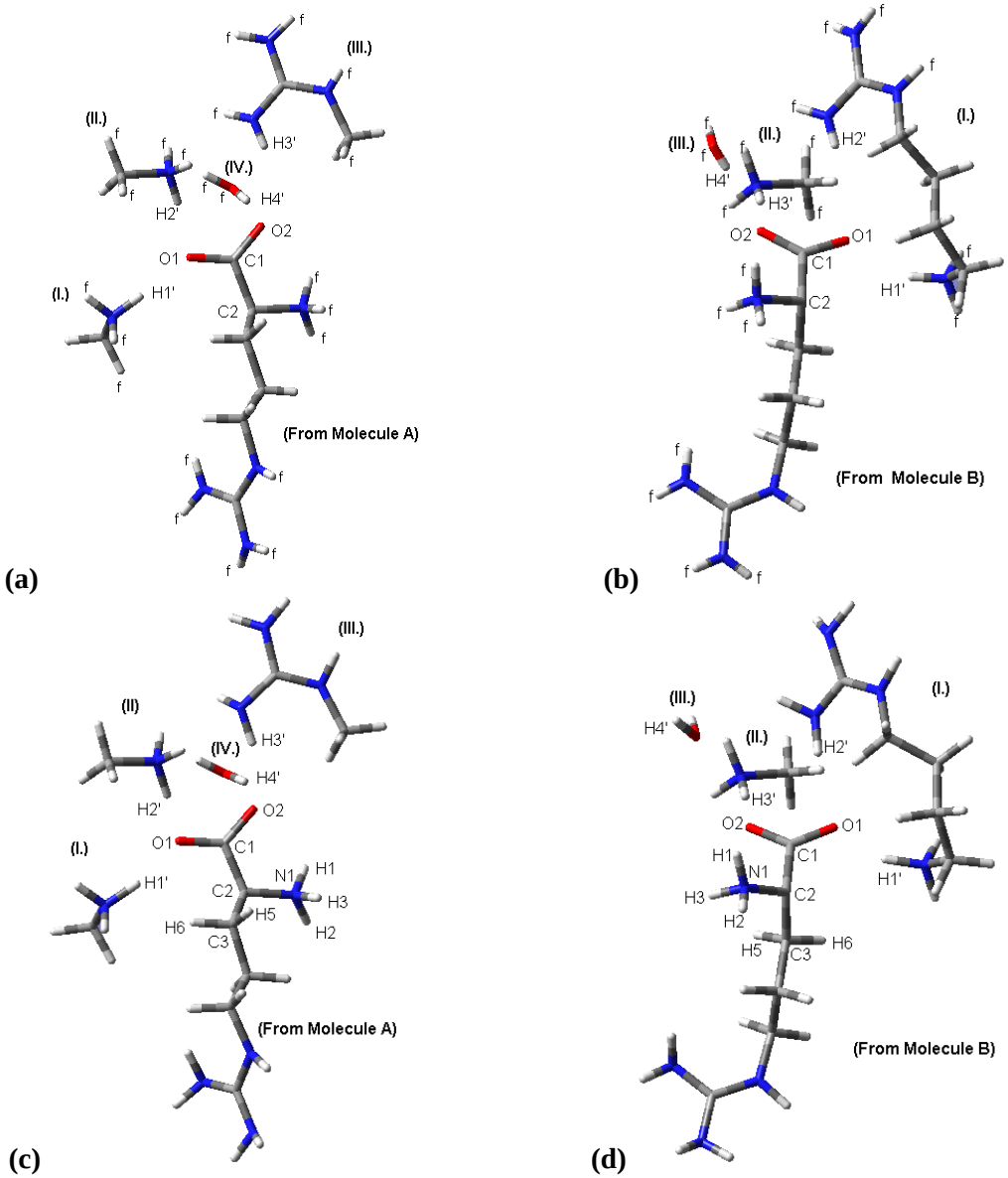

Fig. 8.22 *The cluster models of R3 (dehydrogenation at C2) from molecules A and B before* ***(a - b)*** *and after* ***(c - d)*** *the geometry optimizations.*

Table 8.12(a) *The DFT calculated hyperfine-coupling tensors from the cluster models of the radical dehydrogenation at C2 from molecule A, and the angular differences between the calculated and experimental eigenvectors.*[a, b]

				Eigenvectors				
Protons	Principal Value[a]	Isotropic value[a]	Anisotropic value[a]	<a>	<b>	<c*>	: Couplings	Angle diff(°)[b]
	10.59		9.31	0.680	0.613	0.403		
H1	-2.99	1.28	-4.27	-0.279	0.724	-0.631		
	-3.76		-5.04	0.678	-0.317	-0.663		
	57.49		10.95	0.214	0.410	0.887	: 17	14.4
H2	41.25	46.54	-5.29	0.975	-0.146	-0.167		
	40.88		-5.66	0.061	0.901	-0.431		
	77.52		8.23	0.002	0.840	0.542	: 16	8.0
H3	66.33	69.29	-2.96	0.987	-0.089	0.135		
	64.02		-5.27	-0.162	-0.535	0.829		
	138.43		7.31	0.881	-0.420	0.220	: 15	6.4
H5	128.67	131.12	-2.45	0.474	0.772	-0.424		
	126.26		-4.86	0.009	0.478	0.879		
	28.58		9.06	0.857	0.329	0.398		
H6	15.41	19.52	-4.11	-0.317	-0.273	0.908		
	14.57		-4.95	-0.407	0.904	0.130		

[a] All these values are in units of MHz. [b] The "Angle diff (°)" is the angular difference between the calculated and the experimental eigenvectors associated with the maximum eigenvalues in units of degrees.

Table 8.12(b) *The DFT calculated hyperfine-coupling tensors from the cluster models of the radical dehydrogenation at C2 from molecule B, and the angular differences between the calculated and experimental eigenvectors.*[a, b]

				Eigenvectors				
Proton	Principal Value[a]	Isotropic value[a]	Anisotropic value[a]	<a>	<b>	<c*>	:Coupling	Angle diff(°)[b]
	10.25		9.70	0.836	0.440	0.329		
H1	-3.44	0.55	-3.99	-0.322	0.877	-0.356		
	-5.16		-5.71	-0.445	0.192	0.875		
	34.05		11.39	0.303	0.418	0.857	: 17	16.6
H2	17.29	22.66	-5.37	-0.378	0.878	-0.294		
	16.64		-6.02	0.875	0.235	-0.423		
	83.42		8.72	0.327	0.838	0.438	: 16	11.8
H3	71.65	74.70	-3.05	0.716	-0.522	0.464		
	69.03		-5.67	-0.618	-0.162	0.770		
	133.33		6.96	0.741	-0.610	0.280	: 15	20.3
H5	124.81	126.37	-1.56	0.640	0.517	-0.568		
	120.97		-5.40	0.202	0.600	0.774		
	35.07		10.40	0.928	0.121	0.353		
H6	19.71	24.67	-4.96	0.132	0.779	-0.614		
	19.23		-5.44	-0.349	0.616	0.706		

[a] All these values are in units of MHz. [b] The "Angle diff (°)" is the angular difference between the calculated and the experimental eigenvectors associated with the maximum eigenvalues in unit of degree.

Table 8.12(c) *The hyperfine-coupling tensors from the DFT calculation on the adjusted cluster model of the radical dehydrogenation at C2 from molecule B with basis set of EPR-II, and the angular differences between the calculated and experimental eigenvectors.*[a, b]

				Eigenvector				
Proton	Principal Value[a]	Isotropic value[a]	Anisotropic value[a]	<a>	<b>	<c*>	:Coupling	Angle diff(°)[b]
	10.34		8.97	0.817	0.498	0.291		
H1	-2.35	1.37	-3.72	-0.499	0.864	-0.077		
	-3.90		-5.27	-0.289	-0.082	0.954		
	52.47		12.4	0.378	0.331	0.865	: 17	15.0
H2	34.04	40.07	-6.03	0.219	0.876	-0.431		
	33.71		-6.36	0.900	-0.352	-0.258		
	73.74		9.05	0.223	0.834	0.505	: 16	5.5
H3	61.5	64.69	-3.19	0.896	-0.379	0.230		
	58.83		-5.86	-0.383	-0.401	0.832		
	143.01		6.82	0.737	-0.614	0.283	: 15	20.6
H5	134.89	136.19	-1.3	0.644	0.511	-0.570		
	130.67		-5.52	0.206	0.602	0.771		
	35.99		10.44	0.927	0.118	0.357		
H6	20.51	25.55	-5.04	0.150	0.754	-0.639		
	20.15		-5.40	-0.345	0.646	0.681		

[a] All these values are in units of MHz. [b] The "Angle diff (°)" is the angular difference between the calculated and the experimental eigenvectors associated with the maximum eigenvalues in units of degrees.

Radical R4 - the unknown radical

The EIE pattern of R4 at <b> as shown in Fig. 8.3, is a three-line pattern with a ratio of ~1:2:1, thus at least two couplings are included in R4. Using the WINSIM program, the EIE pattern could be simulated with two couplings: 13.66G and 12.36G (see Fig. 8.23b). The EIE at <a> becomes a four-line pattern with peak ratio of 1:1:1:1, and the WINSIM simulation indicated two couplings in EIE are 15.60G and 8.90G (see Fig. 8.23a). The coupling of 13.66G at <b> and 15.60G at <a> is from line 18, and the 2nd coupling was not detected in the experiments. The EIE pattern at <a> from the partially deuterated crystal as shown in Fig. 8.24 is a two-line pattern with space of 16.3G. This indicates that coupling 18 is from a nonexchangeable proton, and the 2nd coupling is from an exchangeable proton. No more information could be obtained from the experiments for R4, thus it is impossible to assign it.

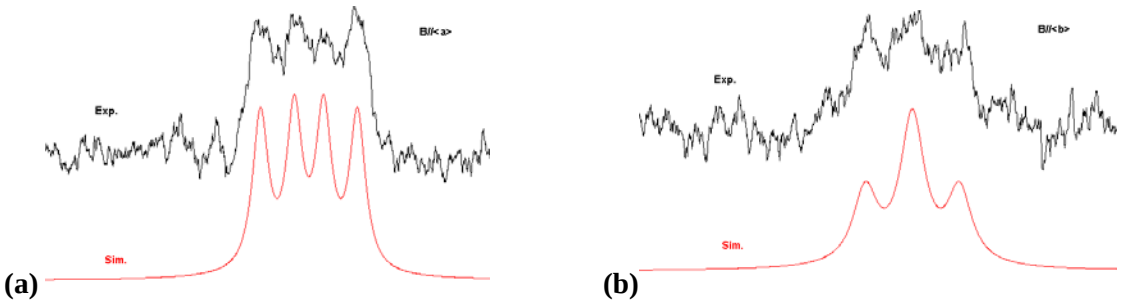

(a) **(b)**

Fig. 8.23 *WINSIM simulations for EIE patterns of R4 at <a>* ***(a)*** *and <b>* ***(b)****.*

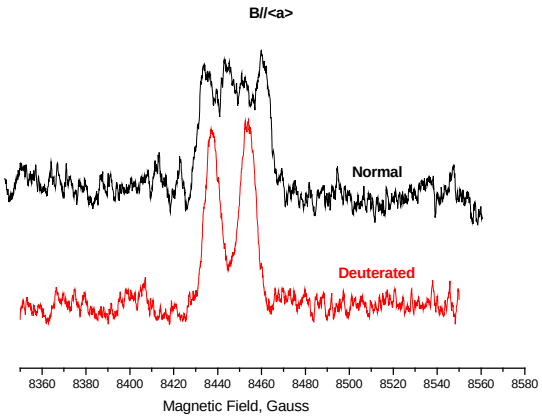

Fig. 8.24 *The comparison of EIE pattern for R4 from the normal and the partially deuterated crystal at <a>.*

EPR simulations

WINSIM simulations reproduced the EPR spectra at <b> and at <c> very well with couplings of R1a-c, and R2-R4, as shown in Fig. 8.25a and 8.25b. From these simulations, the concentrations of radicals R1a-c, and R2-R4 can be estimated as ~30% of R1a, ~13% of R1b, ~12% of R1c, ~25% of R2, ~15% of R3 and ~5% of R4.

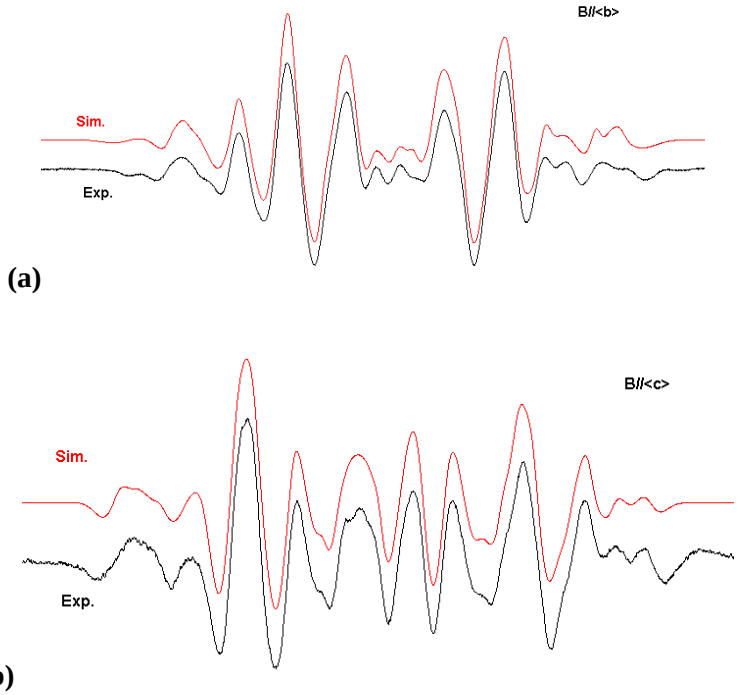

Fig. 8.25 *WINSIM simulations for EPR spectra at <b>* ***(a)*** *and <c>* ***(b)*** *detected at 66K in L-arginine·HCl·H_2O single crystal irradiated at 298K.*

8.3.2 Experiments at 298K

Fig. 8.26 shows the EPR, ENDOR and EIE for B//<b> detected at 298K in the crystal X-irradiated at 298K. Three distinct EIE patterns were detected and assigned to three different radicals RI, RII and RIII. From the analysis described latter, the EIE patterns of RII are from two conformations of a same radical, denoted as RIIa and RIIb. It can be seen from the comparison of EPR and EIE that the strong eight-line pattern in the EPR spectrum is mainly from RI. The ENDOR spectrum was obtained by choosing the magnetic field of a strong peak in the center of the EPR, as indicated by the arrow in Fig. 8.26. Based on EIE patterns, the ENDOR lines can be assigned to radicals RI-RIII. Lines α1, β1 and β2 were assigned to RI, α2 and β3-β5 were assigned to RIIa, α3 and β6-β8 were assigned to RIIb, β9-β11 were assigned to RIII. A comparison of tensors from radicals RI, RII and RIII suggests they might be the same radicals as R1, R2 and R3, respectively, detected at 66K as described above.

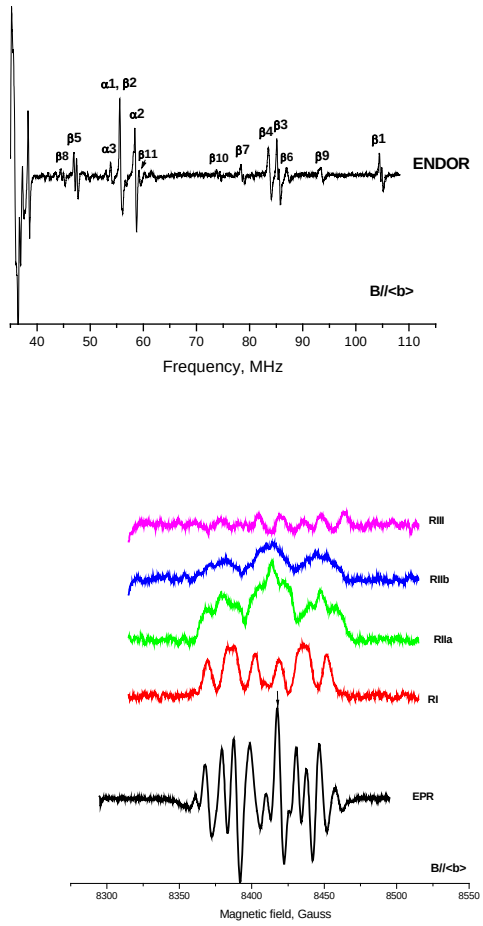

Fig. 8.26 *ENDOR, EPR and EIE detected at 298K in the crystal L-arginine·HCl·H_2O irradiated at 298K.*

Radical RI- the main-chain deamination radical:

The angular dependence curves of couplings α1, β1 and β2 are shown in Fig. 8.27, and their coupling tensors are listed in Table 8.13. Coupling α1 is typical of an α-coupling, while β1 and β2 are typical of β-couplings. Using the tensors of α1, β1 and β2, the EIE patterns are reproduced well, as shown in Fig. 8.28. Thus the major couplings in RI are one α- and two β-couplings. Comparison of the EIE patterns from the normal and the partially deuterated crystals (see Fig. 8.29) indicated that the couplings in RI are from nonexchangeable protons.

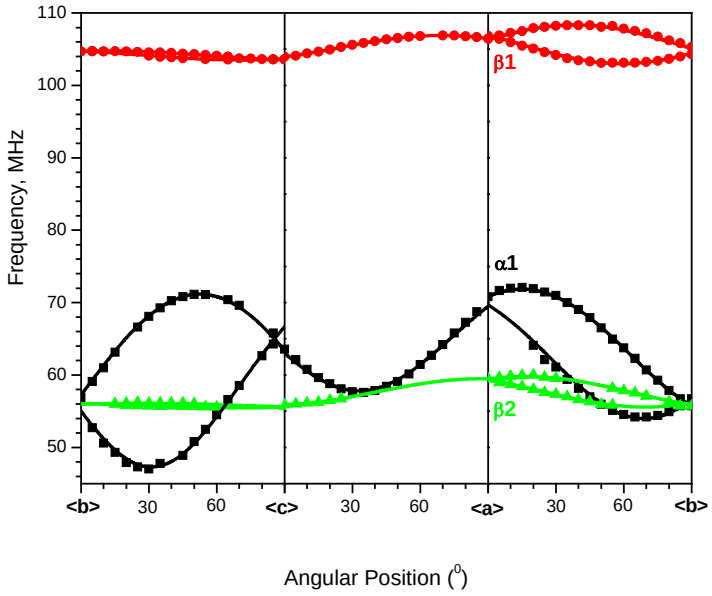

Fig. 8.27 *Angular dependence curves of couplings in RI.*

Table 8.13 *Hyperfine coupling tensors in radical RI.*[a, b]

Tensors	Principal values[a,b]	Isotropic Values[a]	Anisotropic values[a]	Eigenvectors[b] <a>	<b>	<c*>
	-88.24(3)		-33.66	0.661(0)	-0.410(0)	-0.628(1)
α1	-52.89(3)	-54.58	1.69	0.750(0)	0.372(1)	0.547(0)
	-22.61(3)		31.97	0.010(0)	-0.833(1)	0.553(1)
	146.29(2)		7.60	0.824(0)	0.528(5)	0.206(1)
β1	135.52(2)	138.69	-3.17	0.068(1)	-0.453(6)	0.889(4)
	134.27(1)		-4.42	0.562(1)	-0.719(4)	-0.409(8)
	48.09(2)		5.69	0.946(0)	0.314(4)	0.078(2)
β2	40.23(2)	42.40	-2.17	0.168(1)	-0.684(8)	0.709(8)
	38.89(2)		-3.51	0.276(3)	-0.658(8)	-0.701(8)

[a]All of the values are in units of MHz. [b] Numbers in parentheses are the estimated uncertainties in the last digit quoted as reported by the statistical analysis.

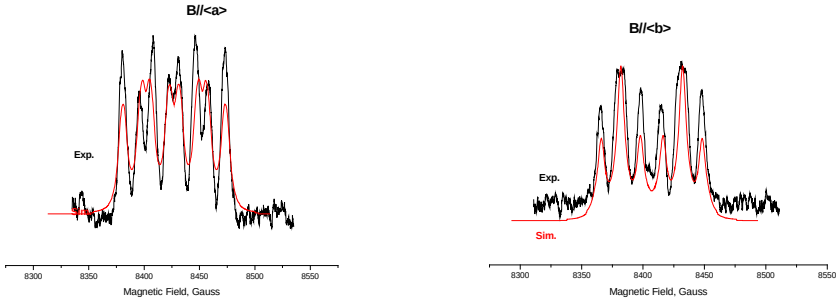

Fig. 8.28 *Simulations of EIE patterns of R1 at <a> and <b> with coupling tensors α1, β1 and β2.*

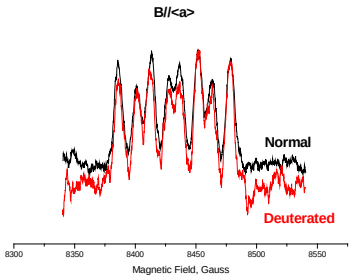

Fig. 8.29 *EIE patterns at <a> of R1 from the normal and the partially deuterated crystals.*

From these characteristics, RI was assigned as the main-chain deamination radical with the spin mainly on C2 (see Schemes 8.3a and 8.3b). Thus, the eigenvectors[I] of tensors α1, β1 and β2 were compared to the corresponding crystallographic directions. As shown in Table 8.14, the eigenvector[I] of α1 is close to directions of C2-H4 in molecules A and B, the eigenvectors[I] of β1 and β2 are very close to directions of C2… H6 and C2…H5, respectively. At the same time, in the crystal, the dihedral angles <N1-C2-C3-H5 and <N1-C2-C3-H6 are ~65° and 2°. If we assume the C2-N1 bond in the crystal is the spin orbital direction in the deamination radical, then H6 can give a large coupling, while H5 gives a smaller coupling, and those agree with the couplings of β1 and β2. Therefore, these results support the assignment of RI to the main-chain deamination radical, and also indicate that RI experienced little

reorientation. From this coupling α1 can be ascribed to H4, couplings β1 and β2 can be ascribed to H6 and H5, respectively. However, no modeling calculation can reproduce the parameters of RI.

Table 8.14 *The comparison between the eigenvectors[a] of coupling tensor in RI and the corresponding crystallographic directions.* [b,c]

Coupling	Eigenvectors[a]			Proton[b]	Directions of Hx….C2 in MA[b]			
	<a>	<b>	<c*>		<a>	<b>	<c*>	Angle Diff (°)[c]
α1	0.010	-0.833	0.553	H4	0.203	-0.890	0.408	14.3
β1	0.824	-0.528	0.206	H6	0.912	-0.262	0.316	17.3
β2	0.946	0.314	0.078	H5	0.823	0.512	0.245	16.6

Coupling	Eigenvectors[a]			Proton[b]	Directions of Hx….C2 in MB[b]			
	<a>	<b>	<c*>		<a>	<b>	<c*>	Angle Diff (°)[c]
α1	0.010	-0.833	0.553	H4	0.069	-0.930	0.362	12.7
β1	0.824	-0.528	0.206	H6	0.956	-0.089	0.279	26.8
β2	0.946	0.314	0.078	H5	0.720	0.641	0.266	25.4

[a]The eigenvectors are the principal directions associated with the largest coupling components. [b] Hx are protons in molecule A (MA) and in molecule B (MB). [c]"Angle Diff (°)" are the angular differences between the experimental eigenvectors and the crystallographic directions in units of degrees.

Results listed in Table 8.15 showed that the isotropic and anisotropic values of α-coupling tensors in R1a, R1b and RI are similar (that from R1c could not be obtained from the experiments). As discussed above, for R1a and R1b, the McConnell relation (1) and the Gordy-Bernhard relation (2) yield the similar spin density estimates (0.74 and 0.83, respectively) for RI indicating that it also is in the sp^2 configuration. As with R1a-R1c, one of the two β-couplings from RI is much larger than the other, indicating a configuration with one much closer to the spin orbital than the other (see Fig. 8.6 and Fig. 8.10). Moreover, the smaller and the larger β-couplings in R1a (5.07MHz and 97.08MHz) are smaller than the corresponding β-couplings in R1b, R1c and RI (~30-70MHz and ~144MHz). The modeling calculations indicated that R1b and R1c are the deamination radical with two O-H dipolar couplings (see Scheme 8.3b), while R1 does not have the O-H dipolar coupling (see Scheme 8.3a). Since the β-couplings of RI are very close to those of R1b, thus RI could be the deamination radical with two O-H dipolar couplings. In addition, the eigenvectors of α-coupling tensor in RI are very similar to these of R1b

Table 8.15 *The coupling tensors in RI compared to those in R1a* ***(a),*** *R1b* ***(b)*** *and R1c* ***(c)***[a, b]

(a)			Eigenvectors				
Tensors	Isotropic Values[a]	Anisotropic values[a]	<a>	<b>	<c*>	Tensors	Angle Diff (°)[b]
		-30.27	0.670	-0.494	-0.555		6.4
1	-55.79	-0.02	0.370	-0.426	0.826	:α1	55.2
		30.30	0.644	0.758	0.103		55.4
		8.31	0.630	0.742	-0.228		85.4
2	97.09	-3.23	0.525	-0.191	0.829	:β1	30.8
		-5.09	0.572	-0.642	-0.510		7.3
		7.81	0.098	0.881	0.462		69.8
3	5.09	-3.63	0.564	0.333	-0.755	:β2	100.2
		-4.17	0.820	-0.335	0.465		95.5

(b)			Eigenvectors				
Tensors	Isotropic Values[a]	Anisotropic values[a]	<a>	<b>	<c*>	Tensors	Angle Diff (°)[b]
		-31.45	0.764	-0.356	-0.538		8.5
5	-53.17	1.05	0.633	0.252	0.732	:α1	14.4
		30.41	0.125	0.900	-0.418		11.6
		8.2	0.889	-0.444	0.112		8.1
6	140.87	-2.66	0.183	0.568	0.802	:β1	10.6
		-5.54	0.420	0.693	-0.586		13.2
		7.39	0.280	-0.952	-0.101		55.7
7	28.47	-2.89	0.224	0.169	-0.960	:β2	58.2
		-4.49	0.931	0.254	0.262		76.1

(c)			Eigenvectors				
Tensors	Isotropic Values[a]	Anisotropic values[a]	<a>	<b>	<c*>	Tensors	Angle Diff (°)[b]
		7.10	0.461	0.787	0.411		28.4
9	144.58	-1.78	0.388	0.238	-0.891	:β1	29.2
		-5.31	0.798	-0.570	0.196		38.9
		8.05	0.034	0.969	0.247		69.2
10	76.47	-2.77	0.947	0.048	-0.318	:β2	95.7
		-5.26	0.320	-0.244	0.915		66.9

[a]These values are in units of MHz. [b]"Angle Diff (°)" are the angular differences between the eigenvectors in units of degrees.

(angular differences < 15°) and very different from those of R1a (angular differences > 40°); also, the eigenvectors of β-coupling tensors in R1a, R1c and RI are quite different. Although the eigenvectors of

tensor β1 in RI are very close to those of tensor 6 in R1b, the eigenvectors of tensor β2 in RI is quite different from those of tensor 7 in R1b with angular differences > 55°. These differences indicate that R1a-c and RI are in quite different conformations. The comparison between the eigenvectors^{I} and the crystallographic directions indicates that RI had little reorientation, and R1a-c reoriented in large degree, which are supported by the geometry optimizations for the models of R1a-c.

Therefore, although no calculated values from the deamination radical model agreed completely with experimental results from RI, from the above analysis, we can conclude three characteristics of RI: 1.) the radical center of RI is in sp^2 hybridization; 2.) RI has two O-H dipolar protons (see Scheme 8.3a); 3.) RI experienced small reorientation, mainly bending of the radical center to the sp^2 configuration.

RIIa and RIIb-the radical dehydrogenation from C5

Couplings α2, α3 and β3-β8 gave similar EIE patterns at three axes. At each axis position, the sum of these couplings is about twice of the width of the EIE pattern, thus the EIE patterns are from two radicals at least.

In order to group the lines into two sets (for RIIa and RIIb), it was necessary to examine similarities of the tensors and ENDOR signal intensities. The tensors from these couplings are listed in Table 8.16a and 8.16b and their angular dependence curves are shown in Fig. 8.30a and 8.30b. Couplings α2 and α3 show large anisotropy, and couplings β3-β8 show small anisotropy along with axial symmetry. Thus, α2 and α3 are assigned as α-couplings, and β3-β8 are assigned as β-couplings. From the tensor comparison shown in Table 8.16b, it can be seen that tensors α2 and α3, β5 and β8 are very similar, tensors β3, β4, β6 and β7 have similar isotropic values, but the eigenvectors of β3 and β4 are closer to those of β6 and β7, respectively. Based on these results, couplings α2 and α3, β5 and β8, β3 and β6, β4 and β7 can be divided into two groups. However, it is still not possible to assign the couplings to each group from this

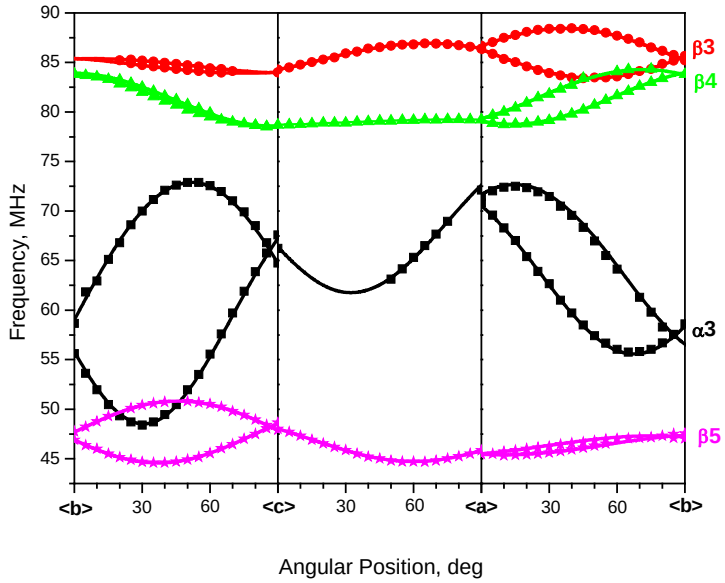

Fig. 8.30(a) *The angular dependence curves of couplings of RIIa.*

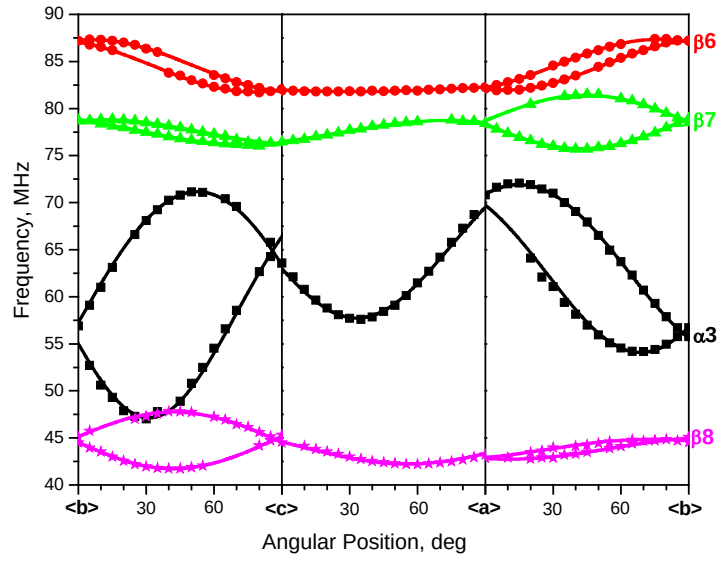

Fig. 8.30(b) *The angular dependence curves of couplings of RIIb.*

analysis alone. At each orientation, ENDOR lines α2, β3-β5 are strong and have similar peak intensities, while lines α3, β6-β8 are weaker and also have similar peak intensities (see Fig. 8.26). Assuming that

Table 8.16 *Hyperfine coupling tensors from radicals RIIa* ***(a)*** *and RIIb* ***(b)*** *in L-arg·HCl·H_2O single crystals irradiated at 298K, and the comparison between tensors of RIIa and RIIb* ***(b)****.*[a,b,c]

(a)				Eigenvectors[b]		
Tensors	Principal values[a,b]	Isotropic values[a]	Anisotropic values[a]	<a>	<b>	<c*>
	-89.52(3)		-32.76	0.696(0)	-0.421(0)	-0.582(1)
α 2	-55.50(3)	-56.76	1.26	0.717(0)	0.355(1)	0.600(0)
	-25.26(3)		31.50	0.046(0)	0.835(1)	-0.549(1)
	105.49(1)		6.62	0.752(1)	0.612(4)	0.245(1)
β 3	96.57(2)	98.87	-2.30	0.155(1)	-0.524(4)	0.837(3)
	94.56(1)		-4.31	0.641(1)	-0.592(3)	-0.489(5)
	96.99(2)		7.51	0.279(1)	0.960(1)	0.036(24)
β 4	85.90(2)	89.48	-3.58	0.959(0)	-0.276(2)	-0.067(7)
	85.55(2)		-3.93	0.055(1)	-0.053(25)	0.997(2)
	31.09(2)		8.71	0.345(1)	0.592(2)	-0.728(3)
β 5	19.73(2)	22.38	-2.65	0.776(1)	-0.616(3)	-0.133(2)
	16.32(2)		-6.06	0.528(0)	0.519(2)	0.672(1)

(b)				Eigenvectors[b]				
Tensors	Principal values[a,b]	Isotropic Values[a]	Anisotropic values[a]	<a>	<b>	<c*>	:Tensors	Ang Diff (°)[c]
	-84.96(3)		-31.68	0.655(0)	-0.414(0)	-0.632(1)		3.6
α 3	-52.30(3)	-53.28	0.98	0.755(0)	0.403(1)	0.518(0)	: α 2	5.6
	-22.58(3)		30.70	-0.041(0)	0.816(1)	-0.576(1)		5.3
	103.50(2)		7.56	0.198(1)	0.969(4)	-0.148(7)		11.4
β 6	92.55(2)	95.94	-3.39	0.854(0)	-0.244(1)	-0.459(3)	: β 4	23.5
	91.76(2)		-4.18	0.481(1)	0.035(7)	0.876(4)		26.1
	91.26(2)		7.20	0.697(1)	0.717(2)	0.025(1)		14.3
β 7	82.41(2)	84.06	-1.65	0.408(1)	-0.425(2)	0.808(2)	: β 3	15.8
	78.52(2)		-5.54	0.590(1)	-0.553(1)	-0.589(2)		6.5
	25.04(2)		8.22	0.352(1)	0.651(3)	-0.672(5)		5.1
β 8	14.19(2)	16.82	-2.63	0.849(1)	-0.524(4)	-0.063(3)	: β 5	8.1
	11.22(2)		-5.60	0.393(1)	0.549(4)	0.738(1)		8.7

[a]All these values are in units of MHz. [b]Numbers in parentheses are the estimated uncertainties in the last digit quoted as reported by the statistical analysis. [c]"Ang Diff (°)" are the angular differences (in degrees) between the eigenvectors of the tensors.

the peak intensity is related to the yield of the radical, and that the couplings from the same radical generally have similar peak intensities, couplings α2, β3-β5 and couplings α3, β6-β8 are grouped into

two radicals, denoted as RIIa and RIIb. That is, the radicals RIIa and RIIb each have one α- and three β-couplings.

Radical R2, with one α- and three β-couplings, also was detected at 66K from the crystal irradiated at room temperature (RT/66K), and was identified as the radical from dehydrogenation at C5 (see Scheme 8.2). Coupling tensors 11-14 of R2 (RT/66K) were compared to those of RIIa and RIIb and as are listed in Table 8.17. For RIIa, coupling tensors α2, β3, β4, and β5 are very close to tensors 11, 12, 13 and 14, respectively. Therefore, this evidence indicates that RIIa is the same as R2 (RT/66K), the result of dehydrogenation from C5. Also, the strong similarity of RIIa (298K) and R2 (66K) indicates that the temperature has very little effect on the geometry of the radical. For RIIb, tensors α3, β8 are very close to tensors 11 and 14, respectively; the eigenvectors of β6 and β7 are close to those of 13 and 12, respectively, but the isotropic value of b6 is larger than that of 13 by 12.9MHz, and the isotropic value of β7 is smaller than that of 12 by 22.5MHz. Therefore, RIIb can be assigned as the same radical form as R2 (66K) and RIIa but with a different geometry. Modeling calculations of the radical from dehydrogenation at C5 supports the conclusion that couplings 12 and 13 are from the two protons bonded to C4.[III] From the analysis described above, the dihedral angles for these two β-protons are ~22° (related to coupling 13) and ~33° (related to coupling 13). By the same method, (from the adjusted Heller-McConnell relation, $a_{iso}(C\text{-}H_\beta) = B_1\rho\cos^2\theta$ and $B_1\rho = 125$MHz) the dihedral angles for the two β-protons related to couplings β7 and β6 are ~35° and ~29°. These results indicate that the major difference between the configurations of RIIb and R2(66K) or RIIa is that the two protons bonded to C4 in RIIb are rotated by ~10° relative to those in R2(66K) and in RIIa, as shown in Fig. 8.31. The intensity of the ENDOR lines indicated that the yield of radical RIIb is much less than that of RIIa.

[III] The modeling calculations of the radical dehydrogenation from C5 supported that in molecule A, coupling 11, 12, 13 and 14 are from H10, H8, H7 and H11, respectively; in molecule B, coupling 11, 12, 13 and 14 are from H9, H7, H8 and H11, respectively.

Table 8.17 *The comparisons between hyperfine coupling tensors from radicals R2(RT/66K) and RIIa, R2(RT/66K) and RIIb.*[a,b]

Tensor (R2)	Isotropic Values[a]	Anisotropic values[a]	Eigenvectors <a>	<b>	<c*>	: Tensor (RIIa)	Ang Diff [b]	: Tensor (RIIb)	Ang Diff [b]
		-30.81	0.688	0.408	-0.601		0.1		2.0
11	-59.81	-0.85	0.726	-0.389	0.567	: α2	2.8	: α3	3.0
		31.66	-0.002	-0.826	-0.564		2.2		2.6
		7.51	0.846	-0.481	0.229		9.4		19.9
12	106.6	-2.25	0.016	0.453	0.892	: β3	9.4	: β7	23.1
		-5.26	0.533	0.751	-0.391		12.2		16.2
		8.93	0.352	0.936	0.013		4.3		12.9
13	83.06	-4.78	0.873	-0.324	-0.364	: β4	18	: β6	7.4
		-4.15	0.337	-0.14	0.931		17.4		13.4
		9.42	0.206	0.571	-0.795		8.9		11.9
14	24.97	-2.62	0.726	-0.634	-0.267	: β5	8.3	: β8	15.1
		-6.8	0.656	0.522	0.545		10.4		18.8

[a]All these values are in unit of MHz. [b] "Ang Diff" are the angular differences (in degrees) between the eigenvectors of the tensors.

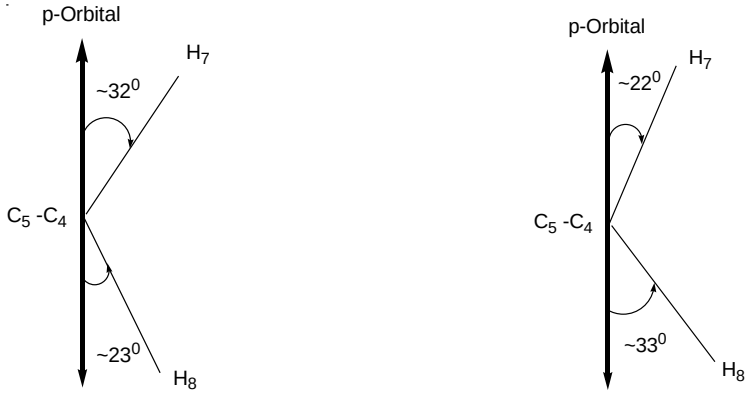

RIIb (RT/RT) R2 (RT/66K)

Fig. 8.31 *The sketch for the β-protons (H7 and H8) configuration of radical RIIb compared to that of R2 (RT/66K) or RIIa.*

8.4 Summary and Discussion

In the crystal irradiated at room temperature, radical RI (detected at 298K) was assigned as the main-chain deamination radical. In the crystal irradiated at 66K, the carboxyl anion radical is assigned as the major radical. The annealing experiments from irradiation at 66K showed that the radicals formed at room

temperature are same as those in the crystal irradiated at 298K (see Fig. 8.32). Combining with the previous studies of irradiated amino acids, the carboxyl anion radical can be assigned as the precursor of the deamination radical. In addition, three conformations of the deamination radical, R1a-R1c were detected at 66K in the crystal irradiated at room temperature. The reversibility of the conformation change from R1a-R1c (66K) to RI (298K) indicated that RI is a stable conformation of the deamination radical.

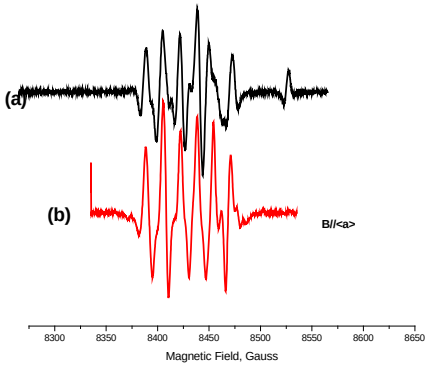

Fig. 8.32 (a) *EPR spectrum for single crystals of l-lys·HCl·H_2O irradiated at 66K and warming to 298K;* ***(b)*** *EPR spectrum for single crystals of l-lys·HCl·H_2O irradiated and detected at 298K. The magnetic field is along <c> in* ***(a)*** *and* ***(b)****.*

Radicals RII and RIII were identified as the radical dehydrogenated at C5 and at C2 respectively detected at 298K in the crystal irradiated at 298K. Radicals R2 and R3 were identified as the same radical as RII and RIII, respectively, after the temperature of the crystal was lowered to 66K. The small conformation change of these two dehydrogenation radicals during the temperature change could be due to the effects of the hydrogen bonds. In these two radicals, the hydrogen bonds related to the carboxyl group, the main-chain amino group and the guanidyl group were not broken and held the radicals firmly, thus little reoirenation occurred. The decarboxylation radical and the radical dehydrogenated at C5 were identified in the crystals irradiated at 66K. From the previous studies of irradiated amino acids[17], the two

dehydrogenation radicals could be the secondary products of the decarboxylation radical, or from the radical losing an electron and then deprotonated at C5 or C2.

However, the stable product of the guanidyl radical anion, the radical detected in the crystal irradiated at 66K, was not found at room temperature.

Reference

1. A. Joshi and R. H. Johnsen, Kinetics of radical decay in crystalline amino acids. II. High-temperature study. *The Journal of Physical Chemistry* **80,** 46-51 (1976).

2. J. J. Tria, D. Hoel and R. H. Johnsen, The kinetics of radical decay in crystalline amino acids. 7. Monohydrates. *The Journal of Physical Chemistry* **83,** 3174-3179 (1979).

3. M. Aydin, M. H. Baskan, S. Yakar, et al., EPR studies of gamma-irradiated L-alanine ethyl ester hydrochloride, L-arginine and alanyl-L-glutamine. *Radiation Effects and Defects in Solids* **163,** 41-46 (2008).

4. B. Olsen, *Study of free radicals in single crystals of L-arginine monophosphate monohydrate at 295K and 77K*. (Master thesis in physics) Physics Institue, University of Oslo, (2008).

5. M. J. Frisch, G. W. Trucks, H. B. Schlegel, et al., **Gaussian 03,** (Gaussian Inc., Wallingford CT, 2004)

6. J. Dow and L. H. Jensen, Refinement of structure of arginine hydrochloride monohydrate. *Acta cryst. B* **26,** 1662-1671 (1969).

7. G. C. A. M. Vanhaelewyn, B. Jansen, E. Pauwels, et al., Experimental and Theoretical Electron Magnetic Resonance Study on Radiation-Induced Radicals in α-L-Sorbose Single Crystals. *The journal of physical chemistry. A* **108,** 3308-3314 (2004).

8. H. M. McConnell, Indirect Hyperfine Interactions in the Paramagnetic Resonance Spectra of Aromatic Free Radicals. *J. Chem. Phys.* **24,** 764-766 (1956).

9. R. W. Fessenden and R. H. Schuler, Electron Spin Resonance Studies of Transient Alkyl Radicals. *J. Chem. Phys.* **39,** 2147-2195 (1963).

10. W. Gordy, *Theory and Application of Electron Spin Resonance*. John Wiley & Sons, Inc, New York, NY, (1980).

11. W. A. Bernhard, The use of alpha hyperfine coupling tensors as a measure of unpaired spin density and free radical geometry. *J. Chem. Phys.* **81,** 5928-5936 (1984).

12. P. A. Erling and W. H. Nelson, Dependence of α-Proton Hyperfine Couplings on Free Radical Geometry. *The Journal of Physical Chemistry A* **108,** 7591-7595 (2004).

13. C. Heller and H. M. McConnell, Radiation Damage in Organic Crystals. II. Electron Spin Resonance of $(CO_2H)CH_2CH(CO_2H)$ in β-Succinic Acid. *J. Chem. Phys.* **32,** 1535-1539 (1960).

14. J. R. Morton, Electron Spin Resonance Spectra of Oriented Radicals. *Chemical Reviews* **64,** 453-471 (1964).

15. S.-i. Kuroda and I. Miyagawa, ENDOR study of an irradiated crystal of L-alanine: Environment of the stable $CH_3CHCO_2^-$ radical. *J. Chem. Phys.* **76,** 3933-3944 (1982).

16. E. Sagstuen, E. O. Hole, S. R. Haugedal, et al., Alanine Radicals: Structure Determination by EPR and ENDOR of Single Crystals X-Irradiated at 295 K. *The Journal of Physical Chemistry A* **101,** 9763-9772 (1997).

17. E. Sagstuen, A. Sanderud and E. O. Hole, The Solid-State Radiation Chemistry of Simple Amino Acids, Revisited. *Radiation Research* **162,** 112-119 (2004).

CHAPTER 9.

SUMMARY AND GENERAL CONCLUSIONS

Three radicals types, R1-R3(LT/LT)[I] were detected in L-lysine·HCl·2H_2O single crystals irradiated at 66K. R1(LT/LT) and R2(LT/LT) were identified as the carboxyl anion radical and the decarboxylation radical, respectively, and R3(LT/LT) could not be assigned. Two small couplings in R1(LT/LT) were ascribed to the protons transferred from neighboring molecules to the carboxyl group through the intermolecular hydrogen bonds after an electron was trapped by the carboxyl group. DFT geometry optimizations performed on cluster models reproduced the radical structures and the proton transfers in R1(LT/LT). In crystals irradiated at 298K, five radicals R1-R5(RT/66K) were observed at 66K. R1a (RT/LT) was identified as the main chain deamination radical. DFT calculations on an ONIOM model with a side chain amino proton transferred to a carboxyl oxygen in a neighboring molecule reproduced the experimental values very well. This suggests that R1a (RT/66K) is the product of deamination and proton loss. The magnetic data show that R1b (RT/66K) is in a conformation different from R1a (RT/66K). The analysis indicated that the two β-protons in R1b have dihedral angles more than 30° different from those in R1a. R2(RT/66K) and R3(RT/66K) gave very similar EIE patterns and coupling tensors, and full geometry optimizations with ONIOM models supported that they were two different radicals, from dehydrogenation at C4 and C5, respectively. These computations ruled out the possibility that they were the same radical with two different conformations. Because too little information was obtained, radicals R4(RT/LT) and R5(RT/LT) could only be assigned tentatively as the side chain deamination radical and the C3 dehydrogenation radical, respectively. DFT calculations using the proposed structures for R4(RT/LT) and R5(RT/LT) agreed with the experimental data. At room temperature, only the main-chain deamination, C4 dehydrogenation, and C5 dehydrogenation radical were detected. (ENDOR from R4(RT/LT) and R5 (RT/LT) was too weak to be detected.) WINSIM

[I] LT/LT stands for the irradiation and observation both at 66K; RT/LT stands for the irradiation at room temperature, and observation at 66K; RT/ RT stands for the irradiation and observation both at room temperature.

simulations for the EPR spectra estimated the relative concentrations of R1-R5(RT/66K) in L-lysine·HCl·2H_2O single crystals as 50% (R1a), 11%(R1b), 14% (R2), 16% (R3), 6% (R4), and 3% (R5).

Four radicals, R1-R4(LT/LT) were detected in L-arginine·HCl·H_2O single crystals irradiated at 66K. R1a(LT/LT) and R1b(LT/LT) were identified as the two configurations of carboxyl anion radical: the β-proton coupling in R1a(LT/LT) is much larger than that in R1b(LT/LT); both have O-H dipolar protons, but they are from the different neighboring molecules. R1a(LT/LT) and R1b(LT/LT) appear to reflect behaviors of the two molecules in the asymmetric unit. R2(LT/LT) was identified as the decarboxylation radical, and R3(LT/LT) was identified as the guanidyl anion radical with an electron trapped by the carbon atom in the guanidyl group. R4(LT/LT) was identified as the radical from dehydrogenation at C5, and this radical also was detected in the crystals irradiated at room temperature with a conformation very similar to that of R2(RT/LT). Four radicals, R1-R4, were detected at 66K and 298K in the crystal irradiated at room temperature. Radical R1 was identified as the main-chain deamination radical, detected in three conformations (R1a-R1c) at 66K. DFT calculations indicated that R1a(RT/LT) has no O-H protons, R1b(RT/LT) and R1c(RT/LT) have two O-H dipolar protons. Moreover, the side chain in R1b(RT/LT) reoriented along with the rest of the radical, while reorientation of the side chain in R1c(RT/LT) was limited, apparently by the environments. At 298K, only one conformation of deamination was detected and was best characterized by the structure with two O-H dipolar couplings. R2(RT/LT) and R3(RT/LT) were identified as the radicals from dehydrogenation at C5 and C2, respectively, but R4 (RT/LT) could not be assigned. The relative concentrations of R1-R4(RT/LT) in L-arginine·HCl·H_2O single crystals are: ~30% of R1a, ~13% of R1b, ~12% of R1c, ~25% of R2, ~15% of R3 and ~5% of R4.

From above results, and from previous studies on irradiated amino acids, the mechanisms of radiation damage to lysine and arginine can be proposed. As shown in Fig. 9.1, the main-chain deamination radical was the product of reduction leading to the carboxyl anion radical, and the

dehydrogenated radicals were the product of oxidation directly or via secondary reactions of the decarboxylation radical.

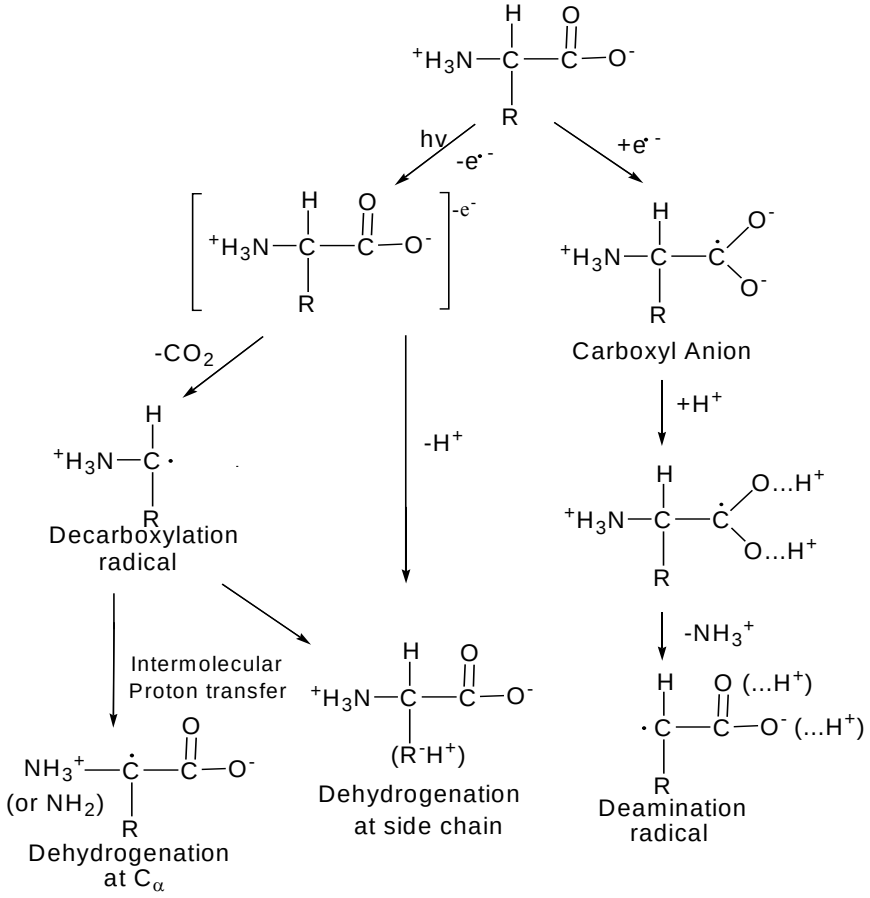

Fig. 9.1 *The reactions in irradiated L-arginine·HCl·H_2O and L-lysine·HCl·$2H_2O$ single crystals.*

Furthermore, from the above results, the possible effects from the radicals in arginine and lysine to DNA-histone complex can be suggested. The main-chain deamination and the decarboxylation radicals were identified as the major radicals in the two types of crystals irradiated at 66K and at 298K, respectively. It is known that linkage of the main-chain amino and carboxyl groups in amino acids builds up the backbone of the proteins (see Fig. 9.2). Thus, main-chain deamination and the decarboxylation in arginine and lysine within histone will break the backbone linkage. This type of linkage dissociation from deamination was found from ESR studies of irradiated peptides.[1, 2] In addition, based on crystallographic studies of the nucleosome, amino protons and carbonyl oxygen atoms are involved in many hydrogen

bonds to DNA and play an important role in association of histone to DNA.[3, 4] Thus, main-chain deamination or decarboxylation of arginine and lysine in histone, can weaken the DNA-histone association. This effect was reported by Lloyd and Peacocke in 1965.[5] More studies on the irradiation damage to DNA in vivo are needed to verify if the main-chain deamination and the decarboxylation radicals can be formed in chromatin and if they can induce the hydrogen bond breakage between histone and DNA.

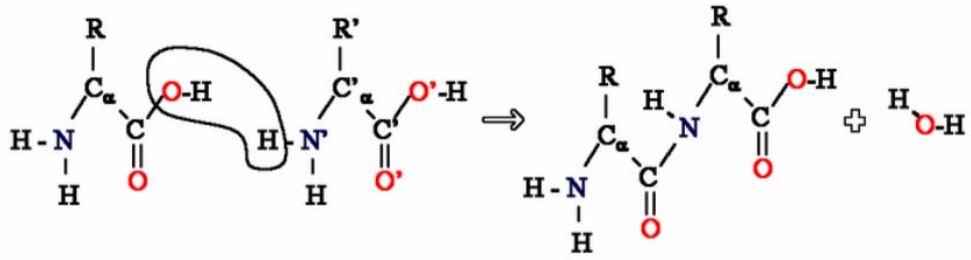

Fig. 9.2 *Creation of peptide bond from two amino acids.*

References

1. J. Sinclair and P. Codella, Radiation damage produced in single crystals of N-acetylglycine. *J. Chem. Phys.* **59,** 1569-1576 (1973).

2. H. C. Box, *Radiation effects-ESR and ENDOR analysis*. Academic Press, INC., New York, NY, (1977).

3. K. Luger, A. W. Mader, R. K. Richmond, et al., Crystal structure of the nucleosome core particle at 2.8Å resolution. *Nature.* **389,** 251-260 (1997).

4. C. A. Davey, D. F. Sargent, K. Luger, et al., Solvent Mediated Interactions in the Structure of the Nucleosome Core Particle at 1.9 Å Resolution. *Journal of Molecular Biology* **319,** 1097-1113 (2002).

5. P. H. Lloyd and A. R. Peacocke, The Action of γ -rays on Deoxyribonucleohistone in Solution. *Proceedings of the Royal Society of London. B* **164,** 40-62 (1966).